UNIVERSITÀ DEGLI STUDI DI MILANO
DIPARTIMENTO DI
SCIENZE DELLA TERRA "ARDITO DESIO"

IPRaMa: Induced Polarization for Raw Materials

A thesis submitted to attain the degree of

Dottore di Ricerca in Scienze della Terra

Presented by

Francesco Dauti

Academic Year

2024-2025

PhD Cycle XXXVII

Advisor: Prof. *Gianluca FIANDACA*

Thesis Reviewers:

Dr. *Burke MINSLEY*

Prof. *Thomas GÜNTHER*

Defense Committee:

Prof. *Albert Sancho FOLCH*

Prof. *Mauro GIUDICI*

Prof. *Denys GROMBACHER*

Prof. *Thomas GÜNTHER*

PhD Coordinator:

Prof. *Giovanni MUTTONI*

La borsa di dottorato è stata cofinanziata con risorse del

Programma di finanziamento PON REACT-EU

Azione IV.5 – Dottorati su tematiche green

Questa tesi riflette solo i punti di vista e le opinioni degli autori, né l'Unione Europea né la Commissione Europea possono essere considerate responsabili per essi.

The doctoral scholarship was co-funded with resources in the frame of the

PON REACT-EU financing Program

Action IV.5 – Doctorates on green topics

This thesis reflects only the authors' views and opinions, neither the European Union nor the European Commission can be considered responsible for them.

besim

Acknowledgements

For this work I acknowledge Emergo s.r.l which co-financed this PhD project, the CSIRO organization, Geoscience Australia and Gaia Exploration for the technical and economic support during my abroad periods.

For the supervision of the project, I acknowledge Prof. Gianluca Fiandaca for his constant example of passion, determination, sacrifice and dedication to the matter and to his group. Together with Gianluca, I acknowledge Dr. Andrea Viezzoli for believing in me and in my attitude providing possibilities, comprehension, opportunities and vision that guided me in the last 6 years.

For the final shape of this thesis, I acknowledge the reviewers of this work, Prof. Thomas Günther and Dr. Burke Minsley. Their time and precious insights not only provided significative improvements to the work but also to my personal growth as scientist.

For my abroad period in the down under (and not only!) I acknowledge the Geoscience Australia Geophysical Acquisition and Processing group, Dr. Yusen Ley Cooper, Dr. Ross Brodie, Dr. Anandaroop Ray, Wayne and Phil, for their lovely technical and human support and to made me feel home down there. Together with them, I also acknowledge Dr. Tim Munday from CSIRO, in Perth, for all the opportunities, inputs and enthusiasm he brought into this project. Closer to home, I acknowledge Isla Fernandez for hosting me in Gaia Exploration in Spain and for sharing with me data and exploration approach to develop part of this thesis. I then acknowledge Dr. Ana Jesus for hosting me at Lisbon University where we spent fruitful times trying to conciliate geology and geophysics. Her contribute deeply improved the geological interpretation and understanding of the geophysical results.

Finally, I acknowledge the groups with which together we shared these years in the good and in the pain. The EEMteam for Hydro and eXploration group from University of Milano, born together with the start of our PhD, Alice, Stefano1, Stefano2, Nicole, Alessandro, Jian and Chiara; and the Emergo crew that supported with enthusiasm this adventure, Cettina, Arianna, Simone, Federico, Sofia, Michele and Antonio il Padre Maestro.

In the end, most importantly, for the disinterested support, patience, comprehension and fundamental presence I acknowledge Laura, my friends and my family.

Abstract

As the global economy transitions to cleaner energy, the ability to accurately map mineral deposits has become a key challenge to achieve decarbonization goals. The development of innovative and non-invasive exploration methods is essential to ensure the sustainable exploitation of natural resources, minimizing environmental impact and respecting local communities. Among the useful indirect techniques that can be applied to describe the ground physical properties, this thesis focuses on the Airborne Induced Polarization (AIP) method.

Electromagnetic (EM) methods—both airborne (AEM) and ground-based—are known to be sensitive to induced polarization (IP) effects when surveying chargeable grounds. Although the relevance of IP phenomena in EM data has been demonstrated in numerous studies, these effects are frequently overlooked in standard exploration workflows. This is largely due to the challenges associated with recognizing IP signatures in EM data space and the complexities involved in incorporating them into inversion frameworks. The modelling of IP effects in EM data often leads to non-unique solutions which increase the model ambiguity and decrease its interpretability: the relationship to both geology and galvanic chargeability become unclear, and the complexity of IP modelling is not repaid.

This thesis investigates various aspects of airborne induced polarization, addressing both methodological challenges and applied case studies across multiple spatial scales. These include a continental-scale study using fixed-wing AEM systems in Australia, a mine-scale investigation in Spain, and a greenfield exploration program in Portugal. In the latter, AIP-derived anomalies identified from airborne data informed the design and execution of targeted ground-based follow-up surveys. Together, these case studies illustrate the potential of AIP methods to enhance subsurface characterization in chargeable terrains and contribute to more effective mineral exploration strategies.

The first study is developed to assess the TEMPEST™ fixed-wing sensitivity to IP effects, first on synthetics and then on real data. This system is currently flying the entire Australia to map the Country's ground resistivity and being able to model also its chargeability would add an important layer of information to geological description and mineral targeting. We first theoretically demonstrate the system sensitivity to AIP effects by computing and mapping one-hundredth-thousand forward responses to define the parametric range of sensitivity to AIP of the method. Then, moving to real data, the synthetic results have been confirmed comparing the modelling results with other helicopter-borne platforms and inverting a portion of 20,000-line km of Australia with ground-proved consistency of the retrieved chargeability models with geology.

The application scale is then reduced, from continental to deposit-scale, and a comparison between ground galvanic Direct Current Induced Polarization (DCIP) and airborne inductive chargeability is carried. The comparison has been done within an active mining project in Spain where a helicopter-borne EM survey overlaps 17 ground DICP profiles. These have been first independently modelled, proposing a multi-mesh approach for AEM data and a consistent modelling for ground DCIP, showing a good comparability between the retrieved models. Then, to uniquely solve the ground chargeability through the merging of the sensitivities of the methods, a joint inversion considering the IP effects is carried between the two and a unified chargeability model is obtained. Through the joint modelling a shared field of sensitivity with the galvanic method is shown and the AIP capability to resolve the ground chargeability consistently with the ground methodology has been demonstrated.

Finally, an AIP survey for a greenfield exploration project in Portugal has been designed to define chargeable targets on which follow-up on the ground. Here, after a feasibility study, two AEM surveys have been flown with different base frequencies, 25 Hz and 12.5 Hz, to improve the near surface resolution and the IP effects recording, respectively . After an independent and joint modelling of the two considering the IP effects, the ground DCIP follow-up has been defined and acquired over an airborne-defined anomaly. The ground results confirmed the airborne model and the approach, from the feasibility to the integration, has been effective. The airborne and galvanic datasets have then been jointly modelled, merging two different inductive base frequency surveys and a three decades DCIP dataset to resolve the ground resistivity and chargeability.

From a general point of view, this work shows that the chargeability models retrieved from different sources (inductive/galvanic) and acquired at different scales is consistent when properly treated. As implication, a regional/continental-scale chargeability mapping can be a valuable tool to define where to develop a next exploration step with a proved physical reliability and with consistency with the galvanic method.

Table of Contents

Chapter 1: Motivation, theory and introduction to the research developments

As overview, this PhD project aims to give a contribute to the understanding of the airborne induced polarization (AIP) method and to its application for mineral exploration. During this project, I worked to improve the use of the AIP-derived chargeability as a reliable tool for geological mapping and mineral targeting. The general aim of this project lies into the development of novel solutions for the exploration for Critical Raw Materials (CRMs).

This chapter focuses on illustrating the general goals of the thesis, the theoretical background, the modelling approach and a few introductory experiments to provide the reader the tools to better understand the work. This is structured in three main sub-chapters: motivation (*1.1*), theoretical background (*1.2*) and thesis outline (*1.3)*. The theoretical sub-chapter is then subdivided in three main sections, each treating a different method used in the thesis (airborne EM in *1.2.1*, galvanic induced polarization in *1.2.2* and inductive induced polarization in *1.2.3*) and containing dedicated sections to specific aspects (e.g., governing equations, acquisition systems, modelling approach, etc…).

All datasets used in this PhD project are public, except those in *Chapter 3* which have been acquired by a private mining company active in the Spanish Pyritic Belt. The data used in *Chapter 2* are acquired within the Australian *Exploring for the Future AusAEM* project while the data used in *Chapter 4* are acquired within the European Horizon *SEMACRET* project. The experiments of this thesis are conducted using a novel modelling algorithm (EEMverter) and its associated software ecosystem (EEMstudio) developed by the EEM-Team for Hydro and eXploration group and the EEM-Team spin-off Company from the University of Milano. Refernces and details will be provided in the continuation of the thesis.

1.1: Motivation

The decarbonization of global economies, essential for mitigating anthropogenic impacts on the Earth's climate system, relies on the secure and sustainable supply of essential mineral resources across the clean energy supply chain. As outlined in the International Energy Agency's report, "The Role of Critical Raw Materials in the Clean Energy Transition," achieving net-zero greenhouse gas emissions—such as those targeted under the European Green Deal—necessitates the deployment of low-carbon technologies that are materially intensive. These technologies rely on a set of critical raw materials, including copper, lithium, manganese, and nickel, which currently lack significant production capacity within the European Union. According to projections by the International Energy Agency (IEA, 2021), the global demand for key raw materials essential to the energy transition is expected to increase by up to 400% by 2040. Within the European Union, demand for rare earth elements (REEs) is anticipated to grow sixfold by 2030 and sevenfold by 2050. Lithium demand is projected to escalate even more significantly—by a factor of twelve by 2030 and twenty-one by 2050—driven largely by the proliferation of battery technologies and electric mobility. Despite this projected surge, the EU currently accounts for less than 3% of global production of critical raw materials and remains heavily dependent on external supply chains. Presently, the EU imports 100% of its rare earth elements from China, 99% of its boron from Turkey, and 71% of its platinum from South Africa. These materials are classified as Critical Raw Materials due to their dual-risk profile: (i) their high economic and strategic significance for key technologies underpinning the energy transition, including permanent magnets, batteries, and fuel cells; and (ii) their high supply risk resulting from a concentrated production base in a limited number of third countries, many of which are characterized by geopolitical volatility, market instability, or weak governance frameworks.

To react to these challenges and strengthen its mineral supply chain, the European Union is promoting innovation at different levels, both bureaucratic and technical, to shorten the path to the objectives of the *European Green Deal*. In support of this, the stipulation of the *Critical Raw Materials Act* in 2021 defined the minimum points to be reached within the year 2030. These can be summarized with:

- at least 10% of the EU's annual consumption for extraction
- at least 40% of the EU's annual consumption for processing
- at least 25% of the EU's annual consumption for recycling
- no more than 65% of the EU's annual consumption from a single third country

Given the current context, there is a growing need for robust technical support to enable efficient, modern, and environmentally sustainable mineral mapping. Among all the initiatives, regulations and projects that the EU is supporting to stimulate the mineral industry in the continent, a common objective underlies them all: minimizing the environmental and social impact of new exploration and exploitation activities. In this sense, the need to locate and exploit novel critical mineral deposits cannot be decoupled from a renewed way to explore, making the technological innovation essential to find effective solutions. Large international projects involving both academia and industry have been financed in the last years to drive innovation in this field. Examples are the Horizon projects, such as the Smart Exploration Project (https://smartexploration.eu/) in 2017 to sustain developments in exploration of CRM, the INFACT project (https://www.infactproject.eu/) in 2020 for new non-invasive geophysical mapping and the SEMACRET project (https://semacret.eu/), to define novel approaches to the mineral targeting started in 2022. As well as research projects, national governments have also founded PhD programmes to contribute to the technological innovation of *green* themes (environment, groundwater, mining) encouraging academic research on specialized topics. Within this framework, this PhD project is situated on the field of geophysical research for mineral exploration with a focus on Airborne Induced Polarization (AIP) method and its application to mineral exploration.

The AIP methodology integrates the strengths of two well-estabilished techniques: ground induced polarization (DCIP) and airborne electromagnetic (AEM). From an exploration perspective, this hybrid approach offers the potential to detect both chargeable zones—often indicative of disseminated mineralization—and conductive bodies associated with massive mineralization, within the scope of a large-scale airborne survey. The theoretical basis of this technique was first established in the late 1980s, when was demonstrated the electromagnetic sensitivity to the ground frequency-dependent resistivity. Subsequent research expanded these principles to airborne EM systems, revealing that characteristic signatures related to ground IP effects can indeed be observed in AEM data. Although the theoretical prove of sensitivity of inductive methods to IP effects, their application in industry for mineral mapping has been limited given the technical differences with the galvanic DCIP (in terms of base frequency, ground energisation, system footprint…) and by the complexity in modelling the AIP effects. At this regard, using a dispersive resistivity to model the EM data largely expands the model space and exposes the inversion procedure to large non-uniqueness, equivalencies and ambiguities. These limitations have often brought over-precautionary modelling approaches to AIP and lead to a lack of confidence in translation of the recovered physical properties into geology. This created crucial unknowns for the application of the inductive IP technique to mineral targeting and geological mapping. Furthermore, the frequent inconsistencies observed in galvanic versus inductive IP comparisons, combined with the well-established efficacy of DCIP methodologies, have reinforced galvanic techniques as the standard for subsurface chargeability mapping.

With this work I focus on the open questions that the Airborne Induced Polarization method still has. Specifically, I aim to reduce of the equivalencies during the AIP modelling, to adopt a consistent modelling between airborne and ground IP to improve the comparability and on the joint inversion between the two. Afterwards, I apply the findings to a real greenfield mineral exploration case. With this approach, I aim to better define the AIP sensitivity to geological targets and understand its potential for mineral targeting. In terms of benefits, being able to effectively model the ground chargeability using an airborne survey could open new possibilities for exploration. It would reduce human and economic risks, driving the ground follow-up with the airborne results, and increase the targeting distinguishing between regional and anomalous features.

1.2: Theoretical background: airborne electromagnetics, induced polarization and inductive induced polarization

1.2.1: Electromagnetic theory: an introduction

Electromagnetic methods are one group of geophysical techniques that allow an estimation of the subsurface distribution of electric properties via non-invasive measured observations. In this thesis, with Time Domain EM methods I mean low frequency methods (~6.25/12.5/25 Hz to 100k Hz, e.g., Legault 2015) that are sensitive primarily to the electrical properties (like resistivity and chargeability) of the subsurface. This excludes high frequency techniques such as ground penetrating radar: these are electromagnetic in nature but fundamentally different from the range of low-frequency methods normally encompassed by the term electromagnetic geophysics. The EM methodologies are divided in two main groups in function of the source with which the ground is energised: the natural source EM methods, that exploit the natural variations in the atmospheric EM field, and the controlled source EM methods, where the energising field is generated by a transmitter (e.g., Nabighian, 1988; Zhdanov, 2017). This thesis will be uniquely focused on controlled source inductive electromagnetic methods and, in particular, with time-domain transient EM (TEM) method.

1.2.1.1: Electromagnetic governing equations and geophysical approximations

All the electromagnetic phenomena are governed by Maxwell's Equations. These four equations give the complete description of the electromagnetic field behaviour relating the electric and magnetic field vectors interaction.

In materials, these presents as:

$$\nabla \cdot \boldsymbol{D} = \rho \tag{1.1}$$

$$\nabla \times \boldsymbol{E} = -\frac{\partial \boldsymbol{B}}{\partial t} \tag{1.2}$$

$$\nabla \cdot \boldsymbol{B} = 0 \tag{1.3}$$

$$\nabla \times \boldsymbol{H} = \boldsymbol{j} + \frac{\partial \boldsymbol{D}}{\partial t} \tag{1.4}$$

Where **J** is the current density (A/m^2), **E** is the electric field intensity (V/m), **B** is the magnetic flux density (T), **H** is the magnetic field intensity (A/m) and **D** is the electric displacement (C/m^2).

Equation 1.2 is a mathematical statement of the Faraday Law: an electric field exists in the region of a time-varying magnetic field, such that the induced electromotive force is proportional to the negative rate of change of magnetic flux. Equation 1.4 is a mathematical statement of the Ampere Law (taking into account Maxwell's displacement current d**D**/dt), namely that a magnetic field is generated in space by current flow and the field is proportional to the total current (conduction plus displacement) in the region.

The field intensity vectors (**E** and **H**) are related to the flux density vectors (**D**, **B**) through the following constitutive equations:

$$\mathbf{D}=\varepsilon(\omega,r,T,P,..)\mathbf{E} \tag{1.5}$$

$$\mathbf{B}=\mu(\omega,r,T,P,..)\mathbf{H} \tag{1.6}$$

$$\mathbf{J}=\sigma(\omega,r,T,P,..)\mathbf{E} \tag{1.7}$$

Assuming $\boldsymbol{E}(t) = \boldsymbol{E}e^{i\omega t}$ and $\boldsymbol{H}(t) = \boldsymbol{H}e^{i\omega t}$.

Where ε is the Electric Permittivity (C·V/m), μ is the Magnetic Permeability (H/m), σ is the Electric Conductivity (S/m), ω (rad/s) is the angular frequency, T and P represent temperature and pressure, r is the position variables.

Taking the curl of equations 1.2 and 1.4, it is possible to separate Maxwell's equations in terms of $\boldsymbol{E}$ and $\boldsymbol{H}$ vectors. The vectorial equations for these take the following forms:

$$\nabla^2 \boldsymbol{E} = (i\omega\mu\sigma - \varepsilon\mu\omega^2)\boldsymbol{E} \tag{1.8}$$

$$\nabla^2 \boldsymbol{H} = (i\omega\mu\sigma - \varepsilon\mu\omega^2)\omega^2\boldsymbol{H} \tag{1.9}$$

and constitutes the equations for the propagation of electric and magnetic fields in an isotropic and homogeneous medium. Here, the terms involving $i\omega\mu\sigma$ are related to the conduction current, whereas the terms involving $\varepsilon\mu\omega^2$ are related to the displacement current.

The physical properties ε, μ and σ and the angular frequency ω can be grouped into one term k^2 given by:

$$k^2 = -i\omega\mu(\sigma + i\omega\varepsilon) = \mu\varepsilon\omega^2 - i\omega\mu\sigma \tag{1.10}$$

Where k is the complex wavenumber.

This allows to re-write the field equations as:

$$\nabla^2 \boldsymbol{E} + k^2\boldsymbol{E} = 0 \tag{1.11}$$

$$\nabla^2 \boldsymbol{H} + k^2\boldsymbol{H} = 0 \tag{1.12}$$

It is possible to distinguish two end-member cases as function of k:

1. At low frequencies (f<10^5 Hz) the displacement currents are much smaller than the conduction current if the ground is not highly resistive. This is because ε for most geologic materials is small ($\varepsilon \approx$ 1-100ε_0 where $\varepsilon_0 \approx 8.86 \cdot 10^{-12}$ F/m) and the conductivity for favourable targets in EM surveys is usually >10^{-2} S/m. In this regime, called inductive regime, the wavenumber is given by:

$$k^2 = -i\omega\mu\sigma \tag{1.13}$$

2. At frequencies of the order of 10 MHz or higher, displacement currents dominate over conduction currents in earth materials of low conductivity ($\sigma < 1$ mS/m). For this case, the propagation parameter is given by:

$$k^2 = \mu\varepsilon\omega^2 \tag{1.14}$$

Another way to express 1.13 is that the magnetic field varies slowly enough that radiation effects can be ignored. Under this condition, called the *quasi-static approximation*, the magnetic field can be considered a potential field describable by the Biot-Savart law:

$$dB = \left(\frac{\mu_0}{4\pi\, r^2} I\right) \mathrm{dl} \times \mathrm{r} \tag{1.15}$$

Where **r** is the distance unit vector of a point with respect of a conductor section d**l**.

This means that the magnetic field has the same time-dependence everywhere, making the force propagation in each space point instantaneous (Fitterman and Labson, 2005). In free space this condition is met when distance between magnetic sources and receivers is less than the wavelength of EM radiation. In conductors, the criterion for use the quasi-static approximation depends upon the electrical conductivity of the material.

1.2.1.2: Induction in a simple loop circuit

The EM system with which the measurements are acquired bases its functioning on the mutual induction that is established between three objects: the transmitting circuit, the investigated halfspace and the receiving circuit. To illustrate the EM physics, I follow the approach proposed by West and Macnae (1991), which simplify the halfspace as a simple loop coupled by mutual induction to the transmitter and receiver loops, as illustrated in *figure 1.1.* This simplification makes allows to focus on the physical meaning of the EM methods, instead of the complex mathematics need to treat properly layered halfspaces.

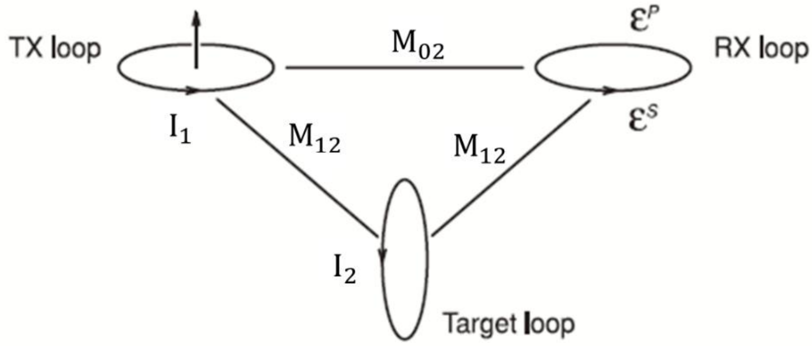

Figure 1.1 Simple loop EM system, schematized (West and Macnae, 1991).

For this description, the subscript "1" is referred at the transmitter loop, the subscript "2 to the target loop and the subscript "3" to the receiver loop.

A current $I_0 e^{i\omega t}$ flows in the transmitter loop under the quasi-static approximation, for which its intensity can be thus considered constant along the loop. Each loop is described through a resistance R and a self-inductance L, and mutual inductances exist among all three loops. For any combinations of the indices i and j ranging from 1 to 3, the flux Φ_{ij} of the magnetic field in the j^{th} loop generated by the current in the i^{th} can be written as:

$$\Phi_{ij}(\omega) = M_{ij} I_i(\omega) \tag{1.16}$$

where M_{ij} is the mutual inductance [H] between loops *i* and *j*, while $L_i = M_{ii}$ is the loop self-inductance.

The electromotive force (*emf*) produced in the j^{th} loop by the time-varying flux is given by:

$$\begin{aligned} emf_j &= -i\omega\Phi_{ij}(\omega) \\ &= -i\omega M_{ij} I_i(\omega) \end{aligned} \tag{1.17}$$

For the target loop, the induced current is given by the *emf* induced by the transmitter divided by the loop impedance:

$$I_2 = \frac{-i\omega\Phi_{12(\omega)}}{R_2 + i\omega L_2} = \qquad (1.18)$$
$$= \left(\frac{-i\omega\tau}{1 + i\omega\tau}\right) \cdot \frac{M_{12}\, I_1(\omega)}{L_2}$$

Where $\tau = L_2/R_2$ [s].

At low frequencies ($\omega\tau \ll 1$), the induced current becomes:

$$I_2 = \frac{-i\omega\Phi_{12(\omega)}}{R_2} \qquad (1.19)$$

That is, the induced current is 90° out-of-phase with respect to the transmitter current. This is called the *resistive limit* when the resistance of the target loop is large compared to its inductive reactance. At high frequencies ($\omega\tau \gg 1$), the current approaches:

$$I_2 = \frac{-\Phi_{12(\omega)}}{L_2} \qquad (1.20)$$

The induced current is in-phase with the transmitter current. This regime is called the *inductive limit*, when the inductive reactance of the target loop is large compared the resistance.

In the target, the *emf* due to the transmitter current (primary *emf*) is given by:

$$emf_2^P = -i\omega M_{12} I_1(\omega) \qquad (1.21)$$

And the *emf* in the target produced by the target current (secondary *emf*) is found by:

$$emf_2^S = -i\omega L_2 I_2(\omega) = \tag{1.22}$$
$$= \; -i\omega L_2 \left(\frac{-i\omega\tau}{1+i\omega\tau}\right) \cdot \frac{M_{12}\, I_1(\omega)}{L_2}$$

In the inductive limit the above equation reduces to:

$$emf_2^S = i\omega M_{12} I_1(\omega) = \; -emf_2^P \tag{1.23}$$

This indicates that at high frequencies the induced currents try to counteract the *emf* due to the primary field. The primary signal, produced by the transmitter current, has a value at the receiver coil given by:

$$emf_3^P = -i\omega \Phi_{13}(\omega) = -i\omega M_{13}\, \mathrm{I}_1(\omega) \tag{1.24}$$

While the secondary signal due to the target current is:

$$emf_3^S = -i\omega \Phi_{23}(\omega) = -i\omega M_{23}\, I_2(\omega) \tag{1.25}$$

Normalizing the secondary signal by the primary:

$$\frac{emf_3^S}{emf_3^P} = \left(\frac{M_{23}}{M_{12}}\right) \cdot \left(\frac{I_2}{I_1}\right) = \left(\frac{-i\omega\tau}{1+i\omega\tau}\right) \cdot \left(\frac{M_{12}M_{23}}{M_{13}L_2}\right) \tag{1.26}$$

The second fraction on the right-hand side of *equation 1.26*, which contains the ratio of the mutual inductances, depends only upon the geometric coupling of the transmitter loop, the receiver loop, and the target. This is the only part of the response that will change as the transmitter-receiver array is moved relative to the target. The first fraction on the right-hand side is the frequency response of the target, which depends upon its electrical properties and geometry (Fitterman and Labson, 2005).

In time domain, energising a homogeneous halfspace with a step turn-off, the EM response is described by the inverse Fourier transform as in equation:

$$I(t) = \left(\frac{M_{12}I_1}{L}\right) e^{-\frac{t}{\tau}}\, u(t) \qquad t \geq 0 \tag{1.27}$$

Where u(t) is the Heaviside step function. And the relative voltage *V(t)* at the receiver:

$$V(t) = M_{13}\left(\frac{\partial I}{\partial t}\right) = I_1 \left(\frac{M_{12}M_{23}}{L}\right) \left[\delta(t) - \frac{e^{-t/\tau}}{\tau}\right] \tag{1.28}$$

Where $\delta(t)$ is the Dirac Delta function.

In the target, an "instantaneous" peak of current is observable (*figure 1.2.a*), followed by an exponential decay (*figure 1.2.c*), as visible in *figure 1.2*.

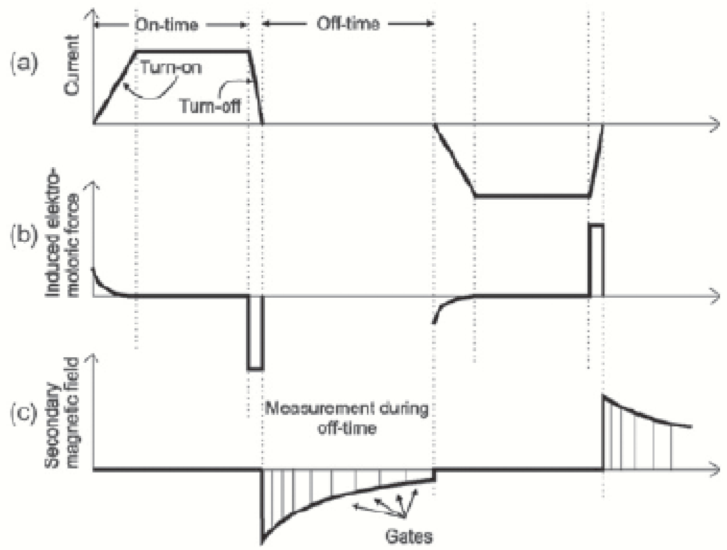

Figure 1.2. Target response in Time Domain. From the top to the bottom: transmitter current (step function); emf behaviour into the target; secondary current recording and sampling at the end of a waveform cycle (Dentith, 2014).

From the equation above follows that a voltage measured on a resistive halfspace will decay faster than a voltage measured on a conductive one. It is also possible to observe that at t = 0 the induced current $\mathbf{I}(t)$ depends only an L, and not a R.

These theoretical considerations are fully valid only if the halfspace is approximated to a single loop circuit. This approximation is not applicable in reality; energising an halfspace with a circular transmitter of radius a, in which the current I flow at ω frequency, the vertical magnetic field **B** is described by (e.g., Effersø et al., 1999):

$$B = \frac{I_a}{2}\int_0^{\infty}\left[e^{-u_0(z+h)} + R(\, e^{u_0(z+h)})\right]\frac{\lambda^2}{u_0}J_1\, d\lambda \tag{1.29}$$

Where h and z are the transmitter and receiver altitude, R is an interface reflection coefficient (for each interface of a layered halfspace), J_1 is the Bessel function of first order, $\lambda = \sqrt{k_x^2 + k_y^2}$ and u_0 is the propagation factor given by:

$$u_0 = \sqrt{\frac{\lambda^2 + i\omega\mu_0}{\rho}} \tag{1.30}$$

1.2.1.3: Time-Domain Electromagnetics method, an overview

In the Time Domain Electromagnetic (TDEM) systems the illustrated change in primary magnetic field is produced by either abruptly turning off or turning on a steady (d.c) current, as shown in *figure 1.3*, that flows in the transmitter loop and obtaining a series of pulses.

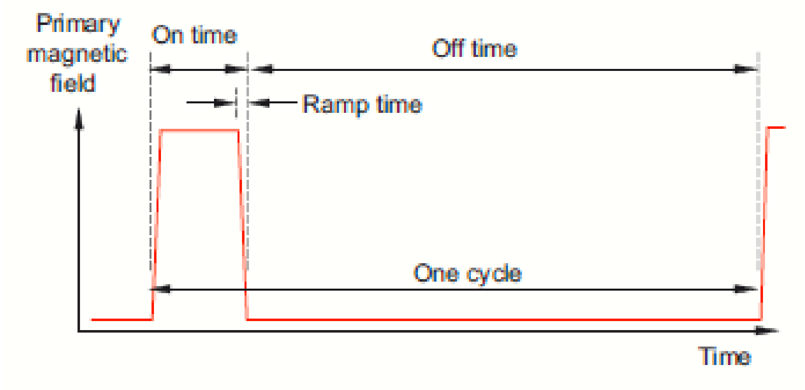

Figure 1.3: A waveform example with illustrated its components (Dentith, 2014).

Each successive pulse has an opposite polarity to the previous one, and these pairs repeat with fixed period that is determined by the system base frequency. The period during which the transmitter is active (i.e. the current flows) is referred as "on-time" while after the current is switched off is referred as "off-time". During the off-time the secondary field produced by the induced currents in the ground is recorded. The ratio off-time to on-time is normally 1 to 1 and defines the transmitter duty-cycle of 50%; it is possible to use also different ratios, such the common 2 to 1, which defines a duty-cycle of 33%. The transmitter current is turned off during the so-called turn-off ramp, that is generally variable from few microseconds up to 2 ms. For airborne acquisitions, the peak current generally ranges from 7 to 250 A; the higher the peak current, the longer it takes to turn off the current; similarly, the higher the transmitter loop area and/or the number of turns, the higher the self-inductance and thus the time necessary to turn the current off.

The secondary magnetic field is measured as a function of time from the end of each turn-off. This is sampled with a frequency in the range of few tens to hundreds of Hertz for AEM systems. To reduce the noise measurement, the recordings are stacked and sampled using logarithmical increasing time windows (Munkholm and Auken, 1996). Assuming a noise with Gaussian distribution, the S/N ratio is proportional to $\sqrt{n}$ where n is the number of measurements in the stack. The log-gating strategy increases the stack size for progressively later time gates, reducing the standard deviation of noise through time by a factor of the square root of the gate length. The ground surveys have a definite advantage on the AEM systems coming from the stacking of measurements at fixed position for a long time. The AEM systems, being moving systems, derive less benefit from this procedure. However, the lesser flight speed of the helicopter-TEM systems, compared with the fixed wing systems, allows to collect and to stack 2 to 3 times more data per km.

An example of *time windows* retrieved after log-gating is visible in *figure 1.4*. With this sampling, the noise slope decreases with a $t^{-1/2}$ factor, with t indicating the off-time acquisition time.

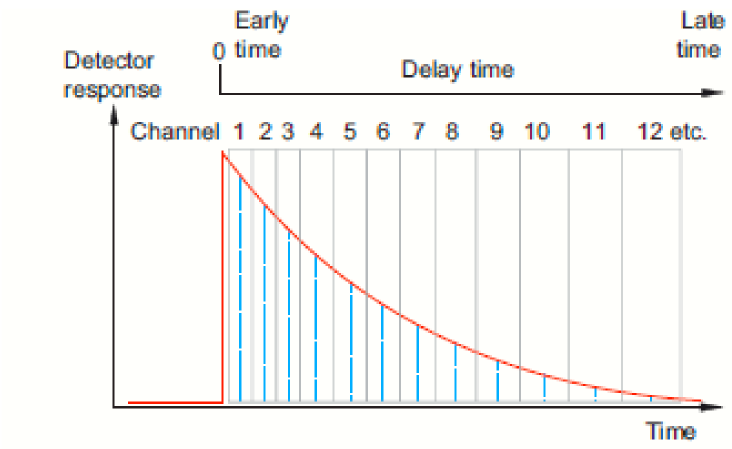

Figure 1.4. Sampling of the recorded secondary magnetic field (Dentith, 2014).

The measured signal (the transient) represents the decay voltage curve proportional to the rate of change of the magnetic secondary field. According to Grant and West (1965), using the ratio between T (where $T = 2\pi \left(\frac{\mu\sigma}{2t}\right)^{-1/2}$) and r (the distance between transmitter and receiver coil), it is possible to define three different transient portions referred to a conductive body over which a theoretical transient is recorded:

a) Early times: $T/r \ll 1$
b) Mid times: $T/r \approx 1$
c) Late times: $T/r \gg 1$

In *a)* the induced currents remain confined near the surface of the conducting body, while in *b)* the surface currents begin to dissipate their energy. Consequently, the innermost parts of the conductor will be subjected to a magnetic field that decays over time. This event repeats itself several times over time, generating a flow of induced currents which diffuse into the innermost portion of the conductor. When the distribution of the induced current pervades the conductor and no longer varies over time, the *c)* is reached.

Another way of looking at the fields induced in the subsurface during a TEM measurement is the approach developed in Nabighian (1979), which states that the effect of all induced currents in the halfspace can be approximated to that of a single filament of toroidal geometry whose centre moves downwards at a speed:

$$v = \frac{2}{\sqrt{\pi\mu\sigma t}} \tag{1.31}$$

And that laterally increases in diameter with a trend equal to:

$$D = \sqrt{\frac{17.48 \cdot t}{\sigma\mu}} \tag{1.32}$$

From the above equations is also visible how induced currents remain for more time in a conductive layer rather than in a resistive one and that the toroidal geometry increases its size in the presence of a resistive layer.

As time goes by, the induced currents spread over increasing volumes and their intensity, due to ohmic losses and density decreasing, decays tending to zero. The attenuation of the primary signal is a consequence of energy loss by the circulating secondary magnetic field. The phenomenon is known as skin effect and depends by the frequency of the electromagnetic field (its rate of change). It determines the penetration of the EM fields into a medium and strongly controls the depth of investigation of EM measurements. For a sinusoidally varying field penetrating uniform conductive medium, the skin effect is quantified, in frequency-domain, in terms of a parameter known as skin depth (δ), that defines the distance over which the amplitude of EM field is attenuated by 1/e (i.e. 37%) of its surface value. It is given by:

$$\delta = \sqrt{\frac{2}{\sigma\mu\omega}} \tag{1.33}$$

where ω is the angular frequency.

It is assumed that the conductivity and the magnetic permeability are frequency independent and that displacement currents can be ignored. This quantity shows instant-per-instant the depth at which the induced current intensity is maximum.

Except for ferromagnetic minerals, the geologic materials have a magnetic permeability that can be approximated as nearly the same as in vacuum, i.e., $\mu_0 = 4\pi \cdot 10^{-7}$(Zhdanov and Keller, 1994); this makes the field attenuation almost exclusively controlled by frequency and conductivity. The fields decay faster in materials of high conductivity and for fields of higher frequencies. The skin depth is a useful quantity to quantify the maximum depth of investigation, using coaxial and coplanar acquisition geometry:

$$z_{max} = 0.55 \left(\frac{M}{\sigma n}\right)^{\frac{1}{5}} \tag{1.34}$$

Where M is the transmitter dipole moment, σ is the conductivity and n the noise level.

Finally, it is interesting to observe that with the skin depth it is possible to evaluate the signal decay at early times and late times for a homogeneous halfspace. The early times behaviour is defined by that time instants for which $2\pi\delta \ll 1$ (Kauffman and Keller, 1983).

1.2.1.4: Airborne Electromagnetic systems

Airborne electromagnetics (AEM) is one of the most popular geophysical methods used in mineral exploration around the world. AEM was initially developed after the Second World War to explore for mineral deposits (Fountain, 1998) and since then has been strongly and continuously enhanced extending his exploration capabilities.

According to Fountain (1998), AEM systems can be classified into two main categories, represented in *figure 1.5*, each including several sub-categories that specify the system features (frequency or time domain, ground or airborne source, etc…):

- Fixed Wing Platform (FTEM, FFEM)
- Helicopter Platform (HTEM, HFEM)

The suffix “FEM” refers to frequency-domain systems while “TEM” to Transient-EM time-domain systems. In this thesis work I focus on the time-domain systems only, given their wider field of application, constant development and a more advanced knowledge on the AIP effects content in their data.

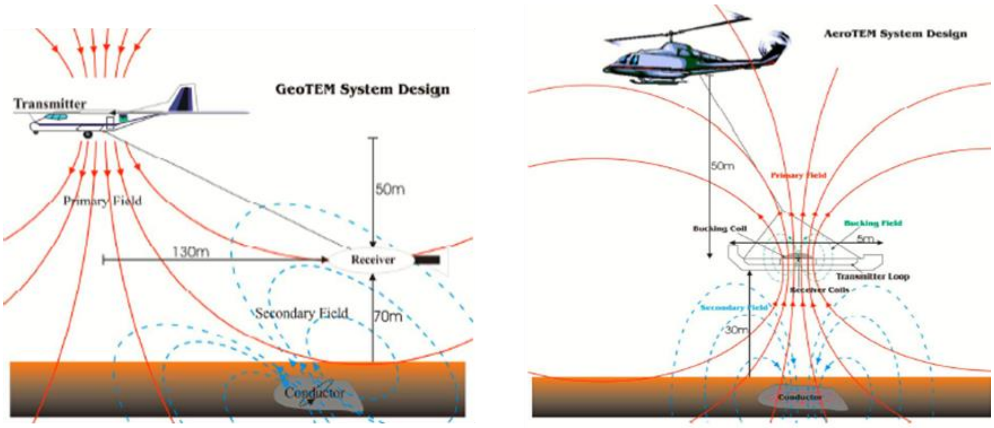

Figure 1.5 On the left: fixed wing airborne system. On the right: helicopter platform system. (Modified from www.fugroairborne.com).

In this thesis work, an entire chapter (*Chapter 2*) is dedicated to the detection and modelling of AIP effects in fixed-wing systems. The reasons of the research have been presented in *section 1.1* and will be illustrated in detail in the dedicated chapter; here, a methodological difference between the fixed-wing and helicopter-borne systems is presented. Both the platforms share the same principle of functioning, using an active source (a current that flows in a loop) to create a primary time-varying magnetic field and using receiver coils to measure the secondary-field ground response. About the differences, as also visible from *figure 1.5*, these systems have different geometrical, operative and processing workflows and configurations. In *table 1.1,* a technical overview of two fixed-wing systems (TEMPEST™, object of study in *Chapter 2*, and SPECTREM Plus, mentioned in *Chapter 2*) and two helicopter-borne systems (SkyTEM, compared with the fixed-wing in *Chapter 2* and HeliTEM[2], object of study of *Chapter 4*) is provided to show the general differences.

AEM System Parameters	**TEMPEST standard (fixed-wing)**	**SPECTREMPLUS (fixed-wing)**	**SkyTEM^{508} (helicopter-borne)**	**HeliTEM^{2} (helicopter-borne)**
Tx diameter (m)	17.6	23.1	28.6 (LM) 30.6 (HM)	35
No. turns	1	1	1 (LM) 8 (HM)	4
Tx Area (m^2)	244	420	536	961
Nominal Tx elevation (m)	120	90	45	35
Nominal peak current (A)	280	1800	7 (LM) 120 (HM)	145
Nominal peak moment (Am^2)	68 320	756 000	4 000 (LM) 492 000 (HM)	557 380
Base frequency (Hz)	25	Optional: 25 75	Simultaneously acquired: 275 (LM) 25 (HM)	Optional: 6.25 12.5 25
Waveform	Square	Square	Square	Square
Duty cycle	50%	100%	25%	50%
Nominal Rx elevation (m)	70	50	47	35
Bandwidth	B.F. – 37.5kHz	Not available	B.F. – 300 kHz	B.F. – 61 kHz
Nominal transmitter-receiver horizontal separation (m)	-115	-120	-12.4	0
Nominal transmitter-receiver vertical separation (m)	-40	-40	+2.09	0
AEM System Parameters	**TEMPEST standard (fixed-wing)**	**SPECTREMPLUS (fixed-wing)**	**SkyTEM^{508} (helicopter-borne)**	**HeliTEM^{2} (helicopter-borne)**
Gate times (ms)	0.013 -16.2	0.026-16.65	0.0234-1.484 (LM); 0.238-19.921 (HM)	0.030 – 9.2 (25Hz); 0.030–20 (12.5 Hz); 0.030–40 (6.25 Hz);

No. channels/Off-time Gates	15	10	19 (LM); 18 (HM)	25
Recorded secondary field type	dB/dt	dB/dt	dB/dt	dB/dt
Delivered secondary field type	B (X, Z components)	B (X, Y, Z components)	dB/dt (X, Z components)	dB/dt (Z component)

Table 1.1 Summary of the main features of two popular fixed-wing (TEMPEST™ and SPECTREM$_{PLUS}$) and helicopter-borne platforms (SkyTEM and HeliTEM^2). The sign of the distances between transmitter and receiver is negative when the receiver is below or behind the transmitter, the opposite when positive.

As overview, the fixed-wing systems typically have an in-offset configuration with the transmitter (Tx) loop separated from the towed receiver (Rx) coil of about 100 m. The high-power transmitter (magnetic moment up to 3 million Am^2 as for the Fugro MEGATEM system) generates a large primary field, which in combination with a large transmitter-receiver separation, results in significant depth of penetration. However, the effect of the large transmitter and receiver separation combined with the higher ground clearance, results in a diminished spatial resolution so that ground geophysical surveys are often required to follow-up the targets detected by fixed-wing systems. Helicopter-borne systems are flown at smaller terrain clearance and at a slower speed compared to fixed-wing systems. These systems also have a much smaller transmitter-receiver separation (being often exactly concentric as for the VTEM, HeliTEM^2 or Xcite systems) giving a higher spatial resolution and monitoring possibilities during flights.

Another significant difference between fixed-wing and helicopter-borne platform is the primary field compensation. In a fixed-wing platform the primary field in the receiver is diminished by the high lateral offset between Tx and Rx. Also, the varying receiver bird position during survey complicates the primary field modelling through processing, forcing the introduction of simplifications and approximations in the recorded data. An example for the TEMPEST™ fixed-wing system processing procedure is illustrated in *section 2.1.2* of *Chapter 2*.

Differently, in helicopter-borne platforms, it is possible to compensate the primary field through geometrical solutions such the SkyTEM's zero-position (e.g. Nyboe et al., 2018) or the VTEM, Xcite, HeliTEM^2 bucking coil. By careful design, the effectiveness of this bucking coil on primary cancellation is reduced rapidly away from the receiver coil, so that at surface its reduction of the primary field is less than 2% (e.g. Legaut, 2015). Alternatively, the SkyTEM system places the receiver in the so-called zero position, i.e. a position around the Tx frame in which the primary field is zero (e.g. Sorensen and Auken, 2004). The cancellation/absence of the primary field results in an accurate measurement of the secondary field recorded during the transmitter off-time that is very diagnostic of high conductance targets. The combination of the helicopter capability to survey at low altitudes at a relatively slow velocity, and the close transmitter/receiver separation significantly enhances spatial resolution, making the system better able to identify closely spaced discrete conductors.

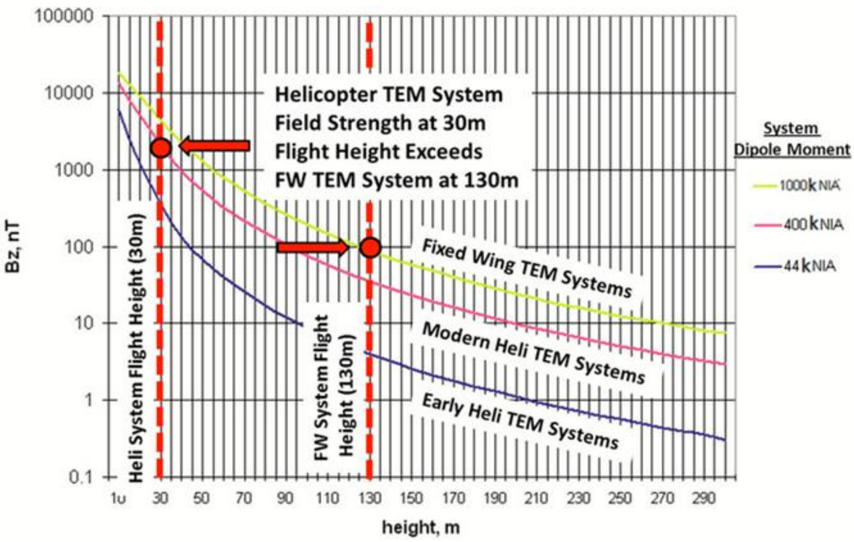

Figure 1.6. Synthetic theoretical primary magnetic field strengths according to flight height and transmitter dipole-moment for Fixed Wing and Heli TEM systems (Legault (after Prikhodko), 2015).

Figure 1.6 compares primary magnetic field strengths for FTEM and HTEM systems based on flight-height and transmitter dipole-moment, which is a measure of system power. The significant differences between these two systems leads to different fields of uses of them. While HTEM-HFEM systems are now widely used for medium-small surveys for both groundwater mapping and mineral exploration, FTEM-FFEM platforms are used for very large surveys with regional mapping purposes, given their technical characteristics. One of the most interesting and pioneering projects involving the use of fixed wing surveys, is the Exploring for the Future Project (Ley Cooper at al., 2020) carried out by Geoscience

Australia with the aim of mapping the mining potential of the entire Australian continent. Further details on this project will be provided in the next chapter.

1.2.1.5: Materials Electrical properties and EM noise sources

As discussed, the ground EM response is controlled by several of its physical properties: conductivity (mS/m), magnetic permeability (H/m) and electrical permittivity (F/m). As reported in *section 1.3.1.1*, the relative magnetic permeability is generally negligible and, from the quasi-static approximation, also the electrical permittivity is not considerably determinant. For these reasons, the parameter that almost exclusively controls the EM response is represented by the electrical conductivity σ (or from his reciprocal, ρ=1/σ, the electrical resistivity) of the subsurface. The typical resistivity range in Earth materials vary from 0.1, to 100 000 $\Omega \cdot m$, as visible in *figure 1.7*.

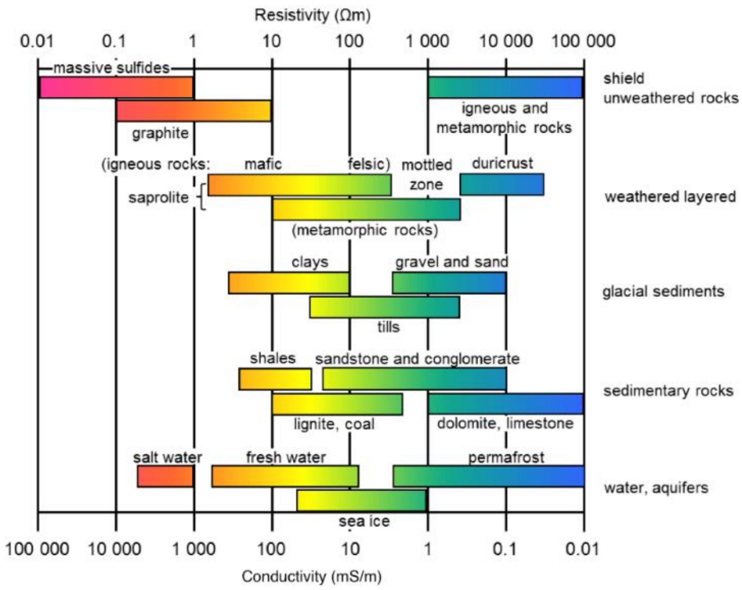

Figure 1.7. Typical resistivity (and conductivity) ranges for the main geological materials (Nabighian, 1987).

The measured EM signal is not only function of the geological materials.

There are also other factors which are important components of the acquired data, such as:

- System geometry
- Intensity and frequency of the circulating current
- Length of the charging and discharging ramps (waveform)
- Topography
- Transmitter terrain clearance

The sources of noise related to the system include the coil motion and the secondary response of the system. The receiver coil movement in the earth's magnetic field produces a large amplitude, low frequency and parasitic signal (Annan, 1983) that can be removed by high-pass filtering. However, rapid oscillations of the receiver coil can add some sensible noise at higher frequency. This noise, very difficult to filter out, represents a challenge for the data provider that need to set-up a mechanically stable (theoretically static) receiver coil during data acquisition. Another source of noise is due to the response of the system. In the HTEM systems, the transmitter and the receiver are far enough from the helicopter, so these effects can be considered weak and constant. However, for HTEM systems but mainly for FTEM systems, the standard compensation procedure consists in measuring the system response at high altitude, before and after each flight, and deconvolving or subtracting these responses from the measured off-time response after acquisition (Allard, 2007). There is also numerous noise sources related to instrumental drifts, generally due to pressure and temperature variations, or to a non-correct instrument calibration that affects the survey performance. Modern surveys can now better manage these issues by actively re-calibrate the instruments and by estimating the noise levels (and so deductible from the measured data).

The noise affecting the measured signal, and not related to the EM system, can be produced by natural causes or derived from cultural sources. The natural noise presents several peaks in the EM noise spectrum; at frequencies below 1 Hz, usually derives from fluctuations in the Earth's magnetic field. Given its low frequency, this noise does not influence the transient measurements. On the contrary, the noise at frequencies higher than 1 Hz, can compromise the TEM data quality. This type of noise originates from lightnings and thunderstorms. This noise varies during the day, being less powerful during the night than during day, and during the year, being stronger during summer compared to winter. The amplitudes are generally 5 to 10 times greater than the vertical field, and when numerous spherical events are present, it is difficult to filter them out because their amplitude and time distribution are essentially random.

The EM data are also affected by noise sources generated by antropic disturbances. For example, the EM system can interact with high voltage lines that have a frequency of 50 Hz in Europe or of 60 Hz in America creating distortion in the dataspace. For solving this issue, the current base frequency is 30 Hz in Europe, 25 Hz in America or odd multiples of these frequencies (Nabighian and Macnae, 1991). Anomalous EM responses can be due to currents induced in metal conductors such as iron fences or distribution networks and pipes that are located above the investigated half-space. These objects can channel the currents and generate an electromagnetic coupling which affects the recorded voltage values. The resulting transient is a signal which decays at late times like t^{-1} instead of $t^{-5/2}$ (Nekut and Eaton, 1990). There are two different types of coupling: capacitive and galvanic. The capacitive coupling is easily recognized also in a single EM transient for its oscillating character, while the galvanic coupling, involving a simple shift of the EM transient, can be more difficult to identify when considering a single transient. The EM coupling is removed through careful manual processing, attributing odd decays to possibly overlapping anthropic sources visualizing the data in a GIS environment.

1.2.1.6: Inductive EM Induced Polarization detection

During the late 1960s, the first studies appeared in which the EM sensitivity to Induced Polarization (IP) effects was demonstrated (Bhatthacharyya 1964, Dias 1968, Morrison et al. 1969). The first IP signature in EM data was recorded in the '80s (Spies 1980) in an EM ground survey for which negative voltages where recorded and their physical explanation have been firstly associated with induced polarization effects of the ground. Only in the late '90s with a work conducted by Smith and Klein (1996), the capability of Airborne EM data to detect IP signals was demonstrated. Compared to EM signals, the IP signals can reach amplitudes even greater than the purely electromagnetic component of the recorded signal. Hence, with the early AEM systems, it was not clear if the measured negatives were from chargeable materials or if they were simply noise generated by power lines or electric fences (Smith and Klein, 1996). However, instruments have improved with time and the validity of negative transients as signal has been firmly established with both synthetics (Macnae, 2016; Kaminski and Viezzoli, 2017; Viezzoli et al., 2020; Dauti et al., 2024) and field examples (Legault et al., 2015, Kang et al., 2017, Grombacher et al. 2021, Dauti et al., 2023). For instance, negative voltages were recorded over the Tli-Kwi-Cho kimberlite deposit consistently with three different AEM systems and with the known mineralization signature (Kang et al., 2017) or in Antarctica by the SkyTEM system in the MacMurdo Valley (Grombacher et al. 2021). As the quality of instrumentation improves, it is expected that more IP signals will be measured in airborne data. This increasing detection ability provides motivation for developing methodologies that can extract chargeability information from airborne IP data. Various approaches, including simple curve-fitting, 1D inversions, and 3D inversions have been developed and successfully applied to field examples (for 1D applications: Kratzer and Macnae, 2012; Kwan et al., 2015; for 3D AIP modelling: Cox et al., 2024; Chen et al., 2025b). Moreover, more advanced phenomenological studies for IP detection and quantification (Viezzoli and Manca, 2019; Viezzoli et al., 2021, Dauti et al., 2024) have shown how the IP effects does not necessarily manifest in the inductive EM dataspace with negative voltages only: the IP effect can distort the recorded transient without giving negatives and opening up to the possibility to mislead the IP-affected transient to resistive response or noise. For this reason, algorithms for IP recognition in the dataspace have been developed (Viezzoli et al., 2021) to map in the data-space the IP-distortion probability in the recorded datasets and that require a dispersive-resistivity modelling. Further details on the IP detection and phenomenology will be treated in the next sections of this thesis.

1.2.2: Induced polarization theory: an introduction

In the early 1930s the effect of polarization currents was recognized during the acquisition of ground georesistivity data. A DC electric current in the ground is abruptly switched off during an energising, the voltage between the potential electrodes does not drop to zero instantaneously. After a large initial decrease, the voltage exhibits a gradual decay and can takes seconds or even minutes to reach a zero value, as can be seen in *figure 1.8*. A similar phenomenon is observed as the current is switched on (Telford, 1990): after an initial sudden voltage increase, the voltage increases gradually over a discrete time interval to a steady-state value.

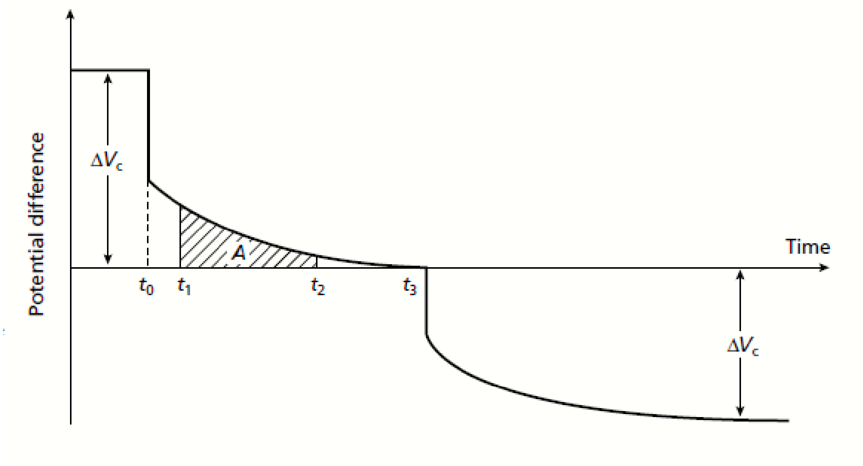

Figure 1.8: The phenomenon of induced polarization. At time t0 the current is switched off and the measured potential difference, after an initial large drop from the steady-state value ΔVc, decays gradually to zero. A similar sequence occurs when the current is switched on at time t3. 'A' represents the area under the decay curve for the time increment t_1-t_2. (Kearey, 2002)

This phenomenon has been termed "Induced Polarization" and is easily observed when electronically conducting minerals or clay minerals are present in the ground. When a variable low-frequency AC source is used, it is found that the measured apparent resistivity of the subsurface decreases as the frequency is increased. This is because the capacitance of the ground inhibits the passage of direct currents but transmits alternating currents with increasing efficiency as the frequency rises. The ground thus acts as a capacitor and stores electrical chargeas it becomes electrically polarized.

The energy storage is the result of the combination of two main effects:

- Variations in mobility of ions in fluids throughout rock structure
- Variation between ionic and electronic conductivity where metallic minerals are present.

The first effect depends on the *membrane polarization (e.g.,* Marshall and Madden 1959; Klein and Sill 1982; Vinegar and Waxman 1984) and/or *electrolytic polarization* and constitutes the base of the so-called *Normal IP Effect.* The second one is known as *electrode polarization* or *overvoltage*.

The membrane polarization can be explained as consequence of the electrolytic flow in the pore fluid as consequence of a passage of current through a rock given by an externally imposed voltage. Most of the rock forming minerals have a net negative charge on their outer surfaces in contact with the pore fluid and attract positive ions onto this surface *figure 1.9a*. The concentration of positive ions extends about 100μm into the pore fluid, and if this distance is of the same order as the diameter of the pore throats, the movement of ions in the fluid resulting from the impressed voltage is inhibited. Negative and positive ions thus build up on either side of the blockage and, on removal of the impressed voltage, return to their original locations over a finite period causing a gradually decaying voltage.

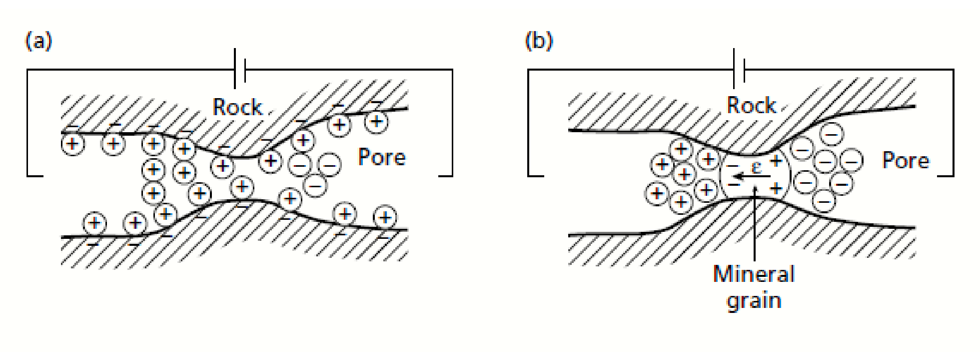

Figure 1.9: Membrane Polarization (a) and Electrode Polarization (b) (Kearey, 2002).

The other component, the electrode polarization (*figure 1.9b*), is related at phenomena that act on the interfaces of materials with different mechanism of electric conduction. Considering a medium in which are present rocks composed by metallic minerals immersed in a porous matrix, containing an anionic-cationic solution in water. Inside the matrix there is an electro-ionic conduction while inside the metallic grains an electronic one. At the interface between matrix and grains an ionic accumulation with opposite charge is established with consequent formation of dipoles.

1.2.2.1: Induced Polarization modelling

Induced polarization (IP) is manifested by frequency-dependent behaviour of electrical conductivity. This phenomenon is also called the 'low-frequency dispersion' of the electrical conductivity (or its inverse, the electrical resistivity). Despite several physical–chemical models that have been developed to describe the frequency dispersion, the most commonly used phenomenological model for field application is the Cole–Cole model (CCM), which was originally formulated for the complex dielectric constant (Cole and Cole 1941).

In geophysical applications, based on the electrostatic analogy for dielectric materials with losses, Pelton et al. (1978) proposed the following original equation for impedance:

$$Z(\omega) = R_0 \left\{ 1 - m \left[1 - \frac{1}{1 + (i\omega\tau)^c} \right] \right\} \tag{1.37}$$

where $Z(\omega)$ is the impendence, R_0 is the DC (low frequency) resistance, c a pure number and $\omega = 2\pi f$ the energising electric field angular frequency. Pelton's equation can be expressed in terms of the complex resistivity. Using Seigel's (1959) definition of the chargeability based on the resistivity:

$$m = \frac{\rho_0 - \rho_\infty}{\rho_0} \tag{1.38}$$

where ρ_0 and ρ_∞ are the low-frequency resistivity limit and the high-frequency resistivity limit ($\rho_\infty \rightarrow \infty$), respectively. Substituting these resistivities for the resistances, one obtains (Kemna, 2000):

$$\rho(\omega) = \rho_0 \left\{1 - m\left[1 - \frac{1}{1 + (i\omega\tau)^c}\right]\right\} \tag{1.39}$$

In details, the four Cole-Cole parameters in equation 1.39 are:

- ρ_0, the DC resistivity ($\omega = 0$).
- m, the chargeability. As firstly defined by Seigel (1959), it is usually expressed in mV/V and its range varies from 0 (no IP effect) to 1000 mV/V.
- τ, the time constant [s], can vary from 10^{-6} to 10^{3} s (Macnae, 2016). It controls the time taken by the material to charge or discharge by $1/e$ as the electric field passes.
- C, dimension-less parameter included in a range of 0 and 1. It describes the frequency dependence of the modelled IP phenomenon.

In particular, τ and c also take on a geological as well as numerical significance: the τ time constant is not controlled by the material geology but from its geometry features, such as grain size and body dimension in mineral exploration (Pelton et al. 1978). The c parameter is directly proportional to the sorting of the encountered geological material (Vanhala and Peltoniemi, 1997). These two parameters strongly condition the effectiveness of the induced polarization.

Pelton et al. (1978) proposed also an equivalent circuit accounting for equation 1.37, depicted in figure 1.10, in which R_0 is relative to the porous fraction where exists only electrolytical conduction, and R_1 to the porous fraction where electrode polarization can be created. The complex impedance $Z' = (i\omega X)^{-c}$ as well as considering the inductive reactance, simulates the metal-ion interface in the presence of mineralized clasts that give rise to electrode polarization. In direct current with $\omega = 0$, the current flows only in the purely-resistive branch of the equivalent circuit; at high frequencies the complex impedance decreases, and the impedance of the circuit tends to an equivalent resistance formed by R_0 and R_1 in parallel.

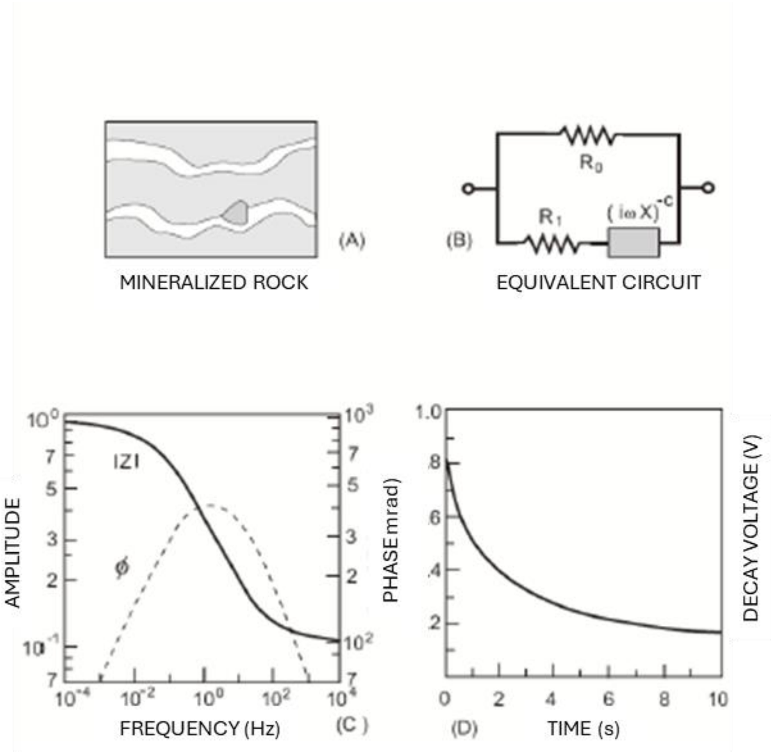

Figure 1.10. Modified from Pelton et al. (1978): (a) A small section of a mineralized rock which has both blocked and unblocked pore passages. (b) An equivalent circuit for the mineralized rock. (c) Typical frequency domain response for the equivalent circuit. (d) time domain response, in seconds, corresponding to the frequency domain response plotted in (c).

In the equivalent circuit, m becames:

$$m = \frac{1}{R_0 + \frac{R_1}{R_0}} \tag{1.40}$$

The voltage decay over time of the equivalent circuit corresponds, for any c to:

$$V(t) = mR_0 I_0 \sum_{n=0}^{\infty} \frac{(-1)^n \left(\frac{t}{\tau}\right)^{nc}}{\Gamma(nc+1)} \tag{1.41}$$

Where I_0 is the intensity of a current that charge the body and Γ is the gamma function with $n \in \mathrm{N}$.

In this thesis, a re-parameterization of the Cole-Cole formula is used for modelling polarization, i.e. the Maximum Phase Angle (MPA) model proposed by Fiandaca et al. (2018). This model expresses the Cole-Cole formula using, instead of the classic parameters m_0 and τ_σ (or τ_ρ), the parameters φ_{max} and τ_φ. The relaxation time τ_φ represents the inverse of the angular frequency ω at which the phase of the Cole-Cole model $\varphi(\omega)$ reaches its maximum, while φ_{max} is the maximum itself. The reason for using MPA parameterization instead of the classic Cole-Cole formula, is that much weaker correlations exists between the MPA parameters instead of the classic ones, considerably improving the inversion results reducing possible equivalencies (Fiandaca et al., 2018).

1.2.3: Induced polarization effects in inductive EM

To explain the IP phenomenology in AEM data, the model presented by Flis et al. (1989) is presented in *figure 1.11*, which shows a small volume of polarizable rock under the influence of a vortex (i.e. inductive) current. Although polarization and inductive currents are coupled, their separation is justified on the grounds that the energy source for the inducted current is a collapsing magnetic field, while for the polarization current, the source is the capacitive nature or the IP phenomenon (membrane/electrolytic and electrode polarization).

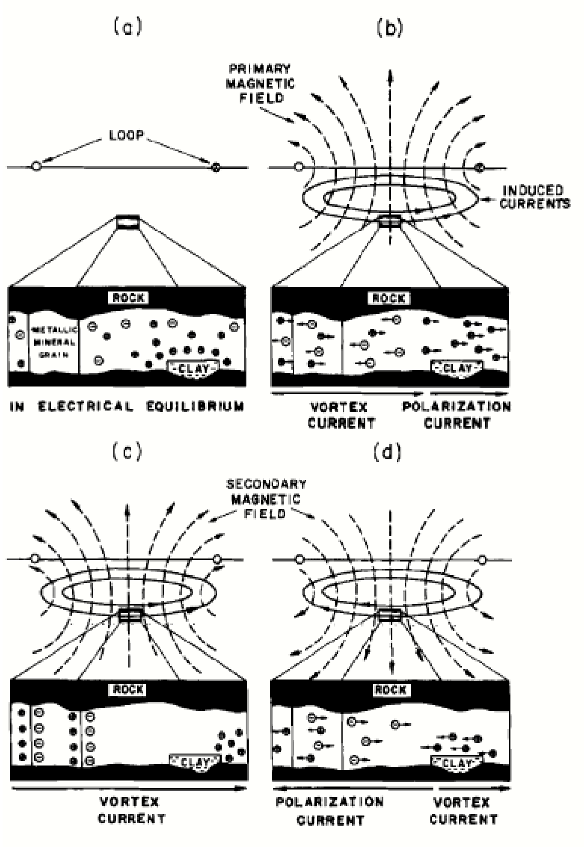

Figure 1.11. Schematics diagram of Flis et al. (1989) of ionic movement in a volume of polarizable rock beneath a TEM transmitter loop. (a) Before transmitter turnoff, ions are in electrical equilibrium with any metallic mineral grains and negatively charged clays present. (b) During turnoff and for a short time thereafter, cations, driven in the same direction as the vortex current, constitute a positive polarization current. (c) At some intermediate time, the ions attain a fully charged state and the polarization current is zero. (d) At later times, the decaying vortex current can no longer support this charged state; the ions drift back to their original positions producing a negative polarization current.

Flis et al. (1989) define two types of current density in the medium:

- the total current density J_{total}, which is computed solving the TEM forward response with a Cole-Cole complex conductivity;
- the polarization current density $J^{0}_{pol} = J_{total} - J_0$, which is obtained subtracting from the total current J_{total} the purely-resistive current J_0 of a medium with resistivity ρ_0.

The inductive current J_0 increases with time during the turn-off of the primary field, reaches a maximum and then fades out due to ohmic dissipation; on the contrary, the polarization current J^{0}_{pol} is positive when J_0 increases and negative when J_0 decreases.

Smith (1989b) argues that the interpretation of Flis et al. (1989) defines the wrong polarization current. In fact, Smith (1989b) and Smith and West (1988) define the polarization current as $J^{\infty}_{pol} = J_{total} - J_{\infty}$, i.e. subtracting from the total current the one of the purely resistive medium obtained for $\rho_{\infty} = \rho_0 \cdot (1 - m_0)$.

The differences between the J_{∞} and J_0 currents and the time evolution of J^{∞}_{pol} is presented in *figure 1.12*.

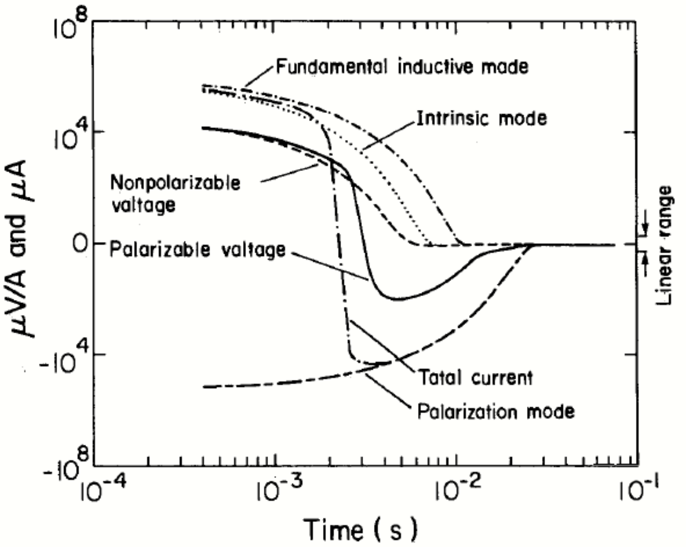

Figure 1.12. Comparison between fundamental inductive mode J_{∞}, intrinsic mode J_0, polarization mode J^{∞}_{pol} and total current J_{total} (from Smith and West, 1988).

For appreciating the differences between the two ways of defining the polarization currents, I believe that it is helpful to re-write the Cole-Cole formula in terms of complex conductivity. The Cole-Cole formula of equation 1.39 can be written in terms of complex conductivity as:

$$\sigma(\omega) = \sigma_0\left\{1 + \frac{m}{1-m}\left[1 - \frac{1}{1+(i\omega\tau_\sigma)^c}\right]\right\} \tag{1.42}$$

Equations 1.39 and 1.42 represent one the inverse of the other when the relative relaxation times obey the relation:

$$\tau_\sigma = \tau \cdot (1-m)^{\frac{1}{c}} \tag{1.43}$$

Equation 1.42 can be re-written in terms of the conductivity at infinite frequency $\sigma_\infty = \frac{\sigma_0}{1-m}$ as:

$$\sigma(\omega) = \sigma_\infty\left\{1 - m\left[\frac{1}{1+(i\omega\tau_\sigma)^c}\right]\right\} \tag{1.44}$$

Multiplying the conductivity of equation 1.44 by the electric field we obtain the total current density $J_{total}(\omega)$ as a function of the infinite-frequency induction current $J_\infty = \sigma_\infty \cdot E$:

$$J_{total}(\omega) = J_\infty - J_\infty m\left[\frac{1}{1+(i\omega\tau_\sigma)^c}\right] \tag{1.45}$$

where the second term in equation 1.45 is the frequency-domain polarization current $J_{pol}^{\infty}(\omega)$ defined by Smith and West (1988). Time-transforming equation 1.45 and convolving it with the current waveform we can obtain the time-evolution of both J_{total} and J_{pol}^{∞} (and, of course, of J_{pol}^{0}).

Without taking parts in the debate between Flis et al. (1989) and Smith (1989b), equation 1.45 has the advantage of making very evident that the total current density is obtained from the sum of the inductive current J_∞ and the polarization current $J_{pol}^{\infty}(\omega) = -J_\infty m\left[\frac{1}{1+(i\omega\tau_\sigma)^c}\right]$, which has always opposite sign compared to the inductive current J_∞. At the same time, it is clear from equation 1.45 that at early times a chargeable medium that obeys the Cole-Cole formula decays as a purely resistive medium with $\sigma = \sigma_\infty$. This consideration explains easily the "pull-up" that it is observed at early times when comparing a Cole-Cole transient with a transient obtained with $\sigma = \sigma_0$, because the Cole-Cole transient has an amplitude corresponding to $\sigma = \sigma_\infty$.

Figure 1.13 shows the effects of IP on a synthetic sounding, with weak ($\left|J_{pol}^{\infty}\right| < J_\infty$) and strong ($\left|J_{pol}^{\infty}\right| > J_\infty$) polarization, in comparison with the $\sigma = \sigma_0$ corresponding sounding. It easily visible that while the sounding with negative gates is recognizable as IP affected; the same cannot be said when the IP currents are weaker than the purely EM currents. This scenario is possible for the conditions in which the investigated medium is both conductive and chargeable. The effect of the chargeability distorts the EM data without giving negatives and complicating IP recognition in the dataspace. At the same time, as for this latter case, a resistive body would be modelled at depth (given by the late-times pull down) below a strong conductor in the near surface losing the chargeability information and mismodelling the ground resistivity. Even for the negative affected data, deleting the negatives would lead to the modelling of a completely wrong model. These examples show how the IP effects do not only affect the late times with negatives or only portions of the EM data: the IP effects distort the entire recorded transient from the early to the late times. If an EM data is affected by IP, the relationships between time and depth ceases to be valid a completely wrong model would be retrieved if the ground resistivity is physically described as non-dispersive.

More examples of forward responses for a homogenous medium will be shown in the next section, illustrating the effect of each parameter on a homogenous halfspace forward response.

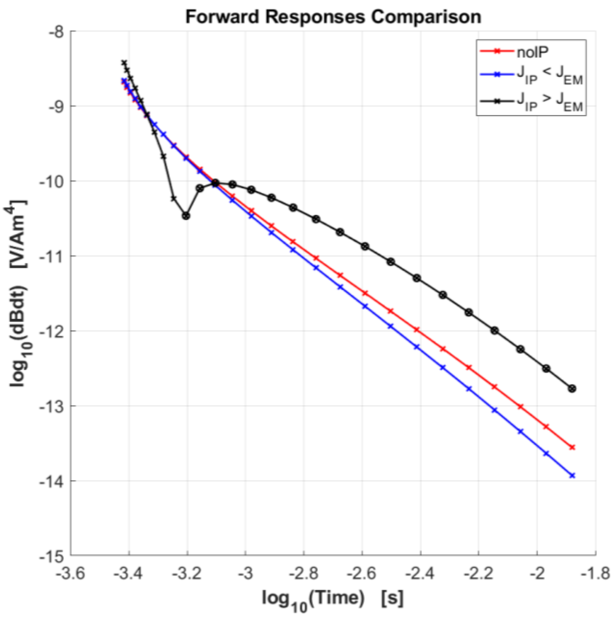

Figure 1.13. Effects of the ground polarization on a synthetic transient. The non-IP affected record is shown in red. In black, the IP distorts the EM data giving negatives at late times and marked early times pull up. In blue, the effects of a smaller polarization are shown, with the late times pull-down without negatives and a smaller early times pull-up. The negative gates are represented by circles while the positives as crosses. The forwards are computed for a 300 Ω· m homogeneous halfspace, with a time constant of 1ms and a frequency dependence of 0.5. The chargeability increases from 20 (blue transient) to 200 (black transient) milliradians.

From the example of *figure 1.13* an example of IP effects on a synthetic sounding is shown. It easily visible that while the sounding with negative gates is recognizable as IP affected, the same cannot be said when the IP currents are weaker than the purely EM currents. This scenario is possible for the conditions in which the investigated halfspace or target is both conductive and chargeable. The effect of the chargeability distorts the EM data without giving negatives and complicating IP recognition in the dataspace. At the same time, modelling these data with a non-dispersive resistivity would give a resistive body at depth, mistaking the late-times pull down with a resistor, and a conductor in the near surface given by the early-times pull-up. This leads to a mismodelling of the ground resistivity as well as to a loss of chargeability information. Even for the negative affected data, deleting the negatives would lead to the modelling of a completely wrong model. These examples show how the IP effects do not affect only the late times with negatives or only portions of the EM data: the IP effects distort the entire recorded transient from the early to the late times. When the EM data is affected by IP, the physical relationships between time and depth ceases to be valid and a wrong model would be retrieved if the ground resistivity is physically described as non-dispersive.

More examples of forward responses for a homogenous halfspace will be shown in the next section, showing the effect of each parameter on a homogenous halfspace forward response.

1.2.3.1: Homogeneous halfspace response

For this set of experiments the forward responses for a homogenous halfspace are computed and illustrated. I used a concentric-loop helicopter system, given the unique relationship between the change of voltages sign with AIP effect. Indeed, as demonstrated by Weidelt (1982), a coincident loop TEM voltage response must always be of one sign if the ground has a linear and frequency-independent electrical conductivity and magnetic permeability (and the EM field is quasi-static). Generation of a single-sign signal arises because the coincident-loop response is a measure of the input impedance of a system which has only one means of energy storage (the magnetic field) and one means of energy loss (joule heating) (Guptasarma, 1984). As consequence, a change of sign in the recorded signal can only be an effect of a capacitive halfspace. As reference, I used a HeliTEM[2] system (see *table 1.1*) for the forward computation.

The synthetic homogeneous halfspace is described with the MPA re-parametrization of the Cole and Cole model (Fiandaca et al., 2018) changing the value of one parameter for each experiment. As reference model, I computed the forward responses for a homogenous halfspace with a resistivity of 200 Ω·m, chargeability of 50 mrad, time constant of 1 ms and frequency dependence of 0.5. In each figure, the black transient is computed not considering IP effects, i.e., using the resistivity only. For the experiments I changed one parameter value per test, as indicated in the figure legend, maintaining the others as in the reference model. This simple experiment wants to illustrate the effect of the variation of these parameters on the forward response. For this reason, the synthetic signals have not been perturbed with noise.

The forward responses have been computed using the EEMverter modelling and inversion algorithm (Fiandaca et al., 2024; more details in *section 1.2.3.5*), developed by the EEM Team for Hydro and eXploration Group of the University of Milano.

Here follows a summary of the main AIP signatures varying each MPA parameter. The following examples are only simple cases to illustrate the effect of the parameters on the data. These largely depends by the background geology, system used for acquisition, first time gate and receiver filters.

The first example is shown in *figure 1.14* for a variation in the resistivity in the forward computation.

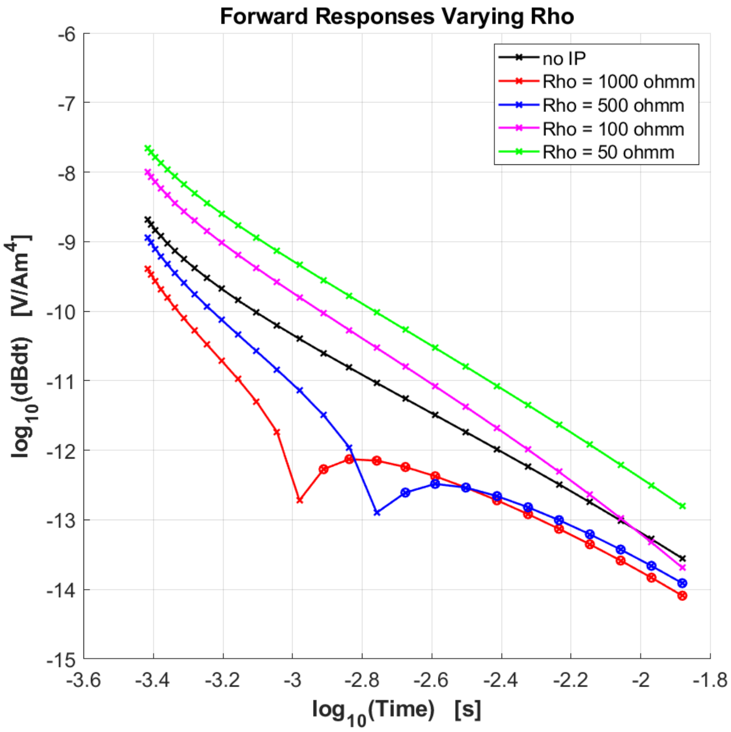

Figure 1.14. Effects on the transient increasing ρ, with φ=50 mrad, c=0.5 and τ=0.001 s. The gates with negative recordings are indicated with circles.

- The number of negatives increases and the time at which the first negative is displayed decreases with increasing resistivity.
- The negative voltages intensity increases with increasing resistivity.
- The IP distortion generally increases with increasing resistivity: the purely EM currents are weaker and decay faster while the IP currents dominate.

In *figure 1.15*, the effects of an increasing chargeability (indicated as Phase in the MPA parametrization) are shown.

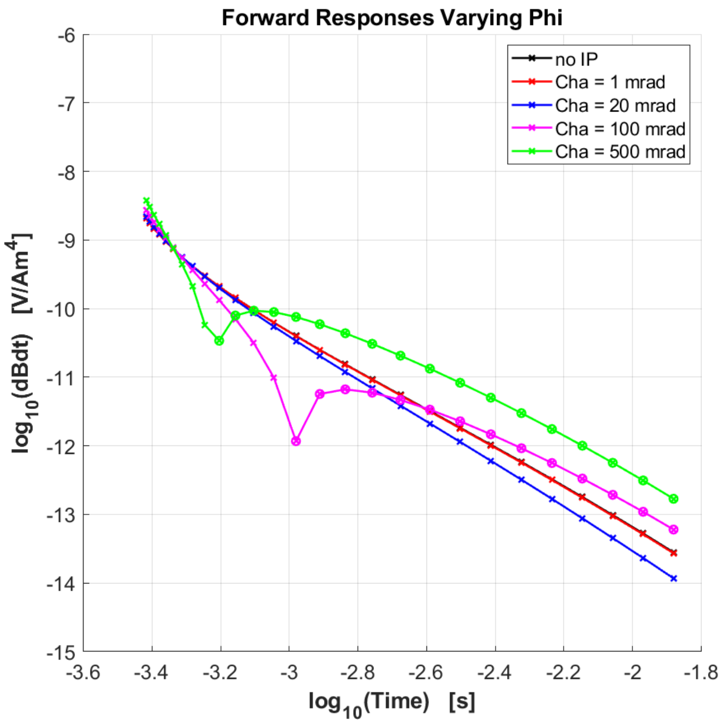

Figure 1.15. Effects on the transient increasing the ground chargeability, with ρ=200 Ω·m, c=0.5 and τ=0.001 s. The gates represented as circles indicate the negative recordings.

Increasing the chargeability (phi):

- The early-time pull-up and late-time pull-down phenomena increases.
- The number of negatives and their intensities increase.
- The time at which the first negative is displayed decreases.
- As for the resistivity, the IP current is stronger, and its effects are earlier visible on the data.

For this time constant and frequency dependence, a ground chargeability of 1 mrad is close to the absence of polarization; no differences are visible between the no-IP transient and the 1 mrad one.

In *figure 1.16*, the effects of the variation in the time constant are shown.

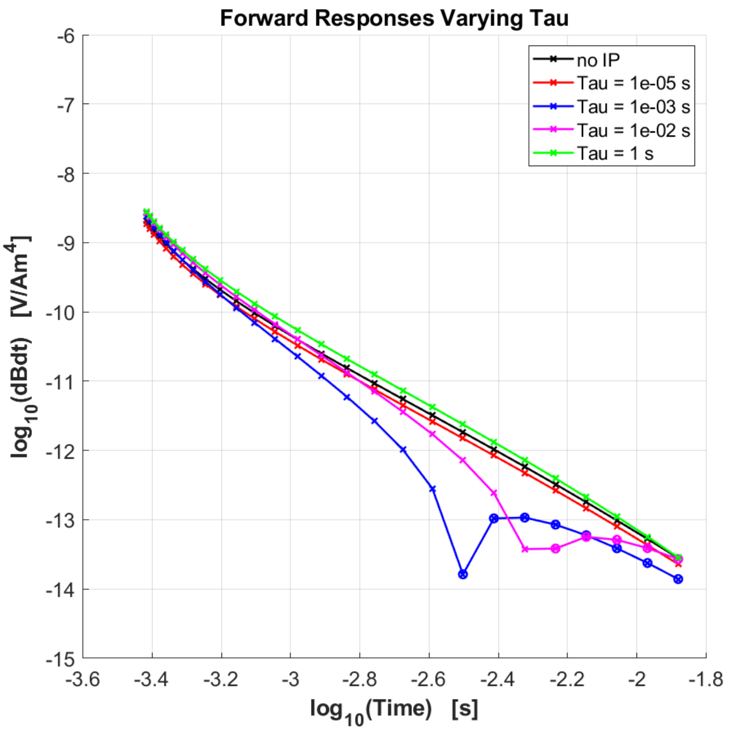

Figure 1.16. Effects on the transient increasing τ, with ρ=200 Ω·m, c=0.5 and m=50 mrad. The circles indicate the negative gates.

A time constant of 10^{-5} s represent a very weakly chargeable body when associated with 50 mrad of phase.

Varying τ:

- The magnitude of IP effects and the presence of negatives change significantly.
- Increasing the time constant the chargeability frequency peak moves to lower frequencies, and the IP effect becomes less evident within the EM bandwidth.
- There is not a linear relation between the time constant and the recorded negatives magnitude; a very low time constant (here 10^{-5} s) can show little IP effects on the data as a very high one (here 1 s). Both the time constants (very high and very low) give an IP response similar to the non-IP affected transient. This because:
    - The effect of the time constant in EM data is highly related with the other spectral Cole and Cole parameter, the frequency dependence *c*. A high frequency dependence concentrates the IP spectra around the frequency where the maximum chargeability is reached. On the contrary, a small c gives extends the frequency peak to a wider range of

frequencies. In terms of effect on the data, if the frequency peak is reached outside the EM bandwidth (i.e., for high time constants), this cannot be recorded by EM data as far as the frequency dependence is small enough to extend its effect within the EM bandwidth.

Finally, in *figure 1.17*, the effects of the variation in the frequency dependence (c) are shown.

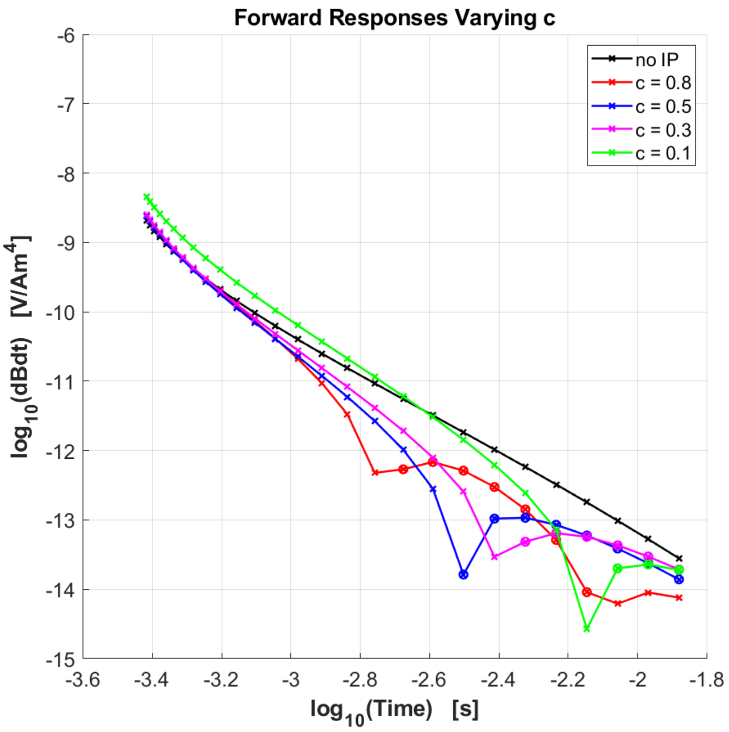

Figure 1.17. Effects on the transient increasing c with ρ=200 Ω·m, tau=0.001 s and m=50 mrad. As in the previous figures, the circles refer to the negative recordings.

Increasing *c*:

- For this time constant it anticipates, in time, the distortions introduced by the ground polarization.
- As mentioned for the previous figure, the effects of the variation in *c* are intrinsically related to the used time constant. If the time constant is within the system bandwidth, a high c increases the magnitude of the IP effects. If the time constant is outside the system bandwidth, a small c spreads the chargeability peak among the frequencies and can make the ground chargeability detectable by the EM system.

From these examples it is visible how an EM transient is sensitive to IP effects but also appears clear how many possible different combinations of the IP parameters allow to resolve a single transient. This makes the inversion strongly exposed to possible equivalent solutions and complicates the correct ground resolution. Moreover, these examples are relative to synthetic data for which no sources of noise are considered; a noise-free environment allows to measure the IP effects for a longer period of time, and, in a theoretical inversion, the “full transient” sensitivity can improve the IP resolution of the ground. For real data, the noise is always present, and the noisy late times can hide the subtle IP effects in EM data. Examples of IP effects in real data are shown in the next section for different environments.

1.2.3.2: Real data examples

The first real data example is shown in *figure 1.18* for a very resistive environment over which some SkyTEM (Brown et al., 2015; Effersø et al., 2018) data have been acquired. On the top of the figure the Low Moment (LM) recordings are shown while at the bottom the High Moment (HM) stripe is shown. An example of sounding is also indicated in the box on the left. The data have been here manually processed, and the removed gates are plotted in grey; in red the negative recordings are displayed while in blue the positives.

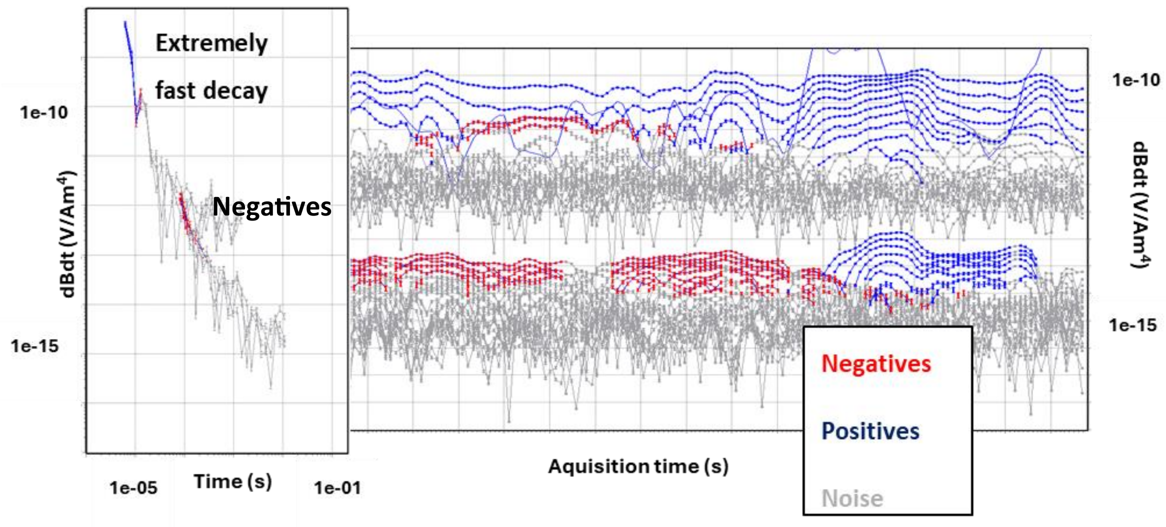

Figure 1.18. Example of Induced Polarization effects on real data for a very resistive environment.

As visible from *figure 1.18*, the more resistive is the environment and stronger are the IP effects, with the High Moment data fully negative and only a few gates in the very near surface that give a positive response in the Low Moment. This happens because the purely EM currents are weak, and the polarization currents dominate the general EM response. As consequence, the recorded signal is largely negative.

In a more conductive environment (as in *figure 1.19a*), the ground polarization distorts the EM signals, but the magnitude of the recorded negative voltages is reduced. On the contrary respect with the resistive environment, here the magnitude of the purely EM currents are stronger and oppose to the IP currents. For this comparison is important to compare only the 25 Hz response of *figure 1.19* that has the same base frequency of the system of *figure 1.18*.

Of course, this description is purely qualitative and means to give the reader a general understanding of how IP manifests in EM data in different environments. A robust prove of these concepts would necessitate to locate the same chargeable body in a perfectly known resistive and then conductive environment. Of course, not an easy task.

Another effect on the IP magnitude in EM data is given by the system's base frequency. In the example of *figure 1.19* an HeliTEM[2] system (Smiarowsky et al., 2020) flew over the same line with two different base frequencies in a quite conductive environment. A lower base frequency allows to record the signal for a longer off-time, increasing the EM system bandwidth and allowing to record longer IP decay times. This solution is often limited by the S/N which worsen for lower base frequency systems.

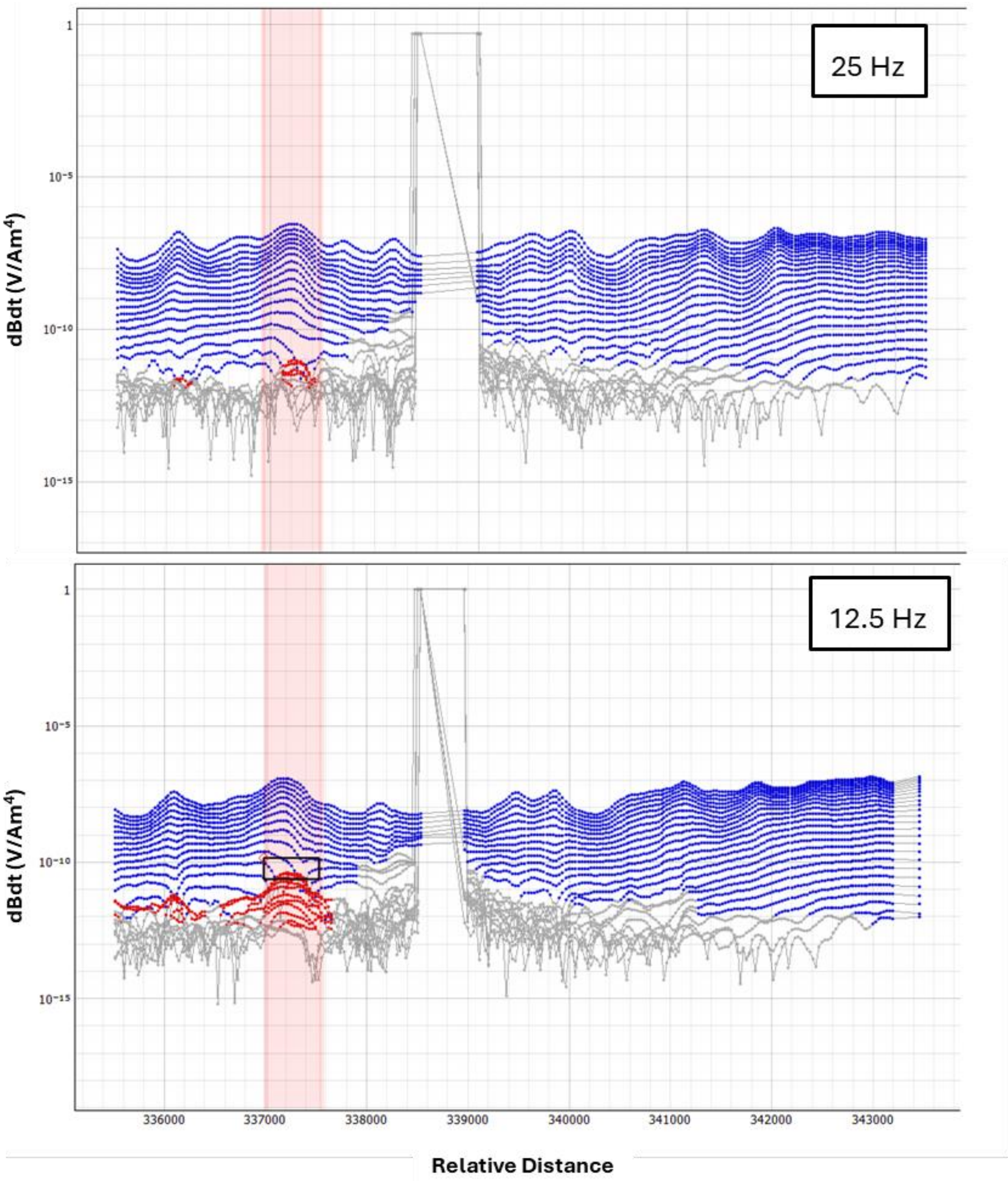

Figure 1.19. EM data comparison for a 25 Hz and 12.5 Hz overlapping flight lines. From figure the increment in negative measure content is visible at late times for the lower base frequency.

In this example (*figure 1.19*) the effect of a lower base frequency is visible with the increment of negative voltages attributable to IP effects. As visible, the fast decays (as after 338000 m or 336000 m on X axis) are stronger in the 12.5 Hz configuration and can culminate in a negative response (as in 336000 m) which could be easily mistaken with noise in the 25 Hz. The fast EM decay in the 12.5 Hz data after 338000 m is also an interesting case to illustrate the IP behaviour: this steep decay is present in the 25 Hz data as well but with a smaller magnitude. Neglecting IP this would be easily modelled but, if the decay was IP-independent, it would not have changed varying the frequencies. In other words, this example represents a case where IP effects are recorded without giving negatives and that would easily be mistaken by non-IP effects.

Reducing the EM system base frequency also improves the modelling of these effects during the inversion, reducing possible equivalencies relating the negative records with the chargeable bodies at depth.

1.2.3.3: Inductive IP response of polarizable materials

In this section I summarize the insights from the real-data examples and the homogenous halfspace examples of *section 1.2.3.1* and *1.2.3.1*.

The complexity of dealing with IP using inductive EM data interests all the aspects of a geophysical workflow: the survey design, the system set-up, the S/N, the physical description of the direct problem, the inversion set-up and concluding with the interpretation of the models. This latter complexity makes the correct use and understanding of AIP even more challenging given the few examples in literature about (e.g. Macnae 2016; Grombacher et al., 2021).

From the physical description of IP effects in EM appears how these effects are subtle and can give responses that are hard to recognize in a dataspace through a simple data scansion. The main reason of this behaviour is the reduced spectral content of EM systems that introduces a limitation at low frequencies to detect low-relaxation-times polarizable materials. The low relaxation time, that is described by the tau parameter in the classic Cole and Cole parametrization, is often related to orebodies (like massive sulphides and tertiary targets as in Macnae, 2016) which represent the common targets of a geophysical application. In this sense, the inductive IP detection limit is given by the EM base frequency: this defines the lower frequency at which is possible to have sensitivity when the ground is chargeable. It is possible to have sensitivity to low-relaxation-time materials when the frequency dependence (parametrized as c in the Cole and Cole model) is small enough to extend the chargeability peak to higher frequencies and making it measurable within the EM bandwidth. In these terms, the detectability of IP effects is largely controlled by the spectral parameters of the target (τ and C) that determine the detection and within the system’s bandwidth. Here, higher is the magnitude of the chargeability parameter *m*, more sensitive is the EM data to the effect of the polarizable ground. Of course, the role of the ground resistivity (ρ) is also crucial: when the conductivity is very high the purely EM currents dominate the IP currents producing small IP effects; on the contrary, in a very resistive environment the IP currents dominate and the EM response that does not reduce the IP contribute of the recorded field at receiver.

From this description appear clear how many possible combinations can give the same “IP signature” in the recorded EM data. The weak IP response, most probably without giving any change of sign in the EM data produced, for instance, by a massive sulphide with a frequency peak outside the EM bandwidth, could be easily mistaken during interpretation with a poorly chargeable body. It is thus crucial to optimize the data acquisition and survey design in function of the possible target to not further complicate an already highly ill-posed inverse problem. To deal with this, inversion and hardware solutions can be attempted. In terms of system’s optimization, a reduction of the acquisition base frequency could improve the AIP detection. This theoretically extends the system’s bandwidth allowing to record bigger time constants and improving the sensitivity to low-relaxation-times materials. An enhancement of AIP in the dataspace is not only useful for the geophysicist to define where the ground is chargeable: it also increases the data sensitivity to the ground polarization helping the inversion to converge towards chargeable solution at depth.

1.2.3.4: Inductive vs Galvanic IP

In the previous sections (*1.2.3.1* and *1.2.3.2*), the theoretical IP response in inductive data has been shown, both on synthetics and in real EM data. Only through a dataspace analysis the complexity in dealing with inductive IP is clear: there are not unique signatures of IP effects in AEM and a large variety of parametrical combinations can give similar responses in dataspace. This complexity is then transferred from the data to model space, exposing the inversion to large equivalences and often making the models difficult to geologically interpret. For these reasons, the AIP application in mineral exploration is a not-common practice and the galvanic DCIP is considered the unique reliable method to measure the ground chargeability. Another critical aspect of AIP is given by the poor comparability of the airborne-retrieved chargeability with ground DCIP chargeability models. Among the experiments in literature, the one from Macnae et al., (2016) is the better known, for which several airborne chargeability models from AEM data have been compared with overlapping DCIP models. Even Viezzoli et al., (2021) compared data from a small ground IP survey with a portion of a bigger AEM survey modelled considering IP. Both concluded that AIP, given its bandwidth, has a limited sensitivity to ground chargeability that is mostly related to very high time constants (i.e., fine-grained materials). The AEM bandwidth is usually a couple of orders of magnitudes higher than that of ground IP data, with a base frequency of 25, 12.5 or 6.25Hz for the inductive and typically 0.5 Hz for galvanic methods. This has been assumed as the main reason of inconsistency between airborne and ground measurement. Reducing the inductive base frequency would extend the acquisition bandwidth allowing to record bigger (i.e. higher) time constants. On the other hand, a smaller base frequency often worsens the S/N, further masking the subtle IP effect in the dataspace. It follows that an adequate feasibility study needs to be carried to verify the noise effect on the data when the base-frequency wants to be reduced for AIP detection.

Another reason of inconsistency between airborne and ground DCIP is the modelling approach. The full secondary voltage decay in DCIP is often turned into its integral chargeability value, as proposed by Oldenburg and Li (1994). The AEM data, even when modelling IP, are modelled as full voltage decays using their complete spectral content for the inversion. The integral chargeability approach cannot have correspondence in AIP inversion: the whole EM decay is inverted for retrieving both conductivity and chargeability information. It follows that a full-decay modelling IP needs to be adopted for comparisons to reduce ambiguities introduced by different approaches.

At this state of the art, any successful case study has shown a comparability between the airborne and ground retrieved chargeability model but improvements in terms of modelling and survey design can help to improve the comparability of the two methods for chargeability mapping.

1.2.3.5: Inductive Induced Polarization modelling approach: the EEMverter modelling and inversion scheme

As mentioned, for this thesis work the EEMverter modelling and inversion algorithm (Fiandaca et al., 2024) has been used to perform all of the forward computations and inversions for both the Airborne EM and of the galvanic DCIP data. This inversion algorithm, developed by the EEM Team for Hydro and eXploration research group from University of Milano since 2021, aims to provide a tool able to handle natively joint inversion of different datatypes, time-lapse inversion, induced polarization and all the dimensionalities (1D, 2D and 3D) in the forward response. Several features are implemented in EEMverter for reaching this purpose, i.e.:

- Definition of distinct meshes for model parameter definition (the model mesh(es), ModMesh), forward computation (the forward mesh(es), ForMesh) and constraint definition (the constraint mesh(es), ConMesh). The model parameters are defined on the nodes of the model mesh(es), and migrated to the forward mesh(es) through (selectable) interpolation(s), and constraints are defined between nodes of mesh(es) and as priors. All ModMesh, ForMesh and ConMesh mesh(es) are defined in vtk format, for being easily visualizable in Paraview (https://www.paraview.org/).

- Parametric definition of electrical properties, such that the (complex) electrical conductivity (and, possibly, permittivity and susceptibility) is computed through functions, possibly integrating petrophysical relations. Examples are the direct inversion of galvanic time-domain induced polarization data in terms of hydraulic conductivity, and the inversion of time-lapse data with direct modelling of temperature.

- Flexible definition of the inversion objective function, such as the data misfit, roughness misfit and prior misfit can be computed with the use of different norms, such as L1, L2, generalized Minimum (Gradient) Support. Distinct norms of distinct types can be assigned to data sets, roughness and prior constraints, and all norm misfits are monitorable through their identifier throughout the entire inversion process.

- Iterative inversion splitable in several inversion cycles. In each cycle it is possible to define: the models inverted in the cycle (for time-lapse inversion); the parameters inverted in the cycles; the constraints used; the data used, and the corresponding norms in the data misfit; the type of forward/jacobian computation, e.g. 1D or 2D/3D; (some) inversion settings, for instance parameter ranges.

These aspects, that define the EEMverter philosophy, provide a flexible architecture to adapt the inversion procedure to explore the equivalencies of the AIP model-space expanded inversion and, more in general, to solve complex geophysical tasks.

Forward computation

The 1D computation of the EM forward response $\frac{\partial B_{z,TD}}{\partial t}$ at the receiver is carried out taking into account the filter characteristics of the receiver, the shape of the transmitter as well as the waveform of the current turn-off. Following Ward and Hohmann, this is achieved computing the forward response in frequency domain (FD) as superposition of horizontal electric dipoles along the transmitter loop sides, or as superposition of magnetic dipoles uniformly distributed within the transmitter, in order to model the transmitter shape. Here the details of the implementation through superposition of electric dipoles:

$$B_{z,FD}(\sigma, h, \omega, x, y, z) = \oint_{Tz\ loop} dB_{z,FD} \tag{1.46}$$

where $\sigma = \{\sigma_1, ..., \sigma_N\}$ and $h = \{h_1, ..., h_{N-1}\}$ represent the electric conductivity and the layer thicknesses of a N-layered 1D model ω, is the angular frequency, x, y, z indicate the position of the receiver and $dB_{z,FD}$ is the contribution of the infinitesimal loop piece of length ds, expressed as:

$$dB_{z,FD}(\sigma, h, \omega, x_*, y_*, z_*) = \frac{I\, ds}{4\pi} \cdot \frac{y_*}{\rho_*} \int_0^{\infty} (1 + r_{TE}) e^{u_0 z_0} \frac{\lambda^2}{u_0} J_1(\lambda \rho_*) d\lambda \tag{1.47}$$

where x_*, y_*, z_* are the receiver coordinates in the reference system that sees the infinitesimal loop piece ds oriented in the x direction and centered at its origin, J_1 represents the Bessel function of order 1, $\rho_* = \sqrt{{x_*}^2 + {y_*}^2}$ is the distance between the receiver and the segment origin, I is the current in the loop, $u_0 = \sqrt{\lambda^2 + \omega^2 \mu_0 \epsilon_0}$ and r_{TE} epresents the reflection coefficient of the electric field transverse to the z axis, defined as:

$$r_{TE} = \frac{Y_0 - \hat{Y}_1}{Y_0 + \hat{Y}_1} \tag{1.48}$$

where the intrinsic admittance of the free space Y_0 and the surface admittance $\hat{Y}_1$ are computed using the relations:

$$\hat{Y}_n = Y_n \frac{\hat{Y}_{n+1} + Y_n \cdot tanh(u_0 h_n)}{Y_n + \hat{Y}_{n+1} \cdot tanh(u_n h_n)}$$

$$Y_n = \frac{u_n}{\hat{z}_n}$$

$$\hat{y}_n = \sigma_n + i\, \epsilon_n \omega$$

$$\hat{z}_n = i \mu_n \omega$$

$$u_n = \sqrt{\lambda^2 - {k_n}^2}$$

$${k_n}^2 = -\hat{y}_n \hat{z}_n$$

$$\hat{Y}_N = Y_N$$

Where the computation of $\hat{Y}_1$is performed iteratively, starting from the last layer N. In all the equations no variations in dielectric permittivity and magnetic permeability are assumed among layers (i.e. $\epsilon_n = \epsilon_0$ and $\mu_n = \mu_0$).

The integral of Equation (1.47) is computed through fast Hankel transforms following Johansen and Sorensen. The time-domain (TD) step response $B_{z,TD,step}$ is then computed through a cosine transform of the imaginary part of FD kernel, while the impulse response though sine transform of the real part of the kernels, as:

$$B_{z,TD,step}(\sigma, h, t, x, y, z) = \frac{2}{\pi} \int_0^\infty \frac{\Im(B_{z,FD}(\sigma,h,t,x,y,z) \cdot \mathrm{F}(\omega))}{\omega} cos(\omega t) d\omega \tag{1.49a}$$

$$B_{z,TD,impulse}(\sigma, h, t, x, y, z) = \frac{2}{\pi}\int_0^{\infty} \Re(B_{z,FD}(\sigma, h, t, x, y, z) \cdot \mathrm{F}(\omega))\, sin(\omega t) d\omega \qquad (1.50b)$$

Where F(ω) represents the FD filter characteristics of the receiver.

The impulse response of the Earth (or a geophysical system) is its theoretical response to an idealized, instantaneous current input—specifically a Dirac delta function δ(t), which has infinite amplitude and zero duration but unit area. If the input current I(t) = δ(t), then the measured voltage response at the receiver is: V(t) = h(t), where h(t) is the impulse response of the Earth/system. The step response of the Earth is the observed transient EM response to a sudden turn-on or turn-off (usually turn-off) of the transmitter current. This is equivalent to applying a Heaviside step function u(t) as the source: $I(t) = I_0 \cdot u(t)$ or $I(t) = I_0 \cdot [1 - u(t)]$. The step response s(t) is the time-integral of the impulse response h(t). Conversely, the impulse response is the time-derivative of the step response: h(t) = d s(t)/dt.

The cosine/sine transforms are solved numerically in terms of Hankel transforms, expressed in terms of Bessel functions of order -1/2 and +1/2, respectively:

$$\frac{1}{\pi}\int_0^{\infty} f(\omega) {}^{cos}_{sin}(\omega t)\, d\omega = \sqrt{r}\int_0^{\infty} f_1(\lambda)\lambda J_{\pm 1/2}(\lambda r) d\lambda \qquad (1.51)$$

Where $r = t\sqrt{2\pi}$, $\lambda = \frac{\omega}{\sqrt{2\pi}}$ and $f_1(\lambda) = \frac{1}{\sqrt{\lambda}} f(\frac{\lambda}{\sqrt{2\pi}})$.

Finally, the time-derivative $\frac{\partial B_{z,TD}(t)}{\partial t}$ of the magnetic field measured at the receiver is computed as the time-derivative of the convolution of the impulse response with the current waveform *i(t)* in the transmitter:

$$\frac{\partial B_{z,TD}(t)}{\partial t} = \frac{\partial (B_{z,TD,impulse}(t) * i(t))}{\partial t} = B_{z,TD,impulse}(t) * \frac{\partial\, i(t)}{\partial t} \qquad (1.52)$$

where the second equality makes use of the rules of the derivative of convolutions. Equation (1.53) is solved as proposed by Fitterman and Anderson (1986) for piecewise linear current waveforms:

$$\frac{\partial B_{z,TD}(t)}{\partial t} = \sum_{j=1}^{M} \Delta_{i_j} \cdot \frac{B_{z,TD,step}(t - \mathrm{t_j} + \Delta t_j) - B_{z,TD,step}(t - \mathrm{t_j})}{\Delta t_j} \qquad (1.53)$$

where the summation is carried over all the M piecewise linear segments of the current $i(t)$ defined in the time intervals {t_j, $t_j + \Delta_j$} with slopes $\Delta i_j/\Delta t_j$.

Inversion

In EEMverter the inversion parameters are defined on model meshes which do not coincide with the forward meshes used for data modelling: the link between model and forward meshes is obtained interpolating the model mesh parameters into the forward mesh discretization, as done for 1D AEM in Christensen et al. (2017), in 3D galvanic IP in Madsen et al. (2020) and in 3D EM in Zhang et al. (2021), Engebretsen et al. (2022) and Xiao et al. (2022a). This spatial decoupling allows for defining the model parameters, e.g. the Cole-Cole ones, on several model meshes, for instance one for each inversion parameter. In this way, it is possible to define the spectral parameters, like the time constant and the frequency exponent in the Cole-Cole model, on meshes coarser than the resistivity and chargeability ones, vertically and/or horizontally, with a significant improvement in parameter resolution. For each dataset of the inversion process, a distinct forward mesh is defined.

The mapping from the forward mesh to the model meshes is done through matrix multiplication. This is done among the model parameters $\boldsymbol{M}$, defined on the mesh nodes, and the matrix $\boldsymbol{F_i}$ that holds the weights of the interpolation. The weights are dependent on the distance between the model mesh nodes and subdivision of the forward mesh on which the forward is computed. The multiplication takes the form of:

$$\boldsymbol{m}_i = f_i(\boldsymbol{M}) = \boldsymbol{F}_i \cdot \boldsymbol{M} \tag{1.54}$$

As for the forward response, the Jacobian matrix is computed in the frequency domain and then transformed into the time domain avoiding the time domain approximation. The time-domain Jacobian in the ith forward mesh is computed as:

$$J_{m_{i,}TD} = A \cdot T \cdot J_{m_{i,}FD} \tag{1.55}$$

where the matrix $\boldsymbol{T}$ holds the Hankel coefficients (as in Effersø in 1999), the matrix $\boldsymbol{A}$ implements the effects of current waveform, gate integration and filters and the frequency-domain Jacobian $J_{m_{i,}FD}$ is calculated in 1-D through finite difference and in 1-D/2-D/3-D using the adjoint method and the chain rule as in Fiandaca et al. (2013) and Madsen et al. (2020), thus allowing to use any parameterization of the IP phenomenon in the inversion:

$$J_{m_{i,}FD} = J_{\sigma*,i} \cdot \frac{\partial \sigma^*}{\partial \boldsymbol{m_i}} \tag{1.56}$$

where $J_{\sigma*,i}$ is the Jacobian of the i^{th} forward mesh with respect to the complex conductivity σ^* and $\frac{\partial \sigma^*}{\partial \boldsymbol{m}_i}$ is the partial derivative of the complex conductivity versus the model parameters (Fiandaca et al., 2024).

Finally, the Jacobian of the model space $\boldsymbol{J_M}$ is computed summing the contributions of all forward meshes up (Christensen et al., 2017; Madsen et al., 2020):

$$\boldsymbol{J_M} = \sum_{\boldsymbol{i}} \boldsymbol{J_{m_i}} \cdot \boldsymbol{F_i}^T \tag{1.57}$$

The Levenberg-Marquardt linearized approach is used for computing the inversion model:

$$\begin{aligned}\boldsymbol{M}_{n+1,j} = \boldsymbol{M}_{n,j} + \left[\boldsymbol{J}_{M,j}^T \boldsymbol{C}_d^{-1} \boldsymbol{J}_{M,j} + \boldsymbol{R}^T \boldsymbol{C}_{R,}^{-1} \boldsymbol{R}_j + \lambda_n \boldsymbol{I}\right]^{-1} \\ \cdot \left[\boldsymbol{J}_{M,j}^T \boldsymbol{C}_d^{-1} \cdot \left(\boldsymbol{d} - \boldsymbol{f}_{n,j}\right) - \boldsymbol{R}^T \boldsymbol{C}_{R,j}^{-1} \boldsymbol{R}_j \cdot \boldsymbol{M}_{n,j}\right]\end{aligned} \tag{1.58}$$

Where $\mathbf{R}$ is the regularization matrix, $\mathbf{C}_\mathrm{d}$ the covariance matrix on the data, $\mathbf{C}_\mathrm{R}$ the covariance matrix on the model roughness, λ the damping parameter, $\mathbf{d}$ the measured data and $\mathbf{f_n}$ the forward response of the n^{th} iteration. The parameter λ is the Marquardt damping parameter (Marquardt, 1963), iteratively updated to stabilise the inversion process through an adaptive algorithm that damps the step size. The damping value λ is defined as the maximum diagonal value of the $\mathbf{J}_{\mathrm{M,j}}^{\mathrm{T}} \mathbf{C}_\mathrm{d}^{-1} \mathbf{J}_{\mathrm{M,j}}$ matrix, reduced by an iterative-dependent scaling factor $\mathrm{f_n}$:

$$\lambda_\mathrm{n} = \max \operatorname{diag}(\mathrm{J}_{\mathbf{M},\mathrm{j}}^{\mathrm{T}} \mathbf{C}_\mathrm{d}^{-1} \mathrm{J}_{\mathbf{M},\mathrm{j}}) \cdot \mathrm{f_n} \tag{1.59}$$

The damping is used to stabilise the solution of the linear system of equation 1.58, but a constraint on the 'step size' of the iteration, i.e. the size of the model update $\mathbf{m}_{n+1} - \mathbf{m}_n$, is also imposed through f_n (the step size is reduced by increasing f_n). When increasing the iteration number n, the scaling factor $f_n$is decreased and the step size is increased ensuring a more robust damping scheme.

In this formalism, the subscript j indicates that the inversion process can be split in different cycles. Each inversion cycle is an independent inversion which uses as starting model the final model of the previous inversion cycle. Each inversion cycle can have different forward mesh (for instance changing the dimensionality of the forward response to 3D after a first general 1D inversion), model discretization, parametrization (for instance to invert for the flight altitude after a first cycle where only the resistivity was modelled) and the regularization. This solution allows to make the inversion more versatile and user-controlled using one unique input file. This solution is helpful for complex inversions such as joint inversions and time lapse inversions.

In equation 1.57, the square matrix $\mathbf{C}_d$ is the data covariance matrix, which accounts for the measurement uncertainties:

$$\mathbf{C}_d = \begin{bmatrix} \sigma_1^2 & \cdots & 0 \\ \vdots & \ddots & \vdots \\ 0 & \cdots & \sigma_n^2 \end{bmatrix}$$

where the diagonal values represent the variance for the data. When it is not delivered by the data provider, the relative standard deviation $\sigma_{k,rel}$ on the k-th datum is computed summing up a signal-level dependent std and a uniform as:

$$\sigma_{k,rel} = \sigma_{k,sig} + \sigma_{uni} \tag{1.60a}$$

$$\sigma_{k,sig} = \frac{\eta_{floor}}{|d_k|}\sqrt{\frac{t_k}{0.001}} \tag{1.60b}$$

where η_{floor} is the noise floor at 1 ms and t_k is the time window at which the data d_k is recorded. The uniform relative error σ_{uni} is generally comprised between 2% and 5%.

When the data uncertainty is delivered by the data provider, it is generally computed summing up a signal-dependent std and a uniform std as well, but the signal-dependent std is computed through stacking.

The matrices $\mathbf{R}$ and $\mathbf{C}_R$ ensure the smoothness of the solution, imposing vertical and horizontal constraints. The rows of the $\mathbf{R}$ matrix define the constraints which penalize the differences between the model parameters:

$$\mathbf{R} = \begin{bmatrix} -1 & 1 & 0 & 0 & \dots & 0 \\ 0 & -1 & 1 & 0 & \dots & 0 \\ \vdots & \vdots & \vdots & \vdots & \vdots & \vdots \\ 0 & 0 & 0 & 0 & -1 & 1 \end{bmatrix}$$

While the square diagonal matrix $\mathbf{C}_R$ represents the covariance matrix, which defines the strength of the constraints (Auken and Christiansen, 2004). The strength or variance of the constraints depends on the expected variation in the underlying geological model. Small constraints allow only small model changes and vice versa

1.3: Thesis outline

This work is developed in four main chapters that focus on different aspects of Airborne IP and at different scales of investigation. The first one, this chapter (*Chapter 1*), is an introductory chapter. The three following chapters (*Chapter 2*, *3* and *4*) correspond to three full papers in submission for publication in peer-reviewed journals, partially re-adapted to fit within this thesis framework. Here below a short summary of each is provided.

In *Chapter 2*, a methodological study about AIP detection and modelling for the fixed-wing systems is carried. For these systems, largely used for continental and regional-scale resistivity mapping (such in Australia, Uganda, Zambia etc…), the AIP detectability has never been demonstrated. Their in-offset geometrical configuration, high ground clearance (about 100 m), large footprint and complex data processing, have leaded the AIP research to mostly focus on helicopter-borne platforms (which have a concentric or quasi-concentric geometry and lower ground clearance during survey) instead that on fixed-wing systems. Nowadays, given the improvement on the geometrical control during flight and the willingness of the data providers to share information about the adopted processing routines, it is possible to re-think the possibility of AIP detection (and modelling) also for this group of AEM systems. For this work, a synthetic study with a large dataspace inspection has been carried to verify the system sensitivity to AIP effects; then, to verify the theoretical results, a real-data modelling comparison with helicopter-borne system retrieved chargeability and drillholes over known mineralization is investigated. The fixed-wing data I used have been acquired with the TEMPEST™ system within the AusAEM project. The potential benefits of this set of experiments are related to the possible chargeability mapping at continental-scale using already acquired fixed-wing data. If the mapping is achieved, it could introduce a significative layer of information to describe the regional ground geology.

In *Chapter 3*, the exploration scale is reduced to the prospect-scale. Here, an extensive comparison between airborne and ground DCIP models is carried after a consistent modelling approach of the two. The airborne EM data are modelled, as for the previous experiments with fixed-wing data, with an innovative multi-mesh modelling approach that aims to reduce the equivalencies during AIP inversion. Then, to quantitatively verify the AIP sensitivity to the ground chargeability, a joint inversion between the airborne and ground data considering IP effects is carried. The survey area for this study is located in Spain in an active mineral exploration tenement for VMS and polymetallic mineralization. In addition to this chapter, the *Appendix* at the end of the thesis shows a comparison between the IP and non-IP modelling of the airborne EM dataset used for this work.

In *Chapter 4*, I apply the modelling approach and the methodological findings developed in *Chapter 3* to a real greenfield exploration project. Here, the airborne IP method is used as a tool to find anomalies and to down-scale the exploration defining the ground DCIP follow-up. The acquired data (two AEM surveys with different base frequencies and the ground DCIP data) are then jointly modelled in a unique inversion scheme attempting to unify the different bandwidths and uniquely resolve the ground chargeability. This experiment has thus a twofold aim: a first technical, for which I use the AIP to find possible targets, and a second one methodological, for which the AIP is compared and jointly modelled with the ground galvanic method. Differently from *Chapter 3*, the ground DCIP is here acquired with a larger bandwidth (3 decades of IP recording time) and the AEM datasets have different base frequencies (25 Hz and 12.5 Hz). This wide spectral range represents a challenge for the joint modelling but enrich the ground spectral description. This project is located in Portugal and is currently under study within the SEMACRET European Horizon Project.

To conclude, with this thesis I aim to provide a contribution to the understanding of the AIP phenomenology and its methodology for mineral application purposes. To do this, I focus to overcome the known complexities that limit the method and the diffusion of its application. I point to reduce the gap between the inductive and the galvanic DCIP methods and to improve the use of AIP as a valuable tool to map the ground chargeability. The link among the chapters of this thesis is the scale-comparison of the AIP application, from the continental mapping to the ground follow-up over airborne-defined anomalies through the methodological comparison of galvanic and inductive IP. To pursue on this field of research, I use novel approaches to AIP modelling as tools, I investigate the IP response at different frequency ranges, and I compare and validate the inductive results with the standard galvanic methodologies to validate the findings.

1.4: References

- Allard, M., (2007), On the origin of the HTEM species, In Proceedings of Exploration 07: Fifth Decennial International Conference on Mineral Exploration, Toronto, Canada.
- Annan, A.P., (1983), Effect of differential transmitter/receiver motion on airborne transient EM interpretation, 53rd Annual International Mgt., Society of Exploration Geophysics, 622-623, https://doi.org/10.1190/1.1893693
- Auken, E. and Christiansen, A.V., (2004), Layered and laterally constrained 2D inversion of resistivity data, Geophysics, 69, 752-76, https://doi.org/10.1190/1.1759461
- Bhattacharyya, B. K., (1964), Magnetic anomalies due to prism-shaped bodies with arbitrary polarization: Geophysics, 29(4), 517–531, https://doi.org/10.1190/1.1439386
- Binley, A., and A. Kemna., (2005), DC resistivity and induced polarization methods, Y. Rubin and S.S. Hubbard editors, Hydrogeophysics. Springer, Dordrecht, the Netherlands. p. 129–156.
- Binley A., Slater L., (2020), Resistivity and Induced Polarization, Cambridge University Press, December 2020, DOI: https://doi.org/10.1017/9781108685955
- Cole, K.S. and Cole, R.H., (1941), Dispersion and Absorption in Dielectrics I. Alternating Current Characteristics. The Journal of Chemical Physics, 9, 341–351 https://doi.org/10.1063/1.1750906
- Cox, L.H.; Zhdanov, M.S.; Prikhodko, (2024), A. Inversion for 3D Conductivity and Chargeability Models Using EM Data Acquired by the New Airborne TargetEM System in Ontario, Canada. Minerals 2024, *14*, 237. https://doi.org/10.3390/min14030237
- Chen, T., Hodges, G., Smiarowsky A., (2015), Extracting subtle IP from airborne time domain electromagnetic data. SEG technical program, Abstracts: 2061-2066, https://doi.org/10.1190/segam2015-5828596.1
- Chen, J., Zhang, B., Fiandaca, G., (2025b), Closing the gap between galvanic and inductive methods – Part II: 3D EM inversion considering induced polarization effect. Geophysical Journal International, in preparation.

- Christensen, N. K., Ferre, T. P. A., Fiandaca, G., and Christensen, S., (2017), Voxel inversion of airborne electromagnetic data for improved groundwater model construction and prediction accuracy. Hydrology and Earth System Sciences, 21(2), 1321-1337, https://doi.org/10.5194/hess-21-1321-2017
- Christiansen, A.V., Auken, E., Foged, N. and Sørensen, K.I. (2007), Mutually and laterally constrained inversion of CVES and TEM data: a case study. Near Surface Geophysics, 5: 115-123. https://doi.org/10.3997/1873-0604.2006023
- Dauti, F., Viezzoli, A., Fiandaca, G., (2023), Joint Inversions of AEM modelling AIP effects: Helicopter-borne, Ground IP and Fixed-Wing systems, Australian Society of Exploration Geophysicists Extended Abstracts, Volume 2023 (2), 8th International Airborne Electromagnetics Workshop, Fitzroy Island, 2023, 2023.
- Dauti, F., Viezzoli, A., Fernandez I., Royall J., Fiandaca, G., (2024), Airborne and Ground IP integration for mineral exploration: a Spanish case study, KEGS Symposium, 2024 Toronto, Canada, March 2nd, 2024.
- Dentith H., Mudge S., (2014), Geophysics For The Mineral Exploration Geoscientist, Cambridge University Press.
- Dias, C. A., (1968), A non-grounded method for measuring induced electrical polarization and conductivity. Ph.D. Dissertation, Univ. of California, Berkley, USA.
- Engebretsen, K. W., Zhang, B., Fiandaca, G., Madsen, L. M., Auken, E., and Christiansen, A. V. (2022). Accelerated 2.5-D inversion of airborne transient electromagnetic data using reduced 3-D meshing. Geophysical Journal International, 230(1), 643-653, https://doi.org/10.1093/gji/ggac077
- Effersø, F., Auken, E. and Ingvard Sørensen, K. (1999), Inversion of band-limited TEM responses. Geophysical Prospecting, 47: 551-564. https://doi.org/10.1046/j.1365-2478.1999.00135.x
- European Commission: Directorate-General for Research and Innovation, European Green Deal – Research and innovation call, Publications Office of the European Union, 2021, https://data.europa.eu/doi/10.2777/33415
- Everett E. M., (2013), Near Surface Applied Geophysics, Cambridge University Press, June 28, 2013.
- Fiandaca, G., Auken, E., Christiansen, A.V., Gazoty, A., (2012), Time-domain-induced polarization: Full-decay forward modelling and 1D laterally constrained

inversion of Cole-Cole parameters, Geophysics 77: E213-E225. https://doi.org/10.1190/geo2011-0217.1

- Fiandaca, G., Ramm, J., Binley, A., Gazoty, A., Christiansen, A. V., and Auken, E., (2013), Resolving spectral information from time domain induced polarization data through 2-D inversion: Geophysical Journal International, 192, 631–646. doi:10.1093/gji/ggs060
- Fiandaca, G., Madsen, L.M. and Maurya, P.K. (2018), Re-parameterisations of the Cole–Cole model for improved spectral inversion of induced polarization data. Near Surface Geophysics, 16: 385-399. https://doi.org/10.3997/1873-0604.2017065
- Fiandaca G., Chen J., Zhang B, (2024), EEMverter, a New Modelling Tool for Electric and Electromagnetic Data with Focus on Induced Polarization, European Association of Geoscientists and Engineers, NSG 2024 30th European Meeting of Environmental and Engineering Geophysics, Sep 2024, Volume 2024, p.1 – 5, DOI: https://doi.org/10.3997/2214-4609.202420166.
- Fitterman D. V. and Labson V. F., (2005), Electromagnetic Induction Methods for Environmental Problems, Investigations in Geophysics: 301-356, https://doi.org/10.1190/1.9781560801719.ch10
- Flis, M.F., Newman, G.A., Hohmann, G.W., (1989), Induced-polarization effects in time-domain electromagnetic measurements, Geophysics, 54(4), 514-523, https://doi.org/10.1190/1.1442678
- Fountain, D., (1998), Airborne electromagnetic systems - 50 years of development. Exploration Geophysics, 29(1–2), 1–11. https://doi.org/10.1071/EG998001
- Grant F. and West, G., (1965), Interpretation Theory in Applied Geophysics, Mc Graw-Hill.
- Grombacher D., Auken E., Foged N., Bording T., Foley N., Doran P. T., Mikucki J., Dugan A., Garza-Giron R., Myers K., Virginia R. A., Tulaczyk S., (2021), Induced polarization effects in airborne transient electromagnetic data collected in the McMurdo Dry Valleys, Antarctica, Geophysical Journal International, 226, (3), 2021, 1574–1583, https://doi.org/10.1093/gji/ggab148
- Guptasarma D., (1984), Positivity of the coincident loop transient electromagnetic response, Geophysics, 49(2), 194-194, https://doi.org/10.1190/1.1441651

- Hine, K., Macnae, J. (2016), Comparing induced polarization responses from airborne inductive and galvanic ground systems: Lewis Ponds, New South Wales., Geophysics, 81(6), B179-B188, https://doi.org/10.1190/geo2016-0204.1
- IEA, (2024), Global Critical Minerals Outlook 2024, IEA, Paris https://www.iea.org/reports/global-critical-minerals-outlook-2024, Licence: CC BY 4.0
- Kaminski, V., Viezzoli A., (2017), Modeling induced polarization effects in helicopter time-domain electromagnetic data: Field case studies, Geophysics, 82(2), B49-B61, https://doi.org/10.1190/geo2016-0103.1
- Kang, S., Oldenburg, D. W., & Heagy, L. J. (2019). Detecting induced polarisation effects in time-domain data: a modelling study using stretched exponentials. Exploration Geophysics, 51(1), 122–133, https://doi.org/10.1080/08123985.2019.1690393
- Kang, S., Fournier, D. and Oldenburg, D., (2017), Inversion of airborne geophysics over the DO-27/DO-18 kimberlites – Part 3: Induced polarization: Interpretation, 5(3), T327-T340, https://doi.org/10.1190/INT-2016-0141.1
- Kaufmann, A.A. and Keller, G.V., (1983), Frequency and Transient Soundings, Elsevier, Amsterdam.
- Karey, P., Brooks, M., Hill, I., (2002), An Introduction to Geophysical Exploration, Blackwell Publishing, Oxford University Press.
- Kemna A., Binley A., Ramirez A. and Daily W., (2000), Complex resistivity tomography for environmental applications. Chemical Engineering Journal 77(1), 11–18, 10.1016/S1385-8947(99)00135-7
- Kwan, K., Prikhodko, A., Legault, J.M., Xie, J., Fisk, K., (2015), Airborne Inductive Induced Polarization Chargeability Mapping of VTEM Data. ASEG-PESA-AIG expanded abstract, Adelaide.
- Klein J.D., Sill W.R., (1982), Electrical properties of artificial clay-bearing sandstone, Geophysics, 47 (11), 1593–1605, 10.1190/1.1441310
- Kratzer, T. and Macnae, J., (2012), Induced polarization in airborne EM, Geophysics, 77(5), E317–E327, https://doi.org/10.1190/geo2011-0492.1

- Kwan, K., Prikhodko, A., Legault, J. M., Plastow, G., Xie, J., & Fisk, K, (2015), Airborne Inductive Induced Polarization Chargeability Mapping of VTEM Data. ASEG Extended Abstracts, 2015(1), 1–4. https://doi.org/10.1071/ASEG2015ab104
- Legault M. J., (2015), Airborne Electromagnetic Systems – State of the Art and Future Directions, Recorder, Jun 2015, 40(6)
- Leggatt, P. B., P. S. Klinkert, and T. B. Hage, (2000), The Spectrem airborne electromagnetic system — Further developments, Geophysics, 65, p. 1976–1982, https://doi.org/10.1190/1.1444881
- Ley-Cooper A. Y., Viezzoli A., Guillemoteau J., Vignoli G., Macnae J., Cox L., Munday T., (2015), Airborne electromagnetic modelling options and their consequences in target definition. Exploration Geophysics 46, 74-84, https://doi.org/10.1071/EG14045
- Ley-Cooper, A. Y., Brodie, R. C., and Richardson, M., (2019), AusAEM: Australia's airborne electromagnetic continental-scale acquisition program. Exploration Geophysics, 51(1), 193–202. https://doi.org/10.1080/08123985.2019.1694393
- Leroy, P., and A. Revil (2009), A mechanistic model for the spectral induced polarization of clay materials, Journal of Geophysical Research, 114, B10202, doi:10.1029/2008JB006114.
- Lin, C., G. Fiandaca, E. Auken, M. A. Couto, A. Christiansen, (2018), A discussion of 2D induced polarization effects in airborne electromagnetic and inversion with a robust 1D laterally constrained inversion scheme, Geophysics, 84(2), E75-E88, https://doi.org/10.1190/geo2018-0102.1
- Macnae, J. (2016), Quantitative estimation of intrinsic polarization and superparamagnetic parameters from airborne electromagnetic data, Geophysics 81(6), E433-E446, https://doi.org/10.1190/geo2016-0110.1
- Madsen, L. M., Fiandaca, G., and Auken, E., (2020), 3-D time-domain spectral inversion of resistivity and full-decay induced polarization data—full solution of Poisson's equation and modelling of the current waveform. Geophysical Journal International, 223(3), 2101-2116, https://doi.org/10.1093/gji/ggaa443
- Marquardt, D., (1963), An algorithm for least squares estimation of nonlinear parameters: SIAM Journal of the Society for Industrial and Applied Mathematics, 11, 431–441. doi:10.1137/0111030

- Marshall D.J., Madden T.R., (1959), Induced polarization, a study of its causes, Geophysics, 24 (4), 790–816 DOI: 10.1190/1.1438659
- McNeill, JD, (1980), Applications of Transient Electromagnetic Techniques, Technical Note TN-7 page 5, Geonics Limited, Mississauga, Ontario.
- Morrison, H.F., Phillips, R.J., O'Brien, D.P., (1969), Quantitative interpretation of transient electromagnetic fields over a layered halfspace, Geophysical Prospecting, 17, 82-101, https://doi.org/10.1111/j.1365-2478.1969.tb02073.x
- Munkholm, M.S. and Auken, E., (1996), Electromagnetic Noise Contamination on Transient Electromagnetic Soundings in Culturally Disturbed Environments, Journal of Environmental Engineering Geophysics, 1, 119 – 12, 10.4133/JEEG1.2.119
- Nabighian, M.N., (1979), Quasi-static transient response of a conducting half-space. An approximation representation, Geophysics, 44, 1700-1705, https://doi.org/10.1190/1.1440931
- Nabighian M. N., (1987), Electromagnetic Methods in Applied Geophysics Theory - Volume 1. Society of Exploration Geophysics.
- Nabighian, M. N. and Macnae, J. C., (1989). Time-domain electromagnetic prospecting methods. in Nabighian, M. N. Ed. Electromagnetic methods in applied geophysics. 2: Society of Exploration Geophysics.
- Nabighian, M.N. and Macnae, J.C., (1991), Appendix A: TEM systems, In Electromagnetic methods in applied geophysics – Application, (ed. M.N. Nabighian): 479 – 483, SEG publication.
- Nekut, A.G. and Eaton, P.A., (1990), Effects of pipelines on EM soundings, 60th SEG meeting, 1990, 60th SEG meeting, Expanded Abstracts, 491-494.
- Nyboe N. S., Mai S. S., (2018), Shallow information from high magnetic moment measurements, AEM2018, International Workshop on Airborne Electromagnetics, Conference Paper.
- Oldenburg, D. W. and Kang, S. (2015), Recovering IP information in airborne-time domain electromagnetic data, 24th ASEG-PESA meeting - Perth, Extended Abstract.
- Pelton W.H., Ward S.H., Hallof P.G., Sill W.R., Nelson P.H., (1978), Mineral discrimination and removal of inductive coupling with multifrequency IP, Geophysics, 1978, 43, 588-609, https://doi.org/10.1190/1.1440839

- Raiche, A. P., Bennett, L. A., Clark, P. J., & smith, R. J., (1985), The use of Cole–Cole impedances to interpret the TEM response of layered earths, Exploration Geophysics, 16(2–3), 271–273, https://doi.org/10.1071/EG985271
- Sattel, D., & Mutton, P, (2015), Modelling the superparamagnetic response of AEM data. Exploration Geophysics, 46(1), 118–129. https://doi.org/10.1071/EG14005
- Seigel, H.O., (1959). Mathematical formulation and type curves for induced polarization, Geophysics, 24(3), 547–565, https://doi.org/10.1190/1.1438625
- Sharma V. P., (1986), Geophysical Methods in Geology, Elsevier.
- Smith R., and West G. F., (1988), Inductive interaction between polarizable conductors: An explanation of a negative coincident-loop transient electromagnetic response, Geophysics, 53(5), 677-690. https://doi.org/10.1190/1.1442502
- Smith, R. S., & West, G. F., (1988), TEM Coincident Loop Negatives and the Loop Effect. Exploration Geophysics, 19(1–2), 354–357. https://doi.org/10.1071/EG988354
- Smith, R.S., and J. Klein, (1996), A special circumstance of airborne induced polarization measurements, Geophysics, 61(1), 66–73, https://doi.org/10.1190/1.1443957
- Smith, R., & Annan, P., (1998), The use of B-field measurements in an airborne time-domain system: Part I. Benefits of B-field versus dB/dt data, Exploration Geophysics, 29(1–2), 24–29, https://doi.org/10.1071/EG998024
- Sorensen, K. I., and Auken, E. (2004), SkyTEM–a New High-resolution Helicopter Transient Electromagnetic System. Exploration Geophysics, *35*(3), 194–202. https://doi.org/10.1071/EG04194.
- Spies, B.R., (1980a), A field occurrence of sign reversals with the transient EM method, Geophysical Prospecting., 28, 620-632, https://doi.org/10.1111/j.1365-2478.1980.tb01247.x
- Spies B.R., (1989), Depth of investigation in electromagnetic sounding methods, Geophysics, 54, 872-888, https://doi.org/10.1190/1.1442716
- Spies, B.R. and Frischkneckt, F.C., (1991), Electromagnetic sounding, In Electromagnetic methods in applied geophysics, Nabighian, M.N., Ed., II, 285-426.
- Sumner, J.S. (1976), Principles of Induced Polarization for Geophysical Exploration. Elsevier, Amsterdam, 227.

- Telford, W.M, (1990), Applied Geophysics, Cambridge University Press; 2nd edition.
- Vanhala, H. and Peltoniemi, M., (1997), Spectral IP studies of Finnish ore prospects, Geophysics, 57, 1545–1555, https://doi.org/10.1190/1.1443222
- Viezzoli, A., Fiandaca, G., Segio, S., Auken., E., (2013), Constrained inversion of IP parameters from Airborne EM data, ASEG-PESA Expanded abstracts, Melbourne, Australia.
- Viezzoli, A., & Manca, G., (2019), On airborne IP effects in standard AEM systems: tightening model space with data space, Exploration Geophysics, 51(1), 155–169. https://doi.org/10.1080/08123985.2019.1681895
- Vinegar H.J., Waxman M.H., (1984), Induced polarization of shaly sands, Geophysics, 49 (8), 1267–1287, 10.1190/1.1441755
- Watt E.L. and Berens V., (2011), Non-prescribed groundwater resources assessment - Alinytjara Wilurara Natural Resources Management Region. Phase 1 – Literature and Data Review: DFW Technical Report 2011/18, Government of South Australia, Department for Water, Adelaide.
- Zhdanov M., (2017), Foundations of Electromagnetic Theory and Methods, Elsevier.

Chapter 2: Airborne chargeability mapping at continental scale: the TEMPEST™ system AIP modelling in the Australian Exploring for the Future Project

Chapter 2, summary

In the previous chapter, a general introduction on the methods and theory to follow this thesis work has been illustrated. It has been emphasized how IP effects can interest airborne EM measurement and how their modelling can both represents an opportunity and a challenge given its complexity. The research on AIP has been historically related to helicopter-borne platforms; this because of their simple geometry and accurate description which allows to reduce the ambiguities during IP modelling.

With this study, I focus on IP detection in fixed-wing systems, for which the induced polarization effects have historically been put in the "too hard basket" and have been typically overlooked. This was mainly due to the system geometrical configuration (and its monitoring) that prevented unambiguous relation between negative voltages and IP effects. A fixed-wing AEM system has nine geometrical parameters that can influence the recorded data: three for the receiver (pitch, yaw and roll), three for the transmitter (roll, yaw and pitch) plus the D_x,D_y, D_Z distance between the transmitter and receiver coils on the three planes. The variation of these parameters can cause ambiguous distortion in the shape of the EM response, complicating the IP recognition in dataspace and introducing further ambiguities during modelling. Also, a tenth parameter common to all the airborne systems, is the transmitter height above ground. For fixed-wing systems this is higher than in helicopter-borne platforms and possibly reduces the system's sensitivity to IP effects. The TEMPEST™ EM fixed-wing system, object of this study, has further complexities given by multiple step signal data processing carried on the recorded raw data: this could alter the recorded signal possibly bringing to a spectral IP content alteration or depletion in the delivered data. These conclusions, however, come from studies carried out in the mid-1960s, which placed considerations theoretically valid but supported by the technological capabilities of the time. Since then, the IP effects have never been a research object for this type of acquisition system. Nowadays, with the rapid accumulation of experience on AIP effects in helicopter EM systems, further research on EM and fixed wing IP is warranted. With this study I first present the results of a set of synthetic experiments oriented to address the IP effects for the TEMPEST™ fixed wing system. Then, a modelling comparison considering the AIP between the TEMPEST™ and the SkyTEM helicopter-borne system is provided for two overlapping lines containing negative records. The results of the modelling show similar chargeability and resistivity models between the two systems and for both the recorded TEMPEST™ secondary field components (X and Z). To conclude, to verify the large-scale chargeability mapping capability of the system, the entire Musgrave Province in South Australia has been inverted considering IP effects and a ground truthing over the Nemo-Babel mineralization is provided.

2.1: Introduction

As indicated in *Chapter 1*, it is known and accepted that the airborne electromagnetic (AEM) data are sensitive to the frequency-dependence of the ground conductivity, i.e., to the induced polarization effects. This phenomenon, referred as airborne induced polarization (AIP), is well known since Spies (1974; 1980), Lee (1975), Flis et al., (1989), Smith and Klein (1996) first demonstrated the presence of IP effects in the Airborne EM data and then many authors (e.g., Marchant et al., 2014; Macnae et al., 2016; Kaminski and Viezzoli, 2017) have extended our understanding of the physics involved and its relationship with geology. These effects manifest in the EM data with typical signatures such as negative voltages and/or "steep decays" of the recorded transients. The negative records are generated when the polarization currents dominate the conduction one (i.e., in a resistive environment or in presence of a very strong chargeable body) and are easily recognizable in the dataspace. These are also uniquely relatable to the ground polarization when the data are acquired with concentric-loop systems (Gubatyenko and Tikshayev, 1979; Weidelt, 1982), such helicopter-borne systems. Differently, for in-offset configurations, the negative voltages can also be consequence of the transmitter-receiver separation complicating the AIP recognition in the dataspace. When the polarization currents are weaker than the purely EM currents, the recorded signal does not change its sign getting distorted only. In these conditions, which are typical of conductive or weakly chargeable grounds, steep decays are produced (i.e., signals that decay faster than the typical $t^{-3/2}$ rate for the B field, commonly delivered for secondary field measurements of fixed-wing systems).

The importance of modelling the IP effects from AEM data has been then shown by authors, such as Viezzoli et al. (2017; 2021) or Macnae et al., (2016), that demonstrated how a wrong conductivity mapping is derived when the capacitive effects are overlooked during the EM inversion. Examples in literature spans from wrong estimation of the depth of conductive features, to wrong cover thickness (typically overestimated in the non-IP inverted models) and to a reduction of the depth of investigation of the retrieved models. On the other hand, using a dispersive-resistivity model to invert the EM data makes the inverse problem strongly ill-posed expanding the model space to potential equivalent solutions. This particularly happens when the data does not show negative recordings; here the IP effect is more subtle and inverting to solve the ground polarization requires a highly accurate description of the EM system (in terms of injected current, geometry, waveform, flight altitude etc…) to not introduce further complexity in inversion. Mostly for these reasons, the majority of the works on airborne IP modelling, phenomenology and detection have been carried for concentric loop helicopter-borne platforms (Viezzoli et al., 2019; Macnae et al., 2016; Hine et al., 2016). The unique relationship between negatives and AIP and the accuracy with which it is possible to describe the geometry of these systems made these platforms more suitable to treat the AIP.

For the other class of airborne EM systems, the fixed-wing systems, an extensive study on their sensitivity to AIP effects has never been carried making the non-dispersive modelling not a practice for these acquired data (Pitts et al., 2021). The geometry of these systems has a high number of degrees of freedom (transmitter and receiver pitch, roll, and yaw, together with horizontal and vertical separation between transmitter and receiver bird) that do not allow to uniquely relate negative recordings with IP effects. Additional challenges arise from the complex processing steps that are employed in the treatment of data acquired with these platforms. This can include deconvolution and re-convolution to B field data, as will be shown for the TEMPEST™ fixed-wing system in *Section 2.1.3*, data-replacement with exponential fitting and frequency-domain filtering that could bring to a possible spectral depletion of IP content in the delivered data. In addition, as for helicopter-systems, IP effects in fixed-wing EM data are often weak and can be obscured by the total EM response. Therefore, they can be difficult to detect and differentiate from noise, lack of signal in restive areas, and two- or three-dimensional effects within the system footprint.

Recent developments in the processing of fixed-wing data (Ley-Cooper et al., 2013; Brodie et al., 2019), in modelling approaches (Fiandaca et al., 2024; Ray et al., 2021), on the understating of AIP (Dauti et al., 2024) and in the system control of fixed-wing systems (Mulè et al., 2013), has allowed to rethink the technical possibility to conduct an extensive work on the fixed-wing capabilities in AIP detection and modelling. Another reason that motivates the study lies into the capability of these systems in mapping large areas in a relatively small amount of time and recording a great quantity of data. An example of a modern fixed-wing AEM application is given by the AusAEM project, part of the Exploring For The Future project undertaken by Geoscience Australia (Ley Cooper et al., 2020), with which the first continental scale airborne EM survey ever flown is carried to map the ground resistivity of the entire Australian Nation. The opportunity to model AIP from these datasets would add a significant additional layer of information for the national geological mapping. Also, a more accurate resistivity modelling would be introduced. Imaging IP processes from fixed-wing and heliborne EM data opens the way for comparisons with ground-IP measurements, which may bring a shift in the way the AEM data are used and interpreted at large scales.

With this work I aim to contribute to the understanding of the fixed-wing systems capabilities in AIP effects detection and modelling. I will focus on the TEMPEST™ fixed-wing time domain system (Lane et al., 2000), as it is used in the AusAEM project, and a large quantity of open-source data are available. First, I aim to verify the TEMPEST™ sensitivity to AIP effects from a synthetic standpoint. Then, the models retrieved from real fixed-wing TEMPEST™ data are compared with overlapping helicopter-borne modelled data. To conclude, a regional scale modelling is carried and verified over a known mineralization.

2.1.1: AusAEM

The AusAEM airborne electromagnetic survey is the Australian national project that aims to map the 3D resistivity of the entire country. Developed by Geoscience Australia since it begins in 2016, it is part of the national Exploring for the Future project financed by the Australian government with a total of $225 million. The project aims to improve the subsoil understanding for minerals, energy and groundwater exploration and to stimulate investments from private companies. In this framework, the AusAEM survey project plays a role to unlock the deep structures and provide tools to regional geological mapping and comprehension. The survey, the largest ever flown in the airborne EM history (Ley Cooper and Brodie, 2019) covers a total of 2.5 million of km^2 with an average line spacing of 20 km for the regional flights. Some infill area has also been flown with a smaller variable line distance (5km on average) over strategical area of interest. The overall flight survey is of 470,000-line km with 20,000-line km of infills. The portion of Australia flown so far is shown in *figure 2.1*.

The data are completely open access, and it is possible download them from the agency website both the raw data and the conductivity models produced by Geoscience Australia.

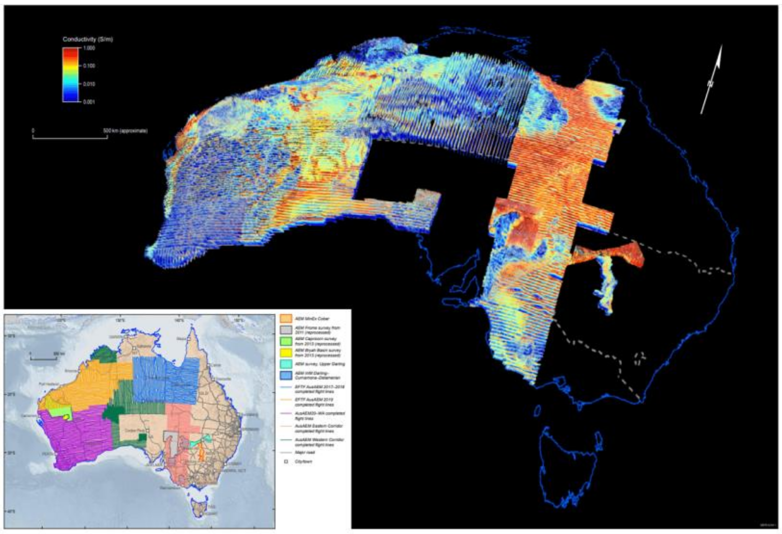

Figure 2.1. Conductivity cross sections produced by Geoscience Australia of the acquired data. The aerial coverage of AusAEM project is visible. From Geoscience Australia website.

2.1.2: The TEMPEST™ EM system

The TEMPEST™ EM system (Lane et al., 2000; Green et al., 2000) is one of the most common fixed-wing systems. Developed since the beginning of the 2000's, by the Cooperative Research Centre for Australian Mineral Exploration Technologies (CRC AMET), has been largely used since 2007 all around the world to map the ground resistivity. It was initially operated by FUGRO, then by CGG Multiphysics and nowadays by XCalibur Smart Mapping.

The system is designed for use in a mid-size aircraft to minimise costs, i.e., larger than magnetics/radiometrics aircraft but smaller than aircraft used for other available high-power AEM systems. TEMPEST™ is configured with a transmitter loop located on a fixed-wing aircraft and receiver coils located in a towed bird. The data provider typically delivers for this system B field data, both X and Z component, as illustrated in *table 1.1* and *table 2.1*., retrieved after a multi-step processing routine. A more detailed description of the TEMPEST™ processing is later presented in this section.

In the *table 2.1*, a list of the specifics for the TEMPEST™ system are listed for the different system's configurations.

	STANDARD	HIGH MOMENT	TEMPEST™ 208
Base frequency (Hz)	25	25	25
Transmitter area (m²)	244	244	154
Transmitter turns	1	1	1
Waveform	Square	Square	Square
Duty cycle	50%	50%	50%
Transmitter pulse width (ms)	10	10	10
Transmitter off-time (ms)	10	10	10
Transmitter turn-off (µs)	42	80	~ 55
Peak current (A)	280	1,200	560
Peak moment (Am²)	68,320	288,000	86,240
Average moment (Am²)	34,160	144,000	43,120
Sample rate (kHz)	75 (on X and Z)	75 (on X and Z)	76.8 (on X and Z)
Sample interval (µs)	13	13	13
Samples per half-cycle	1,500	1,500	1536
System bandwidth	25 Hz to 37.5 kHz	25 Hz to 37.5 kHz	25 Hz to 38.4 kHz
Nominal Flying Height (m)	120	120	100-120
EM sensor	Towed bird -3 component dB/dt coils	Towed bird - 3 component dB/dt coils	Towed bird - 3 component dB/dt coils
Nominal Tx-Rx horizontal separation (m)	117	117	115
Nominal Tx-Rx vertical separation (m)	41.5	41.5	
Stacked data output interval (ms)	200 (~12 m)	200 (~12 m)	200 (~12 m)
Number of output windows	15	15	15
Window centre times	13 µs to 16.2 ms	13 µs to 16.2 ms	- 13.3 µs to 16.2 ms

Table 2.1: Summary of the features of the TEMPEST™ systems configuration.

In terms of system-control, recent improvements (Ley-Cooper et al., 2013; Brodie et al., 2019) allow an improved monitoring of the system geometry. This involves measuring the orientation of both the transmitter loop located on the aircraft and the receiver coils located inside the towed bird. These orientation measurements are used to compensate the ground response data for the effects of variations in the system geometry, improving the primary-field removal procedure described below.

Very low noise levels are achieved by recording the received signal at a high sampling rate, 76.8 kHz, and then applying multi-step signal processing techniques (Lane et al., 2000). The signal processing operates in the frequency domain to perform a full deconvolution of the measured response, removing the system transfer function characteristics and dynamically compensating for variations in the transmitted waveform. To assist interpretation, the deconvolved ground response signal is converted to a 100% duty cycle square-wave B-field response, allowing a single transient decay to be presented for the full 20 ms half cycle length available for a base frequency of 25 Hz (Lane et al., 2000). The processing steps for the TEMPEST™ 's raw data can be summarized as:

1. reduction ('cleaning' and stacking)
2. deconvolution of system response
3. primary-field removal
4. conversion to square-wave magnetic (B) field response
5. windowing

The following illustration is referred to a 25 Hz system.

At point (1), fully streamed data sampled at 76800 Hz are used. Firstly, the spherics are removed through wavelet transform threshold filtering. Then, the stacking procedure is applied on the streamed data with each recording half-cycle containing 1536 digital samples (76800/25/2). In the streamed data, every second half-cycle are flipped in polarity and groups of 150 half-cycles (in 3 seconds) are then stacked together with a Hanning window filter shape. This operation is carried to largely remove the coil motion in Earth's field noise (i.e. the low frequency), the coherent noise (such as the 50 Hz powerline noise) and the VLF noise. After the stacking procedure, the data are transformed to frequency domain where a notch filter is applied to remove residual VLF noise and a low-pass filtering to reduce residual coil-motion noise.

In frequency domain, the deconvolution procedure is applied (2) to remove the system self-response. The system transfer function between the transmitter-loop and the received dB/dt response is measured at high altitude, in absence of any ground response. The deconvolution is performed using all the 1536 samples per half cycle. The inputs are the observed sensor voltage (V), the observed transmitter current (I), the high-altitude reference voltage (V_a) and the high-altitude reference transmitter current (I_a). Defining the system transfer function (T) as:

$$T(\omega) = \frac{V(\omega)}{I(\omega)}$$

(2.1)

And the high-altitude transfer function (T_a) as:

$$T_a(\omega) = \frac{V_a(\omega)}{I_a(\omega)}$$

(2.2)

A frequency response can be computed, assuming a linear transfer function and a dipole source, as:

$$\Psi(\omega) := \frac{T(\omega)}{T_a(\omega)} = \frac{g}{g_a} + \frac{R_g(\omega)}{g_a}$$

(2.3)

Where $R_g(r)$ is the frequency response of the ground (the Fourier transform of the impulse response), g is the coupling between the transmitter loop and the receiver coil and $g_a$the corresponding factor for the high-altitude reference data. The term $\frac{g}{g_a}$ represents the deconvolved primary field to be removed subsequently. This term is equal to one if the system geometry at survey altitude is the same as it was for the reference line. This deconvolution procedure considers: the effect of the current sensor, the effect of the receiver coil response function and of the gradual changes in the shape of the transmitter waveform (using a pre- and post-flight reference waveform).

After the deconvolution, the primary field is removed (3). This depends on the system geometry (that is not perfectly measured), i.e., as mentioned, by g and g_a. Given the uncertainty on the receiver-coils with respect to the transmitter-loop as well as transmitter-loop and receiver-coil attitude, there is uncertainty in the estimate of the coupling factor g. To deal with this, an earth response at zero frequency is computed to extrapolate the term $R_g(\omega)$, introducing a pre-imposed earth response on the resultant data (e.g., layered-model response, sum of exponential decays). In the TEMPEST™ processing routine, this aspect has a large impact on the IP-content depletion from the recorded data.

After the primary field removal, the $R_g(\omega)$ response can be multiplied by the Fourier transform of any "suitable time-domain transmitted waveform", as in point (4) of the processing routine. In the case of the standard TEMPEST™ B-field data, the "suitable time-domain transmitted waveform" is a 100% duty cycle square wave with 20 ms pulse width with 1 A current step. Then, the result of the operation is inverse Fourier transformed to a time domain waveform.

After the transforming back to the time domain, the time-series is then windowed (5) to produce 15 standard windows using a box-car windowing function.

Processing in the frequency domain gets a full deconvolution of the measured response, removing the system transfer function (system response) and compensates for variations in the transmitted waveform throughout a survey. The processing 'allegedly' also removes the variable primary field effects that result from changes in coupling between the receiver coils in the towed bird and the transmitter loop; this can be orders of magnitude higher than secondary response and IP effects. Moreover, historically, a wide variety of site-specific digital signal processing techniques have been applied to the original data to "suppress noise" or to highlight specific elements of the ground response. This complicates possible generalizations of the processing routines and estimations of the data spectral content.

2.2: Synthetic sensitivity study

For this first set of synthetic experiments, I aim to investigate if the TEMPEST™ system can detect AIP effects with a large dataspace and model-space inspection. The workflow follows the approach proposed by Pitts et al. (2021) for the SPECTREM system (see *table 1.1* for technical specifications), which shows significant sensitivity to IP effects. The SPECTREM system has significative analogies with the TEMPEST™ system, particularly in terms of geometry and general functioning. Both the systems are fixed-wing time domain systems with a towed bird carried at a vertical nominal distance of 50m, and a horizontal nominal distance of 100m from the craft, on which the transmitter is located (Klinkert et al., 1999). This, as for the TEMPEST™ flies at 100 m of altitude from the ground. One of the main differences between the two systems is in the nominal peak magnetic dipole that SPECTREM can reach of 300.000 Am^2 (versus the 144.000 Am^2 of the TEMPEST™ high moment). This difference has of course consequences on the S/N, that is improved in the SPECTREM and could improve the detection of the subtle IP effect reducing noise. Another main difference with the TEMPEST™ system is in the energisation: while the TEMPEST™ measures with a 50% duty cycle, while the SPECTREM operates with a 100% duty cycle, allowing to measure longer decays to detect smaller conductive bodies. As consequence, the raw data processing is different given that the primary magnetic field has to be always known for being removed from the recorded total field to retrieve the secondary measurement. From a general point of view, also the SPECTREM signal processing (illustrate in Legatt et al., 2000) presents multiple steps such as the TEMPEST™, complicating possible predictions on the effects on the IP spectral content in the recorded data. In this sense, for both the systems, a detailed analysis of the effects of the processing steps on the IP content could help in a better understanding.

As mentioned, the only work in literature on AIP for fixed-wing systems is the one proposed by Pitts et al. (2021). In the work, several forward responses computed changing the parametrical combination of 1D chargeable models have shown how the system can detect IP effects above the system noise level.

In the workflow, a comparison is carried out between forward responses of simple two-layer models with and without IP effects. For each couple of forward responses, a percentage difference is computed to quantify the distortions produced by the chargeability to the non-AIP affected forward response (with same resistivity values). After the computation of 500k forward responses for different model parametrizations, the distortions are imaged in 2D maps, with two sets of parameters varying in the axes (e.g., rho and phi and rho and thickness of the first layer) and fixing the remaining.

The workflow is illustrated in detail in the three points below:

1. Define two synthetic models, parametrized with:
    a. a first layer with dispersive resistivity representing the IP effect
    b. the analogous model without IP, with the same zero-frequency resistivity

    As dispersive resistivity model, the Maximum Phase Angle (MPA) re-parametrization of the Cole and Cole model proposed by Fiandaca et al. (2018) has been used. Here, the model space is described as {ρ, φ, τ_φ, C}, where the maximum phase φ of the complex conductivity (i.e. minimum phase of complex resistivity changed of sign) is used instead of the classic Pelton chargeability m_0 (Pelton et al., 1978), and the relaxation time τ_φ is defined as the inverse of the frequency (not angular) at which the maximum phase is reached. With this parametrization the parameter correlations are decreased, in particular between the phase and frequency dependence if compared with the Pelton's m_0 and c parameters. In *table 2.2* the correspondence between the Cole and Cole chargeability and the MPA maximum Phase is presented. The relation between the two is not linear: the differences between τ_φ and the Cole and Cole τ_ρ increase with an increase of m_0 or/and with a decrease of C. The conversion below is computed for a resistivity (ρ) of 100 Ω·m, a time constant (τ_φ) of 10^{-03} s and a frequency dependence (c) of 0.5.

Cole and Cole chargeability [mV/V]	MPA phase (φ) [mrad]
1	0.2
10	2
100	21
500	141
900	424

Table 2.2. Conversion between the Cole and Cole chargeability and the MPA phase for a resistivity of 100 Ω·m, a time constant of 0.001 s and c of 0.5.

2. Compute the 1D forward response for both the models.
3. Compute the percentage difference between the forward responses, as *in equation 2.4*:

$$Distortion_i = \sum_{j=1}^{n} \frac{100\%}{n} \left\| \frac{fwr_{NOIP_j} - fwr_{IP_j}}{fwr_{NOIP_j}} \right\| \tag{2.4}$$

   Where the subscript j is referred to the gate number that goes from 1 to *n* (number of gates above the noise level).

   The percentage difference is computed for the gates whose difference (between the AIP and non-AIP forward responses) is higher than the noise level to quantify the detectable distortions only. A simple noise model has been used, with a noise floor set at $10^{-17.5}$ T at 1 ms and decreasing in time as $t^{-\frac{1}{2}}$, a value compatible with the TEMPEST™ noise measured in AusAEM (Ley Cooper et al. 2020). The uncertainties for each time window are computed as in equations 1.60.

With this approach I assume that all the measured distortions can be attributable to IP effects only. Two examples of comparison between a purely resistive and polarizable models forward responses for the TEMPEST™ Z component are represented in *figure 2.2*.

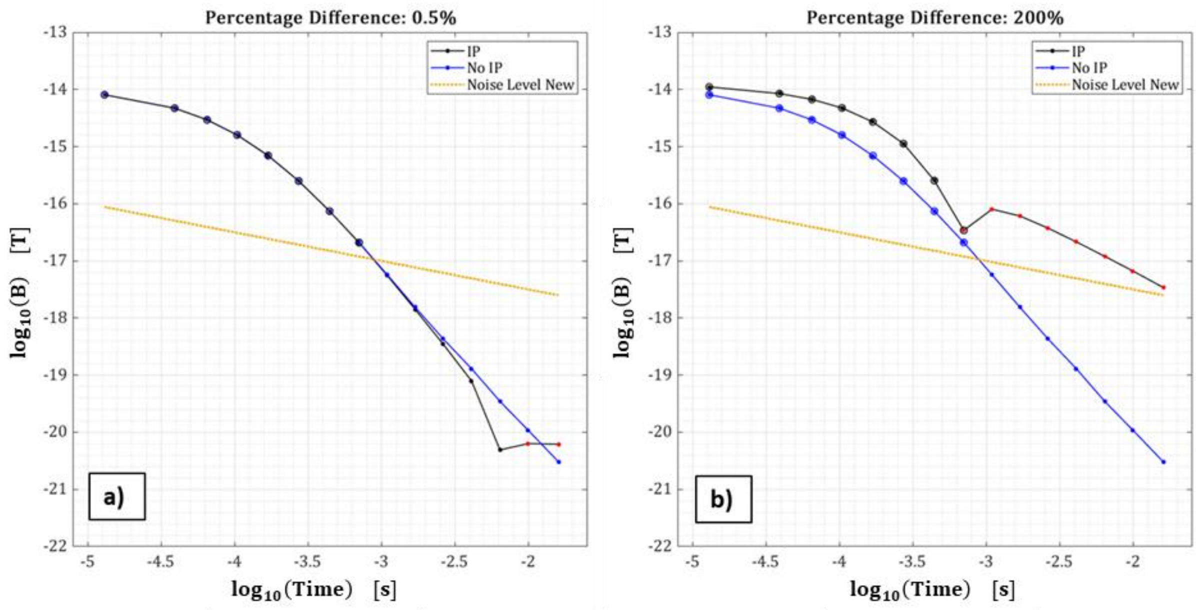

Figure 2.2. Examples of distortion produced by different amounts of chargeability for a homogeneous halfspace. For both figures, in blue is shown an Airborne EM transient not affected by IP effects, in black its equivalent computed on a chargeable halfspace while in yellow is shown the noise level. The amount of distortion produced by the chargeable ground is computed as in equation 2.4 is indicated in the title.

In *figure* 2.2*a* and *2.2b*, both the forward responses are computed for a conductive (25 Ω·m) first layer of 30m of thickness over a resistive second layer. In blue the forward response for the purely resistive halfspace is represented while in black its respective for the polarizable halfspace. On the lefthand side (*figure 2.2a*) the AIP forward response is computed for a weakly polarizable first layer (φ = 0.2 mrad, $\tau_\varphi=10^{-03}$ s, c=0.2; corresponding to 3 mV/V) while on the righthand side (*fig. 2.2b*) for a strongly polarizable first layer (φ = 115 mrad, $\tau_\varphi= 10^{-03}$ s, C=0.2; corresponding to 780 mV/V). In *figure 2.2*, the AIP negative gates are represented in red, the noise level is represented by the yellow dashed line and the round-shaped dots represent the time windows over which the mean percentage distortion is computed, i.e., where both the forward responses are above the noise level. The value of the percentage distortion is shown in the title of the figures, and it is visible how, as expectable, increasing the first layer chargeability the distortion increases.

The workflow described in points 1, 2 and 3 is repeated for 500k forward responses, both for the X and the Z components. The models are defined with a two-layers configuration. Here, the shallow layer parametrization varies at each workflow cycle (repetition of point 1, 2 and 3) while the deeper layer is maintained purely resistive. Although only the shallow layer can be chargeable, this assumption allows to reduce the ambiguities and better link the AIP distortions to simple geological configurations. In this simplified 1D geology, the deep layer is representative of the basement and the layer above can represent a wide range of geological configurations, from the outcrop to the thick cover, generic sources of IP effects in AEM measurements (Viezzoli and Manca, 2019). The parametric ranges for which I computed the forward responses are listed in *table 2.3*:

Parameter	**Minimum Value**	**Maximum Value**	**Number of values**
Resistivity [Ω·m]	1	1000	35
Phase [mrad]	1	300	35
Frequency Dependence	0.1	0.9	3
Time Constant [s]	1e-05	1	5
First layer Thickness [m]	5	100	10

Table 2.3. Parametrical range with which the forward responses are computed. The "number of values" indicates the number of samplings (comprise between the minimum and maximum value) with which I sample the model space for the specified parameter.

The parametrical ranges are set to span, after their combination, a wide range of possible geological settings that can be described with a two layers configuration. The end-members parameters represent possible geological limit-scenarios. For instance, a phase value of 300 mrad (~600 mV/V) is very high for environmental application, for which without electrode polarization a maximum value of few tens of mrad can be reached (considering the linear relation between surface polarization and surface conduction described in Weller et al., 2013), but reasonable for mineral polarization. The time constant is linearly related to the grain size of the chargeable particle (Pelton et al. 1978) and, increasing the grain size, the chargeability typically decreases (Pelton et al., 1978; Martin and Weller, 2023). Regarding the frequency dependence, a value of 0.5 corresponds to a Warburg case polarization while, when c tends to 0, to a Constant Phase Angle configuration (e.g., Van Voorhis et al., 1972). When the frequency dependence c is small, the time constant is less resolved given the wide spectral range covered by the chargeability frequency peak. For glacial environments, a frequency dependence higher than 0.8 is necessary to fit the data together with time constants lower than 10^{-05} s (e.g., Lorentzen et al., 2024). For sedimentary materials, such as clay and sands, the spectral behaviour is strongly related to the water content (e.g., Breede et al. 2012), the effective pores and the effective area of the geologic material. More in general, the clay minerals show a high chargeability, given their larger specific surface, and increase the total chargeability in sand-clay mixtures. With the proposed parametrization it is possible to span from a conductive cover over a resistive basement (representative of a typical Australian configuration) up to a chargeable resistive shallow layer that can represent an outcrop without cover. It is important to also highlight that, from literature (Macnae et al., 2016), the AEM systems, are considered sensitive to high-frequency polarizations (given the limits in the system base frequency) and to strong chargeabilities only. This means, in geological terms, sensitivity to non-economic minerals, clays and fined grain materials. With this set of experiments, I also aim to verify if for high time constants (of 1 s) and low chargeability these EM systems have sensitivity to IP effects.

For the computation of the forward responses the TEMPEST™ system is described as:

- Tx – Rx horizontal distance: 100 m
- Tx – Rx vertical distance: 50 m
- Tx altitude: 120 m
- Rx and Tx Pitch: 0°
- Rx and Tx Yaw: 0°
- Rx and Tx Roll: 0°

We decided to use zero values for pitch/roll and yaw in the simulations because in AusAEM generally low values are recorded for these attitude parameters, as it is shown in *figure 2.3*, which presents the histograms of all recorded attitude values for the infills of the AusAEM project flown over the Musgrave Province (Western-South Australia). The survey is approximately 20,000 line-km and will be treated for regional modelling in the next section of this paper. The mean and standard deviation values for the pitch, roll and yaw distribution is shown in *table 2.4*. The extensive use of the TEMPEST™ system provided improvements to many aspects of this system (e.g., Mulè and Smiarowski 2013; Brodie et al., 2019) including the monitoring and active measurement of the system geometries during the acquisition. This provides fundamental information for the TEMPEST™ modelling reducing possible ambiguities during inversion. With the low values shown in *figure* 2.3 and *table 2.4*, no spurious IP-like effects should be triggered in the measured data.

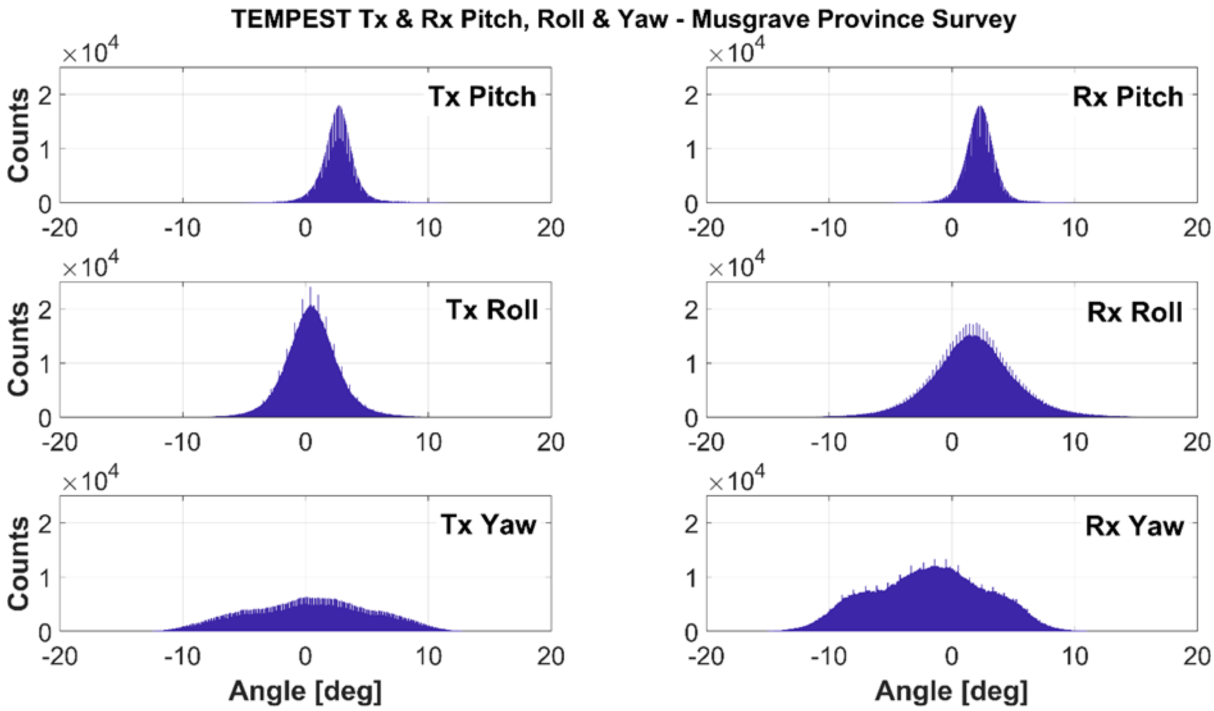

Figure 2.3. Measured transmitter and receiver pitch, roll and yaw for a portion of AusAEM dataset recorded over Musgrave Province in Australia. The collected recordings are relative to a survey of approximately 20k line kilometres.

Table 2.4 indicates the mean and standard deviation of the pitch, roll and yaw distributions of *figure 2.3*.

	Mean (degree)	**Standard Deviation (Degree)**
Tx Pitch	2.6	1.5
Tx Roll	0	2
TX YAW	0	5
Rx Pitch	2	2
Rx Roll	2	4
RX YAW	- 2	5

Table 2.4. Recorded Pitch, Roll and Yaw mean and standard deviation values for the Musgrave Province

Examples of forward responses computed varying the receiver pitch and roll are shown in *figure 2.4*. The responses are computed for a purely resistive two-layers model, with a first layer resistivity of 50 Ω·m and a thickness of 50 m above an infinite-thick 1000 Ω·m layer.

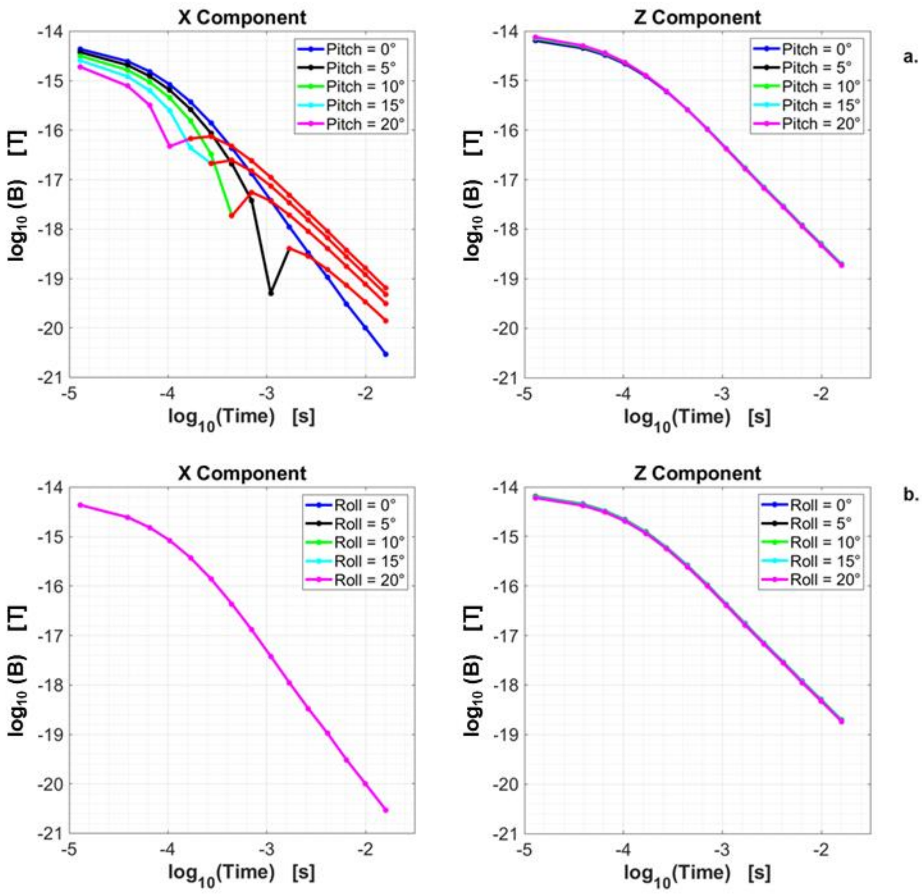

Figure 2.4. Examples of forward responses varying the receiver pitch (a) and roll (b) for the TEMPEST™ system. The responses are computed for a two-layers model, with a first layer resistivity of 50 Ω·m and a thickness of 50 m. The second layer has an infinite thickness and a resistivity of 1000 Ω·m.

From *figure 2.4* it is visible how the effect of spurious values of pitch and roll affect the TEMPEST™ recordings. As visible, the X component shows a high sensitivity to the receiver pitch orientation, introducing strong IP-like shapes as the angle increases. Differently, the Z component does not show any distortion that could be related to ground polarization.

2.2.1: Synthetic sensitivity study: results

To summarize the results (point 3 of the workflow), the computed percentage differences are plotted in a 2D space as in *figure 2.5*.

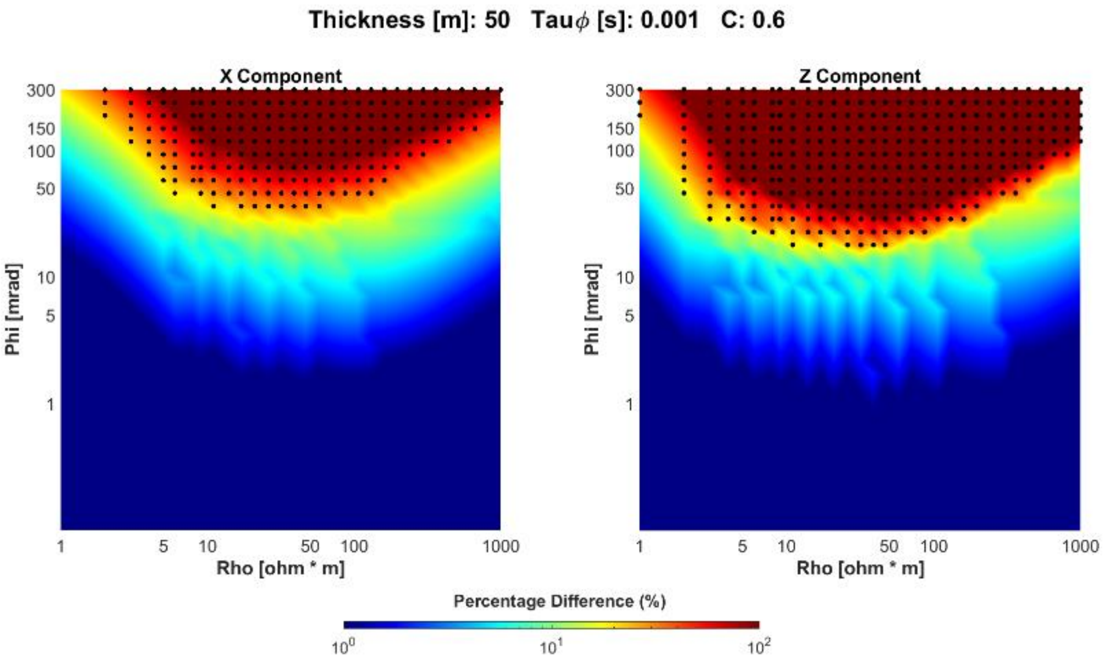

Figure 2.5. Representation of the amount of distortion produced by IP effects for a resistivity-chargeability varying space. The thickness, time constant and frequency dependence are kept fixed and shown in the title. The colour bar indicates the percentage of distortion. The X component distortion is shown on the left while the Z component on the right. The black dots represent where negative voltages have been produced in the IP forward response.

Given the number of model parameters, three of them (first layer thickness, τ_φ and C) are maintained fixed and visible in the title, while two (ρ and φ) can vary on the axis. The distortion value is higher than 0 where there is sensitivity to AIP, and it can span up to the 100% where all the gates are distorted. Given that the AEM data are typically fitted within a few percent of the recorded value (2%-3%), with a post-stacking error generally much smaller than 5%, it is possible to assume that a distortion higher than 5% can be significative to produce artifacts if the AIP effected data are fitted with a non-dispersive resistivity (e.g. Kaminski and Viezzoli, 2017; Viezzoli et al., 2021). In the *figure 2.5*, the black dots indicate where at least one negative gate is recorded in the IP forward response. These negatives can only be produced by the IP effects and not by the geometry (considering the typical AusAEM values for pitch/roll/yaw of *figure 2.3*) The results are here shown both for the Z and X component of the B field forward response.

The computed percentage differences are here referred to a two-layer model with 50 m thickness, a time constant of 0.01 s and a frequency dependence of 0.6. The results show how and where the IP effects distort the signal varying the resistivity and chargeability of the first layer.

Results shown in *figure 2.5*, show that for both the B-field components, the forward responses show significant AIP distortions (more than 5%) where the shallow layer is weakly chargeable and very conductive or very resistive. For the very conductive domain (where the resistivity is lower than 30 Ω·m), the pure EM currents are strong enough to overcome the opposite sign polarization currents to avoid the production of significative distortions. A similar behaviour is visible when the ground is very resistive (more than 500 Ω·m): the signal falls into noise (as shown in *figure 2.2*) and the IP effect is not detectable. At the same time, for both the scenarios, increasing the shallow layer chargeability to around 10 mrad (relatable to fine-grained cover), the IP effects become significative to generate artifacts during modelling if neglected (giving a distortion higher than 5%). As general trend the AIP distortions become more significant increasing the first layer resistivity, i.e. where the purely EM currents get weaker, and increasing the shallow layer chargeability, i.e. where the IP currents get stronger. As visible from *figure 2.5,* where the first layer is highly chargeable and the signal does not fall into noise, it is possible to detect negative voltages related to IP effects.

These considerations are valid both for the Z and for the X component. The main differences between the two for this set of experiments are relative to the negative voltage distribution, that interests smaller chargeability values for the vertical component, and, in the very conductive domain, the Z component shows AIP distortions where the X doesn't.

It is also necessary to highlight the spectral characteristics of this set of experiments; the small time constant and the frequency dependence here used describe a relatively fast polarization of the ground. As mentioned in the previous section, this is considered in literature the limit beyond which is no more possible to measure AIP from airborne inductive platforms. At this regard, in *figure 2.6*, I present the results of the experiments increasing the time constant of the shallow layer to 1 s. The model-space is here described as in the previous set of experiments (in *figure 2.5*) with only the time constant increased.

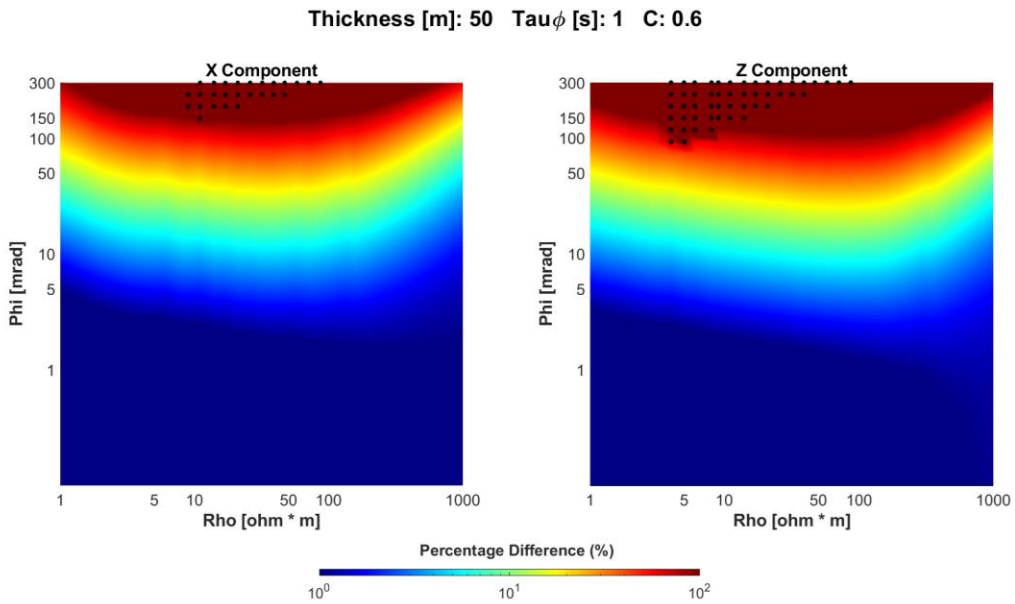

Figure 2.6. Distortion plot varying resistivity and chargeability increasing the time constant to 1 s. The black dots represent where negative voltages have been produced in IP forward response.

Comparing the results of *figure 2.5* with *2.6*, the parametric range where the distortions are detectable is very similar. The main difference is in the reduction of negative voltages and in the increase of detectable distortions in the very high resistivity domain when the higher time constant is used. The absence of negatives is consequence of the longer charging and discharging time of the polarizable ground (i.e. the higher time constant) which shifts the signal change of polarity at later times. For very resistive ground, this can be below the noise level but giving significative distortions. When the ground chargeability is high, as visible from *figure 2.6* and *2.7,* negative voltages can be recorded also for this time constant. An example of decays for 1 s time constant is shown in *figure 2.7*.

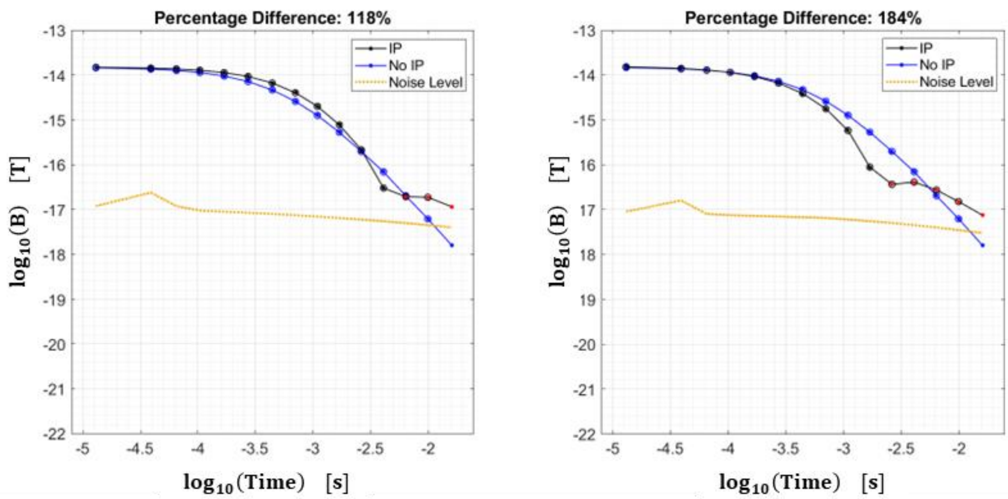

Figure 2.7. IP affected (black) versus non-IP affected comparison for both X (left) and Z component (right). The percentage difference between IP and non-IP distorted signal is displayed in title and computed as eq. 2.4. The forward responses are computed for a two-layers model. The first layer has a resistivity of 40 Ω·m, a chargeability of 180 mrad, a time constant of 1 s, a frequency dependence of 0.6 and a thickness of 25 m. The second layer is purely resistive (1000 Ω·m).

Although the negative records are not often recorded, the EM forward response shows sensitivity to IP even for high time constants and for low chargeability ranges. Follows that the IP distortion produced by the chargeable ground is recorded in the data, is not easy to recognize and leads to a mismodelling of ground resistivity if AIP is not taken into account.

In *figure 2.*8 the effect of the first layer conductance ($thk \cdot \frac{1}{\rho}$) on AIP detection is shown. Differently from the previous figures, the first layer resistivity and the thickness vary while a quick chargeability (i.e. characterized by a small time constant) is maintained fixed for all the forward responses. It is here visible for which resistivity-thickness parametric range the AIP is measurable and a linear relation with the decrease of conductance (lowering in thickness or increasing in resistivity) is visible. In geological terms, the effects of an altered cover (chargeable and conductive) on the TEMPEST™ EM measurements are recorded. Assuming a cover resistivity between 1 and 20 Ω·m, thinner is the cover, stronger are the AIP effects and negative voltages can be produced. Increasing the cover thickness the conductance increases, and the polarization currents don't overcome the EM eddy currents. This plot provides information also where the conductive cover is completely absent: here the signal falls into noise and it is not possible to detect AIP effects. As in the other examples, the AIP distortions are stronger for the Z than for the X component given the offset between the transmitter and the receiver that does not allow to measure the change of sign in the horizontal component of the magnetic field.

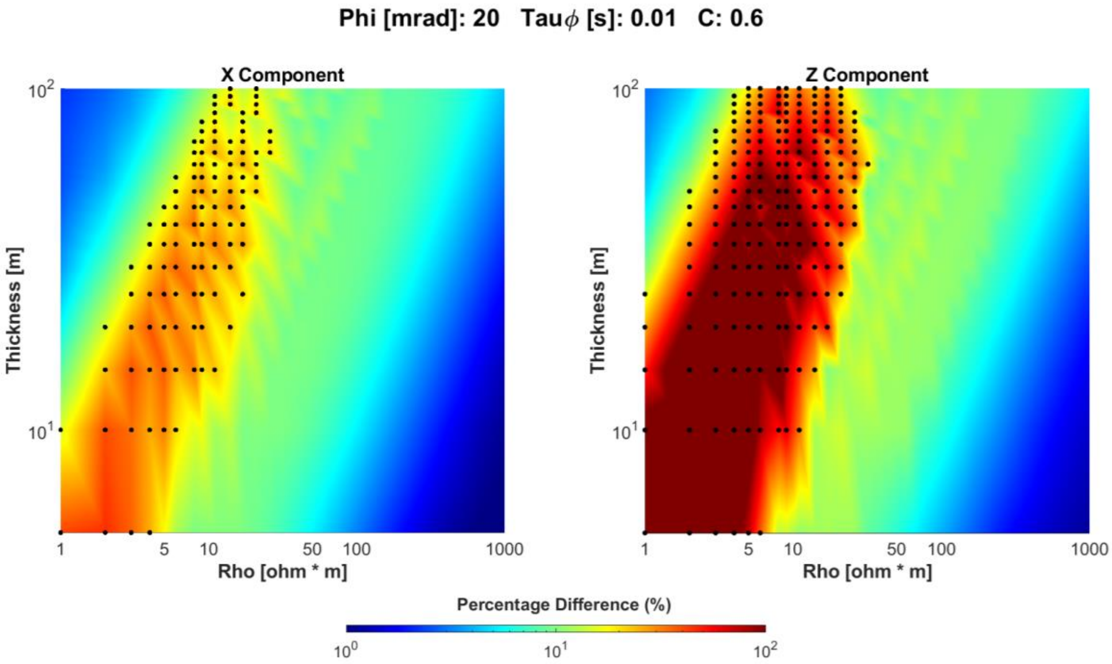

Figure 2.8. Distortion plot for a thickness-resistivity space. The other parameters are fixed and shown in the title. The graph shows the variation of distortion produced by AIP varying the ground first layer conductance. The black dots represent where negative voltages have been produced in the IP forward response.

In conclusion of the synthetic experiments, the study has shown that the TEMPEST™ fixed-wing system is sensitive to AIP effects for large and different set of geologic domains, both for its horizontal and vertical component. When a first layer over a resistive basement is polarizable, few milliradians (or mV/V) of chargeability are enough to significantly distort the recorded data for a wide range of parameters. The absence of AIP distortion is often where the first layer is very conductive and poorly chargeable or where it is very resistive and the signal falls into noise. For this latter domain, the detectability of AIP increases proportionally with the time constant: it has been shown how slow-chargeable materials, characterized by high time constants (considered out of the sensitivity range of the AEM), can give very strong distortions in the recorded data. Also, AIP effects not always manifest with negative measurements; more often, they can distort the recorded data orders of magnitude higher than the data uncertainty without producing unique markers of IP effects (like the negative recordings could be) in the dataspace. This subtle behaviour makes the AIP effects recognition even more challenging but, at the same time, neglecting these during the modelling can bring to the recovery of a wrong resistivity model.

To verify the synthetic results, the maps of the negative voltages of the AusAEM TEMPEST™ datasets have been produced and compared with other available geophysical and geological national maps. The distribution of negatives has been produced only where there are more than three consequent negative records in the same transient, above the noise level (i.e. 10^{-17} nT at 1 ms as described in the workflow) and neglecting the negative measurements in the first 2 gates, i.e. those that could be consequence of the geometrical offset in conductive environments. For this negative mapping the same noise level of the synthetic study has been used. The first comparison has been done with the Australian depth-of-basement map produced by Geoscience Australia in 2015 (Wilford et al., 2015) to prove the results shown in *figure 2.5,* 2.*6* and *2.8*. The map is shown in *figure 2.9*.

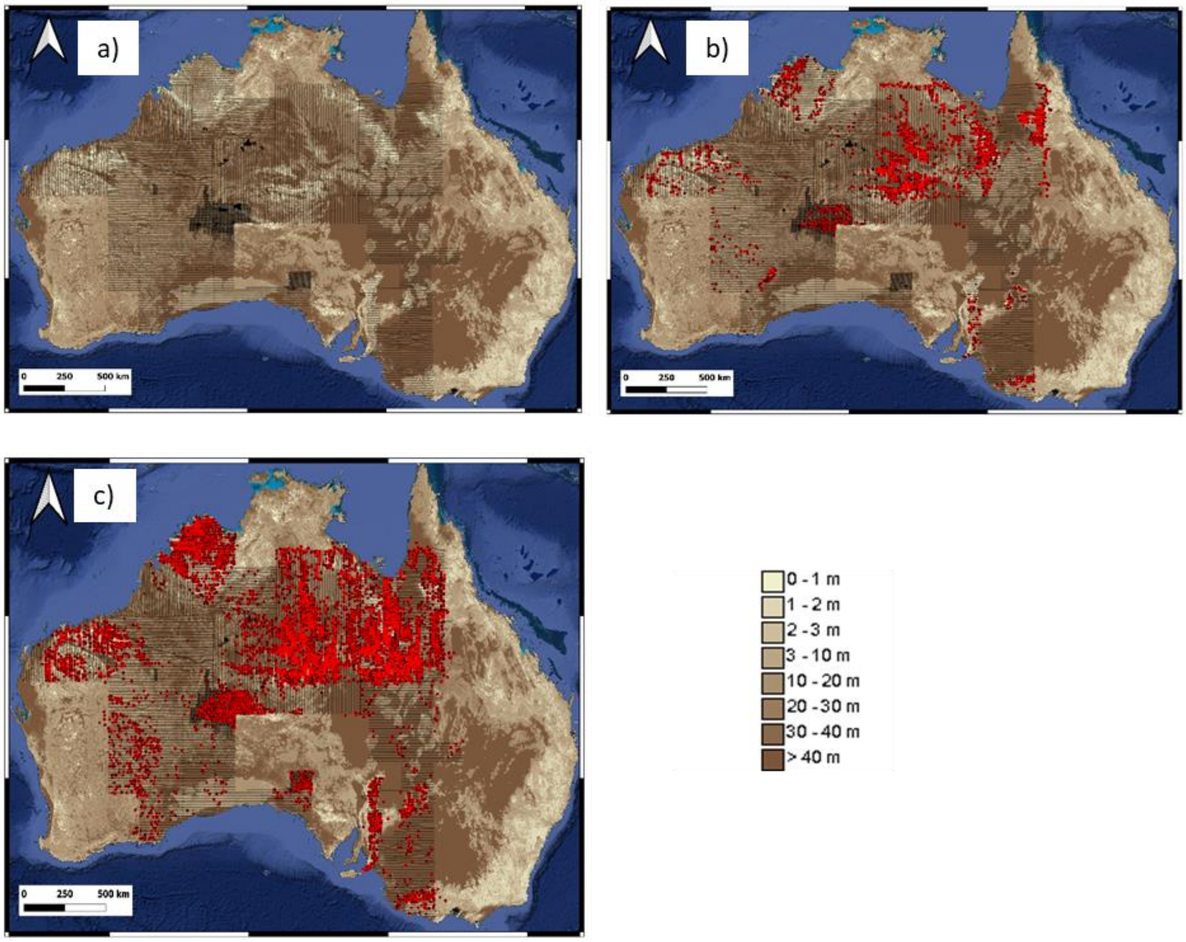

Figure 2.9. Map of negative voltages over the cover thickness base-map. In (b) the map of negatives for the Z component is shown while in figure (c) for the X component. The colour bar in the bottom right indicates the values of cover thickness.

Assuming a quick polarization for the regolithic cover ($\tau_\varphi < 0.01$ s), a good spatial correlation between the area that shows a thinner cover, and the negative measurements is shown consistently with the synthetics. The spatial correlation with the geological features is also visible from the comparison of the negatives with the lithological map closeup in *figure 2.10,* with a zoom over the Pilbara (in North West), Musgrave (South East) and Kimberley (North) regions.

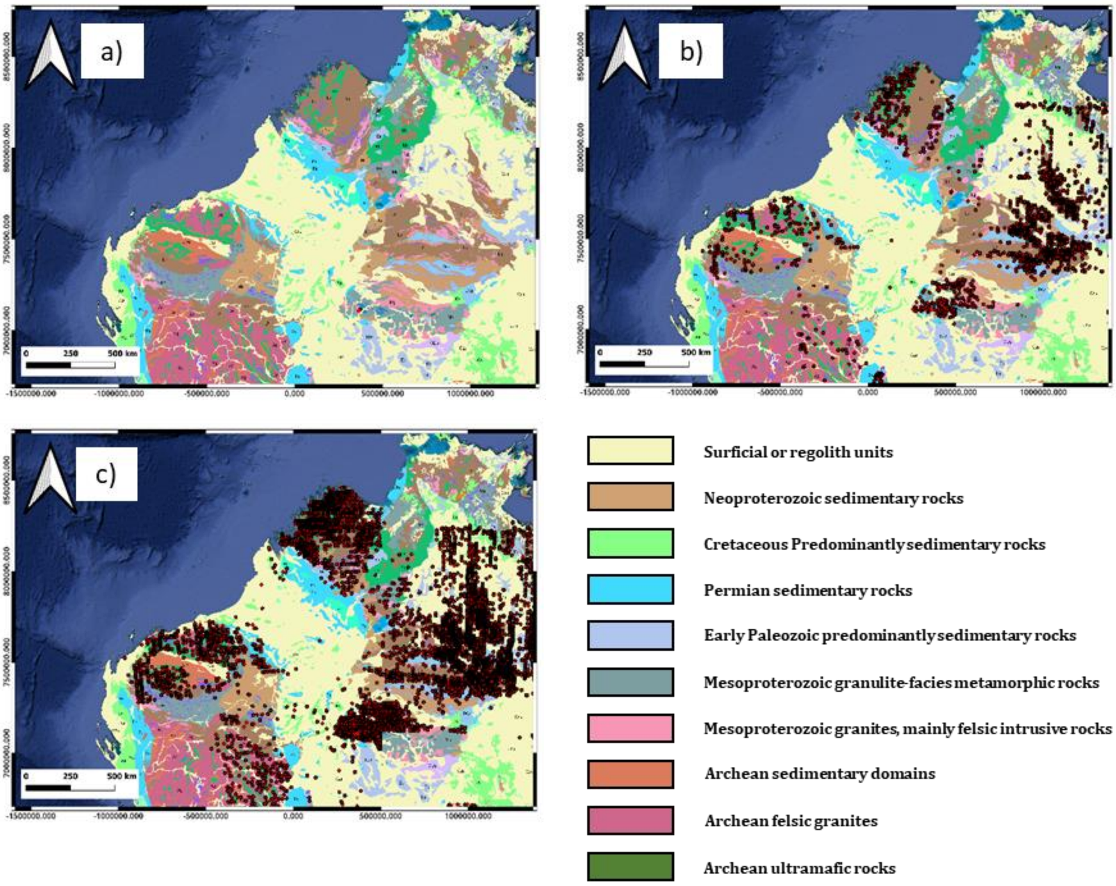

Figure 2.10. Detail of the map of negatives over Pilbara (N-W), Kimberly (N) and Musgrave (S-E) regions for Z component in (b) and X component in (c) of TEMPEST™ system. A simplified geological legend is shown in the bottom right.

The near surface geology map of Australia Map (2012 edition) shows a good correlation between the negative distribution and the outcropping Archean granitic domains in the three regions is visible (in pink in the map). In the specific, a correlation is visible with the high-grade Paleoproterozoic metamorphic complexes in the Musgrave (in grey), with the ultramafic Archean basalts (in green) in Kimberley and Pilbara and with the Paleoproterozoic sedimentary sequences in brown in the map. It is interesting to notice that not all the sedimentary sequencies are coincident with negative voltages. For instance, while in the Pilbara and Musgrave region there is a correspondence between the two, in the Kimberley and in the outcropping region between the Musgrave and the Kimberley the overlap is only partially controlled by the Proterozoic sediments. This behaviour could be explained by the heterogeneity of the sedimentary body, composed by a mix of mudstones, siltstones, conglomerates and breccias slightly metamorphosed that can give a different physical response for different assemblages. Differently, the felsic magmatic bodies negatives could be related to the presence of magnetite (Pittard and Bourne 2019) or disseminated sulphides in veinlet system that can give a polarizable response. At this scale, these correlations are anyway only general considerations, and a site-specific interpretation is necessary to evaluate the detailed relationships between the geological domains and the negative distribution. Although the resolution of the geological map is lower than the EM measurements, it is possible to assess a geologic control on the mapped negatives in the TEMPEST™ data. In contrast with the results of the synthetic modelling, the analysis of the real data shows that the negatives are more frequently expressed in the X component than in the Z component of the recorded *B* field. For the horizontal component, as also seen in *figure 2.4*, the negatives can be consequence of variations in the receiver pitch during the flight as well as to 3D effects. Further details about the X component behaviour in real data will be treated in the next section, where real data are modelled considering IP effects.

2.3: Real data inversions

In this section I consider results from the assessment of modelling field data at various scales. First, I compare the modelling results between the TEMPEST™ system with the helicopter-borne SkyTEM system models for two overlapping lines. This is done to verify the robustness and the comparability of the TEMPEST™ retrieved chargeability and resistivity models with the better-known helicopter airborne IP modelling. Then, a first regional-scale airborne chargeability mapping has been attempted using a portion of the AusAEM TEMPEST™ dataset. To conclude, to verify the accuracy of the regional scale modelling, a comparison of the retrieved results over a known mineralization is provided.

All the three experiments have been done using data acquired in the Musgrave Province in South Australia. This is a well-known area, object of recent geological and geophysical studies (Soerensen et al., 2018, Munday et al., 2020, Symington et al., 2022) both for mineral and hydrogeological purposes. Geologically, the area is an east-west elongated Mesoproterozoic orogenic belt with a width of some 50 km and 500 km of strike length, bounded by younger continental basin (Howard et al., 2015). It comprises a variety of high-grade amphibolite to granulite metamorphic grade basement rocks, overprinted by several major tectonic events and intruded by granitic plutons, layered mafic to ultramafic intrusions of the Giles Complex, and by mafic dykes. The third real data experiment has been done for an exploration project related to the Giles Complex intrusion. From an exploration standpoint, the area is a prospective for magmatic nickel-copper, PGE's, orogenic and intrusive gold, and iron oxide copper gold (IOCG) mineral system, characterized by an extensive conductive transported cover overlying an in-situ regolith (Howard et al., 2015). In this context, the Airborne EM plays a crucial role to explore beneath a conductive cover that can mask and/or distort the geophysical expression of a buried mineral system or a deep aquifer. Also, the Musgrave's geological setting can fit the two-layers model used in the synthetic case study of the previous section: as illustrated by Munday et al. (2020) the altered conductive and chargeable cover overlays a resistive basement and as shown with the synthetics, the effects of a shallow chargeable ground can be measured by the TEMPEST™AEM system.

2.3.1: Modelling approach

All the inversions, as the forward computation in the synthetic section, have been performed using the EEMverter inversion algorithm presented in s*ection 1.2.3.5*. For the inversion, the model parameters are mapped in two different model meshes, as proposed by Fiandaca et al. (2021) and Dauti et al. (2024), with different geometries and regularizations and parametrized with the Maximum Phase Angle (Fiandaca et al., 2018b). The resistivity and chargeability are mapped in a 2D (X-Z) model mesh and are vertically and laterally regularized with loose constraints (200%-300% of lateral allowed variation). Differently, given the small spectral content of the AEM data (limited to 2 decades), the spectral parameters (τ_{φ} and C) are keep fixed with depth and are free to change laterally only. This regularization aims to reduce the correlations between the parameters and to increase the sensitivity of the chargeability at depth during inversion, as shown by Fiandaca and Viezzoli (2021). For the purposes of this study, a 21-layer model was used for the SkyTEM inversion modelling the HM and LM data and a 15 layers model for the TEMPEST™ Z and X data. This has been chosen as consequence of the

TEMPEST™ smaller number of time windows (15) and bigger footprint which do not guarantee a high sensitivity to resolve small electric layers.

The layered inversion model has been vertically discretized from surface to 600 m for the TEMPEST™ system and to 400 m for the SkyTEM system, with log-increasing thicknesses. The difference in the model maximum depth has been chosen after some modelling tests for which the TEMPEST™ Z component was retrieving a reliable resistivity model at depth always above the depth of investigation (DOI). The DOI is computed using the approach proposed by of Fiandaca et al. (2015).

For both the inversions, the starting model has been defined as homogenous for resistivity (of 300 Ω·m) and chargeability (10 mrad). The spectral layer in which the time constant and the frequency dependence parameters are mapped has been described with a lateral homogeneous starting model, with τ_{φ} of 0.001 s and a c of 0.5. All the inversions have been configured using the same starting model (with a different vertical discretization) and regularization to avoid model-driven biases during the modelling. While the SkyTEM's HM and LM have been jointly modelled, the X and Z components of the TEMPEST™ system are modelled separately. This decision was taken to evaluate the differences in sensitivity of the two components to IP effects.

All the datasets have been manually processed, removing outliers and defining the noise floor as in equations 1.60a and 1.60b of *Chapter 1*. The noise floors have been set at 10^{-12} V/Am^2 for the SkyTEM HM data, at 10^{-08} V/Am^2 for the SkyTEM LM data, at 10^{-18} T for the TEMPEST™ Z component and at 10^{-17} T for the TEMPEST™ X component. The base noise level has been defined inspecting the data and considering the noise floor of the area. The uniform data uncertainty is set to the 5% of the voltage value for each time window for the TEMPEST™ and SkyTEM data. The uncertainty value for both datasets has also been manually refined for localized instances where the data showed anomalous decays.

The same noise model and starting model have been applied for both the experiment about the SkyTEM – TEMPEST™ comparison and for the TEMPEST™ regional modelling. This has been defined after dataset inspection and is supported by the analogous geological context and absence of human-related noise sources of the area.

2.3.2: First experiment: SkyTEM and TEMPEST™ modelling comparison

For the first experiment two lines of TEMPEST™ HM (references in Ley-Cooper A.Y., 2017a and 2017*b*) data from a survey acquired in the Musgrave Province are used. The data have been acquired in 2016 for the CSIRO organization and are coincident with a SkyTEM312Fast survey (Munday et al., 2019). A comparison of these two systems is provided with *table 1.1* in the first chapter of this thesis. The study area with the two surveys is shown in *figure 2.11*.

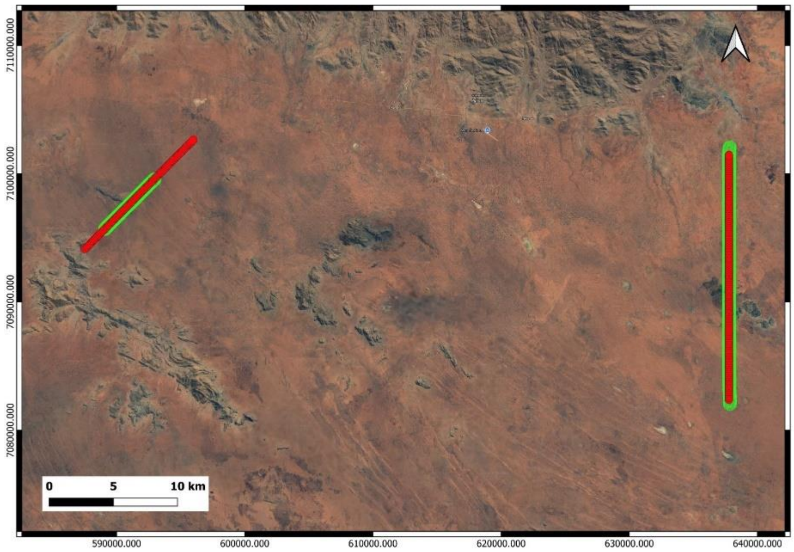

Figure 2.11. Overlapping TEMPEST™ (in red) and SkyTEM (in green) lines in the Musgrave region used for the modelling comparison.

In the dataset, to testify the presence of a chargeable ground, strong negative voltages have been recorded in the eastern SkyTEM line (as visible in the data stripe of *figure 2.12a).* As mentioned, the secondary field negative measurements are uniquely related to AIP effects when measured with a concentric-loop system (e.g, Weidelt 1982; Smith and West, 1988). Even though the SkyTEM system is not a perfect concentric-loop system (transmitter and receiver does not share the same centre, as illustrated in *table 1.1*), it can be approximated as concentric-loop. The distance between the centres of transmitter loop and receiver coil is small enough (12.4 m) in comparison with the system's footprint (about 20-30 m in a conductive near surface) to avoid the recording of geometrical negative voltages.

As visible in *figure 12a*, in the SkyTEM data measured strong negative voltages (in red) above the noise level attributable to AIP effects. In the same location, weak negatives have been measured by the TEMPEST™ Z component while strong sign reverse data are recorded in the X component. This can be explained with the faster decay of the X component that allows to see small IP effects earlier. Also, given that the X component is normally positive when far from geometrical effects, the IP effects appear more obvious as negative measurements, as seen in the data stripe (i.e. the EM data channels in profile). The results of the data modelling are shown in *figure 2.12a* and *figure 2.12b* for the easternmost line. In the *figure 2.12a*, the acquired data for the two systems is shown, in black, with its relative forward response retrieved after the last iteration of inversion (in yellow). Regarding the data fit, the data misfit is computed as in *equation 2.5*.

$$\chi = \sqrt{\frac{1}{n}\sum_{j=1}^{n}\left(\frac{d_{obs_j} - d_{fwr_j}}{\sigma_j}\right)^2} \tag{2.5}$$

Where d_{obs} indicates the measured data, d_{fwr} the forward response and σ the uncertainty related to each *j-th* time window of the recorded data; n indicates the number of time gates. The uncertainty on the data is set as indicated in *section 2.3.1*.

As general comment, a good data fit (generally below 2) has been retrieved after all the inversions; an example of data-fit for a group of SkyTEM data showing negative gates responses with double sign reversal is also shown in *figure 2.13*.

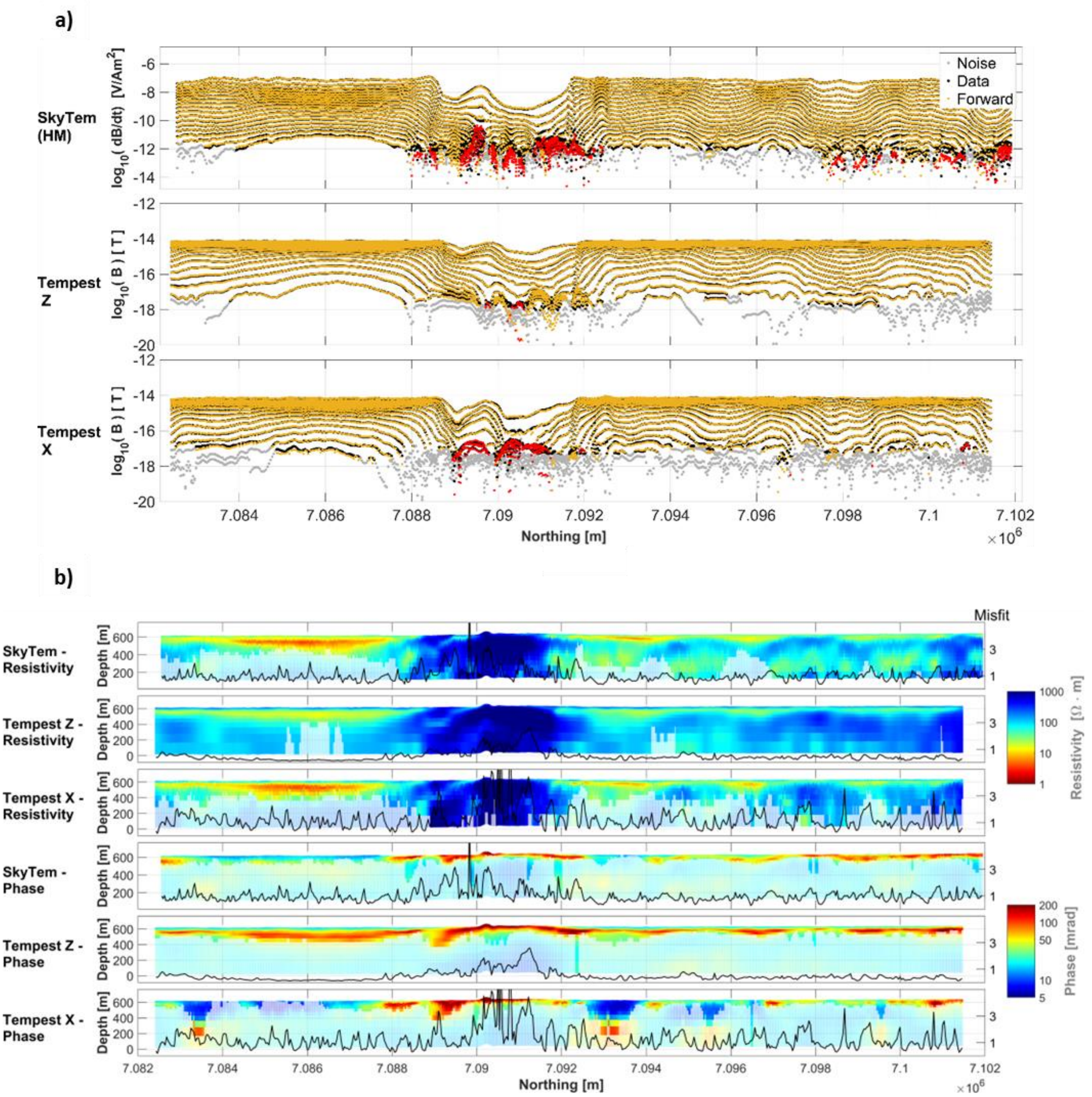

Figure 2.12. At top, (a), acquired data (black) and relative last iteration forward response (in yellow/gold) of inversion for both SkyTEM and TEMPEST™ systems (both X and Z component). For the SkyTEM only the High Moment is shown, given the larger presence of negative recordings, but the inversion has been performed using both High Moment and Low Moment. In red the negative recordings are displayed for both systems. In (b), the retrieved resistivity (plot 1, 2 and 3 from the top) and chargeability (plot 4, 5 and 6) models are displayed. The continuous black line shows the inversion misfit computed for each sounding and its value is shown in the right axis.

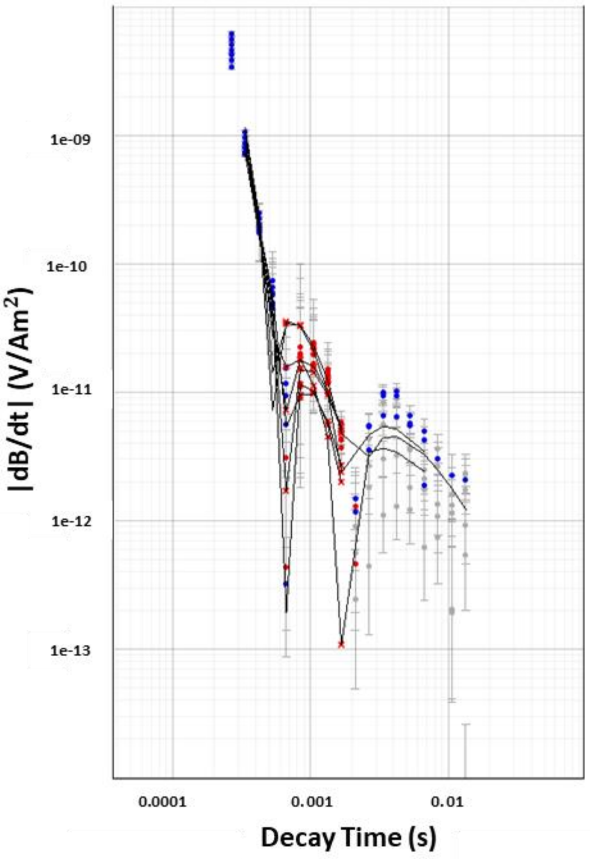

Figure 2.13. Example of data fit for a group of SkyTEM HM transients with a double change of sign (positive-negative-positive). The group of data are token at 7.092·10⁶ Northing. The data is coloured (blue for positive voltages, red for negatives, grey for noise) while the forward response is in black.

In *figure 2.12b*, the model comparison is shown. The three resistivity models (SkyTEM HM and LM jointly modelled, TEMPEST™ Z and TEMPEST™ X) are compared on the first three sections of the figure while the respective chargeability models are shown below. In these sections, the shading represents the computed depth of investigation (DOI) while the continuous black line in the bottom of each section represents the obtained data fit and its scale is on the right axis of each section.

As visible from the cross sections, a 100 m conductive cover overlies a more resistive bedrock hosting more conductive bodies for all the resistivity models. The chargeable domain, uncoupled with the conductive domain in the near surface, is stronger where the EM signal is weaker and where the negative voltages have been measured in both the SkyTEM HM (with an example with a fitted double change of sign in *figure 2.13*) and in the TEMPEST™ X component. In the same location, a much smaller sign change is recorded in the TEMPEST™ Z component but a chargeable domain, spatially coherent with the SkyTEM one, has been retrieved. For this line, the SkyTEM and TEMPEST™ chargeability models correspond very well in the resistive area of the model, between Easting $7.088 \cdot 10^{-6}$ and $7.092 \cdot 10^{-6}$ m. In the more conductive zones, SkyTEM and TEMPEST™ Z chargeability models show similar features in the near surface, where however the TEMPEST™ Z model exhibits more continuous and intense layering, often above the DOI. Conversely, the TEMPEST™ X chargeability model shows strong similarities with SkyTEM at greater depths (e.g. between Easting $7.092 \cdot 10^{-6}$ and $7.094 \cdot 10^{-6}$ m), again with anomalies more often above the DOI. It has to be highlighted that the DOI computation in this study follows Fiandaca et al. (2015), where also the correlation between the Cole and Cole parameters contributes to the DOI calculation. Following this approach, anomalies that have a considerable effect on the data can result under the DOI when they are correlated with anomalies at the same depth of other parameters. In this sense, the TEMPESTTM X component gives a more data driven anomaly which, in this specific case, results above the DOI.

Regarding the negative data content, a coherent behaviour with what seen in the synthetic study is noticeable. Where the ground is more resistive, the pure EM currents are weaker, and the IP effects are stronger. This is reflected both in the SkyTEM data and in the TEMPEST™ data, more in the X component than in the Z. Despite the differences in the negative recordings content, a spatially coherent chargeable near-surface domain has been retrieved for both systems also where negatives are absent. This behaviour is consistent with the known distribution of regolith materials in the area as discussed by Munday et al., (2020a, 2020b and 2023). The chargeability – regolith coupling has been confirmed by drilling and has been attributed to the distribution of magnetite and maghemite in the landscape following weathering and transport. Anand and Pain (2002) have noted that resistant magnetite and secondary maghemite, concentrated by landscape processes within the regolith, are common across Australia. When maghemite is developed, it can display a variable remanence, susceptibility, chargeability and superparamagnetic behaviour (Clark and Emerson, 1991; Clark, 1997; Bella and Emerson 2021). In regolith-dominated terrains, such as found in the study area, fine grained magnetic materials occur throughout the regolith and are often found concentrated in lenses or layers within transported materials (Macnae et al. 2020).

This chargeability distribution is also visible for the other inverted line (*figure 2.14*). In contrast with the previous line (*figure 2.12*), any negative data have been recorded for both the SkyTEM and TEMPEST™. However, as visible in *figure 2.14b*, a chargeable domain coupled with the conductive cover has been modelled in all of the inversions. Even between this TEMPEST™ and SkyTEM comparison, for both resistivity and chargeability, a good comparability is reached. This line overlaps a known AEM late time anomaly, the Valen anomaly (Munday, 2023; Macnae et al., 2012), visible in both the dataspace and model space for both the systems at around 592000 m Easting. The conductor is weaker for the X component of the TEMPEST™ data.

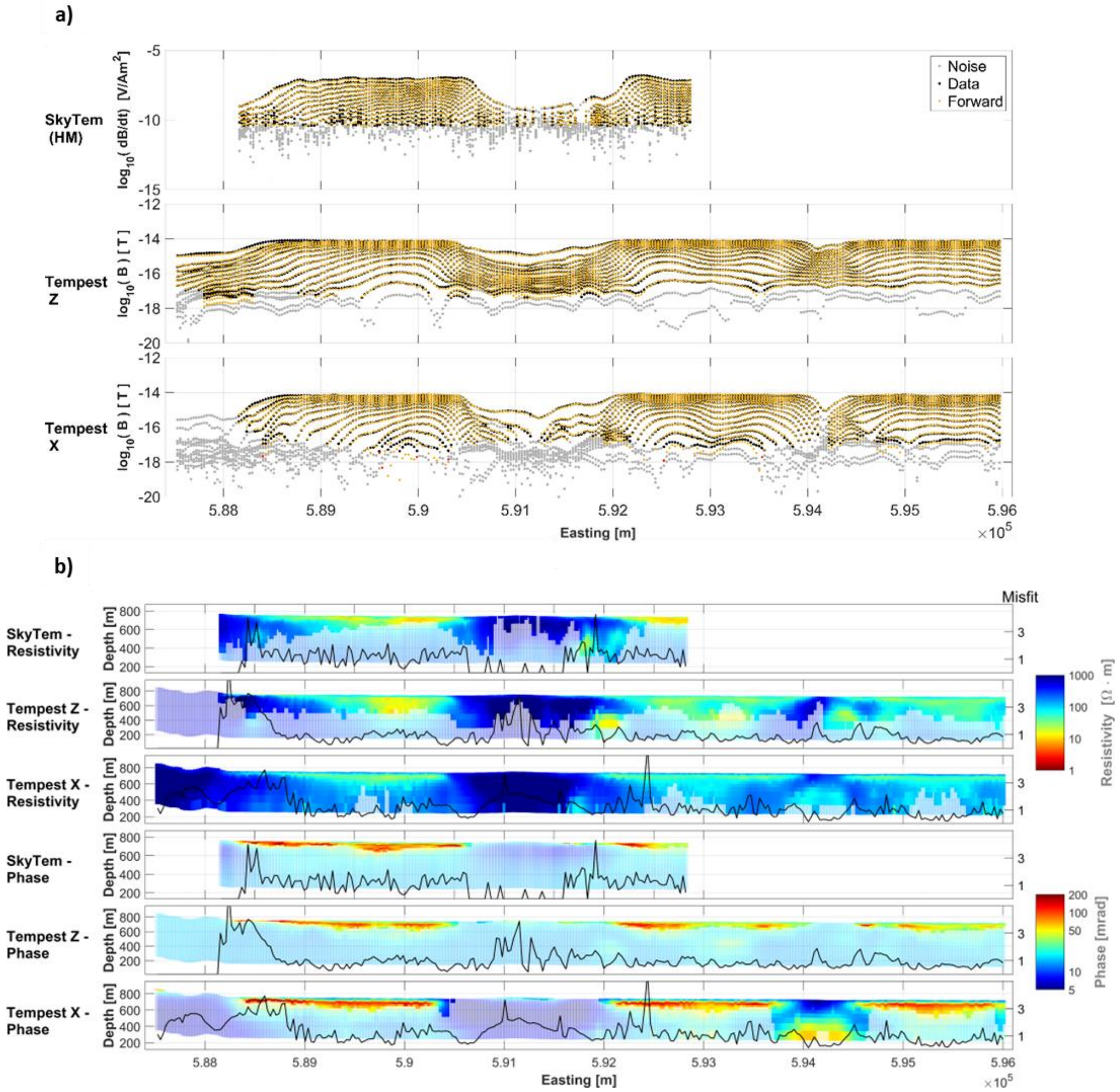

Figure 2.14. In (a), SkyTEM and TEMPEST™ (Z and X) data stripe in black and forward response (in gold) after inversion. In (b) the retrieved models with inversion misfit computed for each sounding is shown as black line.

In summary, a good correlation is noted between the TEMPEST™ and SkyTEM modelled chargeability and resistivity/conductivity responses, supporting the assertion that AIP can be defined from fixed-wing AEM such as the TEMPEST™ system.

2.3.3: Second experiment: regional scale modelling

Following the comparative study between AIP models generated from overlapping SkyTEM and TEMPEST™ datasets, I undertook a more detailed examination of a larger TEMPEST™ data set, acquired as part of the AusAEM project, covering the western Musgrave Province, in South Australia. These data were acquired using the standard TEMPEST™ system (see *table 2.1* for details) and modelled taking into consideration AIP effects. The dataset comprised approximately 20,000-line km of TEMPEST™ data flown with a line spacing of ~2 km (Ley Cooper et al., 2023). Given the large amount of data, these data have been pre-processed using a slope-based filters to remove the noisy gates and then manually refined to remove the remaining outliers and assigning data error bars. The entire dataset has been modelled using the same approach as described in *section 2.3.1*, both considering and not considering AIP. The starting model for the non-AIP inversion is analogous with the one used for the IP inversions (in terms of resistivity and vertical discretization).

For this modelling test, only the Z component of the TEMPEST™ has been used. This choice has been made after an evaluation about the better S/N for this component in the region. Although in conductive areas the noise content between the Z component and X is similar, when the cover is thinner and the resistive outcrop is closer to surface the X component gets noisier, and the data are poorly informative of the subsurface. Moreover, given the horizontal component sensitivity to pitch variations, I assumed safer (in terms of model reliability) to attempt the regional-scale modelling on the Z component only.

The results of the modelling of the regional-scale TEMPEST™ are shown in *figure 2.15.* In this figure, derived models are overlain on the surface geology for the area shown in *figure 2.15a*. A gridded resistivity-depth interval (50 m below the ground surface) modelled from data without considering the AIP is shown in *figure 2.15b*. Results from inverting the data set with IP, for the same depth interval are presented in *figure 2.15c* and 2.15*d*. The chargeability depth interval (for the same depth) slice is shown in *figure 2.15c*, and the IP modelled resistivity in *figure 2.15d*. The more conductive parts of the landscape are associated with mapped areas of cover. The most chargeable areas (*figure 2.15d*) at 50 m below the ground surface appear to be confined to mapped areas of outcrop/subcrop where weathering/erosion is likely to have left a thin regolith. Examining the modelled resistivities with (*figure 2.15b*), and without (*figure 2.15d*) AIP included, they look similar.

In *figure 2.15.e* the percentage difference between the IP and non-IP retrieved resistivities is shown. The difference is computed as in *equation 2.6*:

$$\text{Percentage Difference}_j = \left| \frac{\rho_{noIP\,j} - \rho_{IP\,j}}{\rho_{noIP\,j}} \right| \tag{2.6}$$

Where ρ_{IP} and ρ_{noIP} represent the dispersive and non-dispersive resistivity value of the j-th layer of the model, respectively. The absolute value has been used to allow for log-scales in the images.

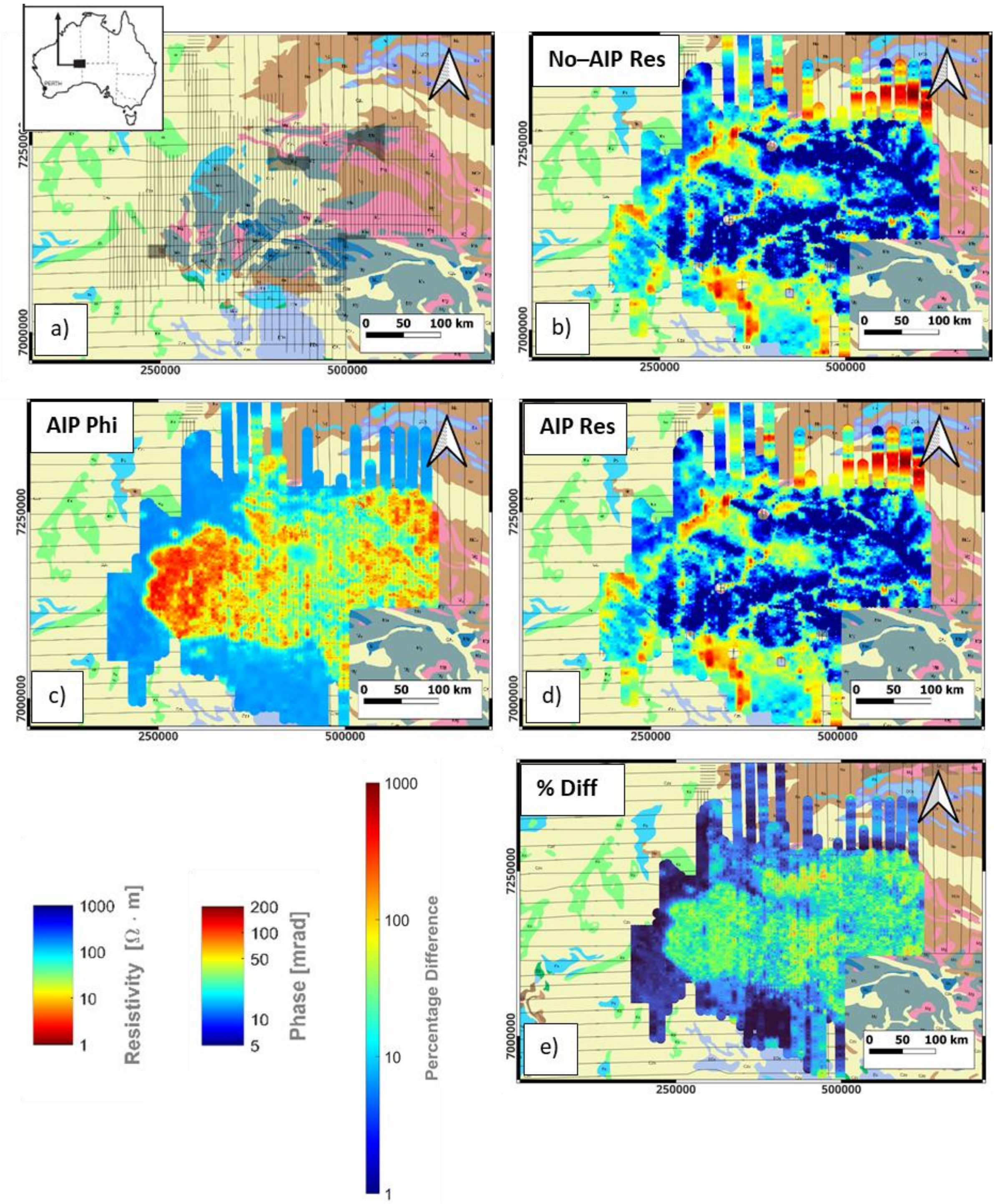

Figure 2.15 AIP and non-AIP models for the Musgrave Province at 50 m depth. The models are retrieved from the TEMPEST™ Z component inversion. In (a) the surface lithology of figure 2.10 is shown; its geological legend is the same as in figure 2.10. In (b), the resistivity model retrieved not considering AIP is mapped. In (c) the chargeability model for the area is shown while in (d) the resistivity retrieved for the AIP inversion. In (e), the percentage difference computed as in equation 2.3 is shown for this depth slice.

As visible from the *figure 2.15e*, nevertheless the AIP modelled resistivities look very similar with the non-AIP results, the percentage difference between the two indicates a significative difference in the retrieved resistivity models. The high resistivity domain retrieved by the inversions correspond with the outcropping geology while the more conductive features are consistent with the cover in the geological map. Consistently with the synthetic study, the chargeability model shows a spatial correlation with the resistive outcrop while generally low chargeability values are mapped over the quaternary domain. As seen in the synthetic study, the conductance of the cover increases and the purely EM induced currents dominate the polarization currents that does not distort the AEM signal into the field of sensitivity of the TEMPEST™ data. More in general, it is visible how the chargeability model is coherent with the geological mapping and uncoupled with ground conductivity. Conductivity and chargeability often give equivalences when EM data are modelled considering IP: this inversion often converges to chargeable and conductive domains for mathematical convenience (given by bigger elements in the Jacobian) but not always respecting the ground geology.

Similar considerations can be generalized for deeper models, as in *figure 2.16*, where a depth slice of resistivity and chargeability at 130 m is shown. In the figure the AIP resistivity modelled is shown in *figure 2.16a*, the non-AIP modelled resistivity is shown in *figure 2.16b* while the chargeability is in *figure 2.16c*. In *figure 2.16d*, the percentage difference between the resistivity models is shown.

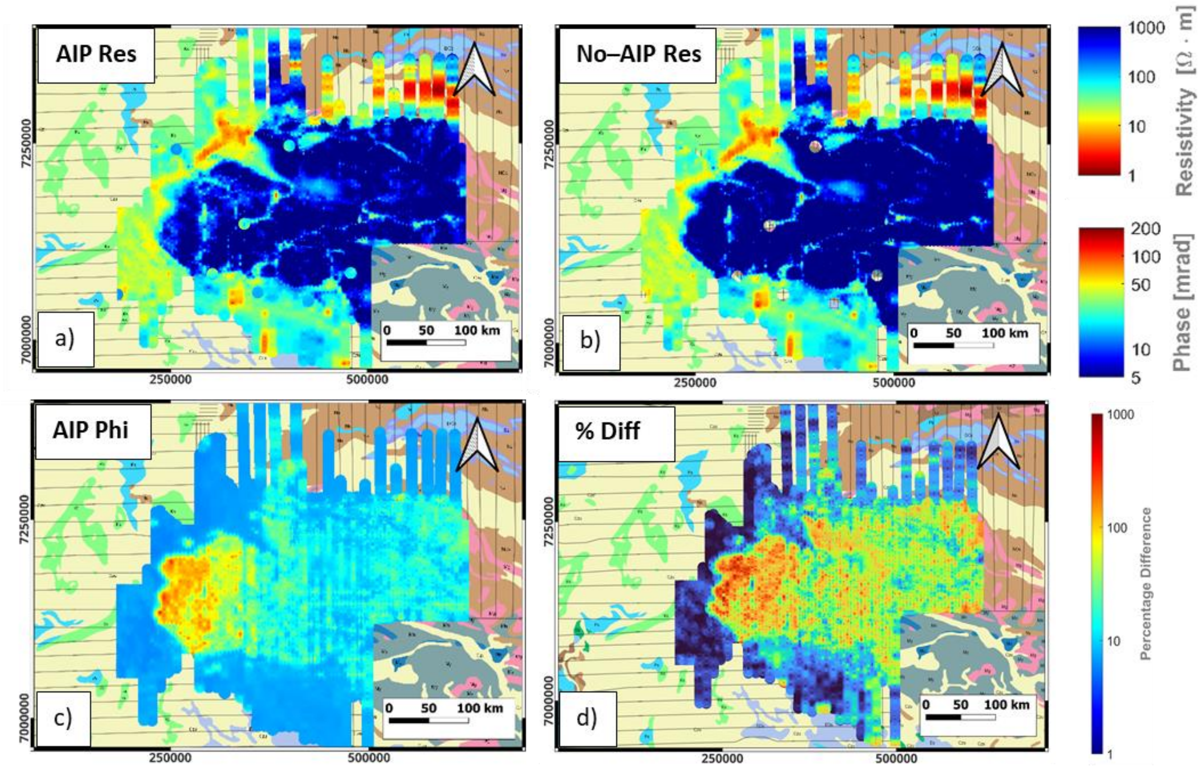

Figure 2.16. Resistivity (a) and chargeability (c) models retrieved for a depth slice at 130 m. The non-AIP inversion result is shown in figure (b). In (d), the percentage difference between the resistivity models is visible.

Increasing the depth, the resistive domain gets stronger while the chargeability reduces. The differences between the resistivity models increases, as also visible in *figure 2.15d*, with the AIP retrieved resistivity that shows more detail at depth in comparison with the non-AIP one. This is consequence of the AIP modelling, where the fast decays given by the AIP distortions are fitted also using the IP parameters instead of only increasing the ground resistivity. It is remarkable the strong percentage difference respects the two resistivity models at this depth, with a difference often higher than the 100%. Increasing the depth, the differences between the resistivity models increase.

To highlight the differences between the AIP retrieved and non-IP resistivity models, in *figure 2.17* the distribution of the resistivities modelled at all the depths are shown. Together with this, the percentage difference of the two, computed as in *equation 2.6*, is shown in *figure 2.17c*.

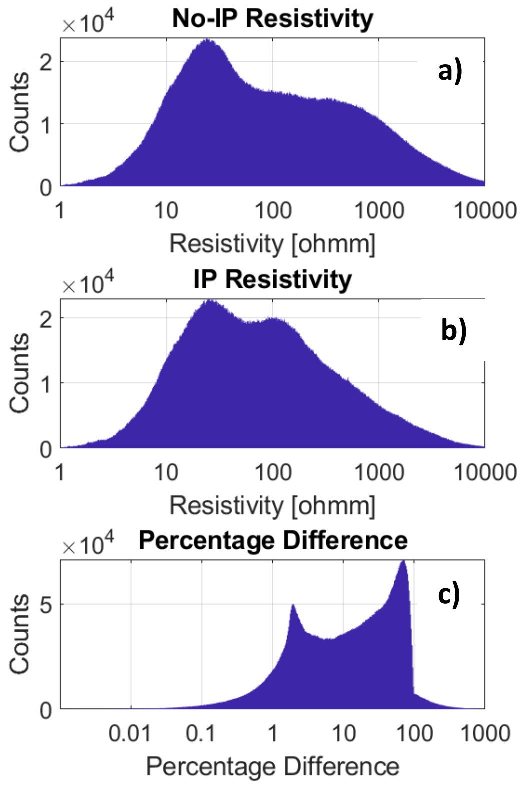

Figure 2.17. Non-AIP retrieved resistivity (a), AIP retrieved resistivity (b) and percentage difference between the two (c).

As visible from *figure 2.17*, the main differences between the IP and non-IP resistivity models are at high resistivities, where the IP modelling fits the fast decays/negatives also with the chargeability instead of only increasing the ground resistivity. The differences between the models span from few percent and reach a peak value at 100% for about $7 \cdot 10^4$ cases.

In *figure 2.18* a comparison of misfits is shown, for non-AIP inversion (*figure 2.18a*) and AIP inversion (*figure 2.18b*). It is here visible how the misfit reduces in correspondence of the chargeable domain of *figures 2.15* and *2.16*, improving the reliability of the retrieved models.

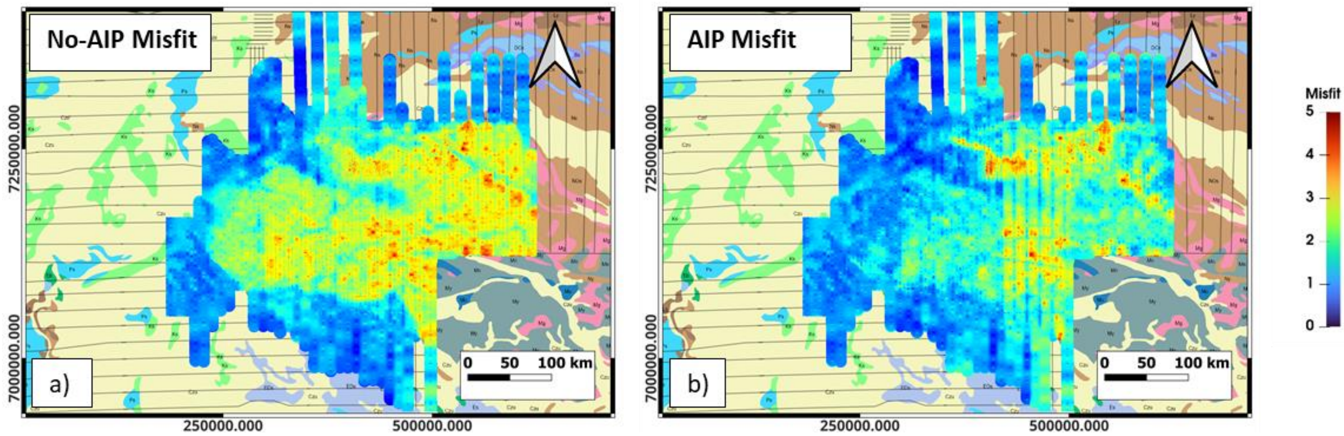

Figure 2.18. Misfit comparisons for the non-AIP (a) and AIP inversion (b). A clear misfit reduction is visible when AIP is considered during modelling.

2.3.4: Third experiment: deposit scale ground truthing

To conclude, a comparison between the Tempest resistivity and chargeability models with geological cross section of a known mineral deposit is presented. The mineralization is the well-known Nebo-Babel deposit (Seat et al., 2007; Godel et al., 2011; Grguric et al., 2018): a Ni-Cu-platinum-element (PGE) sulphide deposit discovered in West Musgrave in the early 2000s. The deposit is hosted in a gabbronorite intrusion and offset by the Jameson Fault that had split the deposit in two main bodies, called Nebo and Babel. The mineralization occurs as massive sulphide breccias and stringers and as disseminated gabbronorite-hosted sulphides (Seat et al., 2007). From Seat et al. (2009), the massive sulphide occurs as lenses of <3 m thickness, in the Babel deposit, in contact with the orthogneiss wall rocks. The mineralogy of the ore deposit is mostly constituted by pyrrhotite, pentlandite, chalcopyrite, and trace pyrite both for the massive portion and for the disseminated. The main host unit of the disseminated sulphides is, mostly, the fine-grained mineralized gabbronorite, the mineralized gabbronorite and the leucogabbronorite. The disseminated portion of the deposit is geometrically defined in the upper hanging-wall contact with the country rocks adjacent to the mineralized gabbronorite hosting the massive sulphides (Seat et al., 2009). In geophysical terms, the massive body gives a conductivity anomaly while the disseminated portion gives a chargeable contrast.

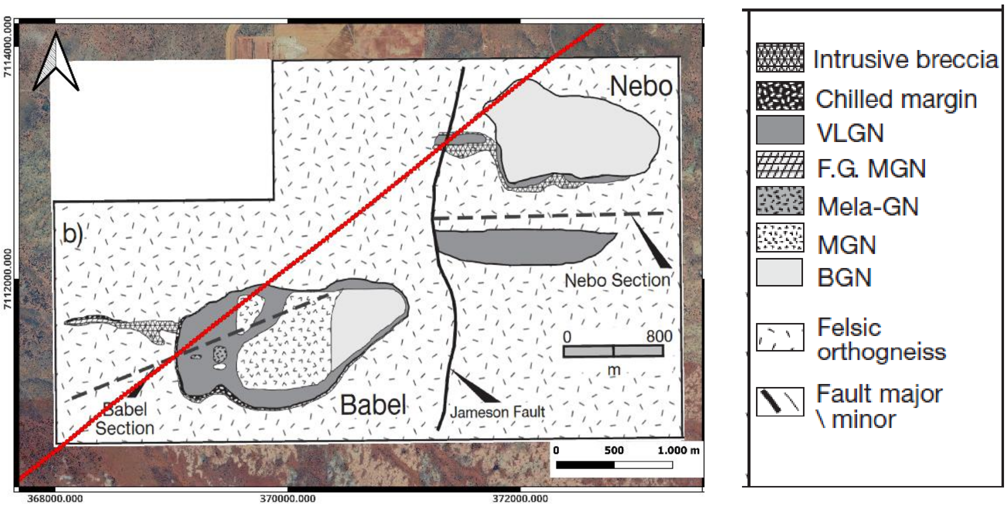

Figure 2.19. AusAEM Tempest portion of line 3608001 (in red) over the surface projection of the Nebo-Babel orebodies from Seat et al., 2009. The geological legend abbreviations indicate: barren gabbronorite (BGN), fine-grained mineralized gabbronorite (F.G. MGN), gabbronorite (GN), mineralized gabbronorite (MGN) and variably textured leuco-gabbronorite (VLGN). The black dashed lines in the map show the location of the geological cross section.

The Nebo-Babel area is overlapped by a portion of one line (L3608001) of the AusAEM TEMPEST™ survey, as shown in red in *figure 2.19*, mostly over the Babel deposit and slightly intersecting the Nebo one in the north-east. The base map of *figure 2.19*, from of Seat et al., (2009), is a projection at surface of the Nebo-Babel deposit. The orebodies are also defined after an extensive drilling campaign. In the map of *figure 2.20*, the geological profiles are shown with a dashed line above each deposit and the one for the Babel body is shown in *figure 2.20*. The scale of the deposit is indicated in *figure 2.20*, both vertical and horizontal.

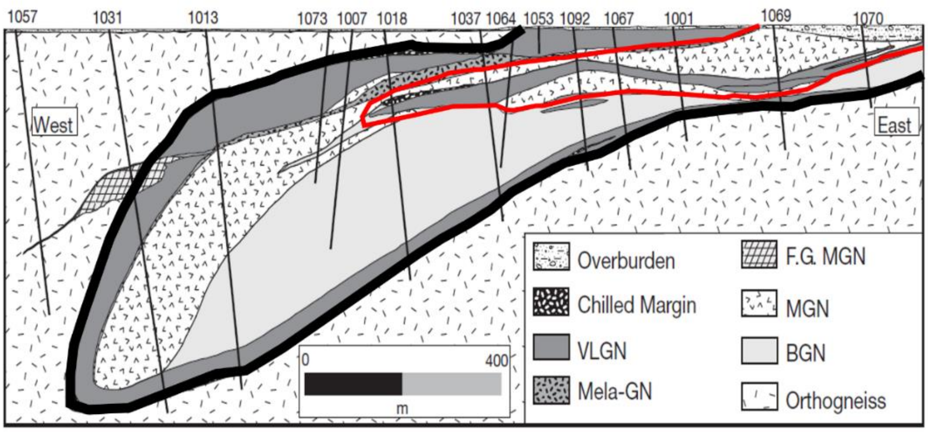

Figure 2.20. Babel geological cross section from Seat et al., (2009) with drillholes location. The geological legend is the same as for figure 2.19. The red outline has been added by the authors to highlight the disseminated mineralization domain while the black outline defines the main conductive orebody. The geological cross-section is indicated in figure 2.19 with a dashed black line in the SE. Equal vertical/horizonal scales are used in the section

The figure, from by Seat et al. (2009), has been modified by the authors of this contribution to highlight the portions of the orebody with different mineralization styles. The red outline encloses the disseminated portion of the deposit hosted in the variably textured leucogabbro and in the mineralized gabbronorite in the upper hanging wall with the country rocks. The black outline describes the deeper massive portion of the deposit that is hosted in the mineralized/fine grained mineralized gabbronorite. In geophysical terms, the deposit is characterized by a chargeable portion with a medium-low conductivity encapsuled within a larger and strongly conductive shape. The TEMPEST™ line models overlapping the Babel deposit (i.e. the ones indicated by the red line in *figure 2.19*), is shown in *figure 2. 21*.

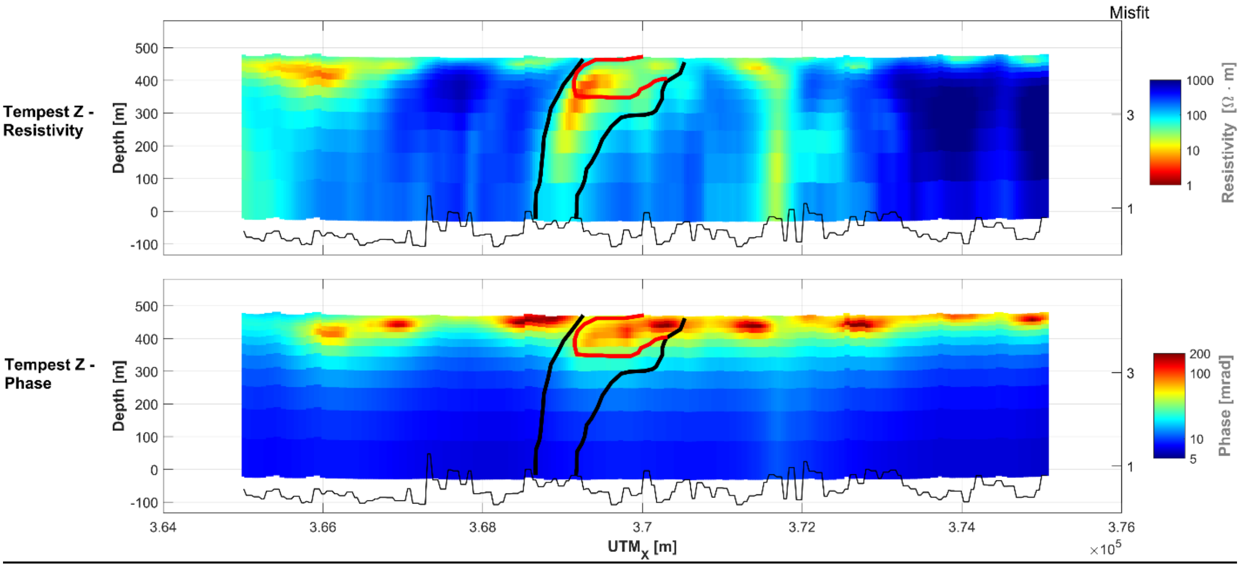

Figure 2.21. Modelling results for the TEMPEST™ line overlapping the Babel deposit. The red outline marks here the chargeable body outline while the black line defines the larger conductive body at depth. The geometrical relationships between chargeable (disseminated) and massive (conductive) portions of the mineralization are defined after AIP modelling from the Tempest data.

The retrieved conductivity and chargeability models consistently describe the Babel orebody with the geological model of *figure 2.20:* in correspondence of the deposit (located at easting $3.7 \cdot 10^5$ m) a chargeable body (in the red outline) is encapsulated in a strongly conductive body (in black). As presented in the literature (Seat et al., 2007; Seat et al., 2009) and supported by the drillholes, the near surface domain is characterized by a lower conductivity and chargeable zone - coherently with the disseminated domain of the orebody - and a larger conductive anomaly in correspondence of the massive mineralization is modelled at depth. The retrieved model mapped the known mineralization and described it not only in terms of conductivity (that still constitutes the discriminant electrical property of this mineral body) but also in terms of chargeability. For this style on mineralisation, the chargeability alone does not define a drilling target but, when associated with a conductive response, provides a more comprehensive description of the anomaly, potentially informing follow-up ground geophysical and drilling investigations.

This result has different levels of importance: it confirmed the TEMPEST™ sensitivity to a chargeable and conductive mineral target, confirmed the reliability of the airborne chargeability model from a geological standpoint, and defined an orebody from a continental scale survey through the use of the airborne Induced Polarization.

2.4: Conclusions

The work reported here demonstrates, through a synthetic forward modelling study, and analysis of field data at a variety of scales. These findings suggest that AIP effects could be present in data from the TEMPEST™ fixed-wing AEM system and that incorporating enhance the accuracy of geological mapping.

The synthetic modelling indicated the possibility of detection of AIP effects for the TEMPEST™ AEM system in a variety of geological scenarios. It demonstrated that AIP effects were likely to affect the TEMPEST™ data predominantly when acquired in thin-cover or outcropping geological domains. In these settings, the IP currents give measurable distortions of the recorded EM data. When the cover conductance is low, the IP currents dominate the EM currents and strong negative voltages can be measured. On the other hand, when the cover gets thicker or its conductivity is particularly high, the IP effects give negligible distortions in the recorded data, and it is possible to model the TEMPEST™ with a non-dispersive resistivity model without retrieving artifacts.

As general observation, the synthetic study has shown how few milliradians of chargeability can result in significative distortions above the noise level also without going negative. This behaviour has been also observed for the synthetic mapping with a high time constant (1 s), for which strong distortions of the recorded data are mapped with a small negative record in the secondary field.

A study of field data with the TEMPEST system in different geological configurations indicates the importance of geology on determining whether IP distortions can be resolved. Geological variations in cover thickness and geology at various scales also influences the presence of TEMPEST™ IP negative recordings. The results from analysis of field data at different scales have shown encouraging possibilities in the modelling of AIP effects from the TEMPEST™ system. TEMPEST™ AIP retrieved resistivity and chargeability models gave a robust comparison with the SkyTEM AIP models for two lines of data in presence and absence of negative measurements in the helicopter-borne data. A good comparability between the TEMPEST™ X component model comparison with the SkyTEM's have also been obtained. This is explained by the quicker decay of the X component data, that favours the measurement AIP.

As well as a geophysical consistency with the helicopter-borne results, also a geological coherence of the chargeability and resistivity models for a larger part of the Musgrave Province in Central Australia has been observed with the mapped lithology. Regional-scale chargeability mapping has been demonstrated from modelling AusAEM TEMPEST™ data with AIP. Here the non-AIP inversion retrieved misfit is higher for large portions of the inverted area when compared with the dispersive resistivity modelling. The scalability of considering AIP in modelling with fixed-wing AEM systems was also demonstrated in a fine-scale investigation of data over the Nebo-Babel mineralization in central Australia. In this example, the airborne derived chargeability response was linked to the disseminated mineralization portion of the Babel orebody in the near surface, while the massive sulphide at depth was modelled by a distinctive conductivity response.

2.5: References

- Auken E., Christiansen A.V., (2004), Layered and laterally constrained 2D inversion of resistivity data, Geophysics, 69: 752-761, https://doi.org/10.1190/1.1759461.
- Brodie, R. C., Ley-Cooper, Y., Lockwood, R., & Murray, D. (2019). AusAEM Year 1: Some aspects of quality control and calibration. ASEG Extended Abstracts, 2019(1), 1–5. https://doi.org/10.1080/22020586.2019.12073132
- Clark, D., and D. Emerson, (1991), Notes on rock magnetization characteristics in applied geophysical studies: Exploration Geophysics, 22, 547–555, https://doi.org/10.1071/EG991547
- Clark, D. A., (1997), Magnetic properties of rocks and minerals: AGSO Journal of Australian Geology and Geophysics, 17, 83–103.
- Dauti, F., Viezzoli, A., Fiandaca, G. (2023), Joint Inversions of AEM modelling AIP effects: Helicopter-borne, Ground IP and Fixed-Wing systems. AEM2023 - 8th International Airborne Electromagnetics Workshop, 3-7 September 2023, Fitzroy Island, QLD, Australia. https://doi.org/10.5281/zenodo.10052623
- Fiandaca, G., Christiansen, A., V., Auken, E., (2015), Depth of Investigation for Multi-parameters Inversions, European Association of Geoscientists and Engineers, Near Surface Geoscience 2015 - 21st European Meeting of Environmental and Engineering Geophysics, Sep 2015, Volume 2015, p.1 – 5 https://doi.org/10.3997/2214-4609.201413797
- Fiandaca, G., Madsen, L. M., and Maurya, P. K. (2018), Re-parameterisations of the Cole–Cole model for improved spectral inversion of induced polarization data. Near Surface Geophysics, 16(4), 385-399.
- Fiandaca, G., Viezzoli, A. (2021), Inversion of Airborne IP data with a multi-mesh approach for parameter definition. Australasian Exploration Geoscience Conference AEGC2021, 13-17 September 2021, Online Conference.
- Fiandaca G., Chen J., Zhang B (2024), EEMverter, a New Modelling Tool for Electric and Electromagnetic Data with Focus on Induced Polarization, European Association of Geoscientists and Engineers, NSG 2024 30th European Meeting of Environmental and Engineering Geophysics, 2024, p.1 – 5, https://doi.org/10.3997/2214-4609.202420166

- Flis, M.F., Newman, G.A., Hohmann, G.W., (1989), Induced-polarization effects in time-domain electromagnetic measurements, Geophysics, 54, 514-523, https://doi.org/10.1190/1.1442678
- Godel, B., Seat, Z., Maier, W., and Barnes, S.-J. (2011), The Nebo-Babel Ni-Cu-PGE sulfide deposit (West Musgrave Block, Australia): Pt. 2. Constraints on parental magma and processes, with implications for mineral exploration, Economic Geology, 557-584, https://doi.org/10.2113/econgeo.106.4.557
- Gubatyenko. V.P. and Tikshayev, V.V., (1979). On the variation of the sign of the electromotive force of induction in the transient electromagnetic field method: Izv. Earth Physics. 15: 217-219.
- Grguric, B.A., Seat, Z., Hronsky, J.M.A. and Miles, G.J., (2018), The Succoth Cu-Ni-Pd deposit: A new taxite-hosted magmatic sulphide system in the West Musgrave Province, Western Australia, Ore Geology Reviews, v.92, pp. 397-415. https:///doi.org/10.1016/j.oregeorev.2017.11.026
- Hine, K., Macnae, J. (2016), Comparing induced polarization responses from airborne inductive and galvanic ground systems: Lewis Ponds, New South Wales. Geophysics, 81(6), B179-B188.
- Howard H.M., Smithies R.H., Kirkland C.L., Kelsey D.E., Aitken A., Wingate M.T.D., Quentin de Gromard R., Spaggiari C.V., Maier W.D., (2015), The burning heart — The Proterozoic geology and geological evolution of the west Musgrave Region, central Australia, Gondwana Research, 27(1), p.64-94, ISSN 1342-937X, https://doi.org/10.1016/j.gr.2014.09.001.
- Kaminski V., Viezzoli A., (2017), Modeling induced polarization effects in helicopter time-domain electromagnetic data: Field case studies, Geophysics, 2017 82:2, B49-B61; https://doi.org/10.1190/geo2016-0103.1
- Lee T., (1981), Transient electromagnetic response of a polarizable ground. Geophysics 46: 1037-1041; https://doi.org/10.1190/1.1441241
- Leggatt, P. B., P. S. Klinkert, and T. B. Hage, (2000), The SPECTREM airborne electromagnetic system — Further developments: Geophysics, 65, p. 1976–1982; https://doi.org/10.1190/1.1444881
- Ley-Cooper A. Yusen and Ross C. Brodie (2013), Inversion of SPECTREM AEM data for conductivity and system geometry SEG Extended Abstracts 2013(1) 1 – 4, doi: 10.1071/aseg2013ab145

- Ley-Cooper, A.Y., (2017a), Musgrave South Australia, Airborne Electromagnetic TEMPEST Survey, 2016-Contractor supplied data. Geoscience Australia, Canberra. https://pid.geoscience.gov.au/dataset/ga/104885
- Ley-Cooper, A. Y., (2017b), SkyTEM helicopter Airborne Electromagnetic Survey Musgrave Region, South Australia 2016- Contractor supplied data and conductivity depth transforms, Geoscience Australia, Canberra. http://dx.doi.org/10.4225/25/599a6f661698f
- Ley-Cooper, A. Y., Brodie, R. C., and Richardson, M., (2019), AusAEM: Australia's airborne electromagnetic continental-scale acquisition program. Exploration Geophysics, 51(1), 193–202. https://doi.org/10.1080/08123985.2019.1694393
- Ley-Cooper, Y., Symington, N. (2023), AusAEM, Western Resources Corridor, Airborne Electromagnetic Survey Blocks. TEMPEST airborne electromagnetic data and GALEI conductivity estimates. Geoscience Australia, Canberra. https://dx.doi.org/10.26186/147688
- Lorentzen, T. H., Kass, M. A., Scheer, J., Tomaškovičová, S., Christiansen, A. V., Maury, P. K., and Ingeman-Nielsen, T. (2024), Exploring the challenges of interpreting near-surface towed TEM data on saline permafrost. Geophysics, 89(3), E113–E128. https://doi.org/10.1190/geo2023-0221.1
- Marchant, D., E. Haber, and D. Oldenburg, 2014, Three-dimensional modeling of IP effects in time-domain electromagnetic data: Geophysics, 79, (6), E303–E314; DOI: 10.1190/geo2014-0060
- Macnae, J., (2016), Quantitative estimation of intrinsic polarization and superparamagnetic parameters from airborne electromagnetic data, Geophysics 81(6), E433-E446: DOI: https://doi.org/10.1190/geo2016-0110.1
- Macnae, J., (2016). Airborne IP detects only fine-grained minerals when compared to conventional IP. ASEG Extended Abstracts, 2016(1), 1–4. https://doi.org/10.1071/ASEG2016ab141
- Macnae J., (2016), Quantifying Airborne Induced Polarization effects in helicopter time domain electromagnetics, Journal of Applied Geophysics, 135, p. 495-502, ISSN 0926-9851 https://doi.org/10.1016/j.jappgeo.2015.10.016
- Macnae, J., Munday, T. and Soerensen, C. (2020), Estimation and geologic interpretation of regolith chargeability and superparamagnetic susceptibility in

airborne electromagnetic data. Geophysics, 85, (5), E153–E162, https://doi.org/10.1190/GEO2019-0395.1

- Martin, T., and Weller, A. (2023). Superposition of induced polarization signals measured on pyrite–sand mixtures. Geophysical Journal International, 234(1), 699-711. https://doi.org/10.1093/gji/ggad091
- Minsley, B.J., Rigby, J.R., James, S.R. et al. (2021) Airborne geophysical surveys of the lower Mississippi Valley demonstrate system-scale mapping of subsurface architecture. Commun Earth Environ 2, 131. https://doi.org/10.1038/s43247-021-00200-z
- Mulè S., Lockwood W., (2013), Evolution of TEMPEST–Bird positioning, ASEG-PESA Conference and Exhibition, 11-14 August 2013 Melbourne Australia.
- Munday, T., (2019), Musgrave Province Airborne Electromagnetic Conductivity Grids. v1. CSIRO. Data Collection. https://doi.org/10.25919/5d0868d48591e
- Munday, T., Macnae, J. and Viezzoli, A. (2020a), Consequences for the Geological Interpretation of AEM data when Inverted for, and Stripped of, Airborne IP and Superparamagnetism Effects. Proceedings of KEGS Symposium 2020 "Success from Innovation" Toronto, Canada, February 29th, 2020, 65-73
- Munday, T., Taylor, A., Raiber, M., Soerensen, C., Peeters, L., Krapf, C., Cui, T., Cahill, K., Flinchum, B., Smolanko, N., Martinez J., Ibrahimi, T., and Gilfedder, M., (2020b), Integrated regional hydrogeophysical conceptualisation of the Musgrave Province, South Australia. https://doi.org/10.13140/RG.2.2.32241.92003.
- Munday, T., McMillan, M., Paterson, R., Soerensen, C., and Dorn, N. (2023), AEM modelling and system options in the search for critical mineral systems in a regolith dominated environment – the Musgrave Province, Central Australia. Proceedings of KEGS Symposium 2023, Toronto, Canada, March 4th, 2023, 55-63
- Pitts B., Dauti F., Devkurran N., Viezzoli A., AIP Effects in Airborne EM fixed wing systems: a SPECTREM theoretical case study, (2021), Australasian Exploration Geoscience Conference AEGC2021, 13-17 September 2021, Virtual Conference.
- Pittard, K., and Bourne, B. (2007). The contribution of magnetite to the induced polarization response of the Centenary orebody. Exploration Geophysics, 38(3), 200–207, https://doi.org/10.1071/EG07020

- Ray A., Bayesian inversion using nested trans-dimensional Gaussian processes, (2021), Geophysical Journal International, 226, (1), 302–326, https://doi.org/10.1093/gji/ggab114
- Seat, Z., Beresford, S.W., Grguric, B.A., (2007), Architecture and emplacement of the Nebo–Babel gabbronorite-hosted magmatic Ni–Cu–PGE sulphide deposit, West Musgrave, Western Australia. Miner Deposita 42, 551–581. https://doi.org/10.1007/s00126-007-0123-9
- Seat Z., Beresford, W. S., Grguric, A. B., Gee, M. A., Grassineau V., N., (2009), Reevaluation of the Role of External Sulfur Addition in the Genesis of Ni-Cu-PGE Deposits: Evidence from the Nebo-Babel Ni-Cu-PGE Deposit, West Musgrave, Western Australia. Economic Geology 104 (4): 521–538., https://doi.org/10.2113/gsecongeo.104.4.521
- Smith, R. S., & West, G. F. (1988). TEM Coincident Loop Negatives and the Loop Effect, Exploration Geophysics, *19*(1–2), 354–357. https://doi.org/10.1071/EG988354
- Smith, R.S., and J. Klein, (1996), A special circumstance of airborne induced polarization measurements, Geophysics, 61(1), 66–73, https://doi.org/10.1190/1.1443957
- Soerensen, C., Love, A., Munday, T., Krapf, C., Costar, A., Inverarity, K., Gilfedder, M., (2018), Uncovering the Musgrave Province in South Australia using airborne EM. ASEG Extended Abstracts, 2018(1), 1–5. https://doi.org/10.1071/ASEG2018abT5_3H
- Spies, B.R., (1980), A field occurrence of sign reversals with the transient EM method, Geophysical Prospecting, 28: 620-632. https://doi.org/10.1111/j.1365-2478.1980.tb01247.x
- Spies, B.R., (1974), Transient Electromagnetic Tests, N.T. and Queensland 1972. Bureau Mining Research, Australian Rec.
- Symington, N., LeyCooper, Y., Smith, M., (2022), West Musgrave AEM conductivity models and data release. Geoscience Australia, Canberra. https://dx.doi.org/10.26186/146278
- Vella L. and Emerson, D., (2012), Electrical Properties of Magnetite and Hematite-Rich Rocks and Ores, ASEG Extended Abstracts, 2012:1, 1-4, https://doi.org/10.1071/ASEG2012ab232

- Viezzoli, A., V. Kaminski, and G. Fiandaca, (2017), Modeling induced polarization effects in helicopter time domain electromagnetic data: Synthetic case studies. Geophysics, 82 (2), E31–E5, https://doi.org/10.1190/geo2016-0103.1
- Viezzoli, A., & Manca, G. (2019), On airborne IP effects in standard AEM systems: tightening model space with data space, Exploration Geophysics, 51(1), 155–169. https://doi.org/10.1080/08123985.2019.1681895
- Viezzoli, A., Dauti, F., and Wijns, C., (2021), Robust scanning of AEM data for IP effects. Exploration Geophysics, 52(5), 563–574. https://doi.org/10.1080/08123985.2020.1856624
- Viezzoli, A., (2023), Lessons learned from a decade of AIP modelling. AEM2023 - 8th International Airborne Electromagnetics Workshop, 3-7 September 2023, Fitzroy Island, QLD, Australia, https://doi.org/10.5281/zenodo.10060517
- Weidelt, P., (1982), Response characteristics of coincident-loop transient electromagnetic systems, Geophysics, 47(9), E1325-1330, https://doi.org/10.1190/1.1441393
- Weller A., Slater L, Nordsiek S., (2013), On the relationship between induced polarization and surface conductivity: Implications for petrophysical interpretation of electrical measurements, Geophysics 78: D315-D325. https://doi.org/10.1190/geo2013-0076.1
- Wilford, J., Searle, R., Mark T., Grundy, M., (2015), Soil and Landscape Grid National Soil Attribute Maps - Depth of Regolith (3" resolution) - Release 2. v7. CSIRO. Data Collection. https://doi.org/10.4225/08/55C9472F05295

Chapter 3: Airborne and Ground DCIP comparison at prospect scale and joint modelling considering IP effects

Chapter 3, summary

In the previous chapter the detectability of IP effects for fixed-wing systems has been demonstrated and modelled from real data. As mentioned, these systems have a wide use for continental and regional mapping and, as shown, can detect ground chargeability responses related to mineralization.

In this chapter, I reduce the scale of investigation to deposit-scale, investigating the comparability between airborne inductive IP and ground DCIP looking for a common field of sensitivity for chargeability mapping. As mentioned in *section 1.2.3.4* the differences between the two methods are many and span from the energisation method to the recording bandwidths and modelling approach. As also seen in the previous chapter, modelling the IP effects from the airborne EM data is complex, with a strongly ill-posed inverse problem and a large model-space that favour equivalent domains among inversion parameters. This complicates the link between airborne chargeability and geological interpretation. In this chapter, I propose and test a multi-mesh inversion to reduce equivalencies in model-space during AIP modelling. Then, I apply this approach to real airborne EM data acquired in Spain, in the Iberian Pyritic Belt, for mineral exploration purposes. This AEM survey overlaps several ground DCIP lines offering the opportunity to compare the models. The DCIP data have been modelled using the same approach of the airborne EM data, following the modelling scheme proposed by Fiandaca et al. (2012), which includes the system transfer function, gate integration, transmitter waveform and the full decay instead of integral chargeability. To conclude, to merge the different sensitivities and improve the understanding of the airborne IP sensitivity field, a joint inversion between ground DCIP and airborne EM considering IP effects is provided.

In addition to this chapter, in the thesis appendix I provide a comparison between the AIP and non-AIP modelled EM data used for this work.

3.1: Introduction

It is recognized and theoretically demonstrated how airborne inductive measurements are sensitive to the frequency dependence of the ground resistivity (Dias 1968, Flis et al., 1989; Smith et al., 1996; Kratzer and Macnae 2012; Marchant et al., 2013) when acquired over dispersive halfspaces. Passing a time varying current through this medium leads to the accumulations of charges at the boundaries between its components and phases; in other words, it produces a measurable Induced Polarization (IP) effect. The electrochemical and electrophysical processes that arise from IP result in the generation of natural elements that act as capacitors or accumulators in the ground, developing a polarization current when the charge relaxation follows the material discharging cycle (Kamenetsky et al., 2014). Under these conditions, the total secondary magnetic field recorded by the EM system is given by the sum of the pure EM currents and of the polarization currents produced by the capacitor. The IP effect typically manifests in EM data as negative voltage responses or with steep decays. It is important to highlight that the absence of negative measurements does not guarantee the absence of ground conductivity frequency dependence: if the ground is very conductive the IP currents distort the EM signal without giving negatives, complicating its recognition in the dataspace.

Although the IP recognition is complex, it is crucial to use a dispersive resistivity during the modelling when necessary. If the ground conductivity is frequency dependent, an appropriate physics of the forward problem must be used to avoid artifacts in the model space during the inversion. Classically, the Cole and Cole model re-written by Pelton et al. (1978) is used to describe dissipative grounds allowing to map the ground chargeability and the spectral parameters as well as its resistivity. The use of four parameters to model the EM data strongly complicates the inverse problem, making it very ill-posed with an expanded model-space suited to equivalencies. This complexity, although the EM-IP chargeability sensitivity to geological targets has been shown by synthetic studies (Viezzoli and Manca, 2019), have often discouraged its use as real exploration tool. Also, a weak comparability with the geology and with the well known and standardly used ground DCIP of the retrieved models has braked the use of the AIP as reliable tool for large-scale chargeability mapping.

Among the differences between the ground DCIP and the Airborne IP, the most obvious ones are in the footprint, in the source field and in the spectral content of the two. Regarding the latter, the AEM frequency bandwidth is usually centered a couple of orders of magnitudes higher than that of ground IP data, with a base frequency of 25, 12.5 or 6.25 Hz. The difference in the base frequencies have been often imputed as the main reason of incompatibility between the methodologies (Macnae et al., 2016): the airborne inductive methods have, at their best, a base frequency of 6.25 Hz that does not guarantee, in terms of spectral content, to measure slow polarization. The mineral deposits detected with galvanic IP show a wide distribution of time constants values but, generally, the maximum peak of phase between the real and imaginary part of the complex conductivity is reached at very high time constants, higher than 1 s (e,g, Macnae et al., 2016). This can imply that the ground and the airborne IP may excite different chargeable domains at different frequencies with a partial overlap at low frequencies, for which the ground DCIP is richer. Nevertheless, an extensive study on the petrophysics of inductive IP and its relationships with the materials is not present in literature and only comparisons with ground DCIP can be done to verify the AIP sensitivity to geological targets, as first proposed by Macnae et al., (2016). In this optic, a major issue not always recognized is the difference in the modelling approaches to attempt the comparisons between the measurements. The ground IP data is usually modelled dropping the spectral information, e.g., turning a full secondary voltage decay into a single value of integral chargeability as in Oldenburg and Li (1994), and mapping the ground intrinsic chargeability only. Also, in the cases when the spectral content is recovered, it is not a common practice to include the system transfer function, the time gates and the transmitter waveform of the ground DCIP system in the modelling; it has been shown by Fiandaca et al. (2012) how these aspects can compromise the correct modelling of the ground DCIP data. In this sense, given the number of variables, grade of freedom in the systems description, inversion parametrizations and modeling assumptions, it is fundamental to use the same modelling approach between DCIP and AIP to obtain a reliable comparison between the retrieved parameters of ground and airborne IP. This, together with a joint modelling of the two methods, can contribute to a quantitative understanding of AIP sensitivity to the geological targets. The joint modelling of inductive and galvanic Induced Polarization effects is complicated, as well as by the non-uniqueness of the inversion procedure, also by the anisotropy of the electrical properties of the ground as mentioned, among others, by Meju et al. (2005) and by Christiensen et al. (2022). To overcome this additional challenge, it is necessary to use an inversion scheme that allows to handle different datasets in a unique flexible modelling framework.

In this introduction, some aspects and limits of AIP modelling and use has been briefly described. It has been highlighted how a non-dispersive parametrization complicates the inverse problem and how it is necessary to define a consistent modelling approach between inductive and galvanic IP to improve the quality of comparison and integration. With this work I aim to give a contribute to these aspects, to improve the understanding and applicability of AIP for mineral exploration. I first start from the application of a novel modelling approach that aims to reduce equivalencies during the modelling. Then, to prove the modelling, a comparison with the ground DCIP lines modelled with a consistent approach will be shown. The AEM data are acquired in Spain, for VMS and polymetallic exploration and overlap 17 ground DCIP lines. Finally, to quantitatively evaluate the AIP sensitivity to ground chargeable bodies, its integration with the ground DCIP and how the methods contribute to ground electrical properties imaging, a joint inversion between the two entire datasets will follow.

3.2: Geological context, exploration approach and study area

Located between southern Spain and Portugal, in Europe, the Iberian Pyrite Belt (IPB) is one of the oldest and still active mining districts in the world (Inverno et al., 2015). The interest in the IPB (*figure 3.1*), which forms part of the Hercynian orogenic belt, is that its Late Devonian to Middle Carboniferous rocks host a huge quantity of volcanic-hosted massive sulphide (VMS) mineralization (1700 Mt of sulphides, totalling 14.6 Mt Cu, 13.0 Mt Pb, 34.9 Mt Zn, 46100 t Ag and 880 t Au), that make the region as the one with the highest concentration of sulphides worldwide (Barriga *et al.*, 1997; Leistel *et al.*, 1998; Carvalho *et al.*, 1999; Saez *et al.*, 1999; Tornos, 2006; Almodovar *et al.*, 2019).

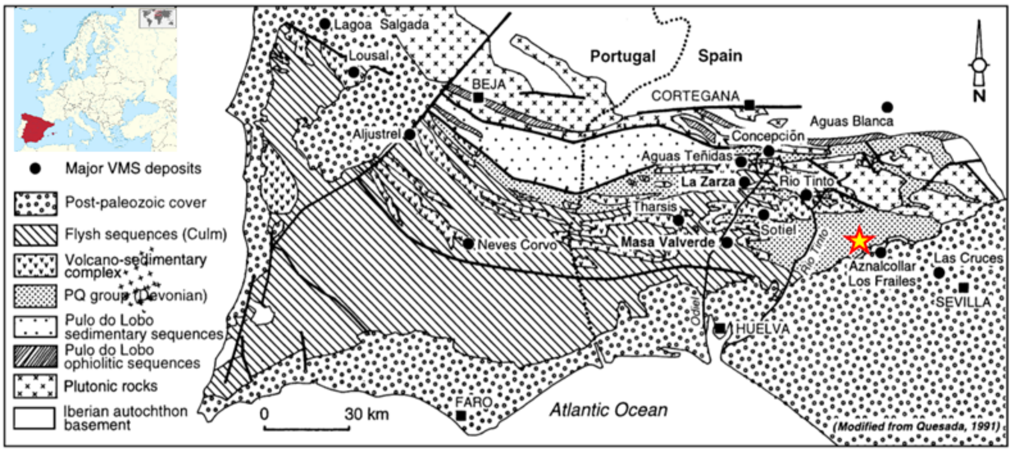

Figure 3.1. Iberian Pyrite Belt simplified geological map and location of the main mineral deposits. The study area is shown with the yellow star. Modified from Quesada et al., 1991.

The mineralization and its environment display several different signatures that are related to the mineralogy and zoning of the sulphide orebodies, calling for the integrated use of complementary geophysical methods. Several non-outcropping massive sulphide deposits associated to the IPB Volcano-Sedimentary Complex (VSC) (Pereira *et al.*, 2008; Oliveira *et al.*, 2013, 2019) were discovered in SW Iberia using interactive interpretation of geological and geophysical models, such as *Feitais* and *Gavião* (Andrade and Schermerhorn, 1971); *Neves-Corvo* (Albouy *et al.*, 1981; Carvalho, 1982; Leca *et al.*, 1983), *Lagoa Salgada* (Oliveira *et al.*, 1993, 1998a, b; Matos *et al.*, 2000) and *Sesmarias* (Kuhn, 2017; Coder and Kuhn, 2020) in Portugal, *Valverde* (Castroviejo *et al.*, 1996; Gable *et al.*, 1998), Las Cruces (Doyle, 1996), *La Magdalena* (Sáenz de Sicilia, 2013) and *Elvira* (discovered by Matsa in 2018, Gisbert et al., 2019) in Spain. Over the last decade, disseminated stockwork mineralization in veins become an important mining resource considering the decrease of the copper cut off and stockwork minor content in penalty elements compared to massive ore (Matos et al., 2020). Commonly, IPB stockwork networks are hosted by VSC felsic volcanic rocks and black shales (Leistel, 1998; Tornos, 2006; Relvas, 2006; Matos *et al.*, 2011) that exist close to the massive ore. In geophysical terms, the gravity has of course played a central role accompanied by EM methodologies (both airborne and ground) to localize dense and conductive massive bodies at depth. Then, the Induced Polarization have been largely used to map the disseminate mineralization in the stockwork around the VMS. In this context, an accurate large-scale mapping of the ground chargeability, as well as its resistivity, through airborne measurements could significantly contribute to the mineral system understanding and to the orebody detection.

The study area, located in this geological framework and shown in *figure 3.2*, is part of a tenement under current exploration by the Pan Global Resources mining company.

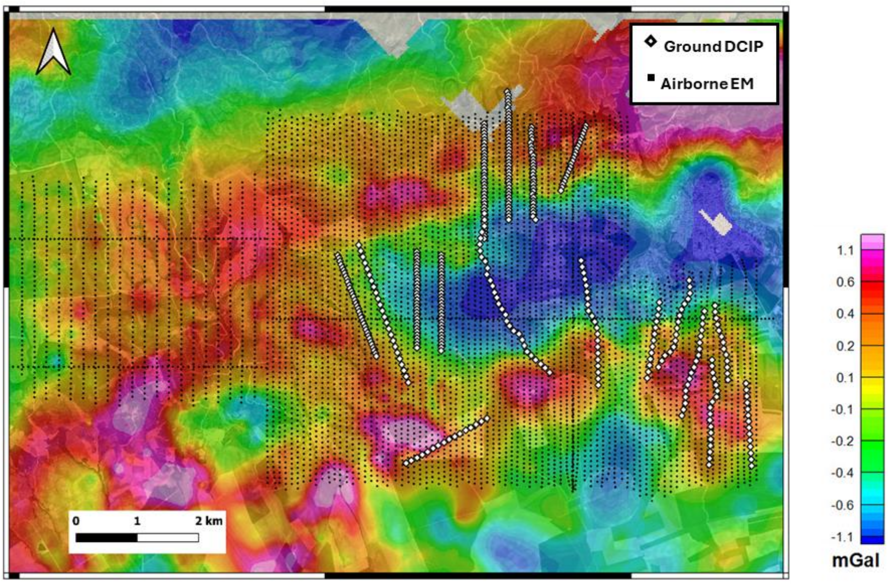

Figure 3.2. Surveys area over the gravimetric residual bouguer anomaly in background. The Airborne EM flight lines are shown in black while the DCIP profiles in white.

The tenement is developed around several gravimetric anomalies possibly related to VMS deposits. The most explored and significant target is the "La Romana" deposit: a shallow Volcanic Massive copper Sulphide, firstly located with a gravimetric anomaly and then shown by EM methods and ground DCIP. For this deposit, the geophysical anomalies have been confirmed by drillings showing a significant tenure of copper and strontium. Many geophysical surveys (ground gravity, EM, DHEM, magnetic, ground DCIP) have been carried in the tenement; in between these, an airborne time domain EM survey (in black in *figure 3.2*) has been acquired by the New Resolution Geophysics XCite™ system (Combrinck et al., 2016) in the spring of 2022 and, in the months after, 17 ground DCIP lines (in white in *figure 3.2*) have been acquired in the same area. The DCIP lines constitute an amount of about 34 km of ground data while the AEM are around 1120-line km.

In particular, the XCite™ AEM system has been flown with a base frequency of 25Hz and with a line spacing of 100 m while the ground DCIP has been acquired with a square waveform of 0.125 Hz of base frequency and a 50% of duty cycle and has been designed with a dipole-dipole configuration with 100 m of electrode distance. For the ground measurement, a VIP 5000 transmitter and an Elrec Terra receiver, both from Iris Instruments, have been used.

3.3: Modelling approach

As general approach, the Airborne EM and the ground DCIP data have been modelled, independently and jointly, using a consistent approach within the EEMverter inversion framework (Fiandaca et al., 2024) also presented in *section 1.2.3.5*. The consistency in the modelling has been maintained at all the levels: in the forward computation, in the inverse problem parametrization and in the model space discretization. In this section the details will be provided. For both the methodologies, the forward computation is carried in the frequency domain and modelling the full voltage decay of both the EM and the IP response for the DCIP measurements. The ground response is then convolved with the transmitter waveform including the gate integration, the instrumental drift and the receiver transfer function. The difference in the forward computation lies in the dimensionality of the forward that is in 1D for the inductive method and in 2D for the galvanic. The ground DCIP forward response is computed following Fiandaca et al. (2012) while the inductive one following as Effersø et al. (1999). For this work, the model-space has been parametrized with a Maximum Phase Angle (MPA) model (Fiandaca et al., 2018) instead of the classical Cole and Cole model re-arranged by Pelton et al. (1978). The MPA Cole-Cole model is a re-parametrized form of the classic Cole-Cole, where instead of m_0 and τ_ρ, the maximum phase φ_{max} and the phase relaxation time τ_φ is modelled.

The phase of the complex conductivity can be defined in terms of both equations 3.1 and 3.2 as:

$$\varphi(\omega) = tan^{-1}\left(\frac{\sigma''(\omega)}{\sigma'(\omega)}\right) = -tan^{-1}\left(\frac{\rho''(\omega)}{\rho'(\omega)}\right) \tag{3.1}$$

The phase reaches its maximum φ_{max} at an angular frequency $\omega_\varphi \equiv 1/\tau_\varphi$ as:

$$\varphi_{\max} = tan^{-1}\left(\frac{\sigma''(1/\tau_\varphi)}{\sigma'(1/\tau_\varphi)}\right) = tan^{-1}\left(\frac{\rho''(1/\tau_\varphi))}{\rho'(1/\tau_\varphi)}\right) \tag{3.2}$$

This parametrisation allows to minimize the correlations between the ColeandCole m_0 and c using the poorly correlated φ_{max} and c and, thus, to improve the resolution retrieved from inversion IP data of the classical Cole-Cole model. The reduced correlation the parameters is shown by Fiandaca et al. (2018) for the DCIP modelling. The model space of the MPA Cole-Cole model is described as:

$$m_{MPA\ Cole-Cole} = \{\rho_0, \varphi_{\max}, \tau_\varphi, c\}$$

For the airborne EM data that have a reduced spectral content, the four parameters have been modelled split into two different model meshes: one for the resistivity and phase and one for the spectral parameters (τ_φ and c). In *figure 3.3*, the meshes are shown.

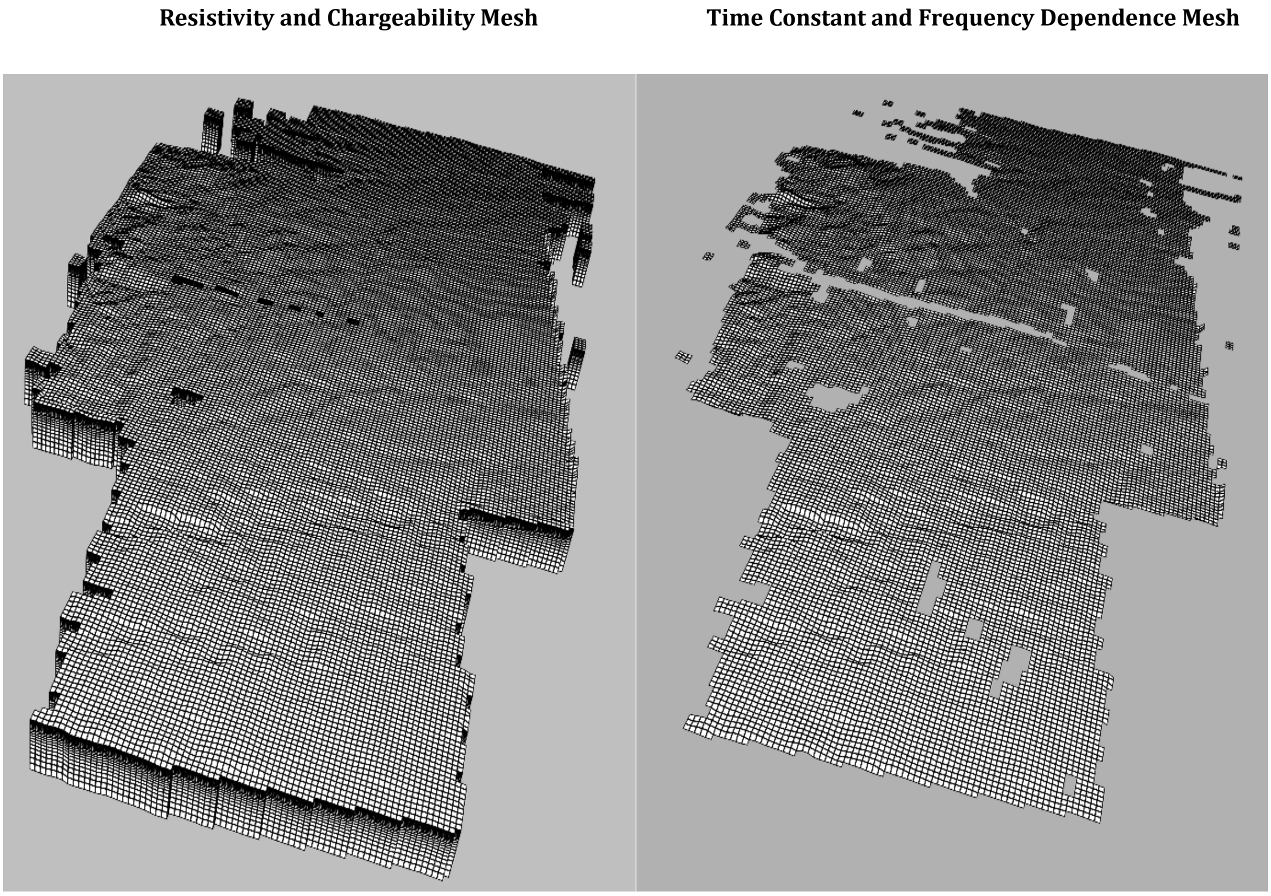

Figure 3.3. Meshes for AIP inversion. On the left the 3D mesh for the resistivity and chargeability mapping; on the right, the 2D mesh for the spectral parameters mapping.

The spectral model-mesh it is defined with one single layer with the parameters values laterally free to vary. This mesh dimensionality reduction is done to decrease the equivalencies at depth between the spectral parameters and the chargeability. Differently, the DCIP lines have not been modelled splitting the model mesh into spectral and non-spectral parameter given its larger spectral content respect with AEM data.

For the airborne EM inversion, the model-mesh is laterally (along X and Y) regularly spaced (40 m) while each layer (Z) has a log-increasing thickness from surface to 500 m depth using 23 layers. The inversion starting model is homogeneous (ρ = 100 Ω·m; φ = 25 mrad; $\tau_\varphi = 10^{-3}$ s; c = 0.5).

For the ground DCIP independent inversions the model meshes are described similarly to the AEM one but in 2D, along the acquisition line. The starting model, vertical and lateral discretization are defined as for the AEM independent inversion.

As mentioned in the introduction (e.g. in *section 1.2.3.4*), using a consistent modelling approach between ground and airborne data, I aim to improve the comparability of the results. The joint inversion between the two datasets is performed as described in the methodological part of 1.2.3.5: each dataset is assigned to a different forward mesh, which allows to compute the data-specific forward response as well as the Jacobian of the whole inversion through equation 1.57; to the same model that can be split in different model meshes. The weights of the datasets are regulated by the data covariance matrix.

The data processing and noise assessment has been carried using the EEMstudio QGIS plugin (Sullivan et al., 2024) and following equations 1.60a and 1.60b to assess the data uncertainty. The EEMstudio software allows to display the recorded EM and DCIP chargeability decays (as well as the apparent resistivity) and to manually remove the outliers after a user inspection. Each DCIP profile and AEM sounding has been manually processed removing the noisy time gates; the uniform data uncertainty has been set as 5% of the AEM recorded data, of 2% of ground DC and 10% of ground IP decays. For AEM data, the noise floor is set at $5 \cdot 10^{-15}$ V/Am^2.

3.4: Airborne IP and Ground DCIP comparisons – Independent inversions

The modelling results of the AEM data considering the AIP effects are shown in *figure 3.4* with resistivity and chargeability (phase) slices at different depths. The ground DCIP lines are maintained over the retrieved model to give a spatial reference among the maps.

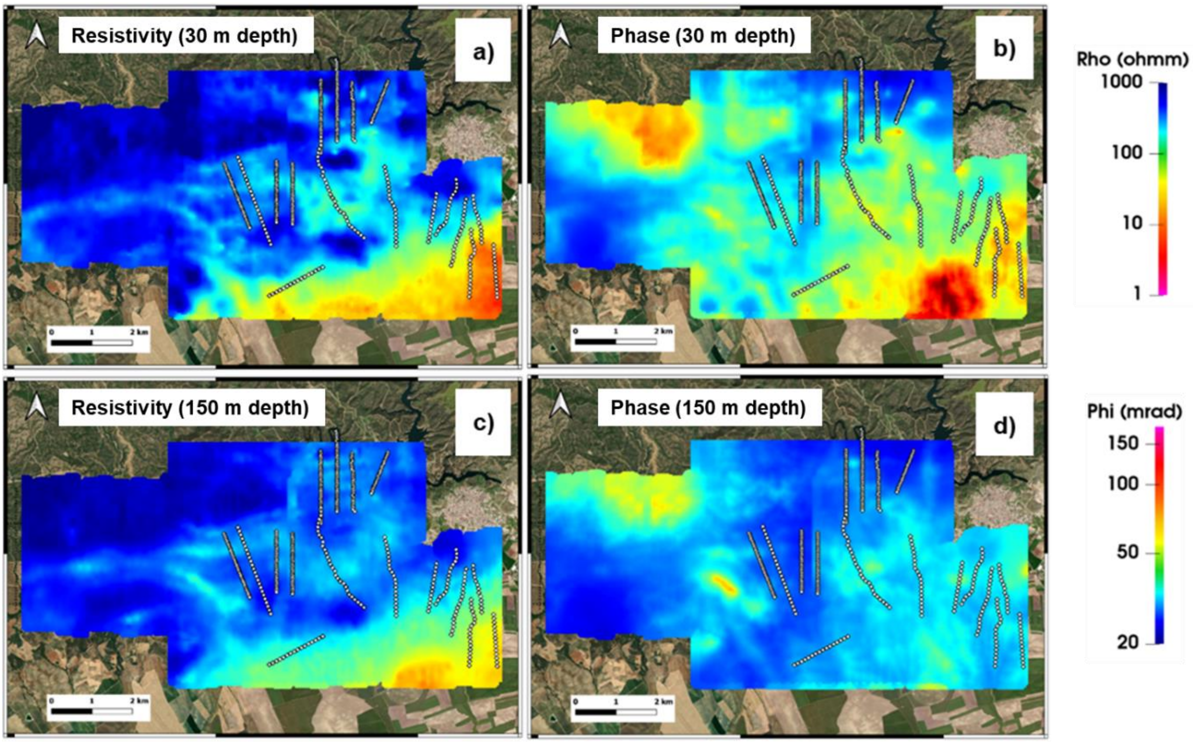

Figure 3.4 Resistivity and chargeability depth slices of the AEM independent inversion. (a) and (b) show the resistivity and chargeability models, respectively, for a depth slice at 30 m. (c) and (d) show the resistivity and chargeability model for a depth slice of 150 m.

As visible in *figure 3.4*, the airborne chargeability model evidence both isolated chargeability contrasts and geological distributed patterns, both in the near surface (*figure 3.4b*, for a depth of 30 m) and at depth (*figure 3.4d*, for a depth of 150m). The same considerations can be extended to the resistivity models (*figure 3.4a* at 30 m and *figure 3.4c* at 150 m), where a more resistive domain in the northern portion of the survey uncover deeper conductive structures also in proximity of the gravimetric anomalies shown in *figure 3.2*. From the slices it is also visible how the very conductive and the chargeable bodies are often uncoupled. This is coherent with the mineralization style of the polymetallic mineralization that, given its weak concentration, it is not particularly conductive but generally gives a moderate-high chargeability. Moreover, the uncoupling of these two parameters adds potentially crucial extra layers of information in the electrical description of the investigated ground, helping in the discrimination between conductive cover, potential targets or host rocks and, more in general, to the mineral system understanding of the flown area.

For these results, it is important to highlight that no negative voltages have been recorded in airborne EM data. The airborne chargeability has been modelled without any clear evidence of IP effects in the dataspace but still retrieving a geologically consistent and coherent model. This chargeability model will be validated by the ground DCIP comparison in the following part of this section.

In *figure 3.5* the airborne data misfit is also shown: widely below 2, it guarantees an accurate fitting of the data with the retrieved model.

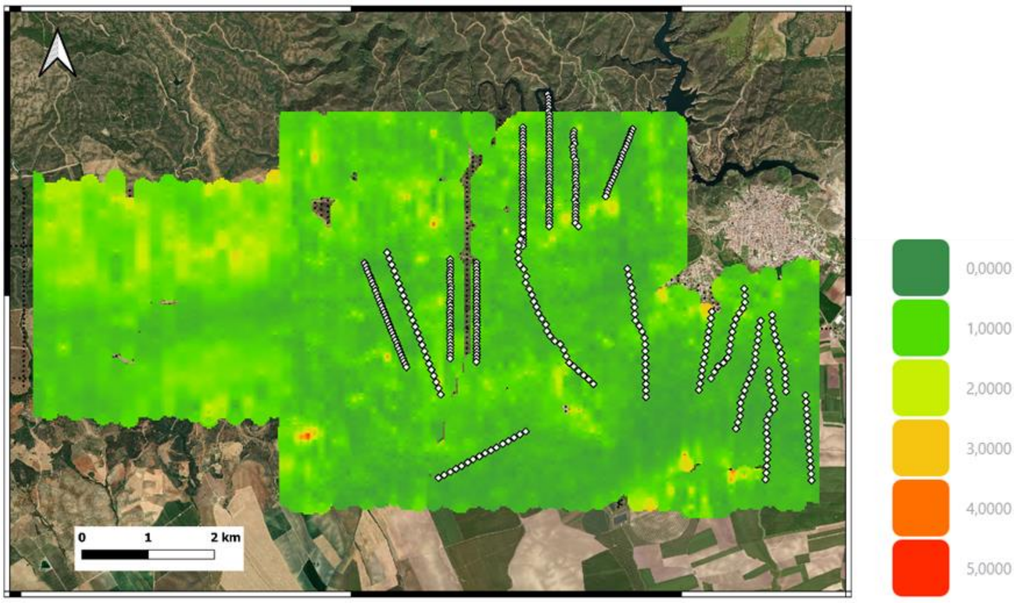

Figure 3.5. AEM data misfit retrieved by the independent inversion considering IP effects.

In *figure 3.6a and 3.6b,* a comparison between the ground DCIP inverted lines and the airborne chargeability models is provided. To compare the results, the airborne chargeability model has been sliced at different depths, as indicated in the caption, to verify the mapping of the chargeable features.

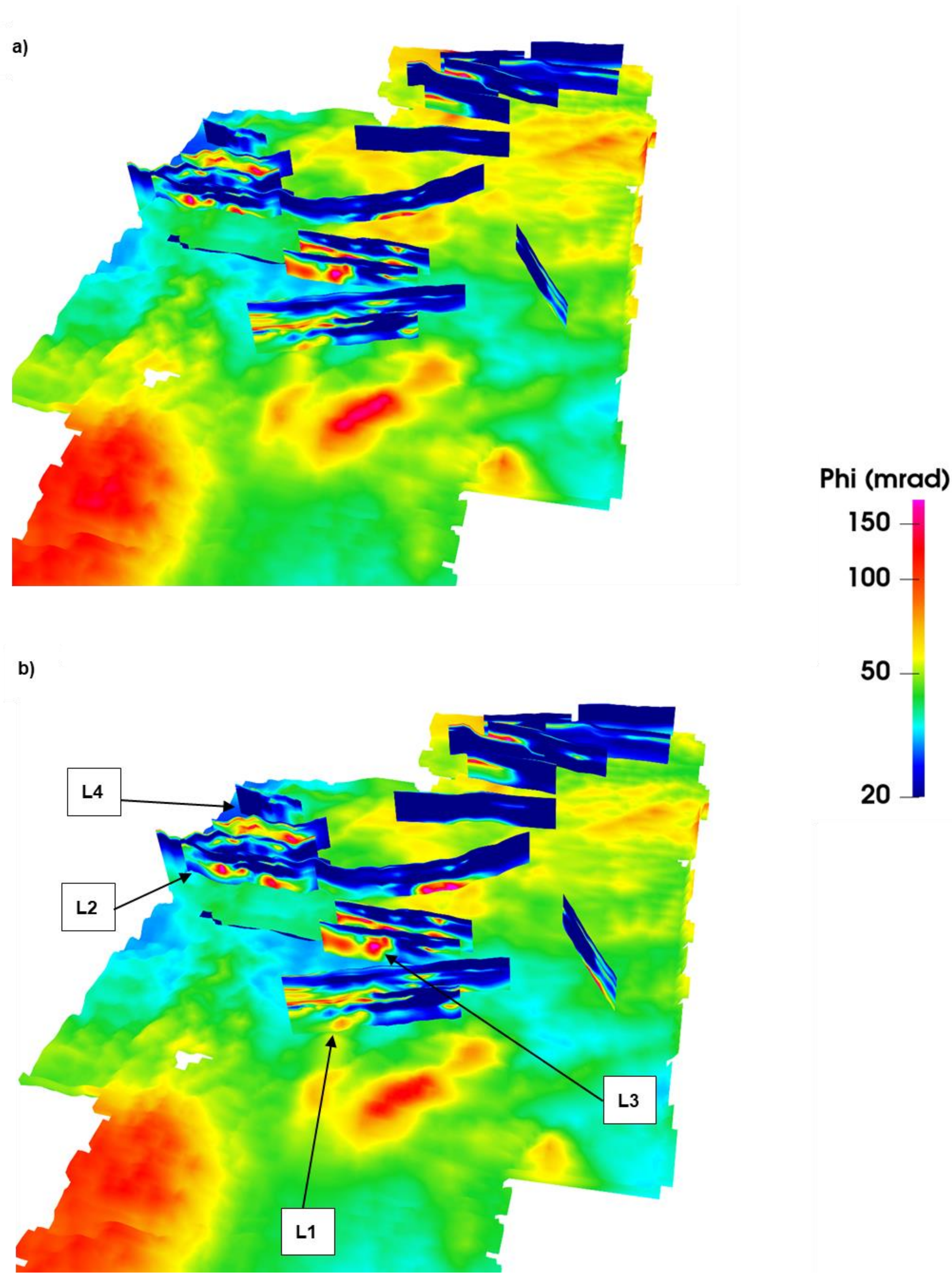

Figure 3.6. Modelled chargeability from airborne EM and ground DCIP independent inversions. In (a) a chargeability depth slice at 120 m is shown, while (b) at 150 m of depth.

The retrieved misfit for the DCIP lines is shown in *figure 3.15*. Here, while the AIP misfit is as well below 2, the DC misfit is often higher as consequence of the poor S/N ratio for these measurements given by strong topography of the area and by the dipole-dipole acquisition sequence; this allows to reach deeper depths with a good lateral resolution but decreases the S/N.

As visible from *figure 3.6*, a good match between the airborne and ground model is retrieved with the lateral chargeability contrasts mapped by the airborne at different depths generally confirmed by the ground models. In terms of magnitudes, the ground chargeability often shows a higher value respect with the airborne model. Nevertheless, the distribution of the airborne chargeability is consistent with the galvanic models where they intersect and showing a geological distribution both in the near surface and at depth. In general, most of the airborne chargeability anomalies and structures have been confirmed by the 17 ground DCIP models, providing a good reliability test to the airborne chargeability modelling approach. The use of a consistent modelling makes the comparison more robust and reliable, reducing the ambiguities introduced by different approaches.

The good comparability between the independent inversions has been reached nevertheless the difference in the base frequencies, the absence of negative voltages in the AEM dataspace and, more in general, in the different energizing method (galvanic-inductive) of the two. The time constant and the frequency dependence parameters modelled for the airborne data are respectively shown in *figure 3.7a* and *3.7b* and different examples of time constants cross sections retrieved by ground DCIP inversions are shown in *figure 3.8a* with their respective frequency dependence in *figure 3.8b*. In the cross sections the computed depth of investigation is show with a white line and is defined as Fiandaca et al. (2015).

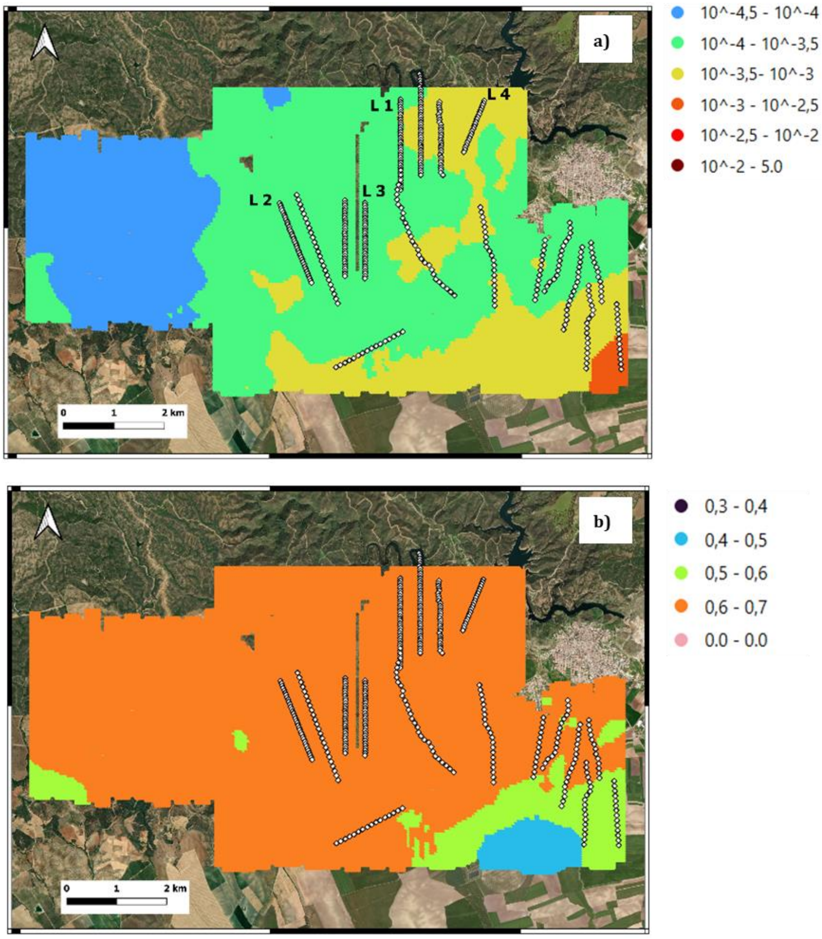

Figure 3.7 Time constant map (a) and frequency dependence map (b) retrieved from AIP independent inversion.

The airborne-retrieved time constants span about three decades, from 10^{-5} s to 10^{-2} s and have been modelled associated with a frequency dependence value of 0.6 for a large portion of the area; this indicates a non-flat chargeability spectrum but peaked on the computed time constant. The spectral parameters maps do not show correlation with the retrieved chargeability of *figure 3.4,* where only the model in the south-west shows high time constant and high chargeability. The isolated chargeable anomalies modelled both in the near surface and at depth are not characterized by spectral contrast.

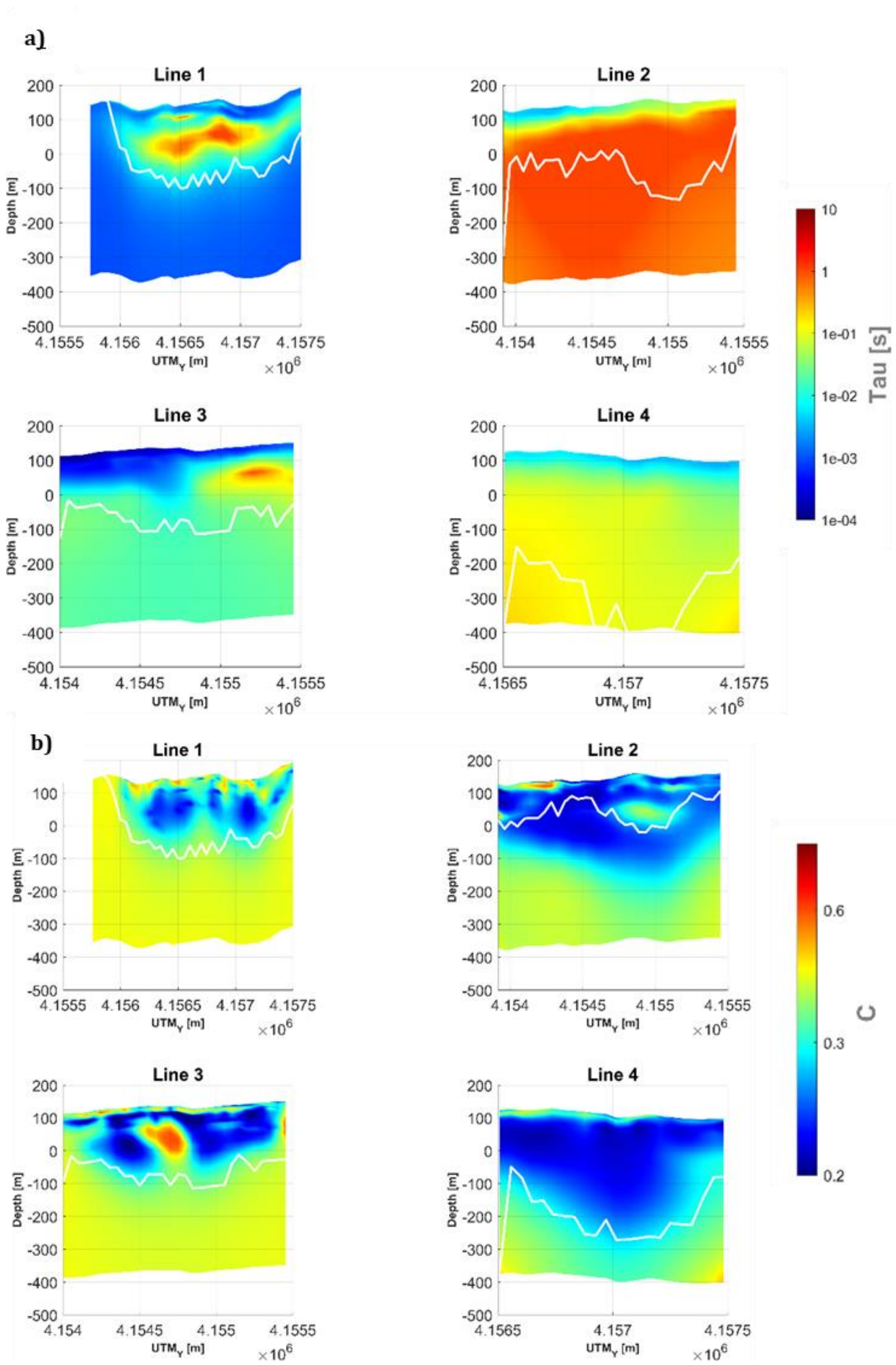

Figure 3.8. Time constant cross sections (a) of the four DCIP profiles indicated in figure 3.6; in (b) their relative frequency dependence. The white line represents the depth of investigation, computed as Fiandaca et al., 2015,

As visible from *figures 3.8a* and *3.8b*, different time constants have been retrieved between the two methodologies over the same line. The DCIP modelled time constants are generally higher than the AIP ones also in correspondence of the matching chargeability contrasts retrieved from both methods (like in line 1 and 2 of *figure 3.7* for the spectral parameters and in *figure 3.6* for the chargeability comparisons). In these places, no time-constant contrasts have been modelled by the airborne while higher time constants in correspondence of the chargeability anomalies are retrieved for the DCIP. The DCIP modelled time constants are also often very high if compared with the smaller frequency range of inductive methods, limited by their high base frequency and theoretically able to record high-frequency IP only. Nevertheless, the AIP maps the chargeable bodies consistently with the DCIP. Particularly, line 2 of *figure 3.8* shows a high time constant at depth (higher than 2) also in correspondence of the chargeability anomaly that have been successfully mapped by the airborne chargeability model in *figure 3.6*. Differently, the line that less matches the airborne chargeability model is line 3 of *figure 3.*8 that, however, shows a time constant which lies within the expectable range for inductive time constants (e.g. Macnae, 2016). Another example of highly chargeable body with a high time constant and mapped by the airborne EM is shown in *figure 3.11b* and, its time constant, in *figure 3.9*.

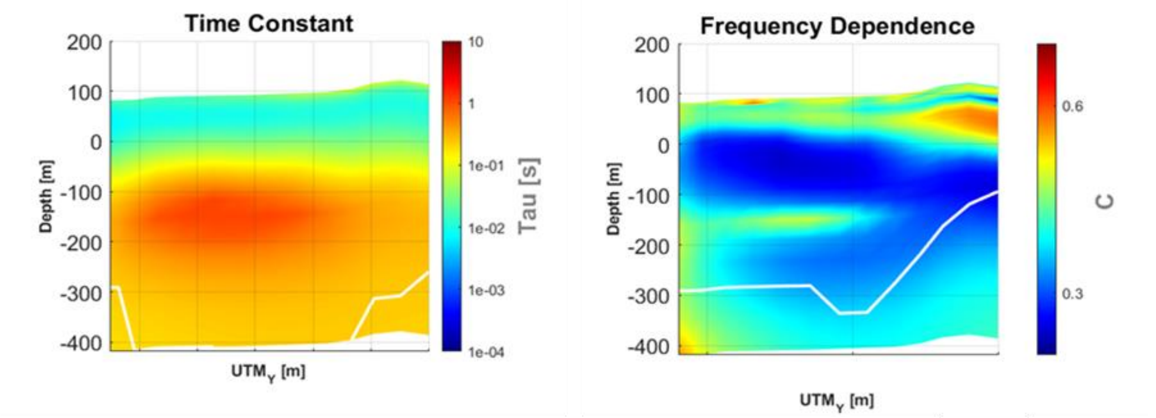

Figure 3.9. Time constant (left) and frequency dependence (right) cross section relative to the deep chargeable anomaly of figure 3.12b.

As visible from *figure 3.12b*, the airborne chargeability that have been modelled at depth for this line is relative to a chargeable body that shows a high time constant from the ground DCIP modelling. The magnitude of the airborne chargeability is smaller than the ground retrieved but the spatial distribution and the lateral contrast is consistent with the DCIP model.

From these examples appears that the ground chargeability is mapped consistently from both techniques regardless the retrieved time constant from the two methodologies. This can be explained as consequence of the spectral behaviour of the chargeable bodies. For these, even if their chargeability phase peak is out of the frequency range of the inductive method, the tail of the chargeable anomaly can lie within the AIP record when particularly strong. This is particularly true for small (0.3-0.6) frequency dependency values that make the spectral peak wider among more frequencies and expands the effect of the chargeable body to higher frequencies. This physical behaviour also explains the difference in magnitude between the airborne chargeable models and the ground retrieved models, as in the example of *figure 3.12b*. These observations are valid for single-peak IP models to fit the IP data. For this comparison, the reliability of the DCIP retrieved time constant is reduced, given its frequent coupling with low frequency dependences. This is mostly consequence of the poor spectral content of this DCIP data, limited to 2 decades and do not allow to accurately resolve the spectral parameters. In the next chapter, (*Chapter 4*) an airborne-ground comparison and joint inversion with DICP data recorded on a larger bandwidth is provided.

More in general, as seen from the airborne-ground comparisons, the magnitude of the ground DICP chargeability is often stronger than the AIP one. This claim is also supported for this case study by the absence of negative voltages in the Airborne EM data. From a phenomenological standpoint, the opposite direction currents are produced during the discharge of the capacitive-ground approximation; these give recordable negative voltages only if strong enough to overcome the purely EM currents or if the discharge time lies within the bandwidth of the EM system. If the discharge, at which the frequency peak is reached, lies outside the frequency boundaries of the EM system, any negative contribute can be recorded in EM data. At the same time, this does not exclude the presence of IP effects within the EM data but makes the IP extraction more complex and the inverse problem more suited to equivalencies. In terms of modelling, under these conditions, the EM sensitivity to the chargeable body is reduced and an approach that reduces the equivalencies is fundamental to being able to resolve for these subtle spectral features.

3.5: Airborne EM and DCIP joint inversion modelling of AIP effects

After the independent modelling, the joint inversion of the two datasets considering AIP effects has been done. The joint inversion has been done modelling the 17 lines of the ground DCIP survey together with the airborne data in the same inversion framework. For this joint inversion, the same model-mesh of the independent AEM inversion has been used; the AEM independent model has also been used as starting model for the joint inversion.

The results of the joint modelling are shown in *figure 3.10* and *figure 3.11* with resistivity (in *figure 3.10a, 3.10b, 3.11a, 3.11b*) and chargeability (in *figure 3.10c, 3.11d, 3.11c, 3.11d*) slices at different depths.

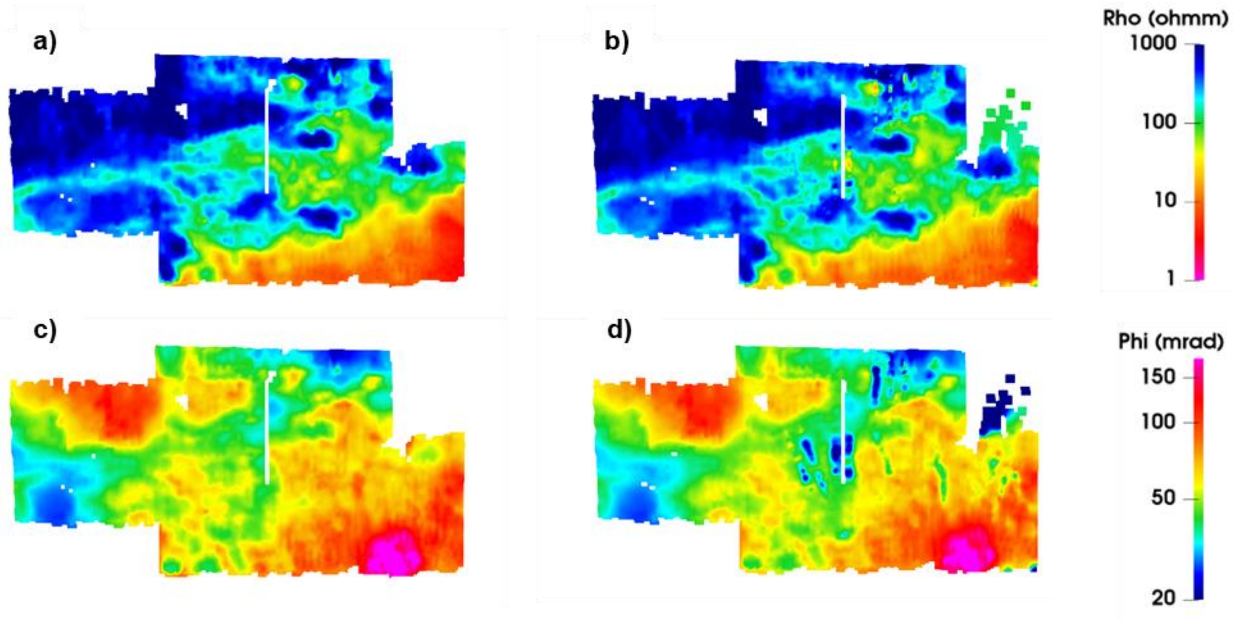

Figure 3.10. Resistivity (a and b) and chargeability (c and d) comparisons between AEM independent (a and c) and joint inversion (b and d). The depth slice is at 30 m.

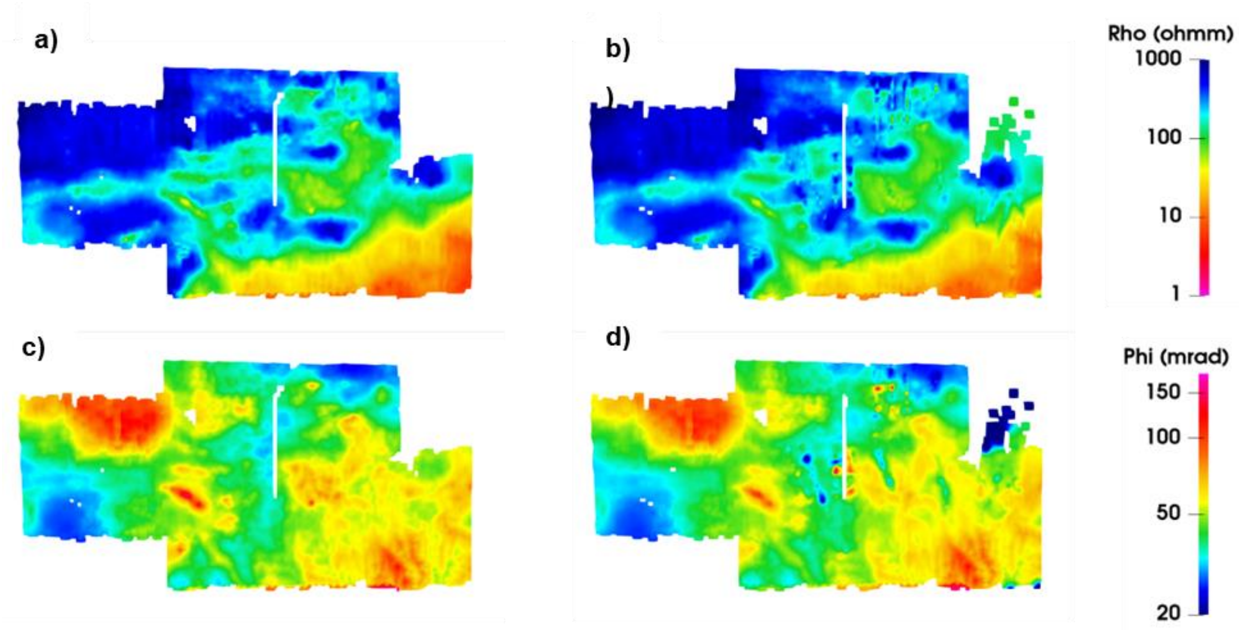

Figure 3.11. Resistivity (a and b) and chargeability (c and d) comparisons between the AEM independent inversion (a and c) and joint inversion (b and d) for a depth slice at 150 m.

As visible and expectable, the joint resistivity and chargeability models vary mostly, but not uniquely, in neighbourhood of the DCIP lines if compared with the AEM independent inversion. This is particularly visible in the near surface chargeability slices (*figure 3.10c* and *3.10d*), as it was also visible in the comparisons between AEM and DCIP independent inversions. This is a consequence of the DCIP sequence that have been used for the ground survey, with a dipole-dipole configuration with 100 m of electrode distance has a lower near surface sensitivity if compared with the inductive method. This lack of sensitivity to near surface is further enhanced during the joint modelling. At depth, the line effect is less marked, and the spatial distribution of the chargeability anomalies is generally consistent with the one retrieved in the AEM independent inversion. Here, the main difference between the two methods lies in the magnitude of the anomaly that is stronger in correspondence of the DCIP lines.

In *figures* 3.*12a* and 3.*12b*, line-by-line model comparisons of resistivity and chargeability independent and joint models are shown. Generally, the independent inversions are comparable with the ground resistivity and chargeability mapped in the same location for both the techniques. Differently, the joint inversions show an increase in the structure, particularly for the chargeability model.

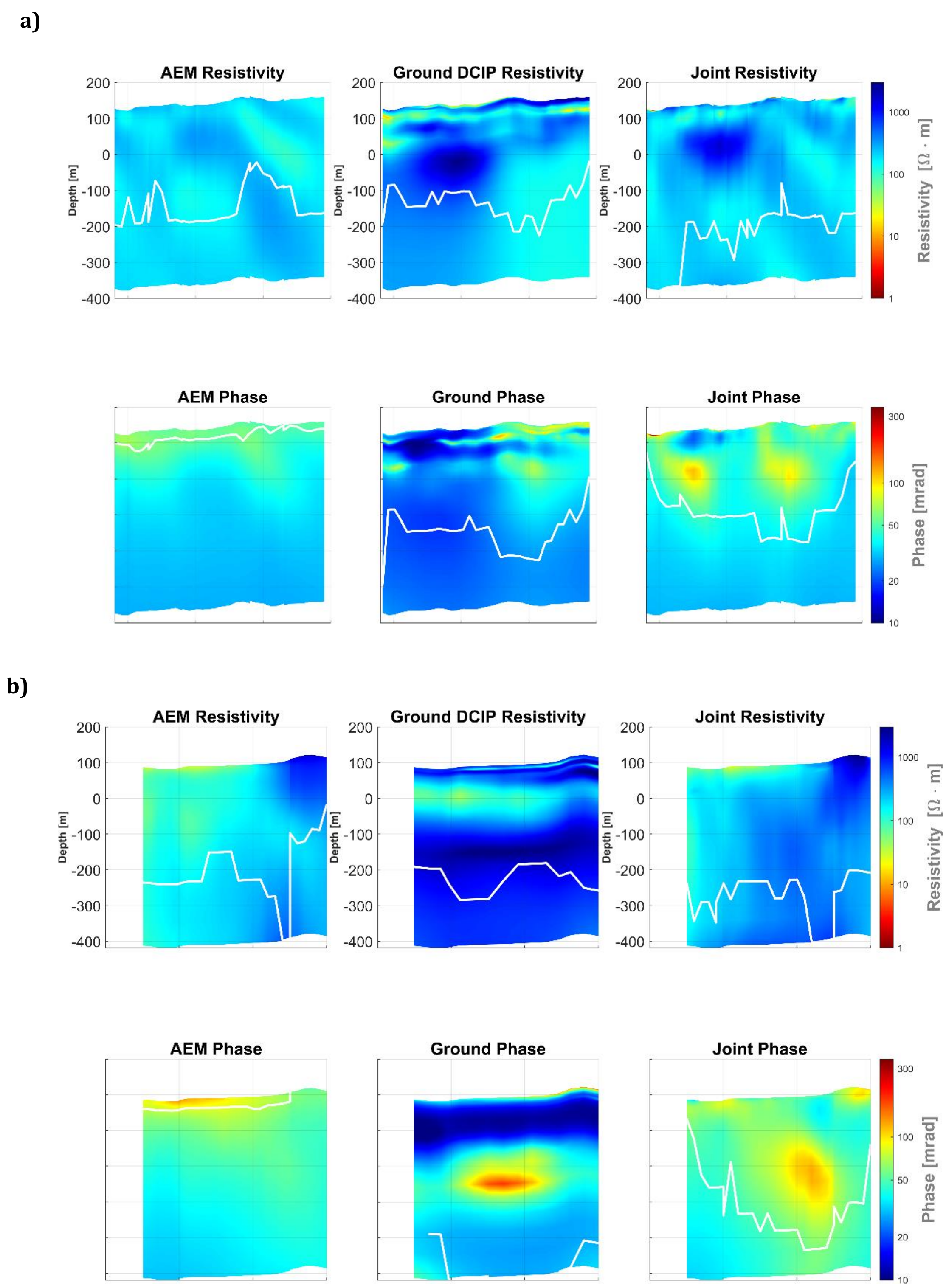

Figure 3.12. AEM vs Ground vs Joint inversion resistivity (top) and chargeability (bottom) comparisons for two lines. Line 2 of figure 3.6 is shown in (a), while in (b) the independent and joint inversions of the line discussed in figure 3.9.

This increase in structure in the joint inversions is consequence of the merge of the sensitivities of the two methods that better constraints the inverse problem and reduces the equivalencies during the modelling. For these methods the sensitivities are also different: the inductive methods have more sensitivity to conductive bodies while the galvanic method, also in function of the used sequence for the acquisition, are more sensitive to deeper and resistive bodies. In *figure 3.12a* and 3.*12b*, two examples of different chargeable targets modelled both from the ground and from the airborne are shown with their respective joint inversion. In figure 3.*12a*, the chargeable bodies are in the near surface and with a medium-high chargeability; the airborne independent inversion maps here the ground chargeability consistently with the DCIP both in terms of magnitude of the anomalies and in terms of spatial distribution. Increasing the depth of the target as in *figure 3.12b*, the strong chargeable body mapped by the ground DCIP is laterally mapped by the AIP as well but with a smaller magnitude. With the joint inversion it is possible to model the data driving the inversion to a unique model merging different sensitivities to different ground characteristics. This helps to reduce the equivalencies of the independent inversion of the same data in the lower sensitivity domains. Consequently, the joint inversion retrieves a chargeability model which merges the different sensitivities of the data, bounding the model space and extending the bandwidth. In term of spectral modelling, the time constant and frequency dependence maps retrieved by the joint inversion are shown in *figure 3.13a* and *3.13b*, respectively.

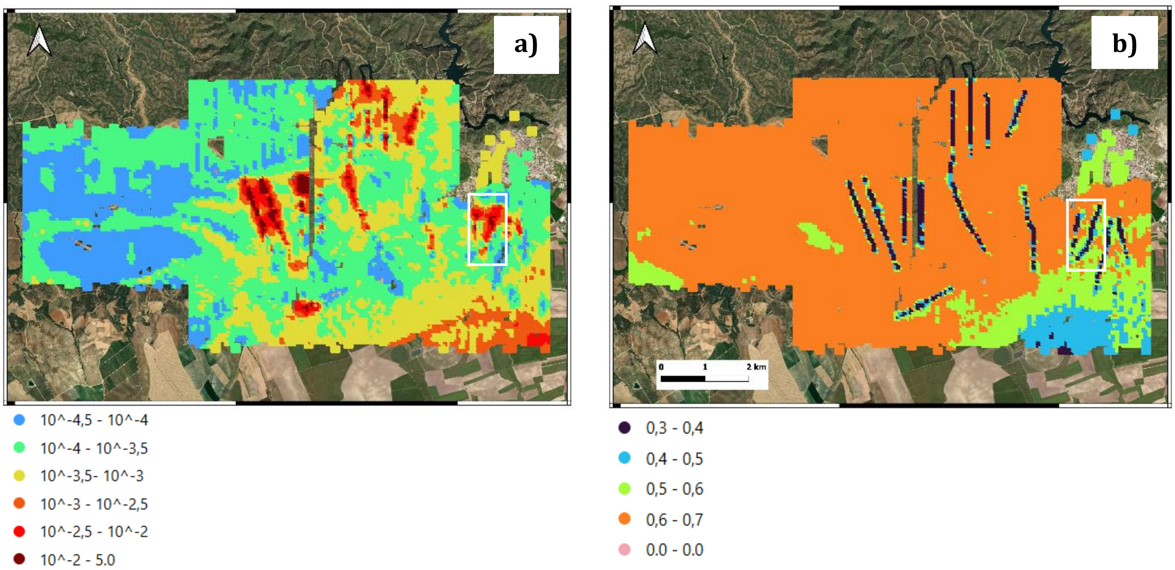

Figure 3.13. Time constant (a) and frequency dependence (b) maps retrieved by joint inversion modelling. In the white box, the location of line of figure 3.9 and 3.12b is indicated.

From *figure 3.13* it is visible how the parameters change if compared with the one modelled from the AEM independent inversion, visible in *figure 3.6.* These generally increase around the DCIP lines, with time constants that goes above 1 s and the frequency dependence that strongly decreases. It is here interesting to notice that despite the high time constant the AEM data are fitted, as visible in *figure 3.14,* as well as the IP data. The frequency dependence that here decreases in correspondence of the DCIP lines, spectrally allows to expand the chargeability peak content in the ground DCIP to the lower frequencies of the AEM data and fitting both the datasets with the same model and time constant. These results also show how the AEM data can be fit, when AIP is considered, with very different models. In this inversion the AEM data accept the low frequency contribute introduced by the DCIP data adapting the spectral parameters; this also shows how a number of equivalent solutions can fit the AEM when IP is modelled. In particular, the equivalencies are here favoured by the absence of negative voltages in the AEM, which introduce uncertainties during the IP modelling. However, the data inversion without IP modelling presents a significantly higher data misfit (1.3 instead of 0.8 as defined in *equation 2.5*), as shown in details in the Appendix of this thesis.

In terms of misfit, the joint inversion misfit is comparable with the retrieved misfit of the independent inversions, as visible from *figures 3.14 and figure 3.15*.

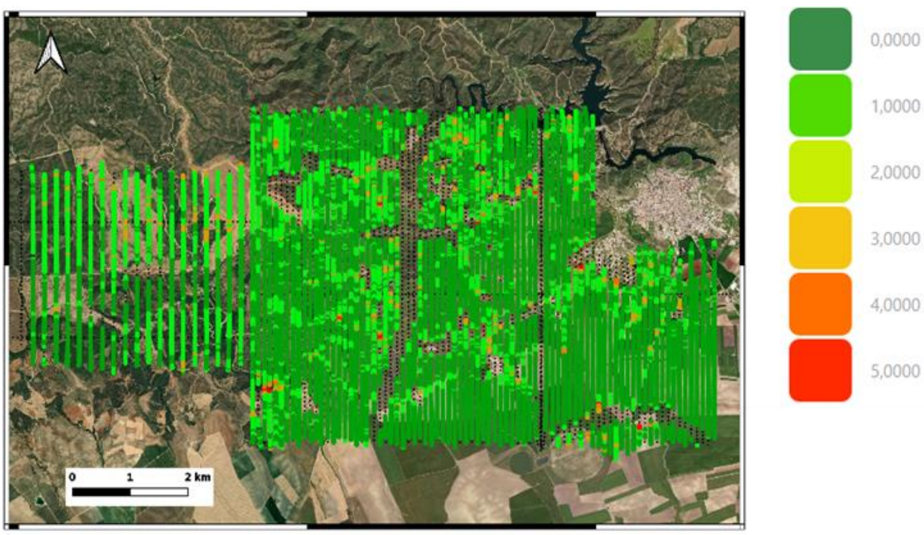

Figure 3.14. AEM joint inversion misfit.

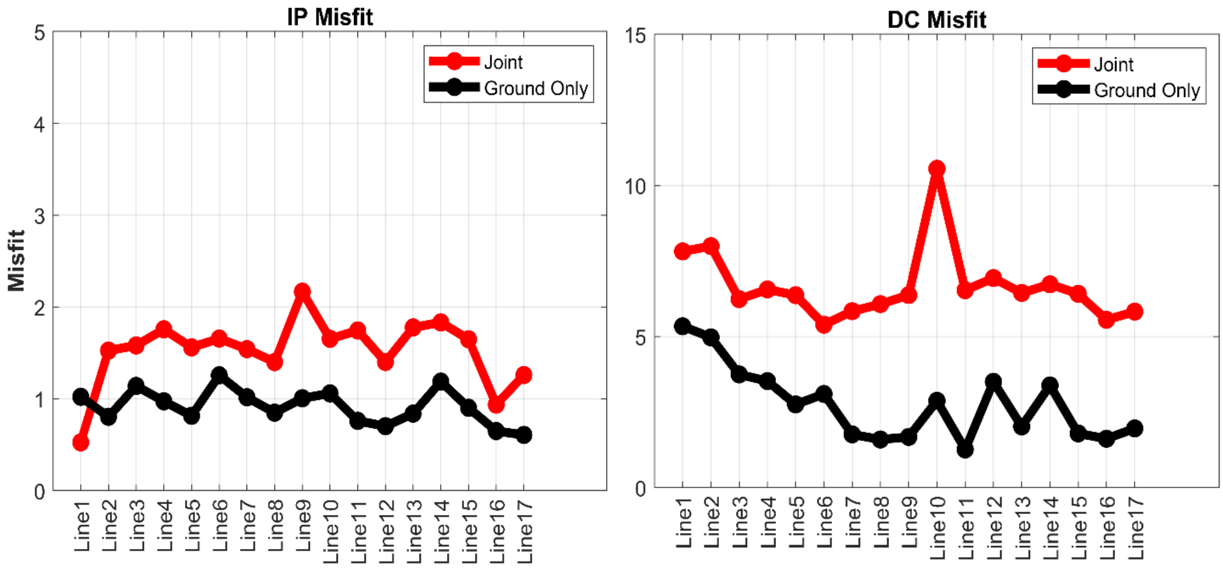

Figure 3.15. Joint inversion misfit for IP (left) and DC (right) galvanic measurements.

In *figure 3.14* the AEM-joint inversion misfit is shown while in *figure 3.15* the line-by-line misfit of the ground DCIP independent inversion versus the joint inversion misfit for the DCIP lines is shown. Although the misfit increases for both DC and IP, the IP misfit remains largely below 2 while the joint DC misfit increases. On the other hand, the DC misfit is generally higher than 2 both in the DCIP independent inversions and even more in the joint modelling. This high misfit, both in independent and joint inversion, can be consequence of the mentioned higher S/N of the dipole-dipole sequence, together with the dry season which increased the contact resistance and worsened the IP recording. These issues on the data, when jointly modelled, further increase the global misfit of the joint inversion.

3.6: Conclusions

In this chapter the airborne inductive chargeability and the ground galvanic chargeability have been compared and jointly modelled. To improve the robustness of the comparison, a consistent modelling which takes into account the full voltage decays, the receiver filters and the transmitter transfer function has been used both for the galvanic and inductive data. For the inductive data, a multi-mesh inversion to reduce the equivalencies during the inversion has been adopted, parametrizing the spectral parameters in a mono-dimensional mesh while the chargeability and resistivity have been set free to change laterally and vertically. This approach has shown a good match between the ground and the airborne retrieved models, with the magnitude of these anomalies stronger in the DCIP inversions than in the AEM inversions. This is consequence of the different bandwidth of the methods: the peak of the chargeable anomalies is content within the DCIP spectral range while in the AEM data only a portion of its spectral curve can be detected. This can lead to a mismodelling of the ground chargeability, creating large equivalent domains in the model-space if the inversion is not properly bounded. At the same time, this means that even if the peak of the chargeability amplitude is not recorded within the EM bandiwdth, it is possible to extract the effect of the ground polarization in a comparable way with the ground DCIP when we success in reducing AIP equivalencies during modelling. This has been also confirmed by the joint inversion modelling conducted between the ground DCIP and the Airborne EM data considering IP effects, inverting the entire datasets in the same inversion scheme and updating a unique model. The results have shown an improvement in the resolution of the chargeability model with a difference in the retrieved structure respect both the ground and the airborne independent inversion. The merging of the sensitivities to different portion of the IP spectra provided by the two reduced the equivalencies and enriched the IP bandwidth with the low frequency contribution given by the DCIP and the high frequency of the inductive. In this sense, for further developments, modelling the EM and DCIP jointly with multiple-relaxations models could improve the bandwidths merging.

With this contribute, the airborne EM and the ground DCIP data have been thus modelled and fitted together, unifying the galvanic and inductive bandwidth of the methodologies and retrieving a unique inversion model that satisfies both the datasets.

3.7: Acknowledgements

For this work I acknowledge the Pan Global Resources mining company for providing us the data to perform the inversions.

3.8: References

- Albouy, L., Conde, L. N., Foglierinni, F., Leca, X., Morikis, A., Callier, L., Carvalho, P., Songy, J. C., (1981), Le gisement de sulfures massifs polymétalliques de Neves-Corvo, Baixo Alentejo, Portugal. Chronique de La Recherche Minière, BRGM, 460: 5-27.
- Almodóvar, G., Yesares, L., Sáez, R., Toscano, M., González, F., Pons, J. M., (2019), Massive Sulfide Ores in the Iberian Pyrite Belt: Mineralogical and Textural Evolution. Minerals 2019, 9(11): 653, 20. https://doi.org/10.3390/min9110653.
- Andrade, R., Schermerhorn, L., (1971), Aljustrel and Gavião. In: Carvalho, D., Goinhas, J., Schermerhorn, L.J.S. (Eds.), Livro guia da excursão 4. I Congresso Hipano-Luso-Americano de Geol. Económica, 32-59. Araujo, V., 2009. Área de Castro Verde, relatório 2º Semestre 2009.
- Barriga, F., Carvalho, D., Ribeiro, A., (1997), Introduction to the Iberian Pyrite Belt. SEG Neves Field Conference. Guidebook Series, 27: 1-20.
- Carvalho, D., (1982). New paths to massive sulphide exploration in the Iberian Pyrite Belt. Com. Serviços Geológicos de Portugal, 68(2): 149-162.
- Carvalho, D., Barriga, F. J. A. S., Munhá, J., (1999), Bimodal-siliciclastic systems – the case of the Iberian Pyrite Belt. Reviews in Economic Geology, 8: 375-408. https://doi.org/10.5382/Rev.08.16
- Castroviejo, R., Gable, R., Cueto, R., Foucher, J. C., Soler, M., Gounot, J., Batsale, J. C., Lopez, A., Joubert, M., (1996), Ensayo de una metodologia innovadora para la detección de masas polimetálicas profundas: Modelo geológico y exploración geotérmica preliminares de la Masa Valverde (Huelva). Bol. Geologico y Minero ITGE, Madrid, 107(5-6): 5-30.
- Combrinck, M., and R. Wright. (2016), Xcite: Great results require more than good data. ASEG-PESA-AIG expanded abstract, Adelaide.
- Christensen N., B., (2022), Joint inversion of airborne TEM data and surface geoelectrical data. The Egebjerg case, Journal of Applied Geophysics, Volume 196, 104511, ISSN 0926-9851, https://doi.org/10.1016/j.jappgeo.2021.104511.
- Doyle, M., (1996). Las Cruces Copper Deposit, Pyrite Belt, Spain. Bol. Geologico y Minero ITGE, Madrid, 107(5-6): 201-204.

- Effersø, F., Auken, E. and Ingvard Sørensen, K. (1999), Inversion of band-limited TEM responses. Geophysical Prospecting, 47: 551-564. https://doi.org/10.1046/j.1365-2478.1999.00135.x
- Flis, M.F., Newman, G.A., Hohmann, G.W., (1989), Induced-polarization effects in time-domain electromagnetic measurements, Geophysics, 54(4), 514-523, https://doi.org/10.1190/1.1442678
- Fiandaca, G., Christiansen, A., V., Auken, E., (2015), Depth of Investigation for Multi-parameters Inversions, European Association of Geoscientists and Engineers, Near Surface Geoscience 2015 - 21st European Meeting of Environmental and Engineering Geophysics, 2015, 2015, p.1 – 5, https://doi.org/10.3997/2214-4609.201413797
- Fiandaca, G., Auken, E., Christiansen, A.V., Gazoty, A., (2012), Time-domain-induced polarization: Full-decay forward modeling and 1D laterally constrained inversion of Cole-Cole parameters, Geophysics, 77: E213-E225. https://doi.org/10.1190/geo2011-0217.1
- Fiandaca, G., Madsen, L.M. and Maurya, P.K. (2018), Re-parameterisations of the Cole–Cole model for improved spectral inversion of induced polarization data. Near Surface Geophysics, 16: 385-399. https://doi.org/10.3997/1873-0604.2017065
- Fiandaca, G., Viezzoli, A., (2021). Inversion of Airborne IP data with a multi-mesh approach for parameter definition. Australasian Exploration Geoscience Conference AEGC2021, 13-17 September 2021, Extended Abstract.
- Fiandaca G., Chen J., Zhang B., (2024), EEMverter, a New Modelling Tool for Electric and Electromagnetic Data with Focus on Induced Polarization, European Association of Geoscientists and Engineers, NSG 2024 30th European Meeting of Environmental and Engineering Geophysics, p.1 – 5, https://doi.org/10.3997/2214-4609.202420166.
- Gable, R., Castroviejo, R., Cueto, R., Batsale, J. C., Foucher, J. C., Soler, M., Gounot, J., Guerin, G., Lopez, A., (1998). Test of the geothermal method for Deep polymetallic ore exploration in Masa Valveere (Huelva). IV Simp. Int. dos Sulfuretos Polimetálicos da Faixa Piritosa Ibérica. APIMINERAL, Lisboa, A.14.1-A.14.23
- Gisbert, G., Losantos, E., Tornos, F., Pons, J. M., Videira, J. C., (2019). Elvira: a new shale-hosted VMS deposit in the Iberian Pyrite Belt. Procedings SGA, 15th Conf., Glasgow, 3: 1256-1259.

- Leca, X., Ribeiro, A., Oliveira, J. T., Silva, J. B., Albouy, L., Carvalho. P., Merino, H., (1983), Cadre géologique des minéralisations de Neves-Corvo (Baixo-Alentejo, Portugal) – Lithostratigraphie, paléogéographie et tectonique. Mémoire du BRGM, 121. Orléans, France, 79.
- Leistel, J., Marcoux, E., Thieblemont, D., Quesada, C., Sanchez, A., Almodovar, G., Pascual, E., Saez, R, (1998), The volcanic-hosted massive sulphide deposits of the Iberian Pyrite Belt. Review and preface to the special issue. Mineralium Deposita, 33: 2-30.
- Macnae, J., (2016), Quantitative estimation of intrinsic polarization and superparamagnetic parameters from airborne electromagnetic data, Geophysics 81(6), E433-E446, https://doi.org/10.1190/geo2016-0110.1
- Macnae, J., (2016), Airborne IP detects only fine-grained minerals when compared to conventional IP. ASEG Extended Abstracts, 1–4. https://doi.org/10.1071/ASEG2016ab141
- Macnae J., (2016), Quantifying Airborne Induced Polarization effects in helicopter time domain electromagnetics, Journal of Applied Geophysics, 135, 495-502, https://doi.org/10.1016/j.jappgeo.2015.10.016.
- Madsen, L. M., Fiandaca, G., and Auken, E. (2020), 3-D time-domain spectral inversion of resistivity and full-decay induced polarization data—full solution of Poisson's equation and modelling of the current waveform, Geophysical Journal International, 223(3), 2101-2116, https://doi.org/10.1093/gji/ggaa443
- Marchant, D., Haber, E., Oldenburg D., (2013), Inductive Source Induced Polarization. Geophysical Journal International. DOI: 192. 602-612. 10.1093/gji/ggs040.
- Matos, J. X., Carvalho, J., Represas, P., Batista, M. J., Sousa, P., Ramalho, E., Dias, P. (2020), Geophysical surveys in the Portuguese sector of the Iberian Pyrite Belt: a global overview focused on the massive sulphide exploration and geologic interpretation. Comunicações Geológicas, 107(Especial III), 41-78.
- Meju, M., and Gallardo, L., (2016), Structural Coupling Approaches in Integrated Geophysical Imaging, Integrated Imaging of the Earth: Theory and Applications, DOI: 10.1002/9781118929063.ch4.
- Xiao, L., Fiandaca, G., Maurya, P. K., Christiansen, A. V., and Lévy, L. (2022), Three-dimensional time-lapse inversion of transient electromagnetic data, with application

at an Icelandic geothermal site. Geophysical Journal International, *231*(1), 584-596, DOI: 10.1002/9781118929063.ch4

- Xiao, L., Fiandaca G., Bo Z., Esben A., Anders A.., (2022), Fast 2.5D and 3D Inversion of transient electromagnetic surveys using the octree-based finite element method. Geophysics. 87, E267-E277, https://doi.org/10.1190/geo2021-0402.1
- Oldenburg, D.W. and Li, Y., (1994). Inversion of induced polarization data, Geophysics, 59(9), 1327–1341, https://doi.org/10.1190/1.1443692
- Oliveira, J. T., Quesada, C., Pereira, Z., Matos, J. X., Solá, A. R., Rosa, D., Albardeiro, L., Díez-Montes, A., Morais, I., Inverno, C., Rosa, C., Relvas, J., (2019), South Portuguese Terrane: A Continental Affinity Exotic Unit. In: Quesada, C., Oliveira J. T. (Eds.), The Geology of Iberia: A Geodynamic Approach, Regional Geology Reviews, 173-206. https://doi.org/10.1007/978-3-030-10519-8_6
- Pelton W.H., Ward S.H., Hallof P.G., Sill W.R., Nelson P.H., (1978), Mineral discrimination and removal of inductive coupling with multifrequency IP, Geophysics, 43(3), 588-609, https://doi.org/10.1190/1.1440839
- Kamenetsky F.M., Trigubovich G.M., Chernyshev A.V. (2014), Three lectures on geological medium induced polarization. L-M University of Munich, Vela Verlag, 56p, ISBN: 978-3-941352-65-0
- Kaufman, S. Geoltrain, R.N. Knoshaug, (1989), Influence of induced polarization in inductive methods, Geoexploration, 26(2), 75-93, https://doi.org/10.1016/0016-7142(89)90054-9.
- Kratzer T., and Macnae J., (2012), Airborne induced polarisation, SEG Technical Program Expanded Abstracts, 1-6, https://doi.org/10.1190/segam2012-0395.1.
- Sáenz de Sicilia, J-L. C. (2013), Focus: Spain. Going for growth. Spain's mining sector presents strong growth prospects. Mining Journal, December, 16-20.
- Sullivan N.A.L., Viezzoli A., Fiandaca G., (2024), EEMstudio: Process and Model Electric and Electromagnetic Data with a QGIS Plugin, NSG 2024 30th European Meeting of Environmental and Engineering Geophysics, Sep 2024, 2024, p.1 – 5, European Association of Geoscientists and Engineers, https://doi.org/10.3997/2214-4609.202420154
- Torres, L., Carvalho, J., (1998), A contribuição dos dados geofísicos obtidos na prospecção de sulfuretos polimetálicos na Faixa Piritosa para ampliar o conhecimento

estrutural da Zona Sul-Portuguesa. IV Simp. Int. Dos Sulfuretos Polimetálicos da Faixa Piritosa Ibérica. APIMINERAL, Lisboa, A.3.1-A.3.6.

- Viezzoli, A., Fiandaca, G., Segio, S., Auken., E., (2013), Constrained inversion of IP parameters from Airborne EM data, ASEG-PESA Expanded abstracts, Melbourne, Australia.
- Viezzoli, A., & Manca, G., (2019), On airborne IP effects in standard AEM systems: tightening model space with data space. Exploration Geophysics, 51(1), 155–169, https://doi.org/10.1080/08123985.2019.1681895
- Zhang, B., E. W. Kim, F. Gianluca, H. Cai, and E. Auken, (2021), 3D inversion off-time domain electromagnetic data using finite elements and a triple mesh formulation: Geophysics, 86, (3), E257–E267, DOI: /10.1190/geo2020-0079.1.

Chapter 4: Airborne IP driven exploration: a European pilot study

Chapter 4, summary

In the previous chapters, different aspects of AIP method have been treated. In *Chapter 1* the ground chargeability has been modelled at regional-scale using fixed-wing data acquired in Australia. Then, in *Chapter 2*, a comparison with DCIP and a joint inversion (airborne-ground IP) have been applied to a dataset flown at deposit-scale in Spain. Both the works have shown that it is possible to retrieve reliable ground chargeability from EM data, proving a good comparability between different EM methods (e.g. between fixed-wing and helicopters), with geology (e.g. with the Nebo Babel deposit in Australia) and with ground galvanic DCIP.

After these encouraging results, in this chapter, the AIP method is applied for generative exploration in a greenfield exploration project. This work is developed in the frame of a European Horizon Project, the SEMACRET project, that aims to define innovative techniques for modern mineral mapping. This has been developed in five sites in Europe (Portugal, Poland (2), Czech Republic and Finland) over known mineralization. In this framework, I focus on the Portuguese test site. Here, the previous work was mostly developed around geological mapping making the site a greenfield exploration project. In this work I first develop a feasibility study to define the system characteristics of the AEM survey to maximise the IP detection. Then, two airborne EM surveys have been flown with different base frequencies, 12.5 Hz and 25 Hz, following the feasibility results. With these datasets the independent inversions have been carried, followed by a joint inversion of the two. Afterwards, the ground DCIP follow-up over an airborne defined anomaly has been acquired; this confirmed the airborne anomaly revealing a potential target in the area. To conclude, a joint inversion between the 25Hz, 12.5Hz and DCIP galvanic data has been carried to solve the ground chargeability unifying the different bandwidths.

This work thus wants to contribute both to a phenomenological understanding of AIP (comparing different frequencies and different methods) and to the methodological applicability for generative mineral exploration.

4.1: Introduction

The critical raw materials (CRMs) exploration and supply is a growing challenge that the national and international communities need to address to achieve the goals of the green energy transition (UN, 2021). The challenge within the challenge, is to find innovative solutions for the mineral mapping and for their exploitation reducing the impact on the environment and on the local communities (Gloaguen et al., 2018; Viezzoli et al., 2018; Ruiz-Coupeau et al., 2020). In this scenario, indirect techniques such as geophysics, play a fundamental role in the success of a low-impact mapping campaign: the more accurate the methodology, the lower the risk of failure of the invasive activities that mining entails. For these reasons many research programs (like the European Horizon Projects, e.g. SEMACRET, INFACT, Smart Exploration, the Australian Exploring for the Future Project) have been developed to improve the approach to the exploration and make it more effective. Among the various geophysical methods, two of the most common techniques for exploration are the Direct Current Induced Polarization (DCIP) and the Electromagnetic (EM) to map chargeable and conductive bodies at depth. Although these techniques have been considered sensitive to different physical properties for a long time, it has been recognized that the effects of a polarizable ground can be measurable by inductive EM measurements (Bhatthacharyya, 1964; Dias, 1968; Morrison et al. 1969; Smith et al., 1996; Macnae et al., 2016; Kaminski and Viezzoli, 2017), both airborne and ground. It has then been shown that is possible to model the inductive IP from the EM data (Viezzoli et al., 2013; Macnae et al., 2016; Fiandaca et al., 2018) to retrieve the ground chargeability distribution and how novel modelling approaches (Dauti et al., 2024; Fiandaca et al., 2024) can increase the inductive chargeability sensitivity at depth with good comparability with mineralized bodies.

With this work, I aim to develop an airborne IP-driven approach to explore for chargeable and resistive targets. The airborne chargeability models are actively integrated with the ancillary information to define the next step of an exploration programme. For this work, differently from the standard use of AEM (i.e. for conductive anomalies mapping), the ground chargeability contrasts are the ground features to map. The motivation for developing this approach includes risk and cost reduction given by the airborne mapping of both the ground electrical properties that allow to add layers of information to the general mineral-system description. At the same time, from a geophysical and methodological standpoint, this represents a challenge. Most of the open questions concerning the use of the AIP technique stem from the intrinsic equivalences in the physical description of the IP phenomena and their management during the inversion process (e.g. Davies et al., 2023). This complicates the assessment of AIP sensitivity to geological and mineral targets and its relationships and reliability for the chargeability mapping. Also, the different base frequencies and modelling approaches between the inductive and galvanic methods have often led to the mapping of incompatible chargeability models in correspondence of known mineralization (Macnae et al., 2016). This leaded to the conclusion for which the galvanic IP is the most reliable tool to map the ground chargeability related to mineralization while AIP is sensitive to fine-grained materials only (Macnae et al., 2016). At the same time, recent works have shown how the use of innovative modelling algorithms (e.g., Fiandaca et al., 2024) can improve the integration between galvanic and inductive methods through consistent and joint modelling of the two (Dauti et al., 2024).

To achieve the goals of this work, to minimize the risks and maximize the chargeability detection, the AEM survey has been optimized since its preliminary stages, before the flights. A feasibility study considering different base frequencies and system configurations has been carried to design the survey. For the study, two different system configurations have been flown with different base frequencies and number of turns in the transmitter loop. The possibility to fly two surveys changing the system specifications allowed to compare the IP response of the ground for different system configurations and to verify accuracy of the modelling of the feasibility study. The flight of two different surveys is not a common practice in exploration but, for research purposes, represents a great opportunity to study the IP response in inductive methods at different frequencies. After the acquisition, the two datasets have been independently and jointly modelled to improve the chargeability mapping of the ground. A ground DCIP follow-up was then acquired over an area of potential interest defined by the previous inversions to attempt the joint modelling of all the datasets. With this work I thus have a twofold intent: I first aim to validate the development of an approach for which the ground DCIP follow-up is driven by a controlled mapping and accurate modelling of the airborne chargeability mapping and modelling. Second, I aim to improve the methodological understanding of the AIP at different frequencies through joint inversion modelling. This is also done including galvanic data, to unify the spectral ranges between galvanic and inductive method. Differently form the work in *Chapter 3*, the DCIP data are here acquired with a recording time of more than 10 s, which largely enrich the spectral content of the galvanic data.

This work aims to contribute to the validation and improvement of the AIP technique as a tool to map mineral bodies through its phenomenological understanding.

4.2: Study area, geological context and ancillary information

The study area is located around Odivelas, in the Alentejo region, in southern Portugal, shown in *figure 4.1a*.

Geologically, the area is in the Ossa Morena Zone, a Variscan terrane comprising several NW-SE belts with well individualised tectonostratigraphic evolution. The SW belt hosts a large 315 km^2 mafic layered intrusion, the Beja Layered Gabbroic Sequence- LGS (Jesus et al., 2014). This work covers the western compartment of the LGS (*ca.* 76 km^2) which outcrops discontinuously under Cenozoic unconsolidated sediments. The exposed sequence ranges from NW to SE and is defined as a primitive unit comprising troctolites and ultramafic cumulates surrounded by olivine leucogabbros (SB I Series; surrounded by Cenozoic cover), a gabbronorite fine grained unit (SB II Series) parental to the ODV I Series oxide gabbros further cropping out further SW around the Odivelas village. The ODV I highly evolved ferro-gabbros host important Fe–Ti–V oxide enrichment (Ti-magnetite + ilmenite) and the basal domains grade into irregular oxide masses (Jesus et al., 2003b). These ores comprise Ti-magnetite (oxidised to Ti-maghemite, also a spinel) and ilmenite and are a potential economic resource of Fe, Ti, and particularly V ($TiO_2 \leq$ 21.4 wt.%; $V_2O_5 \leq$ 1.6 wt%; Jesus et al., 2003). The ores do not outcrop but, according to old exploration reports (Silva, 1945), they form irregular bodies of considerable size (< 5 ton each) that are close to the topographic surface and lie at approximately right angles to the NW-SE, S dipping regional layering. The geological map of the area is visible in *figure 4.1b* where the Cenozoic cover was left transparent for the sake of readability; as such, most of the gabbroic rocks display in are surrounded by Cenozoic sediments except at NW where they are in contact with a diorite margin.

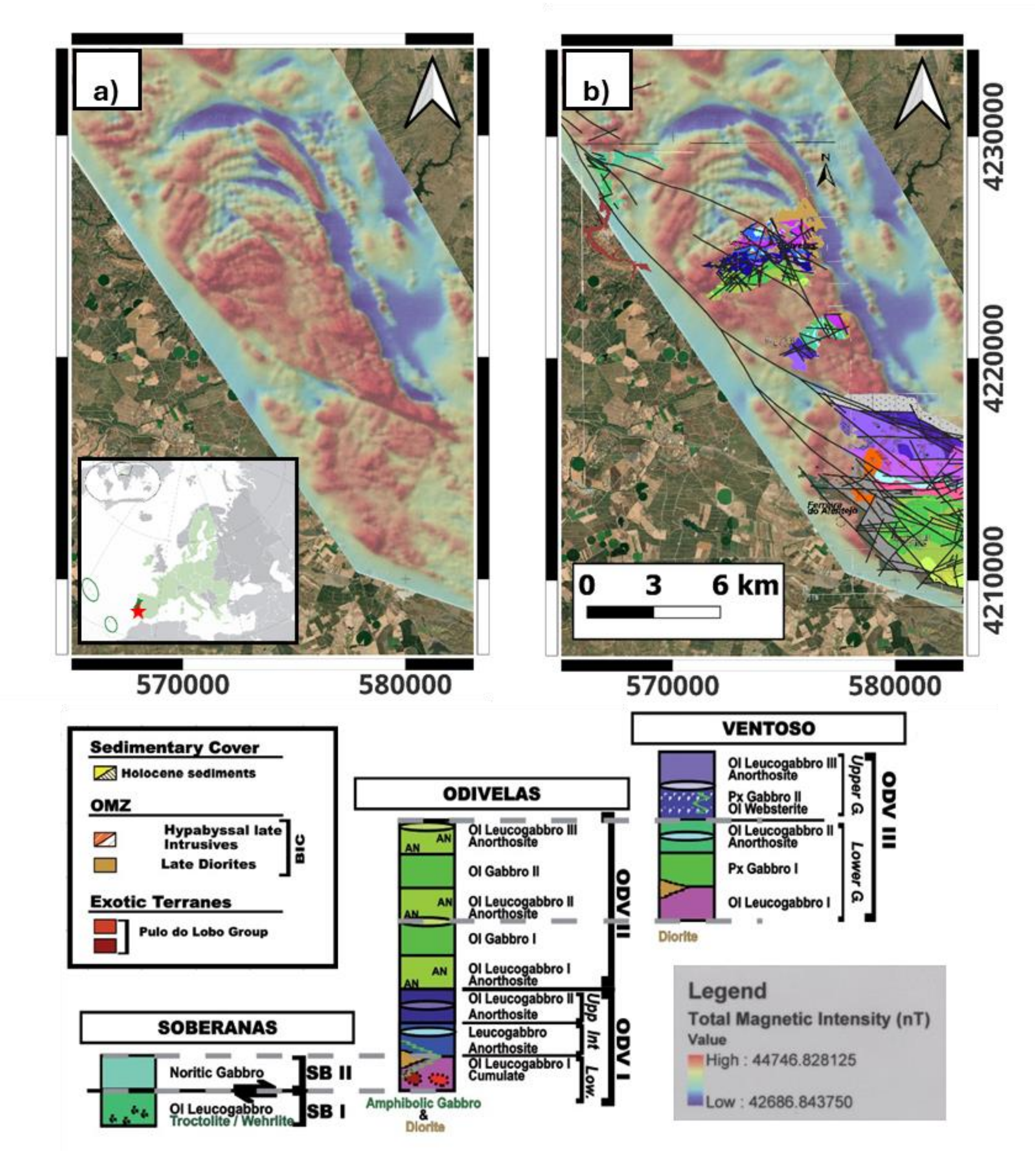

Figure 4.1. Aeromagnetic map of the project area acquired by the GTK in (a). Geological mapping, modified from Jesus et al. 2011 and its relative legend, in (b). These information represent the main ancillary information before this work. In the geologiacl map the cover is hided and is in correspondence of the non-mapped domains.

In terms of physical properties, the Fe-Ti-V oxides show a magnetic response given the large distribution of magnetite among the oxides within the gabbro. Electrically, the gabbroic host rocks are generally very resistive (1000-10000 Ω·m). Although the oxides are also very resistive, when heavily disseminated ore in the rock such as in Odivelas, they can yield a moderate conductive response (between 50 and 150 Ω·m). The oxides can provide a strong chargeable response when rich in ilmenite (Wynn et al., 1985, 1986 and 1988; Lèvy et al., 2019) and more moderate or absent when richer in magnetite. Ilmenite is present as single/mixed crystals in the oxide ores and surrounding gabbros with magnetite /ilmenite ratios between 0.5-6; in the gabbros ilmenite further occurs as exsolution lamellae within magnetite host crystals. These properties make the Induced Polarization method the appropriate technique to detect this mineralization style. The area offers several challenges, however. Field accessibility is often difficult due to the extensive ultra-intensive style agriculture (almonds and olives trees). Furthermore, despite extensively geological mapping and geochemical data acquisition based on surface data, geological knowledge of the mineral system at depth is chiefly absent due to the lack of drilling. These aspects complicated the choice of a site to deploy the localized DCIP survey and strengthen the need of an airborne survey to have a large-scale overview of the mineral system at depth. In the early 2000s an aeromagnetic survey has been flown by the Geological Survey of Finland in the scope of a regional mineral exploration survey covering also the area of interest. The retrieved total magnetic intensity map is shown in *figure 4.1a*. In the light of these constraints, the airborne EM survey here reported has been flown to map the ground resistivity and chargeability at depth and to define the area of interest where to follow-up on the ground.

4.3: Airborne EM feasibility study and survey acquisition

A synthetic feasibility study was done to assess the AEM sensitivity to the physical response of the oxides, and to optimize the system configuration to their detection. This has been carried for different geological configurations and system geometries. The available system for the survey and tests was the well-known HeliTEM[2] system (Smiarowski et al., 2018; *table 1.1* of this thesis for details) developed by XCalibur Smart Mapping.

The feasibility study was done computing a number of 1D forward responses using the EEMverter modelling and inversion algorithm (Fiandaca et al., 2024) presented in *section 1.2.3.5*, varying the parametrization of a synthetic three layers model to simulate the AEM response at different target characteristics. The ground is described as a layered earth and it is parametrized using the Maximum Phase Angle (MPA) re-parametrization of the Cole and Cole-Pelton model (Pelton et al., 1978), as proposed by Fiandaca et al. (2018). The ground is thus described with four parameters, $\{\rho,\varphi,\tau_\varphi,C\}$, where ρ is the ground resistivity (Ω·m), φ is the maximum phase between the real and imaginary part of the complex resistivity -representing the ground chargeability (expressed in mrad)-, τ_φ (s) is the time at which the maximum phase is reached and c is the frequency dependence.

The possible customization of the system were: the base frequency (25Hz, 12.5Hz and 6.25Hz), the transmitter number of turns (four or two) and the transmitter diameter. Given the resistive environment, a smaller dipole moment would significantly reduce the S/N and the option to use a smaller transmitter diameter has thus not been taken into account. In terms of IP records, lowering the EM base frequency expands the system bandwidth and favours the recording of slower decays of a polarizable body. At the same time, particularly for a resistive environment, a lower base frequency can decrease the S/N and does not improve the information content of the recorded data. Differently, reducing the number of turns in the transmitter reduces the coil self-inductance and allows a faster turn-off of the recorded signal improving the near-surface sensitivity of the data. The comparison among the recorded waveforms with a zoom at the turn-off after a zero-time shift are shown in *figure 4.2*. Both the waveforms and the zero-time values have been provided by the XCalibur company.

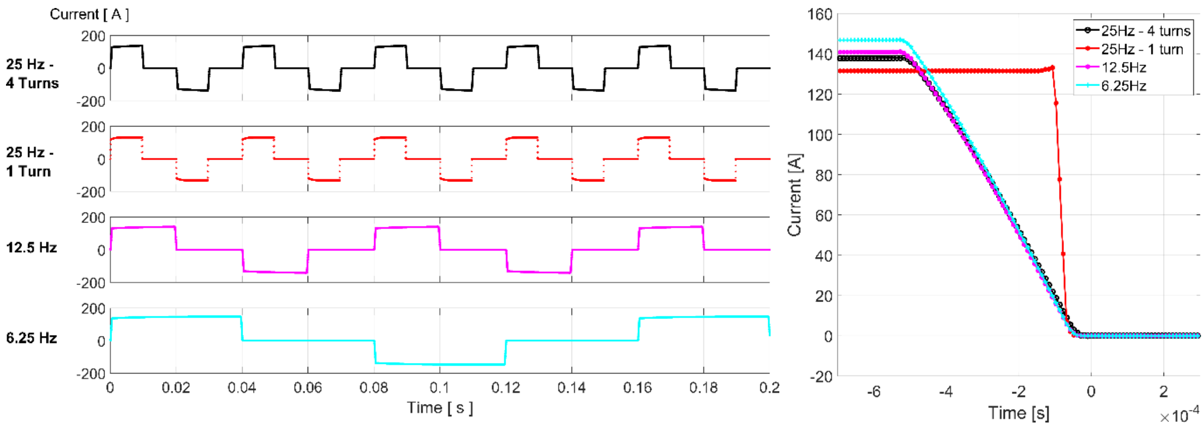

Figure 4.2. Waveforms comparison between different HeliTEM² configurations, (left). Turn-off comparison, on the right. The waveforms have been provided by the XCailbur company.

From *figure 4.2* the different waveforms for different base frequencies are shown. It is visible how the turn-off time significatively decreases reducing the number of turns in the transmitter coil. This goes from $5 \cdot 10^{-05}$ s to $1 \cdot 10^{-05}$ s reducing the temporal distance from the turn off, when the eddy currents start to form, to the first recording time, improving thus the near surface resolution. These effects are also visible in the synthetic forward responses computed and shown in *figure 4.3* and *4.4*. Here, for each geological configuration, the forward responses for different base frequencies and different number of turns (for the 25 Hz system) have been computed. The noise level is shown with a continuous black line, and, in the decays, the negative voltages are indicated with a circle while the positive gates with a cross. For the experiments, the oxides have been parametrized as moderately conductive (150 Ω·m), chargeable (100 mrad) with a large polarization time for AEM (time constant of 0.01 s) and a thickness of 20 m. To define the best system configuration for their detection, the forward responses have been computed for geological settings and the spectral characteristics of the targets. Examples will follow in the next figures.

In *figure 4.3*, the forward responses variation at the increase of the depth of the oxide are shown for each system setup as indicated in the title of the figures. The oxides are parametrized with the values previously indicated and are located below a 50 Ω·m purely resistive layer, that describes the altered host rock, and above a very resistive layer that represents the bedrock.

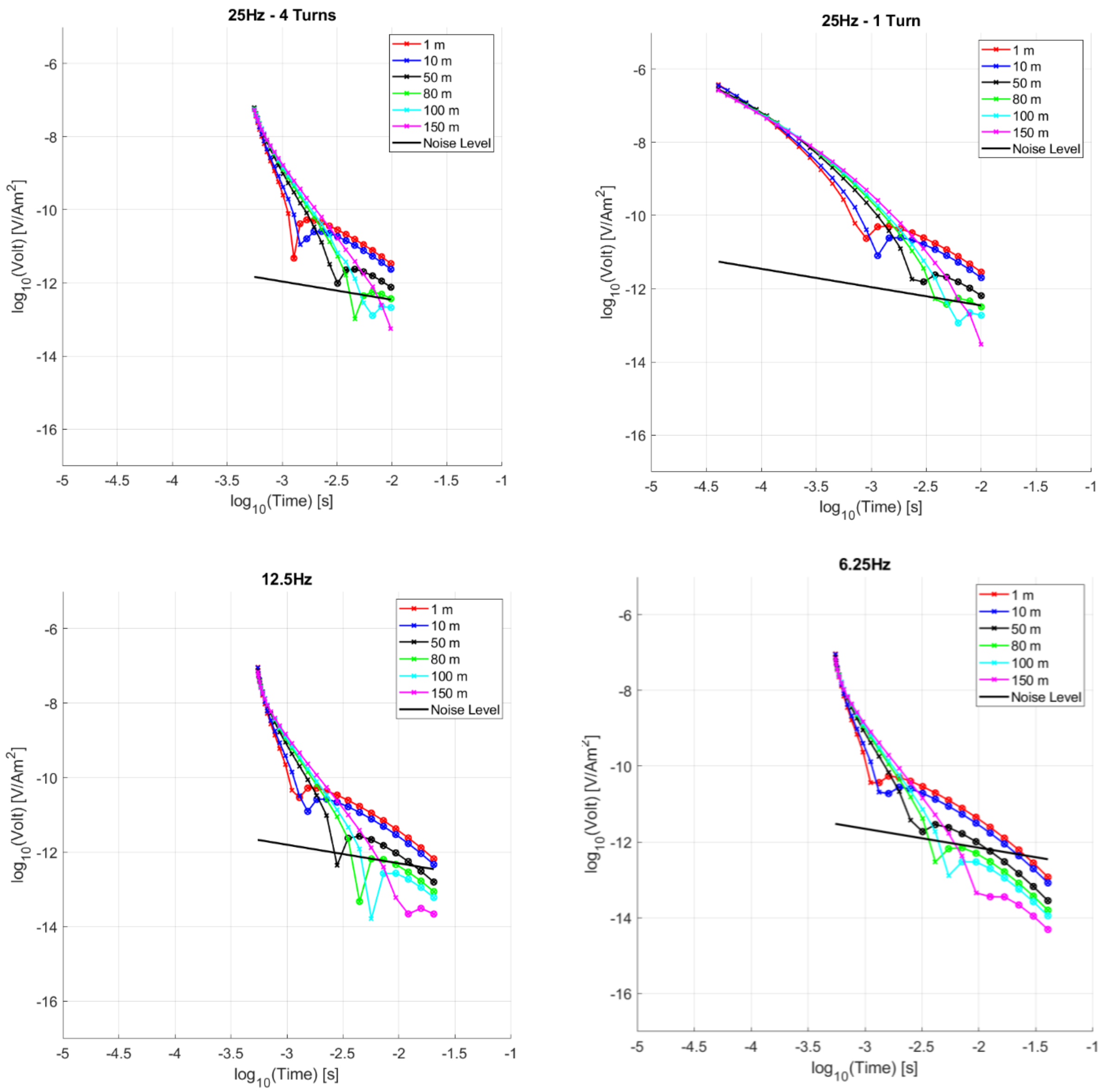

Figure 4.3. Forward model examples for different base frequencies varying the depth of the chargeable and resistive target. The negative voltages are indicated with circles while positives with a cross.

For the forward computation, the zero-times are set at the beginning of the ramp turn-off, i.e., when the eddy currents start to develop in the very near surface. Although the data providers often deliver datasets with a zero-time referred to the end of the turn-off ramp, I used this formalism to highlight the differences about near-surface resolution capabilities among different system configurations.

It is visible that the higher is the base frequency, the better is the S/N ratio of the computed forward responses. It is also evident how the variation in the depth of the target has a bigger effect on the early times of the 25Hz 1-turn configuration, indicating a higher early-time sensitivity for this configuration. In terms of negative voltages content, all the configurations can detect the effect of the chargeable oxide layer above the noise level, up to a depth of 80m. This occurs for all the systems except for the 6.25 Hz configuration for which the noise contaminates the data at 0.01 s. For this set of forward responses, the 12.5 Hz system allows also to measure negative voltages completely above the noise level for its entire off-time when the chargeable layer is shallow (1-10m). Similarly, for a chargeable layer at 50 m depth, the 12.5 Hz allows to measure negative responses at gates up to 0.1 s above the noise level, more than the other systems, showing a good compromise between negative voltages detection and S/N.

In terms chargeability detection, the absence of negative records in the dataspace does not exclude the presence of IP effects, as shown in synthetic studies (Viezzoli and Manca 2019). The negative voltages are produced by the polarized ground during its discharge, i.e., when the charges return to their steady state in absence of the external electric field. To measure the negative voltages two conditions are necessary: that this opposite-sign currents are stronger the purely EM currents that proceed downward, and that the ground discharges (and charges) within the recording time of the EM system. The ground charge and discharge time, that is described and parametrized in the Cole and Cole dispersive model (Pelton et al., 1978) by the time constant, strongly controls the possibility to record negative voltages in the EM data. If the peak of phase is reached within the EM bandwidth it is more probable to measure negative voltages in EM data. On the contrary, the IP effects cannot give negatives but strongly distort the recording, as also seen in the previous chapters. Non-negative IP effects which are more difficult to be recognized in the dataspace and make the inversion vulnerable to equivalencies during the modelling. A system configuration that favours the recording of negative voltages is thus preferred to detect chargeable bodies.

The effect of the variation of the time constant of the target for an oxide level at 80 m depth between an altered cover and a resistive bedrock is shown in *figure 4.4*. This set of forward responses is computed to verify if the data has sensitivity to the variation of the time constant parameter and which is the effect of its variation in the recorded data and in the negative content. From the figure it is evident how the AEM system has sensitivity to different time constants, showing a variation in the recorded by increasing the τ_φ of the chargeable layer. It is also clear how the system base frequency controls the possibility to better record larger time constants: a lower base frequency allows to record a slower ground polarization which produces opposite currents after a longer time. Given that the signal polarity -change time happens at the same time for each time constant among the various systems, the longer is the recording time (the larger is the bandwidth of the system) and the capacitor discharge happens within the measuring off-time. It is important to remark that the time constant is not the only parameter that controls the change of polarity of the EM data. Assuming an end-member scenario, in a highly resistive environment where the purely EM currents are weak and decay faster, the effect of the polarization currents produced is earlier visible in the off-time. In contrast, in a conductive environment, the purely EM currents contrast the change of polarity of the secondary magnetic field delaying the signal sign change (or the IP manifestation). In this sense, from the figures it is visible how a very short time constant does not produce any effect in terms of negative voltages in the forward response. For these bodies the polarization currents are too quick to overcome the purely EM currents and change the polarity of the secondary magnetic field even if the environment is quite resistive.

In general, although the effects of a higher time constants are better visible and solvable for a lower base frequency system, these effects are often below the noise level and thus not detectable.

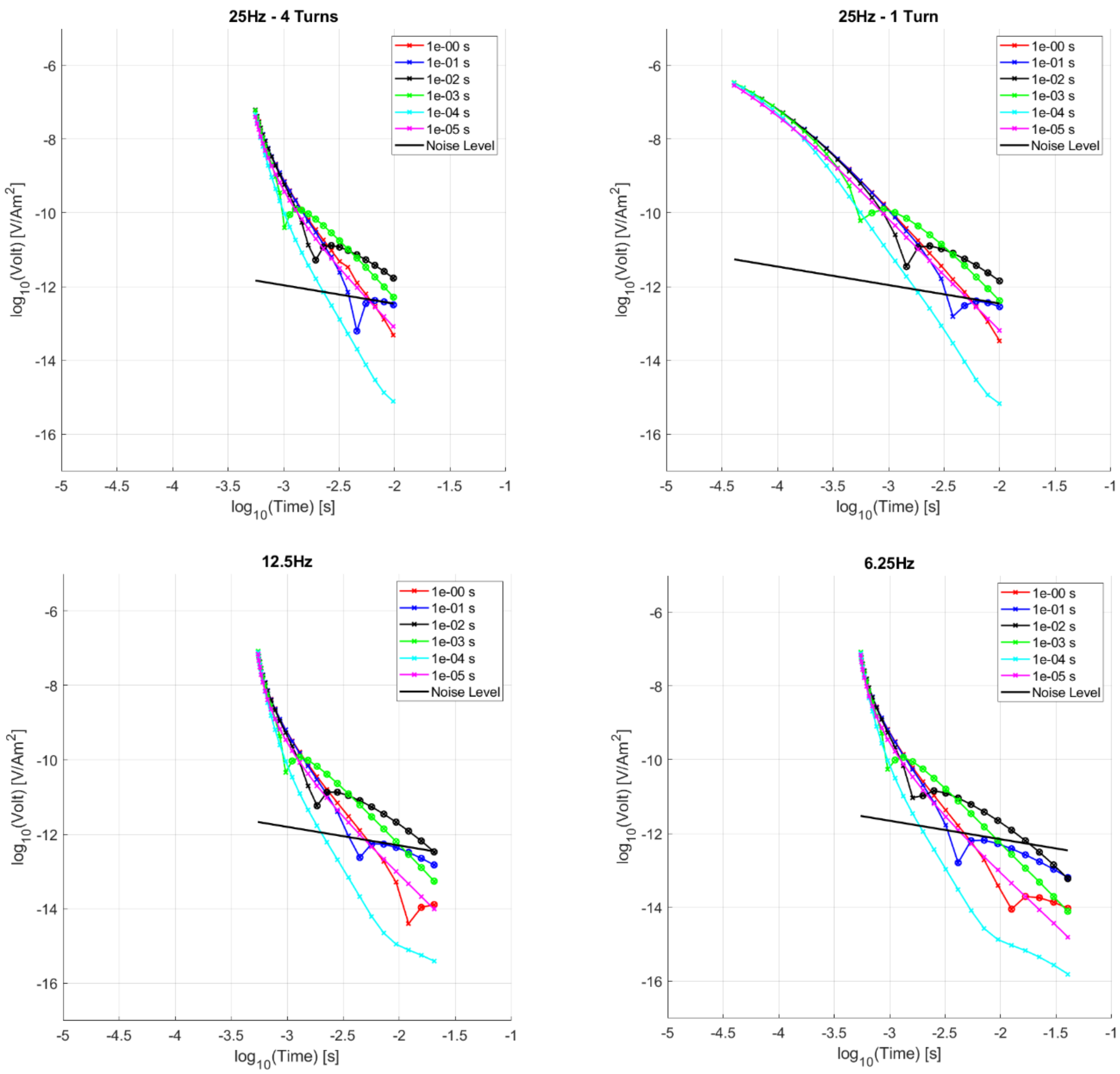

Figure 4.4. Forward models examples for different base frequencies varying the time constant of a chargeable target located at 80 m of depth. As in the previous figure, crosses represent positive voltages while circles negatives.

After the results of the feasibility, both the 12.5 Hz and the 25 Hz (with 1 turn in the transmitter loop) base frequencies have been chosen for the survey. As seen, a lower base frequency system guarantees an improved detection of the IP signature in the data having a theoretical larger spectral content that allows recording a higher number of negative data above the noise level. As mentioned, the negative recordings are not the only expression of IP effects in the AEM data but also help reducing the ambiguities during the modelling, being uniquely related to a polarizable ground. This system, in this geological framework, represents a good trade-off between a good S/N and the possibility in recording IP. On the other hand, the 25Hz base frequency with 1 transmitter turn, with its fast turn-off, allows to strongly improve the near-surface sensitivity and resolution better than any other system without worsen the S/N. The 12.5 Hz system was flown over a larger area, producing both infill lines spaced 200 m and regional lines spaced 1 km. The 25 Hz experimental configuration was flown over some of the 12.5 Hz lines, completely overlapping the infills and a portion of the regional survey. With these two surveys the ground imaging for both the chargeability and resistivity wanted to be improved and the IP response of a polarizable ground at different base frequencies systems wanted to be verified. The flight surveys are shown in *figure 4.5a* with the 12.5 Hz survey in black and the 25 Hz survey in white. In *figure 4.5b* and 4.*5c* the number of the remaining negative voltages after the manual processing of the recorded data are plotted, respectively for the 25 Hz and 12.5 Hz. Finally, in *figure 4.5d*, a detail over the infill area and the mapped geology is shown.

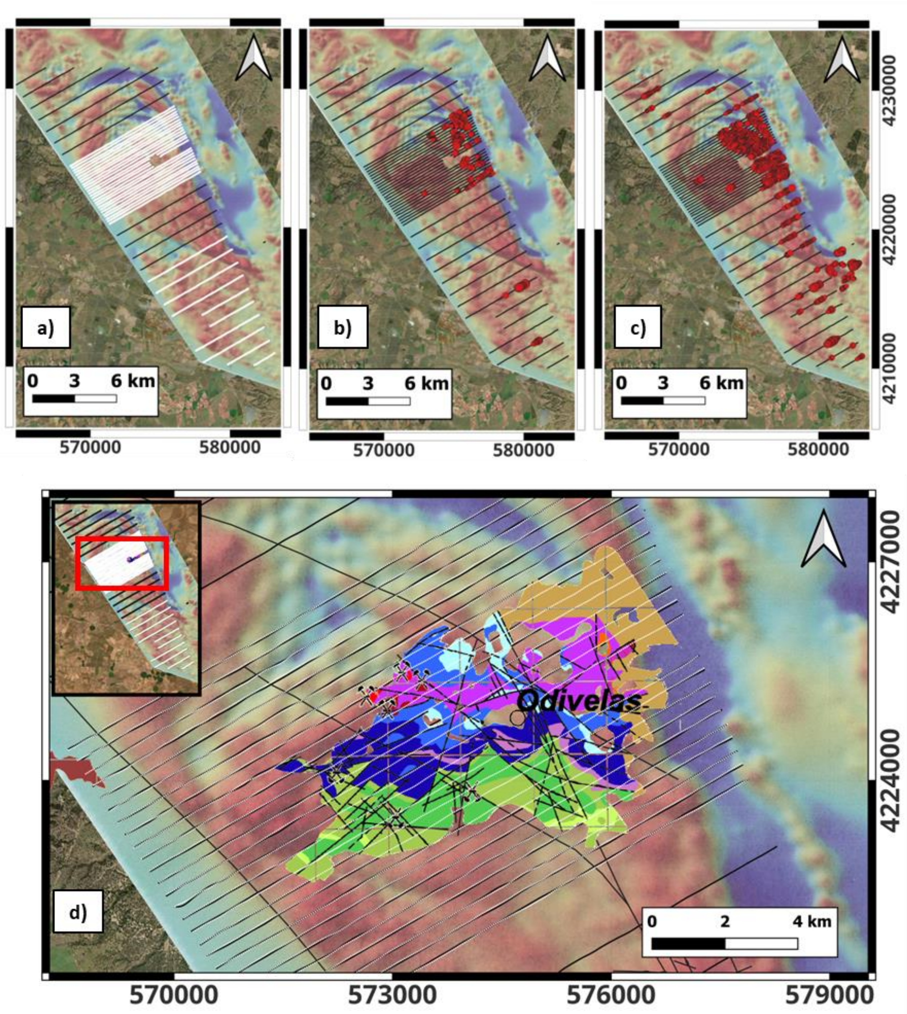

Figure 4.5. Flown surveys in the study area (a) and remaining recorded negative voltages after manual processing (b and c). In (a), the 12.5 Hz survey is displayed in black while the 25 Hz re-flown lines are shown in white. In (b) the number of negative voltages remaining after the manual processing is shown for the 25 Hz survey while in (c) for the 12.5 Hz. In (d) a detail over the mapped geology of the infill area is shown, for which both surveys have been acquired. The geological legend is the same as in figure 4.1.

As visible from *figure* 4.*5b* and 4.*5c*, the synthetic results of the feasibility study have been confirmed by the negative voltage content in the acquired data. The number of negative gates after the manual processing is higher both in terms of number and in lateral distribution respect than the 25 Hz. Also, a correlation between the aeromagnetic map in the background and the negatives distribution is also visible in the eastern portion of the infill area, in correspondence of the outcropping rocks of the bottom of the Odivelas (ODV I) sequence where the oxides are hosted.

4.4: Airborne EM independent modelling and joint inversion

4.4.1: Modelling approach

The acquired data have been modelled using the EEMverter inversion scheme (Fiandaca et al., 2024) illustrated in *section 1.2.3.5*, both independently and jointly, considering the IP effects. In terms of inversion architecture, the peculiarity of this scheme is in the use of separate and independent voxel meshes to compute the forward response and to map the model parameters during the inversion. The parameters are mapped at the vertex of the model mesh and are linked to the forward mesh through a distance-rescaled interpolation, as indicated by Fiandaca et al. (2024). The possibility to have independent meshes for the model parameters allows to have, potentially, one mesh for every model parameter and to use, for each, different regularization and lateral and vertical discretization. This gives flexibility to the inverse problem, allowing to adapt different strategies to solve the parameters during the inversion and increasing the control on the inversion process. This is particularly useful for AIP inversions, where the high number of parameters exposes the inverse problem to strong equivalencies; for these inversions, the regularization and model discretization are crucial to reduce the range of possible solutions to fit the data. It is possible to use multiple forward meshes for each dataset that contribute to the inversion, as for the previous work in *Chapter 3* and illustrated in *Chapter 1* (*section 1.2.3.5*). This solution simplifies the use of different datasets to resolve the same model-space and, thus, to perform joint or time-lapse inversions.

For the inductive data, a 1D modelling has been carried following the approach from Effersø et al. (1999) and illustrated in *section 1.2.3.5 – Forward computation*. This also includes the implementation of the effect of the transmitter waveform, transfer function and shape, and of the receiver filters and the time gates as in Sullivan et al. (2023). The model-space is parametrized using the MPA parametrization (Fiandaca et al., 2018), as done for the forward response computation in the feasibility study, for which the correlation between the parameters is intrinsically reduced, especially between the frequency dependence and the phase (i.e., the chargeability). After inversion, the depth of investigation is computed as in Fiandaca et al. (2015).

No variability in the magnetic susceptibility is modelled. The vacuum magnetic susceptibility (μ_0) value is used for computing the forward mapping as in Effersø et al. (1999). The neglection of susceptibility effects in the modelling is not fully justified in our field example, which show magnetic anomalies, but susceptibility modelling would introduce strong equivalences in the model-space that would prevent any inversion attempt. The magnetic susceptibility modelling in highly magnetic domains could represent a future starting point for research in EM modelling.

Regarding the model discretization, two different solutions have been adopted for independent and the joint inversion. For the first one, the chargeability and resistivity have been modelled in a 2D mesh defined along the survey flight line. For the joint inversion, the resistivity and chargeability mesh are structured with 3D cells regularly spaced (40 m) along the X and Y direction. This approach was selected to facilitate the joint inversion, considering the imperfect overlap between the two surveys and to obtain a continuous model for the area. Vertically, the two models are consistently discretised with an 18 layers configuration from surface to 400 m of depth. For both the independent and joint inversions, the spectral parameters (τ_φ and C) are mapped in a 2D mesh defined along X and Y with no vertical layers. This approach, also proposed in *Chapter 3*, has been adopted to reduce the equivalencies and to improve the chargeability mapping at depth.

Regarding the starting model, the same has been adopted for all the inversions. These are parametrized with a homogenous model with 50 Ω·m resistivity, 15 mrad phase, 1 ms time constant and 0.5 of frequency dependence.

Before inversion, the acquired data have been manually processed using the EEMstudio plugin (Sullivan et al., 2024) which allow to display the EM transient and to manually remove the noise-related outliers. In this area, the surveys have been designed to avoid the flight over infrastructures that could introduce EM coupling with recordings (e.g., powerlines or pipelines). At each time gate a 5% of uniform error is assigned together with a noise floor of 10^{-12} V/Am^2 for 12.5 Hz data and 10^{-11} V/Am^2 for the 25 Hz data. An example of data stripe for these datasets is visible in *figure 1.19* of *Chapter 1*.

4.4.2: Modelling results

The results of the modelling of the AEM data considering the IP effects for both for the 12.5Hz and 25Hz independent inversions and the joint inversion are shown in the next figures (4.*6* and 4.*7*) for different depth slices.

In *figure 4.6*, a depth slice comparison between the resistivity and chargeability models is shown for a depth of 30 m; as visible, the three inversions show a consistency among them for both the parameters and with an improvement in detail in the joint model. This latter is given by the merge of the sensitivities of the two systems, with the good near surface resolution of the 25 Hz and the larger bandwidth of the 12.5 Hz that improves the IP recognition and its modelling. This joint model fits both the dataset (as visible in *figure 4.8*) within the same inversion scheme and producing a unique model that satisfies both the datasets and bandwidths.

A comparison the independent inversions shows that the 25 Hz model has an improved lateral near surface resolution over the 12.5 Hz, which is consistent with the pre-flight feasibility studies. In the 25 Hz, the resistivity contrasts are sharper (this is better visible in the infill area), with more defined resistive and conductive domains respect with the 12.5 Hz. This is particularly clear in the central portion of the infill, where some small wavelength conductive anomalies within the resistive body are better resolved in the 25 Hz than in the 12.5 Hz model. The improvement in the resolution of the 25 Hz system is also evident by the wider range of retrieved resistivities, for which the conductive and resistive bodies are generally stronger than in the 12.5 Hz model. Differently, the chargeability contrasts are sharper in the 12.5 Hz model: smaller-scale chargeable and non-chargeable domains are resolved where the 25 Hz model tends to retrieve a more homogenous model. This behaviour is also consistent with the results of the feasibility study. The joint inversion produces a merged model with the lateral resolution of the 25 Hz in the resistivity and of the 12.5 Hz in the chargeability.

The near-surface slice (*figure 4.6*) also displays a remarkable correlation between the chargeability lateral distribution and the magnetic map in the background. This correlation looks mostly controlled by the magnetic gabbroic body than by the cenozoic cover that, as visible in the western and southern portion of the infill, is very conductive but less (or very weakly) chargeable than the magnetic domain. This anti-correlation between the conductive and the chargeable domains is given by the stronger EM currents that develop in the thick (given that it is visible also in the deeper resistivity slice of *figure 4.7*) conductive body which dominate the IP currents. The contact between the conductive and the chargeable bodies likely traces a major tectonic boundary concealed underneath the Cenozoic cover. As seen in *figure 4.5d*, this corresponds to a major regional fault separating the Beja Layered Gabbroic intrusion and the South Portuguese Zone that is, in this section, mostly composed by slaty lithologies and terrigenous series (Onèzime et al., 2002). Another interesting correlation is also between the 80-200 Ω·m resistivity and the high chargeability lateral distribution. These are consistent where the oxide-rich lithologies (ODV I Series) are mapped and are uncoupled in the very resistive domain, where the oxide-devoid ODV II Series is in magmatic stratigraphic contact with the ODV I Series trough the regional SW dipping layering.

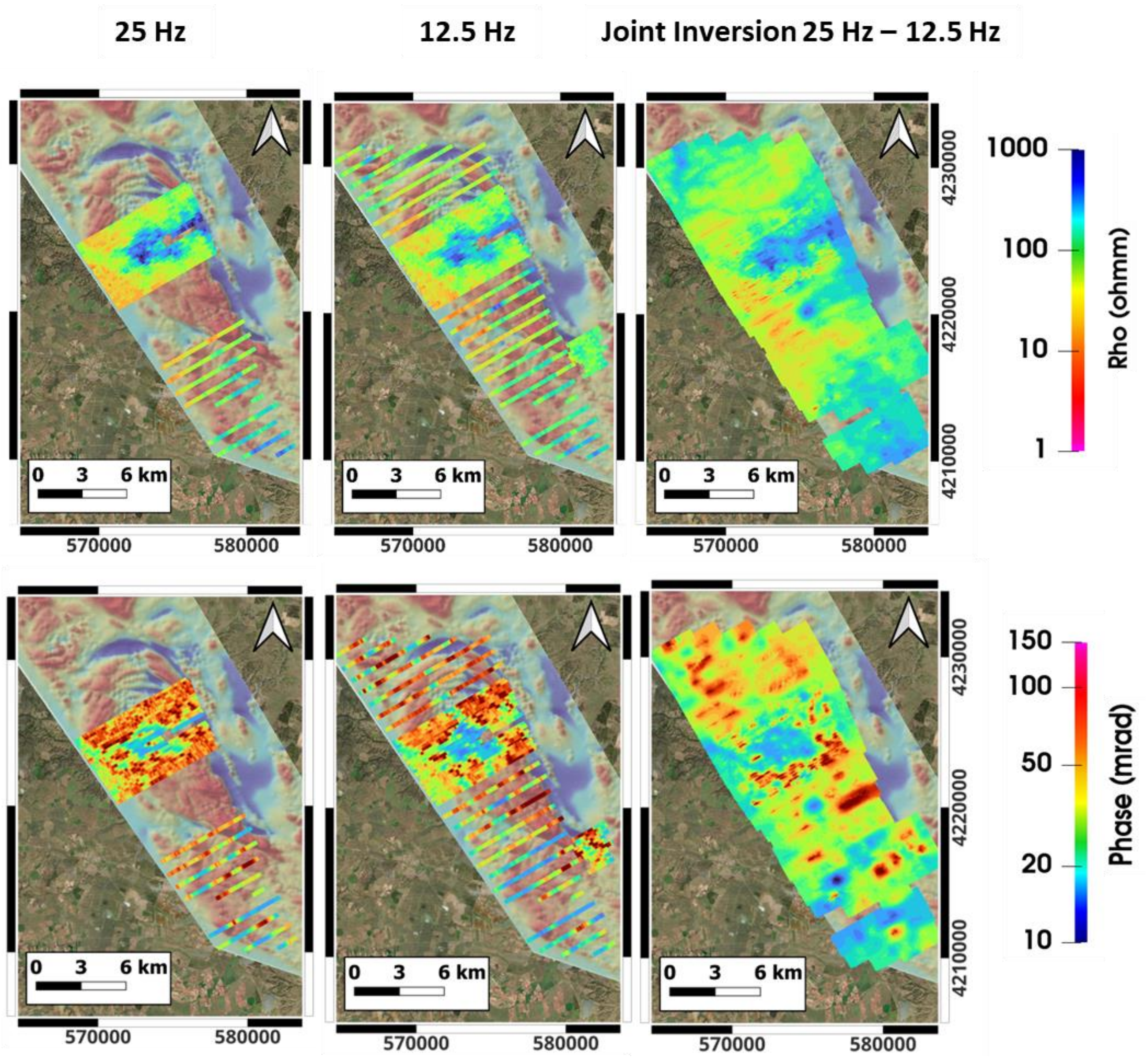

Figure 4.6. Resistivity (top) and chargeability (bottom) models for independent and joint inversion of 25 Hz and 12.5 Hz datasets. The model is relative to a slice at 30 m of depth.

In *figure 4.7*, a comparison among inversions for a deeper layer (110 m) is shown. As in the previous comparison, the lateral distribution of both the resistivity and chargeability models are consistent between the different inversions, the geology and the aeromagnetic map. For this comparison the correlation between the magnetic domains related with the oxides and the chargeability distribution is more striking. This is particularly visible in the infill block, with the resistivity of the model that decreases and uncouples with the chargeability distribution that, at the same time, correlates with the Total Magnetic Intensity (TMI). Even here the chargeability distribution shows more detail in the 12.5 Hz model, better defining lateral contrasts in the mapping and highlighting high-chargeability zones. The same considerations can be extended to the 25 Hz resistivity model if compared with the 12.5 Hz model that shows a reduced range of values and a smaller lateral resolution for the parameter. In the comparison at this depth, the chargeability model retrieved by the joint inversion shows a different magnitude and distribution of the chargeable features if compared with the independents. Although the lateral distribution of the chargeability is consistent among the slices, in the joint result the high-chargeability area is particularly highlighted by a strong phase contrast with the surrounding bodies. This is remarkable in the infill block, where the interpolation done by the inversion is smaller and the higher resolution is given by a denser distribution of data. This strongly conductive body is in correspondence of a magnetic and resistive domain of about 200 Ω·m and in geological proximity with the ODVI series, the bottom of the LGS sequence that hosts the oxides with a higher concentration.

Although the chargeable bodies are better defined both in magnitude and in lateral resolution in the joint inversion model, it is also visible from *figure 4.6* how in both the 12.5 Hz and 25 Hz independent inversions the same structures are mapped at different depths. This results, that will be treated more in detail in the comparisons with the ground DCIP, suggests that even if IP effects detection in inductive measurements is improved reducing the base frequency of the system, a higher base frequency does not make the system not sensitive to IP effects. With a higher base frequency, the negative voltages detection that simplifies the IP dataspace recognition and inversion is worsened but, at the same time, the IP and the EM bandwidth can overlap. This overlap can happen with different ratios between the amplitudes of IP and EM spectra making the IP effects recognizable. If the peak of the chargeability spectra happens at low frequencies (high time constants), the overlap between the EM and IP will be smaller. This does not mean that the EM data are not sensitive to IP but makes the inversion process more complex: the number parameters to describe the physics of induced polarization is high and the EM bandwidth is smaller, increasing the possibilities to lose the IP effects in equivalencies during modelling. At the same time the capacitive effects are into the data and failing to model them can creates artifacts. A modelling approach oriented to a model-space reduction can help in this sense, to extract the IP effects even when subtle in the EM spectral content. In this sense, the joint inversion contributes to the equivalency reduction, merging the spectral contents and expanding the bandwidth of the data both. The results of the mapping from the joint inversion are in this sense improved, with the equivalencies more constrained respect the independent inversions and with thus a sensitivity enhanced to subtler IP contents.

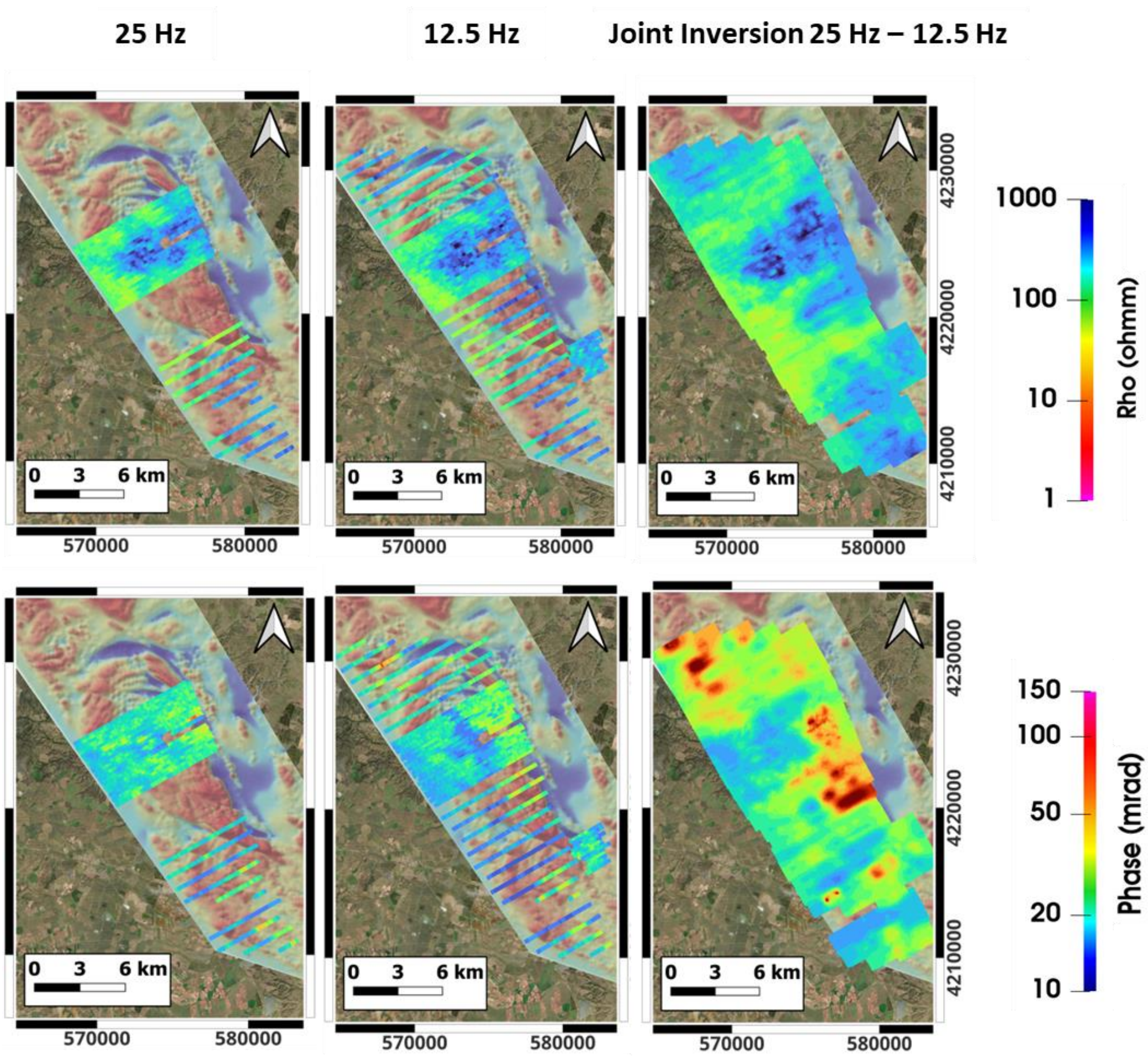

Figure 4.7. Resistivity (top) and chargeability (bottom) models of 25 Hz, 12.5 Hz and joint model for a slice at 110 m depth.

The inversion misfit is shown in *figure 4.8.* where both the inversions, independent and joint, show a good fit for both the datasets. The fit worsens for the joint inversion, going from less than 1 on average to around 2 i.e., remaining acceptable. The misfit increment is explainable given the differences between the two datasets. Although they have been flown over the same area, they have not been acquired simultaneously, and a different frame position can intrinsically introduce inconsistency between the two datasets.

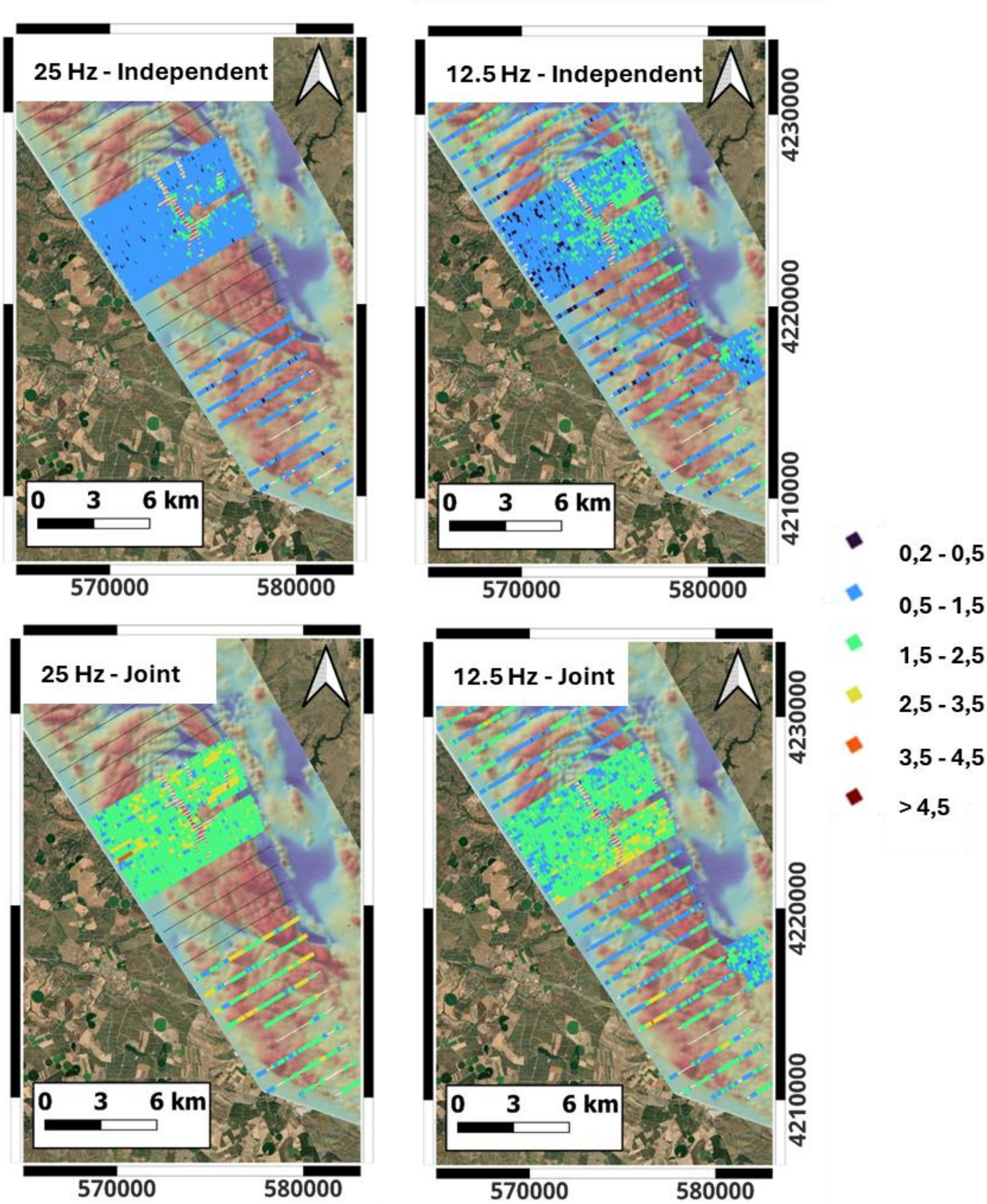

Figure 4.8. Joint inversion misfits of independent (top) and joint inversions (bottom) for both 12.5 Hz and 25 Hz surveys.

The ground DICP follow-up was designed based on these results and considering additional constraints such as geological information, the aeromagnetic TMI map, the field accessibility and the resistivity and chargeability models obtained both from the independent and joint inversions. Within the area with the infills, the domain with the stronger chargeability anomaly was chosen as of potential interest for a ground follow-up. Two DCIP profiles were acquired overlapping, as much as possible, the AEM flight lines as shown in *figure 4.9*. The objective was to demonstrate the airborne chargeability mapping via a ground DCIP truthing and, from the exploration point of view, to test the use of the AIP as a reliable source of information to drive the exploration decisions.

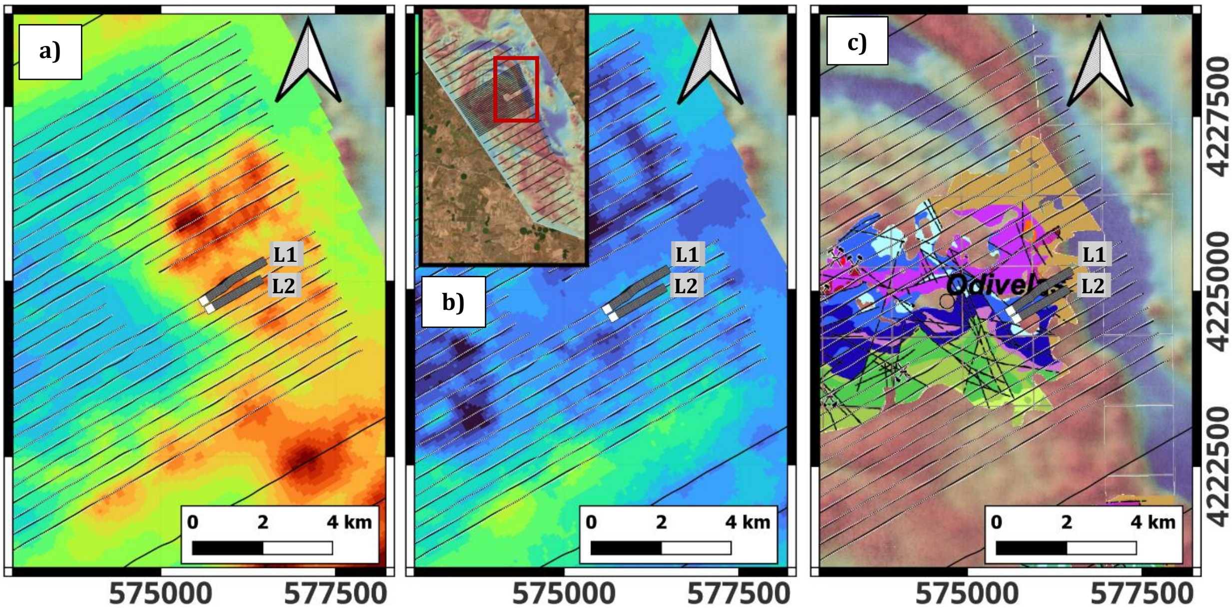

Figure 4.9. Ground DCIP lines, indicated as L1 and L2, over a zoom on the airborne chargeability (a), resistivity (b) and geology (c) of the infill area. The colorscales of (a) and (b) are the same as in figure 4.6.

4.5: Ground follow-up independent modelling and joint inversion

4.5.1: DCIP survey design

The ground DCIP follow-up has been done in July 2024 for a total of 2 km with 10 m electrode spacing and acquired using a multiple gradient sequence with an ABEM Terrameter LS2 instrument. A 100% duty cycle configuration was used for the current injection. In the first and last current pulse, the time in which the current is delivered is the sum of the acquisition time and the resistivity integration; for the survey 4.1 s plus 4.1 s for a total of 8.2 s was used, respectively. In terms of stacking, a stacking 2 made of 5 pulses (positive, negative, positive, negative, positive) was used; the first and the last pulses with a current time of 8,2 s, while those in between have a current time of 12.3 s (made of acquisition delay plus two resistivity integration). Consequently, the full waveform was made of pulse length of 8.2 + 12.3 + 12.3 + 12.3 + 8.2 seconds. The three central stackings were used to compute the IP decay, with an acquisition time until 12.3 s. A minimum value of 20 mA, and a maximum of 200 mA were set for the current. The data were acquired as full waveform, with a sampling rate of 3750 Hz and processed using the approach proposed by Olsson et al. (2015).

4.5.2: DCIP processing and joint modelling approach

After the full-waveform processing, the DC data and the IP data have manually processed using the EEMstudio QGIS plugin (Sullivan et al., 2024) to remove the outliers from the IP decays and the DC apparent resistivities. The EEMstudio plugin allows to visualize the recorded IP decays and to remove, manually, the noisy time gates after a user inspection. After the data processing, the DCIP data have been modelled, as the inductive data, using the EEMverter algorithm illustrated of *Section 1.2.3.5*. At each IP window, a uniform noise of 10% is set, while 5% for the DC.

The DCIP modelling has been carried consistently with the inductive data, modelling the full voltage decay instead of the integral chargeability and modelling the transmitter waveform, receiver transfer function and gate integration following Fiandaca et al. (2012). The differences with the inductive modelling are related to the forward dimensionality, that is 2D for the DCIP data as proposed by Fiandaca et al. (2013), and in the model mesh description for the parameter mapping in the model-space. Here, given the larger spectral content and resolution of the IP decays (that are recorded for more than 3 decades of time), the mesh separation between the spectral parameters and the resistivity and phase is not adopted for the galvanic inversion.

The model-mesh has here been built as a regular 2D mesh along each DCIP line, with a lateral cell size of 10 m and vertically log-increasing from surface to 450 m of depth using 23 layers.

As for *Chapter 3*, the joint inversion has been carried modelling each DCIP profile with the overlapping soundings of the AEM datasets. This has been done solving both the resistivity and chargeability with a unique model. Differently from the previous joint inversion, the ground DCIP data are a larger number (~1370 quadrupoles) if compared with the AEM data (~60 soundings). This impacts the objective function: the unbalanced data distribution could let the DCIP data dominate the misfit computation driving the inversion towards a model which satisfies the galvanic data only. To overcome this, I run the galvanic-inductive joint inversion starting with an inversion cycle where only the joint AEM datasets have been used. Once reached the convergence using only the inductive datasets, the galvanic-inductive joint inversion starts from the inductive joint inversion model. This solution has been adopted to balance the inversion and reduce the tendency of the galvanic data to dominate the joint modelling, starting the complete joint inversion from an inductive-driven starting model.

4.5.3: Modelling results and discussion

The modelling results are shown in *figure 4.10* and *figure 4.11* with a line-by-line comparison of the DCIP profiles with the inductive independent and joint inversion. On the bottom, the joint inversions between the HeliTEM^2 12.5 Hz, 25Hz and ground DCIP data is also shown. This latter joint inversion has been done to unify the bandwidths of the galvanic and of the two inductive methods and merging the different sensitivities to solve the ground electrical properties. In detail, in *figure 4.10*, the independent inversion results of the inductive (*4.10a* and *4.10b* for 25 Hz and *4.10c* and *4.10d* for the 12.5 Hz) and galvanic data (*figure 4.10e* and *4.10f*) are shown together with the joint inversion of the two airborne EM survey (*figure 4.10g* and *4.10h*) over the DCIP profile and with the joint inversion of the AEM the DCIP data for the line 1 (*figure 4.10i*, *4.10l*).

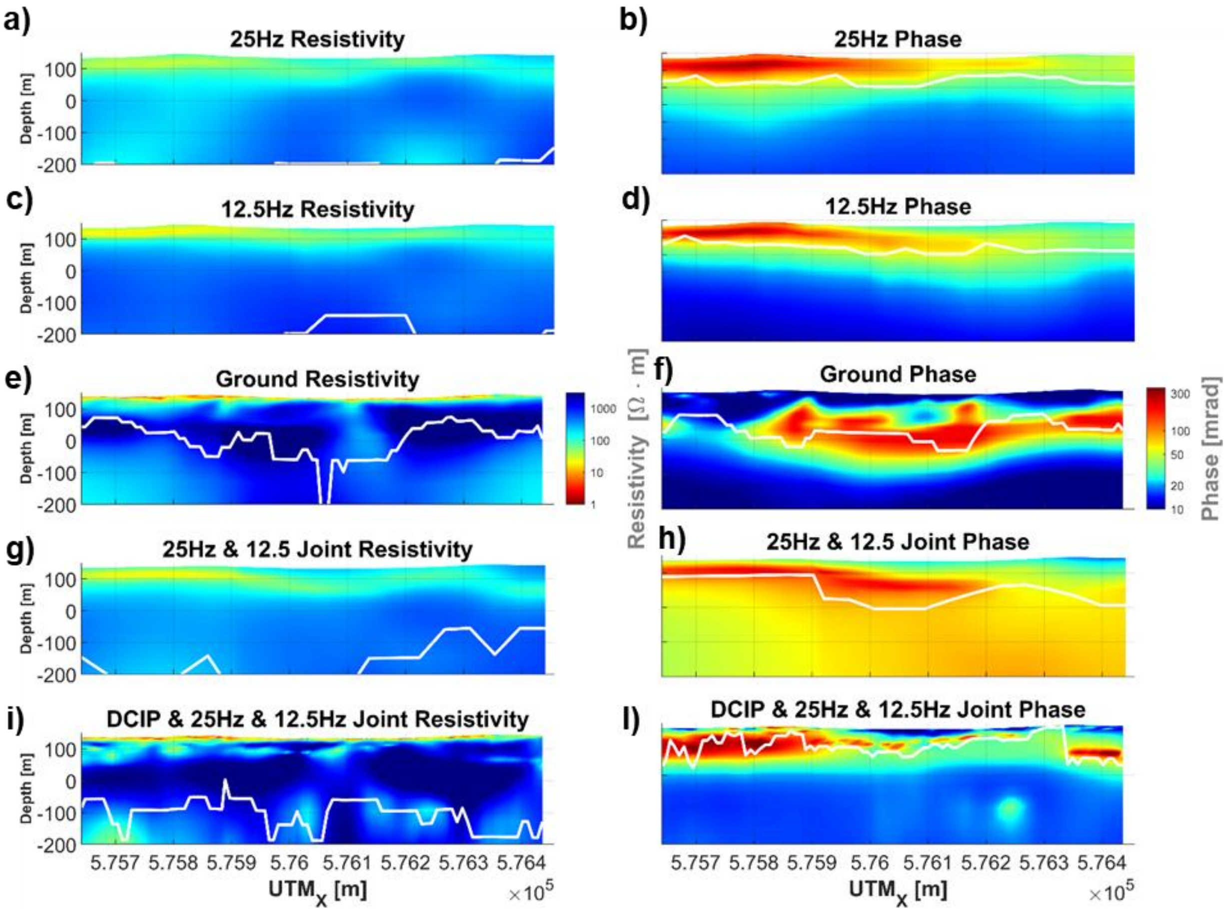

Figure 4.10. Inductive independent (a and b for the 25 Hz; c and d for the 12.5 Hz) and joint inversions (g and h) over the same line (L1) of the northern ground DCIP profile. The DCIP galvanic independent inversion (e and f) and the full joint inversion (i and l) between the galvanic and inductive methods is shown. The inversions are shown both for the resistivity (left column) and chargeability (right column).

The ground DCIP (*figure 4.10e*, *4.10f*) model confirms the presence of a chargeable and resistive body at depth, as indicated by the airborne mapping.

From figure it is also visible, as expectable, how the DCIP model (*4.10e* and *4.10f*) retrieves a chargeability with a higher lateral and vertical resolution in comparison with airborne chargeability models (*4.10a*, *4.10b*, *4.10c*, *4.10d*). The magnitude of the airborne chargeability is generally lower than the ground retrieved one and, particularly for the 25 Hz model (*4.10b*), also the spatial distribution of the mapped chargeability is different if compared with ground DCIP. For the 25 Hz model, the chargeability tends to maintain the chargeable layer largely in the near surface, giving a moderate chargeability contrast at depth, as also visible from the maps of *figure 4.7*. This can be consequence of the reduced spectral bandwidth of the higher frequency inductive method: this reduces the system's sensitivity to ground polarization, complicating the modelling and favouring potential equivalent solutions during inversion.

The 12.5 Hz (*4.10d*) method provides a more comparable chargeability model with DCIP. Although it maps a near-surface chargeable body in the westernmost portion of the section (also present in the 25 Hz model) that is absent in the DCIP model, the 12.5 Hz inversion tends to define a chargeable body around 100 m of depth (close to coordinate UTM_x $5.76 \cdot 10^5$ m). Considering the depth of investigation (DOI) of DCIP and airborne models, the chargeable body at depth is mapped in the same location by both methodologies (with different magnitude and resolutions).

An improved comparability with ground DCIP chargeability model is retrieved by the airborne inductive joint inversion (*figure 4.10g* and *4.10h*) of the two datasets. As for the independent inductive inversions, the resolution is much lower in the inductive models if compared with the ground DCIP but, differently, the magnitude of the two chargeability models is similar and the distribution at depth above the DOI is more comparable. In the inductive joint inversion (as well as in the global joint inversion between galvanic and inductive) the near surface chargeable body is maintained at the westernmost portion of the section. The improvement in the chargeability mapping of the joint EM inversion can be attributable to a reduction of equivalencies, with the model-space better constrained by the different sensitivities of the two EM base frequencies. As discussed in the previous section, the 25 Hz system has a fast turn-off that provides a high sensitivity to the near surface. The 12.5 Hz system, with a larger off-time, allows to record later time gates that expand the data spectral content and allow to better record negative voltages above the noise level.

Regarding the resistivity mapping, the ground DCIP model shows an improvement in the near surface resolution but with a good consistency with the airborne model, with a shallow conductive layer over a more resistive body.

The joint inversion between both the galvanic and the two inductive datasets is shown in the last line of *figure 4.10 (4.10i* and *4.10l*). Here, the bandwidths of the two methodologies are unified in the same inversion to resolve the ground electrical properties. The high frequency sensitivity of the inductive methods is merged with the low frequency sensitivity of the galvanic, producing a model that differs from the independent inversions both in the resistivity and chargeability. For this joint inversion, the chargeable body is mapped at depth with a spatial consistence with the ground DCIP and 12.5 Hz inversion, with the peaks of chargeability matching the maximum of phase of the inductive joint inversion. At near surface, the shallow chargeable body is mapped consistently with the 12.5 Hz and 25 Hz chargeability models. In comparison with the inductive joint inversion, the top of the deeper anomaly is consistently mapped. At depth, it maintains the same thickness obtained with the independent ground DCIP inversion. The shallow chargeable layer observed in the westernmost part of the inductive models and joint inversion is not present in the DCIP results.

From a geological standpoint, the section runs entirely on top of gabbroic rocks with the exception of the NE very last meters where a decrease in resistivity response and lack of chargeability may reflect the outcropping diorites, whose soils have lower clay contents. The uppermost conductive-chargeable layer visible in all AEM models marks the weathering, clay rich soils overlaying the gabbros but disappears from DCIP (joint) inversions. The latter show a well-defined conductive-chargeable anomaly that should correspond to (semi) massive oxide accumualtions that are sectioned by carbonate-bearing shear zones. For this interpretation the improvement in resolution provided by the joint inversion allowed to discriminate between the gabbroic alteration and the semi-massive oxides within the gabbro.

The same inversions were performed for line 2 obtaining analogous results. This is shown in *figure 4.11*.

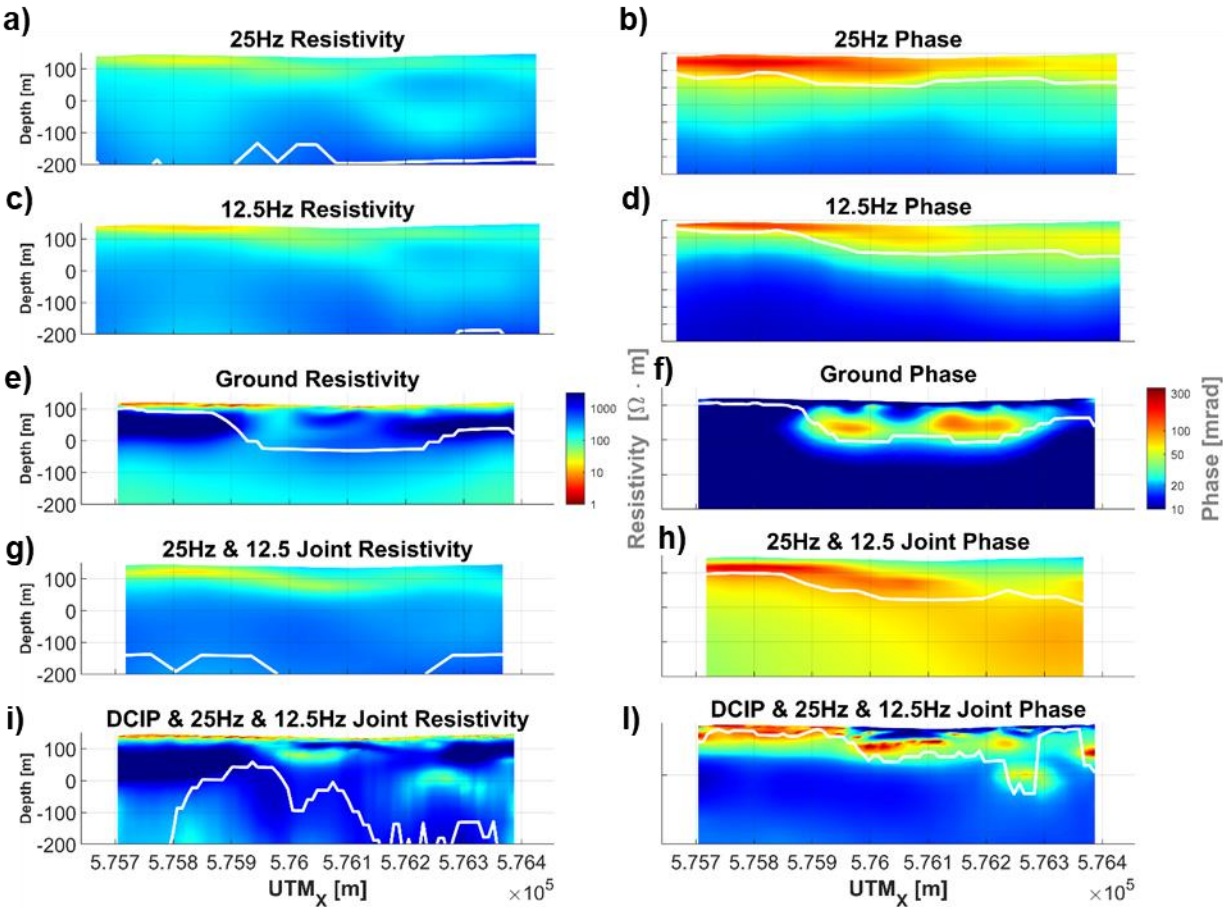

Figure 4.11. Inductive independent inversions for the 25 Hz (a and b, resistivity and chargeability, respectively) and 12.5 Hz (c, d). In 4.11e and 4.11f, the DCIP independent resistivity and chargeability model are shown. The joint inversions over the same line (L2) for the two AEM dataset is shown in figure (g and h). At bottom, (i) and (l), the joint inversion of the AEM datasets with the DCIP is shown.

As for the previous line, the ground DCIP (*figure 4.11e* and *4.11f*) model confirms the presence of a chargeable body at depth and, also for this line, it shows differences with the independent EM inversions (*figure 4.11a, 4.11b* for the 25Hz and *figure 4.11c* and *4.11d* for the 12.5 Hz). The independent inductive chargeability models define a shallow near-surface layer in the westernmost portion of the survey, differently with DCIP model, together with a weak chargeable layer at depth in the 12.5 Hz while absent in the 25 Hz. The inductive joint inversion marks a stronger chargeability contrast at depth in correspondence of the DCIP anomalies with a much lower resolution. For this latter inductive model, the magnitude of the chargeability contrast is more similar with DCIP. For this line, the near-surface chargeability inductive layer is defined where the DCIP data has been removed for the presence of an infrastructure. The galvanic – inductive joint inversion shows similarities with both the methodologies, defining a structure which merges the sensitivities of the two methods and the independent models.

The difference in chargeability mapping between airborne and ground methods arises from the narrower spectral bandwidth inherent to inductive techniques. These methods have reduced sensitivity at low frequencies, which can be partially mitigated during survey planning—by lowering base frequencies—or during data modelling, through constraints on spectral parameters and optimized inversion strategies, as explored in this study. Nonetheless, the potential for improving AIP modelling remains fundamentally constrained by the limitations of both instrumentation and methodology. When a detailed comparison between airborne and ground chargeability mapping is carried, as in this case, the effects of the lack of sensitivity of the EM data are highlighted. For this comparison in particular, the difference in recording time between the two methods is significant. The EM data span approximately two decades of recording time, whereas the DCIP data extend across three decades. This broader temporal range substantially enhances the low-frequency content of the DCIP data, widening its spectral bandwidth and increasing its gap with AEM. The promising results obtained in *Chapter 3 (*as in *figure 3.6),* were achieved using datasets with similar off-time windows—thereby ensuring comparable spectral content. Moreover, the physical principles governing galvanic and inductive methodologies are inherently distinct, leading to differing sensitivities and spatial resolutions in subsurface imaging. Galvanic methods operate by directly injecting a controlled current into the ground through a electrodes, with the resulting voltage differences measured at discrete points using potential electrodes. This direct electrical contact enables strong coupling with the subsurface, making galvanic techniques particularly sensitive to lateral and vertical variations in electrical resistivity and chargeability, especially in the near-surface. They are highly effective at resolving compact resistive or conductive bodies, especially when these features are close to the electrode array. In contrast, inductive methods employ time-varying magnetic fields generated by transmitting coils to induce eddy currents in the subsurface. Due to the diffusive nature of electromagnetic propagation in conductive media, inductive techniques are governed by the diffusion equation rather than a wave equation. This results in a depth-dependent loss of resolution: sensitivity diminishes with depth and becomes increasingly biased toward conductive features, while resistive bodies tend to produce weaker responses. Additionally, the broad spatial footprint of EM fields leads to lower spatial resolution compared to galvanic methods, especially at shallow depths. These fundamental differences in physics not only influence data acquisition and processing strategies but also impose distinct limitations and advantages when interpreting subsurface features, introducing intrinsic differences. Follows that is also significative to consider the differences in data distribution between the two methods: given its large footprint, the AEM data is under-sampled before inversions to one sounding every 30 m while the DCIP data have been (for this study) acquired with 10 m of electrode distance. This aspect, together with the differences in bandwidths and with the intrinsic different physics of the methods, contributes to the inconsistency in the chargeability mapping between the two.

At the same time, considering this number of differences, with this airborne IP survey design and modelling approach a chargeable body at depth has been defined, compatible with the mineralization target, and confirmed, with grades of differences, by a DCIP ground follow-up survey.

Considering both ground follow-up profiles lines it emerges that the joint inversion between galvanic and inductive data shows a general difference in the resistivity and chargeability model when compared with the independent inversions The AEM and the joint inversions show a shallow chargeable anomaly on the west of the profile, completely not seen by both DCIP-only inversions. This apparent contradiction is explainable when looking at the spectral parameters of the inversions (see Figure 4.12), which show very low tau values on the west part of the section, making it impossible to image those features with only ground DCIP.

Geologically, the NE portion of the line (from coordinate UTM_X $5.761 \cdot 10^5$ m to UTM_X $5.764 \cdot 10^5$ m) showing less resistive and less chargeable features corresponds to the LGS marginal diorites and its contact with the more conductive gabbroic rocks; the 12.5 – 25 Hz joint inversion suggests a gently dipping N contact between the gabbros and diorites. Some deeper (0 m) features beneath the diorite may correspond to oxide-rich gabbro that are preserved beneath the diorite. The thin conductive layer in the SW end overlaps the Cenozoic cover which here is thin and should bear very low water contents at the dry season when both air and ground data were acquired. This signal, particularly evident in 12.5 Hz independent inversion should therefore be enhanced by the weathering profile of the gabbro that comprises highly plastic montmorinolite rich clays which are able to retain structural water even in the dry season; this horizon appears as chargeable in airborne data but disappear in combined 12.5 – 25Hz joint inversions. This model enhances a strongly chargeable horizon which is best resolved by air-ground joint phase inversions. The SW dipping nature of these most conductive and chargeable horizons strongly suggests the presence of gabbros with heavily disseminated oxide conformable to the SW dipping layering; the intensity of the anomalies at places, such as the elliptical features in the DCIP data may correspond to semi-massive oxide concentrations. Close to the transition from Cenozoic to gabbro there are very important shear zones which include several meters of deformed and metassomatised gabbro and siliceous–carbonate hydrothermal precipitate infills. The galvanic-inductive joint inversion shows a clear imaging of these structures suggesting that they intersect and compartmentalize the conductive-resistitve oxide gabbros.

The time constant and frequency dependence of the ground DCIP for the joint galvanic-inductive are shown in *figure 4.12a* and *4.12b* respectively for line1 and line 2.

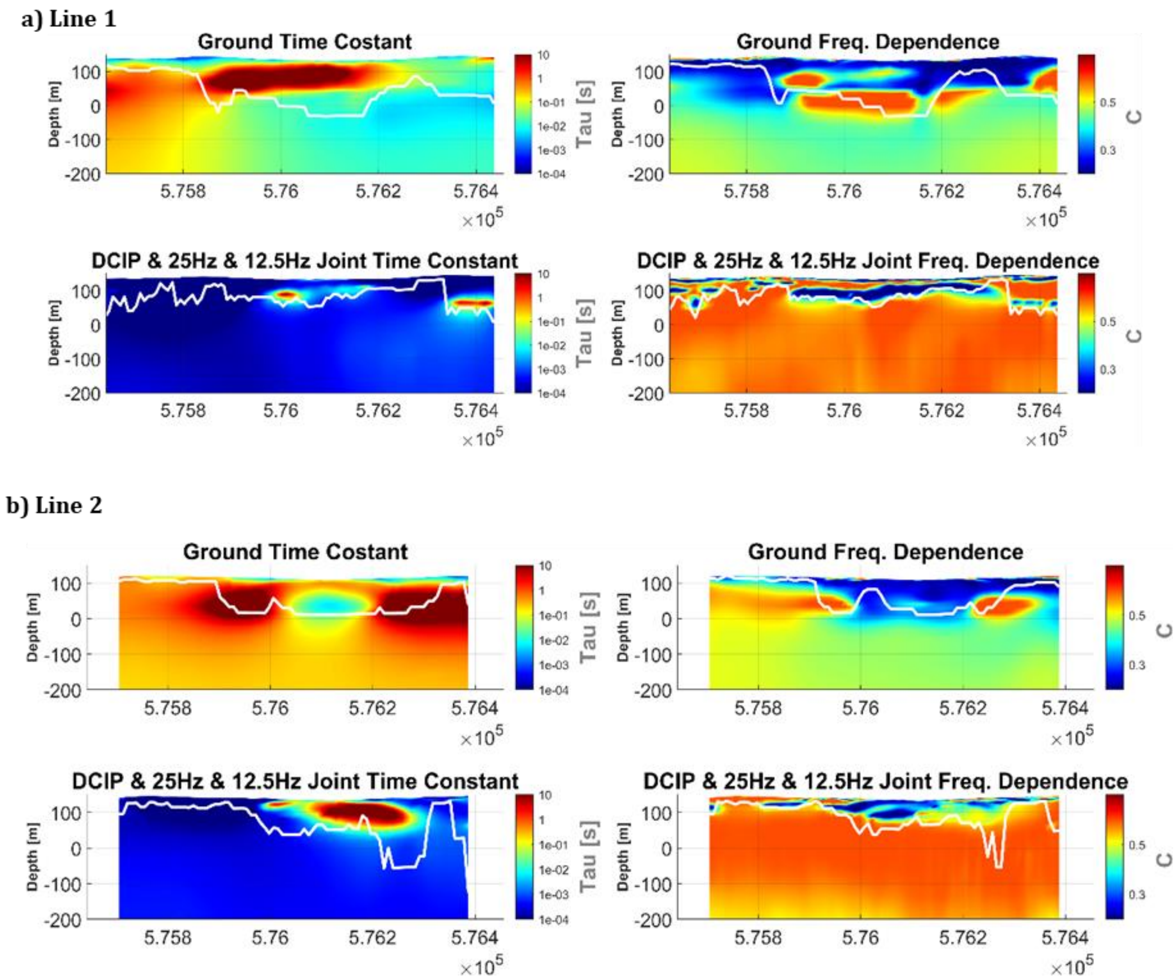

Figure 4.12. Time constant and frequency dependence comparison between ground independent inversion (on top of (a) and (b)) and the joint inversion (at bottom of the figures). In (a) the results for northern line (L1) are shown while in figure (b) for the southern line L2.

From *figure 4.12* it is visible how the time constant and frequency dependence highly change in comparison with the DCIP independent model to adapt the spectral content to fit the inductive datasets. Areas of lower values for the frequency dependence appear in the joint inversions, allowing to honour the spectral content of both galvanic and inductive data. At the same time the joint inversions show lower time constant, thanks to the contribution of inductive data in the imaging of the IP spectral content. Comparing the joint inversion models of spectral parameters with their relative chargeability models in figures *4.10l* and *4.11l*, it is visible how the frequency dependence controls the chargeability mapping. In fact, the chargeable anomalies in the joint inversion, as well as in the AEM-only inversion, extend to the west part of the profiles, where the time constant is low. On the contrary, the DCIP-only inversion is not able to map this shallow chargeable area.

These models are consequence of the use of a single-peak relaxation time to fit two datasets within a broad frequency range. A possible solution could be the use of multiple relaxation times to satisfy both the sensitivities at high and low frequencies.

The inversion misfits retrieved for the joint inversions are shown in *figure 4.13* and *4.14* for both the lines and for the inductive datasets with some examples of decay fit for galvanic measurements.

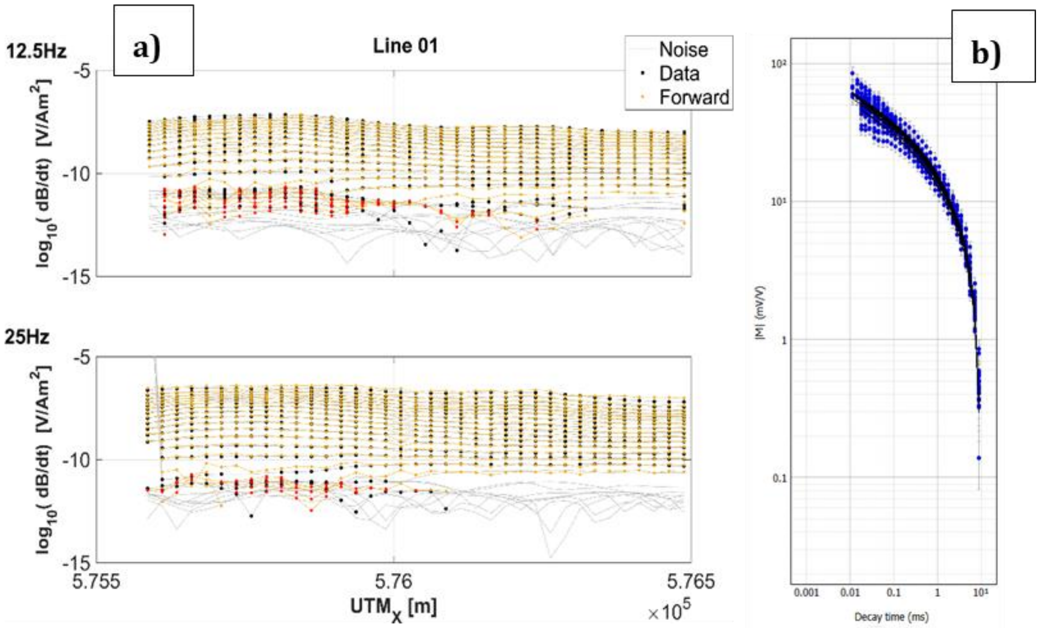

Figure 4.13. Retrieved data-fits for joint inversion between galvanic and inductive data at line 1. In (a) the data-fits for the inductive data are shown, while in figure (b) some examples of galvanic data fit over the airborne negative voltages are plotted. In black is represented the forward response while in blue the acquired data.

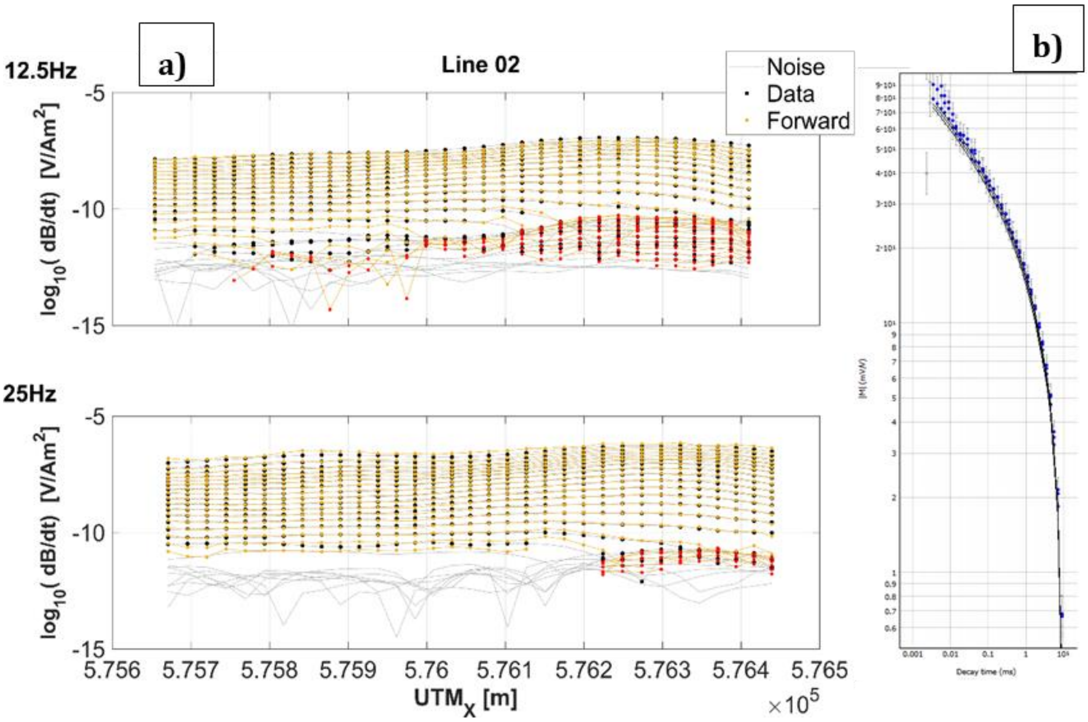

Figure 4.14. Retrieved data-fits for the joint inversion between galvanic and inductive data for line 2. In (a) the data-fits for the inductive data are shown, while in (b) some examples of galvanic data fit over the airborne negative voltages are shown.

For both the lines, a good data fit was obtained for both the galvanic and the inductive data, fitting both the negative voltages (in red in the figure) and the IP decays (acquired over 3 decades) recorded by ground DCIP data. The inductive fit is lower at the early times, where the sensitivity contrasts are higher and improves at late times. A good fit of galvanic data is reached in joint inversion over the negative voltages in inductive measurements. The ground DCIP global misfits are generally below 2 for both independent and joint inversions for the IP decays, with an error bar of the 10% of the recorded data. The consistency in the misfit values between the independent and joint inversion indicates how the data, both galvanic and inductive, accepts the joint inversion model reached by the unified spectral content modelling.

4.6: Conclusions

With this work two aspects of induced polarization effects in airborne EM data have been evaluated: the first one, for exploration purposes, two airborne EM surveys have been successfully designed, acquired and modelled to locate potential resistive and chargeable bodies for a greenfield exploration project. After this, a ground DCIP follow-up has been designed and acquired confirming the presence of the AIP defined resistive and chargeable anomalies. Second, from a phenomenological standpoint, the IP ground response has been studied through joint inversion of multiple AEM frequencies and DCIP data.

From a methodological standpoint, airborne IP technique has been used as a key geophysical tool to successfully define where to downscale the exploration. This has been carried for non-canonical resistive and chargeable targets, and in an area high logistical complexity to carry extensive ground DCIP measurements. To do this, the AIP survey has been optimized from survey design to modelling approach. This involved an initial feasibility study to define the airborne system characteristics to be flown, concluding to use two different system with two different base frequencies (12 Hz and 25 Hz with 1 turn), to improve both the data information content (improving near surface resolution and negative content, with 25 Hz and 12.5 Hz, respectively) and to understand the IP response at different EM base frequencies. The acquisition confirmed observations on synthetic data carried in the feasibility: the near surface resolution improves with the 25 Hz data and a higher content of negative recordings above the noise level is reached with the 12.5 Hz. The data have then been modelled independently and jointly, through a multi-mesh approach which uncouples the spectral parameters and reduces the equivalencies during inversion. This defined chargeable and resistive bodies in the survey area in both the datasets; then, these have been further modelled by the joint inversion of the two. The joint inversion provided a unique model with an improved near-surface resolution and a better-defined chargeability distribution, i.e., which merged the information content of the two datasets. The joint inversion helped in the definition of the ground follow-up area; this consisted in the acquisition of two DCIP profiles over a chargeable and resistive anomaly. These have been modelled following a consistent approach with inductive data, both independently and then jointly with the two inductive surveys. The independent ground DCIP show differences both in terms of resistivity and chargeability with the inductive models but confirmed the presence of the chargeable body at depth. This claim has been also confirmed by the results of the joint inversions between galvanic and inductive datasets, which converged to a model which merged the information of the independent inversions and unified the spectral content of the methodologies to the IP effects. As result, a chargeability model consistent with the other inversions is reached, given by an adaptation of the spectral parameters to the different methodological spectral contents. These results suggest how the EM method has a field of shared sensitivity with the DCIP method to the ground chargeability demonstrating how AEM can be a reliable tool for airborne chargeability mapping.

4.7: References

- Bhattacharyya, B. K., (1964), Magnetic anomalies due to prism-shaped bodies with arbitrary polarization: Geophysics, 29(4), 517–531, https://doi.org/10.1190/1.1439386
- Dauti, F., Viezzoli, A., Fiandaca, G., (2023), Joint Inversions of AEM modelling AIP effects: Helicopter-borne, Ground IP and Fixed-Wing systems. AEM2023 - 8th International Airborne Electromagnetics Workshop, 3-7 September 2023, Fitzroy Island, QLD, Australia.
- Davies L., Ley-Cooper A. Y., Sutton M., Drovandi C., (2023), Bayesian detectability of induced polarization in airborne electromagnetic data, Geophysical Journal International, Volume 235 (3), 2499–2523, https://doi.org/10.1093/gji/ggad073
- Dias, C. A., (1968), A non-grounded method for measuring induced electrical polarization and conductivity. Ph.D. Dissertation, Univ. of California, Berkley, USA.
- Effersø, F., Auken, E. and Ingvard Sørensen, K. (1999), Inversion of band-limited TEM responses. Geophysical Prospecting, 47: 551-564. https://doi.org/10.1046/j.1365-2478.1999.00135.x
- Fiandaca, G., Auken, E., Christiansen, A.V., Gazoty, A., (2012), Time-domain-induced polarization: Full-decay forward modelling and 1D laterally constrained inversion of Cole-Cole parameters, Geophysics 77: E213-E225. https://doi.org/10.1190/geo2011-0217.1
- Fiandaca, G., Christiansen, A., V., Auken, E., (2015), Depth of Investigation for Multi-parameters Inversions, European Association of Geoscientists and Engineers, Near Surface Geoscience 2015 - 21st European Meeting of Environmental and Engineering Geophysics, 2015, p.1 – 5, https://doi.org/10.3997/2214-4609.201413797
- Fiandaca, G., Madsen, L.M. and Maurya, P.K. (2018), Re-parameterisations of the Cole–Cole model for improved spectral inversion of induced polarization data. Near Surface Geophysics, 16: 385-399, https://doi.org/10.3997/1873-0604.2017065
- Fiandaca G., Chen J., Zhang B, (2024), EEMverter, a New Modelling Tool for Electric and Electromagnetic Data with Focus on Induced Polarization, European

Association of Geoscientists and Engineers, NSG 2024 30th European Meeting of Environmental and Engineering Geophysics, Sep 2024, Volume 2024, p.1 – 5, https://doi.org/10.3997/2214-4609.202420166.

- Flis, M.F., Newman, G.A., Hohmann, G.W., (1989), Induced-polarization effects in time-domain electromagnetic measurements, Geophysics, 54(4), 514-523, https://doi.org/10.1190/1.1442678
- Gloaguen R., Ghamisi P., Lorenz S., Kirsch M., Zimmermann R., Booysen R., (2018), The Need for Multi-Source, Multi-Scale Hyperspectral Imaging to Boost Non-Invasive Mineral Exploration, IGARSS 2018 - 2018 IEEE International Geoscience and Remote Sensing Symposium, Valencia, Spain, pp. 7430-7433, doi: 10.1109/IGARSS.2018.8518742.
- Onézime, J., J. Charvet, M. Faure, J.-L. Bourdier, and A. Chauvet, (2003), A new geodynamic interpretation for the South Portuguese Zone (SW Iberia) and the Iberian Pyrite Belt genesis, Tectonics, 22, 1027, doi:10.1029/2002TC001387, 4.
- Jesus A.P., Mateus A., Munhá J. M., Tassinari C., (2014), Internal architecture and Fe–Ti–V oxide ore genesis in a Variscan synorogenic layered mafic intrusion, the Beja Layered Gabbroic Sequence (Portugal), Lithos, 190–191, 111-136, ISSN 0024-4937, https://doi.org/10.1016/j.lithos.2013.12.001.
- Jesus, A. P., Mateus, A., Waerenborgh, J. C., Figueiras, J., Alves, L. C., and Oliveira, V. (2003), Hypogene titanian, vanadian maghemite in reworked oxide cumulates in the Beja Layered gabbro complex, Odivelas, southeastern Portugal. The Canadian Mineralogist, 41(5), 1105-1124, https://doi.org/10.2113/gscanmin.41.5.1105
- Kaminski, V., Viezzoli A., (2017), Modeling induced polarization effects in helicopter time-domain electromagnetic data: Field case studies, Geophysics, 82(2), B49-B61, https://doi.org/10.1190/geo2016-0103.1
- Lévy L., Maurya P. K., Byrdina S., Vandemeulebrouck J., Sigmundsson F., Árnason K., Ricci T., Deldicque D., Roger M., Gibert B., Labazuy P., (2019), Electrical resistivity tomography and time-domain induced polarization field investigations of geothermal areas at Krafla, Iceland: comparison to borehole and laboratory frequency-domain electrical observations, Geophysical Journal International, 218, (3), 1469–1489, https://doi.org/10.1093/gji/ggz240

- Macnae, J. (2016), Quantitative estimation of intrinsic polarization and superparamagnetic parameters from airborne electromagnetic data, Geophysics 81(6), E433-E446, https://doi.org/10.1190/geo2016-0110.1
- Onézime J., Charvet J., Faure M., Chauvet A., Panis D., (2002), Structural evolution of the southernmost segment of the West European Variscides: the South Portuguese Zone (SW Iberia), Journal of Structural Geology, 24 (3), 451-468, ISSN 0191-8141, https://doi.org/10.1016/S0191-8141(01)00079-7.
- Pelton W.H., Ward S.H., Hallof P.G., Sill W.R., Nelson P.H., (1978), Mineral discrimination and removal of inductive coupling with multifrequency IP, Geophysics, 1978, 43, 588-609, https://doi.org/10.1190/1.1440839
- Ruiz-Coupeau S., Jurgens B., Kesselring M., Herrero-Solana V., (2020), Sustainability in Mineral Exploration—Exploring Less Invasive Technologies via Patent Analysis, 12(22):9761. https://doi.org/10.3390/su12229761
- Silva, J.M., (1945), Notas sobre o jazigo de Ferro de Odivelas. Estudos, Notas e Trabalhos, Instituto Geológico e Mineiro Portugal, 1 286–292.
- Smiarowski A., Miles P., Konieczny G., (2018), CGG's New Helitem-C AEM Systems, ASEG Extended abstract, 2018:1, 1-4, DOI: 10.1071/ASEG2018abT7_3F
- Smith, R.S., and J. Klein, (1996), A special circumstance of airborne induced polarization measurements, Geophysics, 61(1), 66–73, https://doi.org/10.1190/1.1443957
- Sullivan N. A. L., Gisolo M., Spagnoli L., Rapiti A., Dauti F., Menghini A., Viezzoli A. and Fiandaca G., (2022), Airborne EM in northern Italy for sustainable and resilient management of groundwater resources, Nuovo Cimento, Year 2023 - Issue 3 - May-June SIF Congress 2022, Article 68, p.1–11
- Vakulchuk R., Overland I., Scholten D., (2020), Renewable energy and geopolitics: A review, Renewable and Sustainable Energy Reviews, Volume 122, 2020, 109547, ISSN 1364-0321, https://doi.org/10.1016/j.rser.2019.109547.
- Viezzoli, A., Fiandaca, G., Segio, S., Auken., E., (2013), Constrained inversion of IP parameters from Airborne EM data, ASEG-PESA Expanded abstracts, Melbourne, Australia.
- Viezzoli, A., & Manca, G. (2019), On airborne IP effects in standard AEM systems: tightening model space with data space. Exploration Geophysics, 51(1), 155–169. https://doi.org/10.1080/08123985.2019.1681895

- Wynn C. J., (1985), Induced Polarization and magnetic response of titanium-bearing placer deposits in the south-eastern United States, US Geological Survey, open-File Report, n85-756.
- Wynn C. J., (1986), Induced polarization used in titanium exploration in onshore and offshore environments, SEG Technical Program Expanded Abstracts 1986, ISSN (print):1052-3812 ISSN (online):1949-4645
- Wynn C. J., (1988), Titanium Geophysics: The application of induced polarization to sea-floor mineral exploration, Geophysics, 53(3), 290-416, https://doi.org/10.1190/1.1442472

Chapter 5: Conclusions and outlook

The supply of critical raw materials is one of the central challenges that the European Union must address to achieve the objectives of the energy transition towards decarbonisation by 2050. To stabilise and protect supplies, it is necessary to develop mineral independence starting from the location of mineral deposits within the continent. This, as well as a socio-political matter, is also a technological challenge for which the exploration and exploitation methodologies need to be safe, reliable and non-invasive. This PhD project, co-financed by the resources in the frame of the PON REACT-EU Program, aims to give a contribute to this field: to develop and improve novel non-invasive techniques for an efficient mapping of mineral deposits. This thesis focuses on airborne induced polarization (AIP) method, for which different aspects have been investigated along the work. The method is based on the possibility to model the induced polarization (IP) effects from the airborne electromagnetic (AEM) measurements. This would allow to map, as well as the ground conductivity contrasts (for which AEM methods are commonly applied), also the chargeability contrasts that could be linked to disseminated mineralization. An effective AIP mapping would thus reduce the exploration risk and cost allowing to drive the ground exploration from a larger scale airborne survey. Also, it has been demonstrated how failing to model IP in EM data brings to an incorrect resistivity modelling, in terms of geometries and thicknesses of the conductive layers. At the same time, as illustrated from the introduction and along the thesis, there are many complexities that have limited the method to an extensive application: the equivalencies during modelling, the unclear relationships between the airborne inductive IP and the ground galvanic methods and the difficulties in the geological interpretation of the airborne chargeability are examples of these. These aspects have historically discouraged the use of this technique for exploration purposes, relating the IP measurement uniquely to the classic galvanic DCIP. Along the chapters of this work, these aspects have been treated with the purpose to improve the applicability and effectiveness of the method for mineral exploration. I evaluated these aspects at different scales of application, from continental to deposit scale and using different inductive (fixed-wing and helicopter-borne) and galvanic (different instruments, settings and sequences) methods to measure ground chargeability.

Starting from the larger scale of application, the first work I present is to evaluate the sensitivity of the TEMPEST™ fixed-wing airborne EM system to AIP effects. This system is largely used for regional and continental-scale resistivity mapping, such in the AusAEM project, and its sensitivity to AIP has never been demonstrated. This work, presented in *Chapter 2*, has been firstly developed over a large synthetic dataspace and model-space inspection (*section 2.2*): the forward responses of several IP-affected transients have been compared with their purely-resistive counterparts. The results show how few milliradians of ground chargeability can give measurable distortions in the TEMPEST™ fixed-wing. The synthetic results have then been validated comparing the map of negative recordings (above noise level) of the entire AusAEM project, which partially covers the Australian country, with the available national geological, radiometric and cover thickness maps. The correlation between the negatives and the thinner cover has been shown also by this mapping

, confirming the synthetic results. When the conductive cover is thin and chargeable above a strongly resistive bedrock, the purely electromagnetic currents decay quickly (also because of the presence of the resistive layer) while the polarization currents continue to develop in the shallow layer. As result, the polarization currents dominate the purely EM currents giving strong negatives in the measured data, expression of the ground polarization. In *section 2.3*, the TEMPEST™ data have been modelled and compared first with the chargeability and resistivity models retrieved by two overlapping SkyTEM helicopter-borne data (*section 2.3.1*) and then with the geological model obtained by drillholes (*section 2.3.4*) relative to the well-known Nebo-Babel deposit. The results showed a good consistency between the airborne chargeability models of the fixed-wing and helicopter-borne methods, and with the geological information of a known deposit. Part of the real-data experiments for the TEMPEST™ system, the modelling of 20,000-

line kilometres of data from the AusAEM project has been carried and retrieving the chargeability and resistivity model of the entire Musgrave Province in South Australia. These results, shown in *section 2.3.4*, have been compared with the non-IP inversion, showing a reduction in the retrieved inversion misfit and an improved comparability with the mapped geology of the area.

Reducing the AIP scale of application, in *Chapter 3*, the airborne inductive chargeability mapping has been compared with the chargeability models retrieved from 17 ground galvanic DCIP profiles. The comparison has been carried in an area under current exploration in the Iberian Pyrite Belt in Spain. The airborne EM data have been here modelled following an approach that points to reduce equivalencies during modelling, exploiting a multi-meshes approach, as indicated in *section 3.3*. Here, the spectral parameters have been mapped in a 2D mesh, while the resistivity and chargeability have been defined in a 3D mesh. This approach is proposed to improve the chargeability sensitivity at depth and to reduce the equivalencies during the modelling between the spectral parameters and chargeability. Moreover, the MPA re-parametrization of the Cole and Cole model, which reduced the correlation between parameters, has been adopted to parametrize the model space. The AIP inversion results have then been compared with chargeability models obtained by the inversion of 17 DCIP profiles. In the galvanic forward modelling the full-voltage decay, the transmitter waveform, the gating and the receiver transfer function are included as for AEM data. This has been carried to reduce ambiguities during comparison introduced by different modelling approaches. The results, shown in *section 3.4*, shows a spatial consistency with the ground DCIP retrieved chargeability models with the airborne mapping confirmed by the ground galvanic profiles. Good compatibility in the mapping has been reached despite the differences in the spectral contents of the two methods, although the ground anomalies have often shown stronger magnitude anomalies respect with the airborne. This is explained by the smaller bandwidth of the airborne method, which not allows to measure the peak of spectral chargeability but its continuation to higher frequencies (at which the AEM is sensitive) only. The effect of a chargeable body with these spectral characteristics are measurable only if the chargeability peak is associated with a low frequency dependence which does not peak the maximum chargeability on a small frequency range. This subtle chargeable response can be easily lost during inversion if the equivalencies are not limited during modelling. The comparison between airborne and ground also show the importance to adopt a consistent modelling: this avoids the introduction of intrinsic differences that do not allow to consistently compare the results. Modelling both the DCIP and AEM data including full voltage decay, receiver transfer function, transmitter waveform and time gates, shown that it is possible to retrieve analogue chargeable structures between airborne and ground IP and allows to develop quantitative comparisons. To improve the phenomenological understanding and methodology, a joint inversion between the two techniques have been carried considering IP effects. The results, in *section 3.5*, showed that it is possible to resolve the ground chargeability merging the different sensitivities of the two methodologies and converging to a unique chargeability model. This has been reached without significatively increase the data misfit, indicating how the datasets accept the contribute of each other dataset adapting their spectral parameters (i.e., reducing the frequency dependence to extend the frequency peak to higher frequencies satisfying both the datasets).

In the last chapter, consistently with the idea of an AIP informed generative exploration approach of *Chapter 2* and with the methodological findings of *Chapter 3*, the airborne IP has been actively used during an exploration programme for the targeting of resistive and chargeable bodies in a greenfield project. To maximize the survey effectivity, a feasibility study (*section 4.3*) for different geological configurations, consistent with the ancillary information, has been carried to verify the system sensitivity to the target polarization and to better design the system characteristics to maximize the IP effects in the dataspace. The study leaded to the flight of two AEM surveys with different base frequencies (25 Hz and 12.5 Hz) to improve both the near-surface resolution and the chargeability mapping. These have been modelled both independently and jointly. From the joint inversion, a model which includes the near surface resolution of the 25 Hz and the larger spectral content of 12.5 Hz to map IP effects is retrieved obtaining a unique chargeability and resistivity model. On the base of the results, the ground DCIP follow-up has been designed and acquired and the anomalies defined by the airborne independent and joint modelling have been confirmed by the galvanic data. In conclusion of the chapter (*section 4.5*), the joint inversion of the ground DCIP data acquired with three decades of gated decays, the 12.5 Hz and the 25 Hz base frequencies has been carried. The comparison between DCIP and AIP independent models shown significative differences. Differently with the previous chapter, for this DCIP acquisition a gradient sequence with 10 m spaced electrodes have been used, acquiring 3 decades of IP signal with a 100% duty cycle. These

DCIP settings largely improve the lateral resolution and enrich the spectral content of the ground measurements. As consequence, the differences with the inductive independent inversions are enhanced, highlighting significative discrepancies in resolution and distribution of chargeability models. Nevertheless, the 12.5 Hz independent inversion defines a chargeable body at depth with a lower magnitude and resolution respect DCIP but with a coherent lateral distribution above the DOI. In these terms, the AIP independent model defines a potential target to follow-up on ground with reliable depth and chargeability contrast. As general observation, as also defined by the feasibility study, reducing the system's base frequency allows to record a longer off-time which potentially increase the negative content related to IP effects. This observation is not generalizable for all the environments: much depends by the S/N of the area and by the spectral characteristics of the mineral target. When is possible to fly multiple base frequencies, a joint inversion of these potentially further reduces equivalences during modelling allowing to better delineate possible chargeable targets. This inversion, compared with the ground DCIP, retrieves a chargeability anomaly with similar magnitude of ground DCIP but with lower resolution. As general conclusion from this work, nevertheless the complexities in terms of non-uniqueness during inversion, lower resolution and intricate decision process, it is possible to retrieve reliable chargeability measurements from AIP for mineral targeting and ground follow-up.

To summarize, this work contributed to the following geophysical aspects of airborne induced polarization method:

- The TEMPEST™ time-domain AEM fixed-wing system has sensitivity to the ground polarization, and it is possible to model the ground chargeability from its data.
- A multi-meshes approach which splits the spectral parameters by the resistivity and chargeability has been applied to AIP modelling. This, together with a consistent galvanic-inductive data modelling, shown an improvement in comparability of airborne IP and ground DCIP chargeability models. These results suggest how it is possible to extract the ground chargeability information using AIP when the equivalencies in AIP are reduced and nevertheless the differences in bandwidth of the methods.

- The airborne chargeability is often weaker, in magnitude, when compared with the ground DCIP retrieved chargeability. This happens when the peak of frequency of the chargeable body is out the EM bandwidth. Reducing the frequency-dependence it is possible to model, within the EM bandwidth, chargeabilities relative to a low-frequency peak and to map consistent chargeable domains with galvanic method. These domains give a lower magnitude in the chargeability model but a spatially valuable chargeability contrast.
- A joint inversion between two AEM base-frequency systems considering AIP has been carried improving the targeting jointly solving the ground chargeability.
- For the first time, a greenfield exploration project has been designed, acquired, interpreted and developed around the airborne IP method for mineral exploration. A ground DCIP follow-up has been here successfully defined and acquired over an anomaly identified through airborne modelling.
- For the first time, a joint inversion between ground DCIP and airborne EM data has been carried including IP effects. It is possible to unify the IP bandwidth merging the galvanic and inductive sensitivity to IP, solving a unique ground chargeability model. When a single-peak chargeability model is used, the spectral parameters adapt to satisfy both the sensitivities. The frequency dependence decreases to extend the frequency peak to a wider range of frequencies which satisfies both the galvanic and inductive measurements.

There are, of course, also many open questions and possible improvements of the general AIP technique and of the work carried for this thesis. These spans from the physical description of the problem to its modelling to the improvement in data acquisition. In terms of AIP modelling, it has been shown how the proposed multi-meshes modelling approach helps in the equivalency reduction but, of course, these are not completely overcome as far as a deterministic approach is used to solve the inverse problem. Including the AIP in a probabilistic framework would quantitatively provide an uncertainty estimation on the retrieved model including the equivalences in the solution of the inversion procedure. At the same time, larger is the dataspace and more complex is the probabilistic inversion both in terms of computation time and convergence. Still in the field of equivalencies during AIP modelling, that represent the main challenge to effectively achieve a correct modelling, the joint inversion proposed in *Chapter 3* and *4*, offers a valuable tool to reduce ambiguities. This exploits the combination of different data sensitivities to solve the ground electrical properties in the same inversion framework. To do this, many complexities must be considered. The large number of parameters and the significative difference in sensitivity of the ground and airborne data make the inversion fit a challenging goal to achieve. The wider DCIP bandwidth often leads the inversion to solutions that difficultly satisfy the AEM dataset and vice-versa. To overcome these challenges the available tools are the choice an appropriate starting model, the accurate data standard deviation (to weight the datasets during inversion) and the maximum-minimum parametrical range within which the inversion can span. In this sense, the more datasets are introduced in inversion the more a-priori geophysical information is needed to reach a common convergence during IP inversions. For instance, as illustrated in *Chapter 3* and *4*, a frequency dependence (the Cole and Cole c parameter) which ranges between 0.2 and 0.6 can extends the chargeability peak to a wider range of frequencies allowing to satisfy both the DCIP (that has more sensitivity to low frequencies) and AEM (with sensitivity to high frequencies) data. The parametrical range for c is crucial to achieve the inversion convergence, allowing to model high time constants, (as seen in C*hapter 3*) often required by the DCIP data, but fitting the AEM data. Even the amount of data per dataset influences the outcome of the inversion: the larger dataset has a bigger weight in the objective function, favouring the inversion toward a solution that minimizes its misfit and neglecting the fit of the other one. This complexity can be overcome weighting the dataset with standard deviations or selecting a starting model retrieved by the independent inversion of one of the two datasets. In joint inversion, an easier convergence is reached where one of the two datasets has less sensitivity, often as consequence of the survey characteristics, such as when a large electrode distance that does not allow a near surface sensitivity to DCIP or when the AEM is not sensitive to the deep structures proposed by the DCIP. In these cases, the inversion converges much easier given the lack of sensitivity of one of the two datasets. Another reason of complexity is in the data quality. The ideal DCIP dataset is acquired with a low contact resistance, in an area with a gentle topography (if modelled 2D), with a perfectly straight profile and far from infrastructures. The same considerations are necessary for the AEM data; these should be acquired with a well monitored system, with the primary field perfectly removed in the delivered data and well described processing routine provided by the provider (i.e., not so often…). The data imperfection competes in the joint inversion complexity, requiring frequent ad-hoc solutions to overcome these. Among possible improvements to our approaches, a verification of the joint inversion through direct borehole would provide fundamental answers to the research. This, as well as to confirm the complex multi-mesh or joint inversion procedure, would also help to calibrate (and verify) the geophysical response of a polarizable body at different IP methodologies. More in general, an extensive comparison with drillholes information from different environments and geological setting would extensively and quantitatively prove the AIP sensitivity to geologic materials. Then, for AIP method, a lab/petrophysical study of the inductive IP response of geological materials at both low and high frequencies would help in this direction.

As general outcome of this thesis work, several aspects of the airborne inductive induced polarization method have been treated to improve the methodological understanding and test its applicability and effectiveness for exploration applications. From this contribute I conclude that the AIP can represent an effective geophysical method to map the ground chargeability, and that it has a significant overlap in the sensitivity with ground chargeability. These conclusions, as demonstrated through the thesis work, can be generalizable at all the exploration scales, from the continental to the deposit one, for which the modelled chargeabilities have been compared and verified with other techniques and with geological mapping to assess their reliability. The scale of application, a key aspect in exploration, has been thoroughly explored in this thesis. Our findings support the effectiveness of an AIP exploration workflow that starts at regional scale, ideally financed by public institutions as in Australia, and provides the input for downscaling the mineral research down to the deposit scale, where the joint interpretation and modelling with galvanic data can increase significantly the model resolution and, eventually, the success rate of the exploration.

Appendix

In this appendix, I provide a comparison between the airborne EM survey of *Chapter 3* modelled considering IP and not. This comparison is carried to highlight the differences and consequences of the two modelling approaches for a dataset which does not show any evidence of IP effects (absence of negative recordings in a survey flown with a concentric-loop configuration). *Chapter 3* do not include this comparison: this has been done to maintain the focus of the work on airborne and ground comparison and their joint inversion.

For the non-IP modelling I used the same starting model, vertical and lateral discretization used for the AIP inversion. The starting model consists in a homogeneous halfspace of 100 Ω·m, vertically discretised with 23 layers of log-increasing thicknesses from surface to 500 m of depth. Laterally, along X and Y, regularly spaced nodes (40 m) have been defined.

A comparison for a near-surface layer at 40 m of depth is shown in *figure a.1*. In *figure a.1a* the result of the non-dispersive resistivity modelling is shown. In figure *a.1b* and *a.1c* the dispersive-resistivity results are shown with resistivity and chargeability, respectively.

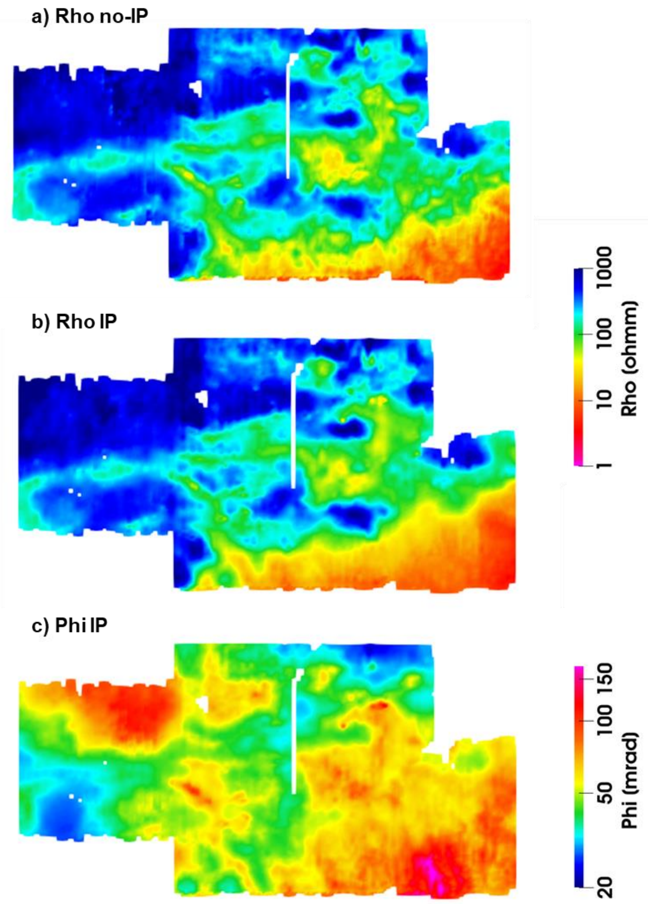

Figure a.1. Figure a.1. Resistivity comparison for a depth slice at 40 m of depth. In (a) the non-IP modelled resistivity is shown, while in (b) the IP modelled resistivity. In (c) the chargeability model.

In the near surface (*figure a.1*) the differences between the two resistivity models are mostly relative to the magnitude of the conductive bodies. In the non-IP inversion, the resistivity model shows higher conductivities in comparison with the IP retrieved models. Even the resolution of the resistivity model for the non-IP inversion looks higher, solving structures with smaller wavelengths. The difference in magnitude is consequence of the AIP modelling: the early times channels, when high in signal, can be modelled either with a strong conductor or with a less conductive but chargeable body. In this latter case, the near-surface layers conductivities decrease. This is also visible by the consistency between conductive domains of *figure a.1b* and chargeable domains in *figure a.1c*. Nevertheless, the lateral distribution of the modelled resistivities is similar between the two, defining resistive and conductive domains consistently within the survey area.

In *figure a.2*, a comparison for a depth slice at 100 m is shown.

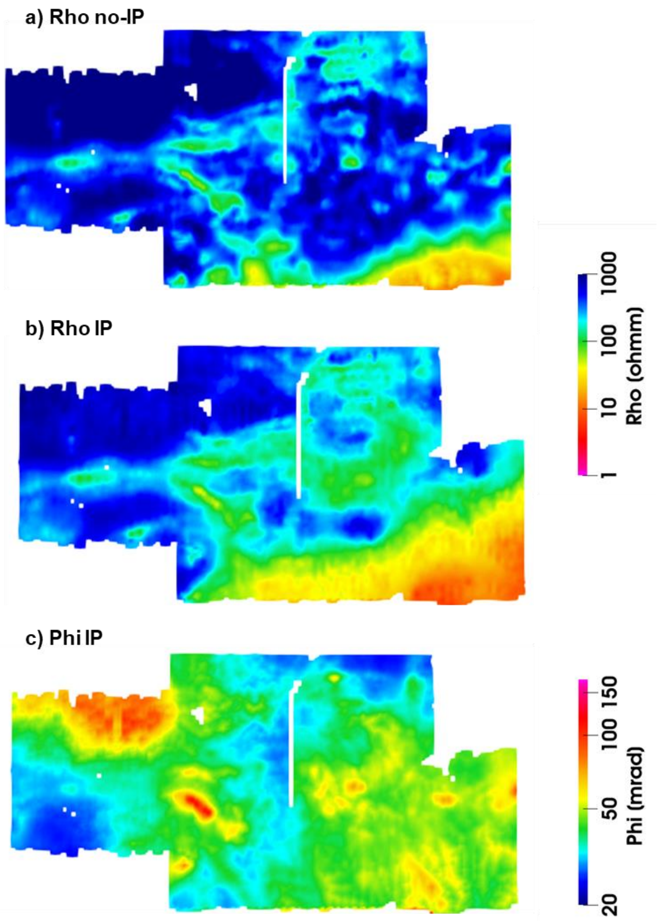

Figure a.2. Resistivity comparison for a depth slice at 100 m of depth. In (a) the non-IP modelled resistivity is shown, while in (b) the IP modelled resistivity. In (c) the chargeability model.

Increasing the depth at 100 m, the differences between the resistivity models increase as visible in *figure a.2*. The conductive isolated bodies (~ 100 Ω·m) defined in the resistivity model of the non-IP inversion largely disappear in the IP resistivity model. These are included in a conductive layer in the central portion of the survey area. In terms of interpretation, the two results give completely different ground description. The non-IP inversion defines isolated bodies which could be chosen as potential drilling targets. The IP inversion defines a moderately conductive layer that could be interpret as a stratigraphical unit. Within this, some isolated chargeable anomalies are defined by the AIP model and confirmed by the DCIP profiles for the area. In terms of modelling, it is common to retrieve, when these comparisons are carried, smaller resistivities at depth for IP-modelled EM data. This because, as for the near surface higher voltages, the fast decays at late times can be modelled either by a very resistive or by a less resistive but chargeable body. As highlighted in *Chapter 3*, I remark again how these data would typically be considered not affected by IP effects given the absence of negatives.

More generally, as also seen in *Chapter 2* comparing IP and non-IP modelling for fixed-wing systems, modelling EM data including IP often leads to retrieve less conductive ground in the near surface and more conductive bodies at depth when compared with non-IP resistivities.

The retrieved inversion misfits computed as in *equation 2.6* are shown in *figure a.4*.

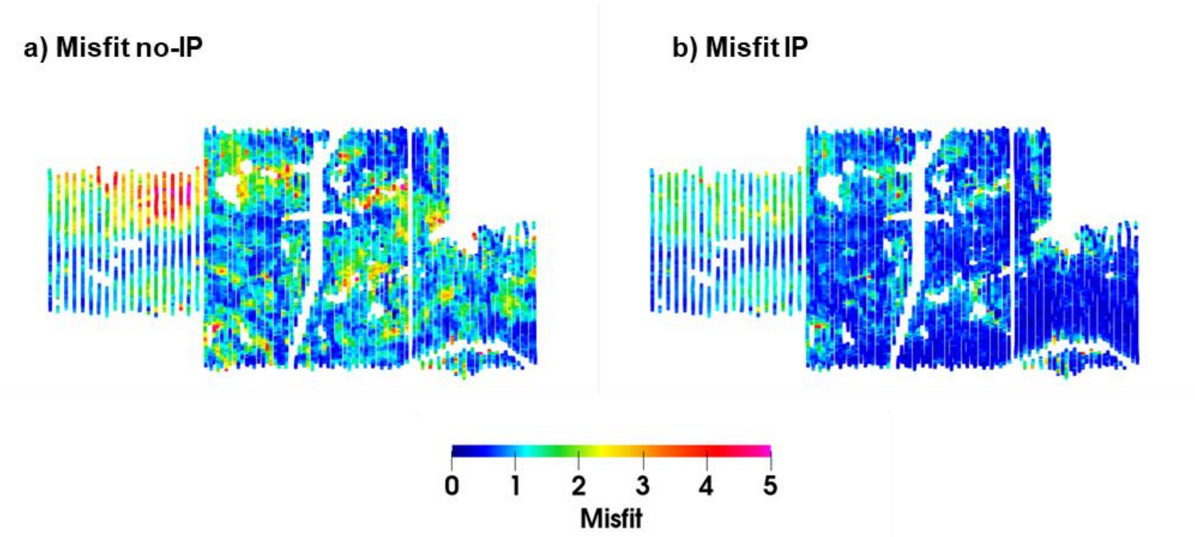

Figure a.4. Misfit comparisons for non-IP (a) and IP (b) inversion.

The inversion misfit generally decreases when the data are modelled considering IP effects. The higher inversion misfit of the non-IP inversion (*figure a.4*) often corresponds to areas where ground chargeability has been modelled, as visible from *figures a.1c* and *a.2*c.